

Luminescence and Photolysis in Organic-Inorganic Hybrid Coordination Polymers

by

Jingjing Yan

A Dissertation Submitted to the Faculty of the

WORCESTER POLYTECHNIC INSTITUTE



WPI

in partial fulfillment of the requirements for the

Degree of Doctor of Philosophy

in

Chemistry

October 2018

APPROVAL PAGE

Doctor of Philosophy Dissertation

Luminescence and Photolysis in Organic-Inorganic Hybrid Coordination

Polymers

Presented by

Jingjing Yan

Approved by

Advisor: Dr. Shawn C. Burdette

Committee member: Dr. John C. MacDonald

Committee member: Dr. James P. Dittami

Committee member: Dr. Joshua R. Farrell

Acknowledgements

First and foremost, I would first like to thank my advisor Dr. Shawn C. Burdette. His rigorous scientific attitude, passion and unsurpassed knowledge not only guided me with my research in six years, but also directed me to become an independent scientist, for which I will always be grateful.

I would also like to thank other members of my dissertation committee for being supportive throughout this journey. Thanks to Dr. John C. MacDonald, for his patience in guiding me through crystallography field. To Dr. James P. Dittami, for his great suggestions and teaching me advanced NMR. And to Dr. Joshua R. Farrell, for his valuable advice on committee meetings.

I would like to express gratitude to all faculties, staffs and graduate students in the Department of Chemistry and Biochemistry for their support. I would like to thank Dr. Christopher R. Lambert for his help on solid state emission experiments, thank Dr. Ronald L. Grimm for valuable discussions and help on XPS. I would also like to thank Andy Butler and Daryl Johnson, for their support on instruments. Andy is always there for instrument training and repairing. I would like to thank Ann Mondor for her constant support.

I would like to thank current and past Burdette group members Dr. Prem N. Basa, Dr. Fasil Abebe, Chelsea Barr, Xiaomeng Liang, undergraduate students Ricky Alvarado, Kady Ferguson, Jonathan Jironvil, REU students Corrianna Boucher, Katherine Fossum for their help during my study. Especially Prem, for his guidance and support on my research.

Finally, to my amazing wife Weicong –I could not be here without your continuous support, encourage and love. You are always there for me, even in the toughest days. I appreciate all your love and tolerance of me. To my lovely son, Alexander (Maoqi), I enjoy every moment with you. You are the best gift for me and I will love you beyond reason. I must express my very profound gratitude to my parents and mother-in-law, and my younger brother Xin, thanks for your unconditional support and love.

Table of Contents

List of Figures.....	v
List of Schemes.....	viii
List of Tables.....	ix
Chapter 1 Photochemistry in Metal-Organic Framework: Emissive, Switchable and Degradable MOF	1
1.1. Introduction.....	2
1.2. Photoemissive MOF	3
1.2.1. Ligand-centered Emission.	5
1.2.2. Ligand-to-Metal-Charge-Transfer (LMCT).	7
1.2.3. Metal-to-Ligand-Charge-Transfer (MLCT).	10
1.2.4. Lanthanide Luminescence and Antenna Effect.....	11
1.2.5. Emission from MOF Guests.....	13
1.3. MOF with Photoswitchable Components	16
1.3.1. Photoswitchable Compound as Linker Sidechain.....	16
1.3.2. Photoswitchable Compound as Guest Molecule	20
1.3.3. Photoswitchable Compound as Backbone Linker.	23
1.4. Photodegradable MOF.....	25
1.5. Conclusions.....	28
1.6. References	28
Chapter 2 Emissive Azobenzenes Delivered on a Silver Coordination Polymer	48
2.1. Introduction.....	49
2.2. Experimental Section.....	50
2.2.1. General Procedures.....	50
2.2.2. Collection and Reduction of X-ray Data.....	56
2.2.3. Spectroscopy	57
2.3. Synthesis and Structure.....	58
2.4. Emission.....	70
2.5. DFT Calculations	73
2.6. Analyte Detection.....	78
2.7. Conclusions.....	80
2.8. Acknowledgement.....	80
2.9. References	92

Chapter 3 Detection of Surface Adsorbed Guests on Emissive MOFs by X-ray Photoelectron Spectroscopy	99
3.1. Introduction.....	100
3.2. Experimental Section.....	102
3.2.1. General Procedures.....	102
3.2.2. Collection and Reduction of X-Ray Data.....	104
3.2.3. Spectroscopy.....	105
3.2.4. X-ray Photoelectron Spectroscopy.....	106
3.3. Synthesis and Structure.....	107
3.4. Photophysical Properties of ABMOF-1 and Guest Molecule Detection.....	111
3.5. Conclusions.....	121
3.6. Acknowledgement.....	122
3.7. References.....	129
Chapter 4 MOF Decomposition and Introduction of Repairable Defects Using a Photodegradable Strut	136
4.1. Introduction.....	137
4.2. Experimental Section.....	138
4.2.1. General Procedures.....	138
4.2.2. Collection and Reduction of X-ray Data.....	140
4.2.3. Spectroscopy.....	142
4.2.4. Photolysis of NPDAC-MOF.....	143
4.2.5. Defects Creation and MOF Repair.....	143
4.3. Design and Structural Considerations.....	144
4.4. Photolabile Strut and MOF Synthesis.....	145
4.5. MOF Photolysis and Reassembly.....	149
4.6. Conclusion.....	157
4.7. References.....	163
Chapter 5 On-Demand Guest Release from MOF-5 Sealed with Nitrophenylacetate Photocapping Groups	169
5.1. Introduction.....	170
5.2. Experimental Section.....	171
5.2.1. General Procedures.....	171
5.2.2. Powder X-ray Diffraction.....	174
5.2.3. Spectroscopy.....	175
5.2.4. Guest Loading, Trapping and Release.....	176

5.3. Guest Trapping Strategy and Photolabile Capping Group Synthesis and Characterization	177
5.4. Guest Molecule Loading and Release	180
5.5. Conclusions.....	189
5.6. Acknowledgement.....	189
5.7. References	196

List of Figures

Figure 1.1. Eu ³⁺ /Tb ³⁺ bimetallic MOFs with different ratio	12
Figure 1.2. Encapsulation and photo-induced release of rhodamine B cargo from AB functionalized MOF capped by β -CD.....	18
Figure 1.3. Isomerization of spiropyran and encapsulation of spiropyran derivative in MOF	22
Figure 2.1. Preparation of AgAAMoP showing the ORTEP diagram of AzoAMoP and AgAAMoP.....	62
Figure 2.2. Preparation of AgAAMmP showing the ORTEP diagram of AzoAMmP and AgAAMmP ...	65
Figure 2.3. Preparation of AgAAMpP showing the ORTEP diagram of AzoAMpP and AgAAMpP.....	66
Figure 2.4. Preparation of AgAAEoP showing the ORTEP diagram of AzoAEoP and AgAAEoP.....	68
Figure 2.5. Preparation of AgAAEpP showing the ORTEP diagram of AzoAEpP and AgAAEpP.....	69
Figure 2.6. Solid state emission spectrum of the five AzoAXxP silver complexes.....	71
Figure 2.7. Solid state diffuse reflectance and emission spectra of AgAAEpP	72
Figure 2.8. Calculated singlet excitation energies of AB, DAAB, AzoAXxP and AgAAXxP.....	75
Figure 2.9. Steady-state emission and quantum yield determination of AgAAEpP.....	77
Figure 2.10. Normalized emission response of AgAAEpP to pyridine and DMA.....	81
Figure 2.11. ¹ H NMR of compound AzoAMmP (3).....	87
Figure 2.12. ¹³ C NMR of compound AzoAMmP (3).....	87
Figure 2.13. ¹ H NMR of compound AzoAMpP (4).....	88
Figure 2.14. ¹³ C NMR of compound AzoAMpP (4).....	88
Figure 2.15. ¹ H NMR of compound AzoAEpP (5).....	89
Figure 2.16. ¹³ C NMR of compound AzoAEpP (5).....	89
Figure 2.17. Powder X-ray diffraction patterns of simulated and experimental AgAAEpP, and after exposure to pyridine and removal.....	90
Figure 2.18. The thermogravimetric analysis (TGA) diagrams of the five aAB silver complexes.	91
Figure 3.1. ORTEP plot, wireframe diagram and space-filling model of ABMOF-1	108
Figure 3.2. Solid state diffuse reflectance and emission spectra of ABMOF-1.....	110
Figure 3.3. Normalized emission response of ABMOF-1 to 2,4-DNP and Stern-Volmer plot.....	112
Figure 3.4. Normalized emission response of ABMOF-1 to 2,6-DNP-4-CF ₃ and Stern-Volmer plot....	113
Figure 3.5. Normalized fluorescence intensity of ABMOF-1 after adding 10 eq different analytes	114
Figure 3.6. Absorbance spectra of analytes and emission spectra of ABMOF-1 and ABMOF-2 suspended in DMF	114
Figure 3.7. XP spectra of ABMOF-1 samples with and without exposure to 2,6-dinitro-4-trifluoromethylphenol (2,6-DNP-4-CF ₃) guest.....	116

Figure 3.8. XP spectra of Zn 2p _{3/2} and F 1s regions for ABMOF-1 exposed to 2,6-DNP-4-CF ₃ in different angles and after argon-ion sputtering.....	118
Figure 3.9. Thermogravimetric analysis (TGA) diagrams of ABMOF-1.....	125
Figure 3.10. Thermogravimetric analysis (TGA) diagrams of ABMOF-2.....	125
Figure 3.11. Digested NMR of ABMOF-1, comparing with original ligands NDC and AzoAEpP.....	126
Figure 3.12. Digested NMR of ABMOF-2, comparing with original ligands BDC and AzoAEpP.....	126
Figure 3.13. Powder X-ray diffraction patterns of experimental and simulated ABMOF-1.....	127
Figure 3.14. Powder X-ray diffraction patterns of experimental and simulated ABMOF-2.....	127
Figure 3.15. PXRD diffraction patterns of ABMOF-1 and after quenching with 2,4-DNP and 2,6-DNP-4-CF ₃	128
Figure 3.16. Completely labeled ORTEP plot of 50% for ABMOF-2, showing highly disordered on the AzoAEpP ligand.....	128
Figure 4.1. HPLC analysis of the photolysis of NPDAC.....	145
Figure 4.2. ORTEP diagram and two-dimensional structure of NPDAC-MOF.....	148
Figure 4.3. Stacking HPLC traces of photolysis products of NPDAC-MOF and the ligand.....	150
Figure 4.4. Powder X-ray diffraction patterns of simulated and experimental NPDAC-MOF, and upon irradiation.....	153
Figure 4.5. ¹ H NMR spectroscopy NPDAC sodium salt after irradiation for 35 mins.....	154
Figure 4.6. ¹ H NMR spectroscopy NPDAC sodium salt after irradiation for 35 mins and extract with hexanes and DCM.....	154
Figure 4.7. Digested ¹ H NMR of PDAC-MOF, NPDAC-MOF, NPDAC30-MOF, irradiation of NPDAC30-MOF for 2 h, expose the irradiated material to PDAC 1 d, and expose the irradiated material to NPDAC for 1 d.....	156
Figure 4.8. Powder X-ray diffraction patterns of PDAC-MOF, NPDAC-MOF, NPDAC30-MOF, irradiation of NPDAC30-MOF for 2 h, expose the irradiated material to PDAC 1 d, and expose the irradiated material to NPDAC for 1 d.....	157
Figure 4.9. ¹ H NMR of NPDAC ligand.....	160
Figure 4.10. ¹³ C NMR of NPDAC ligand.....	160
Figure 4.11. Digested ¹ H NMR of PDAC-MOF.....	161
Figure 4.12. Digested ¹ H NMR of NPDAC-MOF.....	161
Figure 4.13. Digested ¹ H NMR of NPDAC30-MOF.....	162
Figure 4.14. Powder X-ray diffraction patterns of experimental and simulated PDAC-MOF.....	162
Figure 5.1. The possible photolysis route of PC1 and photoproducts in HPLC.....	181
Figure 5.2. The possible photolysis route of PC2 and photoproducts in HPLC.....	182

Figure 5.3. CV release profile from CVMOF without capping and photos taken in the process.....	185
Figure 5.4. In dark and photo-triggered CV release profile from CVMOF@PC1, CVMOF@PC2 and CVMOF@TPAA.....	187
Figure 5.5. ¹ H NMR spectroscopy of PC1 after irradiation for 20 mins.....	188
Figure 5.6. ¹ H NMR of photoproducts after PC2 photolysis.....	188
Figure 5.7. Powder X-ray diffraction patterns of experimental and simulated MOF-5.....	190
Figure 5.8. The thermogravimetric analysis (TGA) diagram of fresh prepared MOF-5.....	190
Figure 5.9. The thermogravimetric analysis (TGA) diagram of CVMOF.....	191
Figure 5.10. UV-Vis absorbance spectra showing photolysis of PC1.....	191
Figure 5.11. ¹ H NMR of [bis-(3-nitro-benzyl)-amino]-phenyl-acetic acid methyl ester (3).....	192
Figure 5.12. ¹³ C NMR of [bis-(3-nitro-benzyl)-amino]-phenyl-acetic acid methyl ester (3).....	192
Figure 5.13. ¹ H NMR of [bis-(3-nitro-benzyl)-amino]-phenyl-acetic acid (4).....	193
Figure 5.14. ¹³ C NMR of [bis-(3-nitro-benzyl)-amino]-phenyl-acetic acid (4).....	193
Figure 5.15. ¹ H NMR of [bis-(3-nitro-benzyl)-amino]-(3-nitro-phenyl)-acetic acid (PC1).....	194
Figure 5.16. ¹³ C NMR of [bis-(3-nitro-benzyl)-amino]-(3-nitro-phenyl)-acetic acid (PC1).....	194
Figure 5.17. ¹ H NMR spectroscopy showing thermal decomposition of compound PC1.....	195
Figure 5.18. CV release profile from CVMOF@DBA.....	195

List of Schemes

Scheme 1.1. Three typical photo-induced responses.....	2
Scheme 1.2. Schematic representation of ligand-centered emission in MOFs	5
Scheme 1.3. A simplified schematic electronic structure diagram showing LMCT and MLCT process in MOFs.	8
Scheme 1.4. Schematic representation of Jablonski diagram.....	11
Scheme 1.5. Schematic representation of lanthanide-centered MOF emission	14
Scheme 1.6. Schematic illustration showing sidechain photoswitchable compound acting as photo-triggered switches	16
Scheme 1.7. Scheme showing a framework structural change is induced by trans-cis isomerization of encapsulated azobenzene guest molecules.....	20
Scheme 1.8. Scheme showing unfavourability of trans→cis isomerization of AB derivatives when embedded as MOF backbone struts.....	23
Scheme 1.9. Scheme showing degradation of MOF caused by photo-induced decomposition	25
Scheme 2.1. Synthetic protocols for preparing five AzoAX _x P ligands	60
Scheme 4.1. The synthetic route of 2 and its photolysis reaction	144
Scheme 4.2. Proposed pathway to the formation of photoproducts from NPDAC (2) photolysis.....	146
Scheme 4.3. Proposed photolysis reactions of NPDAC and NPDAC-MOF.....	151
Scheme 4.4. Fully or partially linker exchange forming NPDAC-MOF or NPDAC ₃₀ -MOF.....	152
Scheme 5.1. The synthetic route of photolabile compound PC1	178
Scheme 5.2. Guest molecule loading, encapsulation and releasing from MOF-5 with photos taken of in the process.....	179
Scheme 5.3. Proposed mechanism of photolysis of PC1	183
Scheme 5.4. Proposed mechanism of photolysis of PC2	183

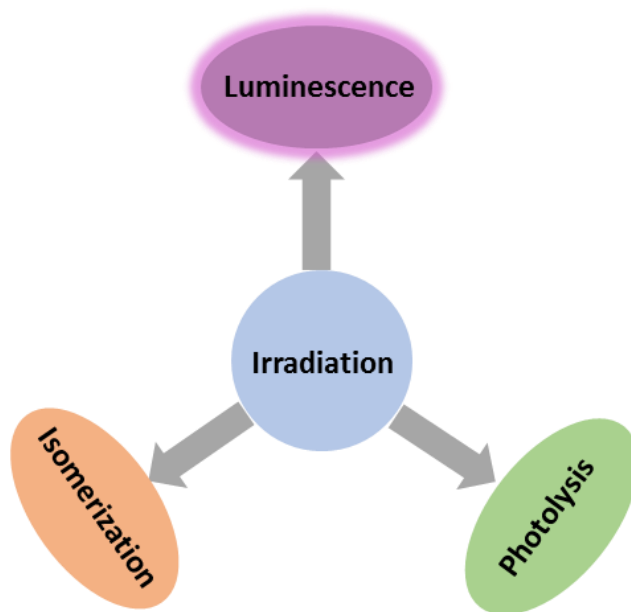
List of Tables

Table 2.1. Selected interatomic distances and angles for the five AzoAX _x P ligands.....	82
Table 2.2. Photophysical properties of AzoAX _x P ligands and coordination polymers.....	83
Table 2.3. Calculated orbital contours for ligands extracted from solid-state structures, as well as azobenzene.....	84
Table 2.4. Calculated orbital contours for ligand clusters of silver-coordinated materials, as well as DAAB.....	85
Table 3.1. Crystal data and structure refinements for ABMOF-1.....	123
Table 3.2. Crystal data and structure refinements for ABMOF-2.....	124
Table 4.1. Crystal data and structure refinements for NPDAC-MOF.....	159

**Chapter 1 Photochemistry in Metal-Organic Framework:
Emissive, Switchable and Degradable MOF**

1.1. Introduction

A photo-induced response is one that occurs upon the absorption of light. In photochemistry, there are three typical photoresponses—photoluminescence, isomerization, and photolysis (Scheme 1.1). As a subcategory of photoluminescence, fluorescence has been widely used in applications such as fluorescent labelling,^{1,2} chemical sensors,^{3,4} and fluorescent lamps.^{5,6} Another type of photoluminescence is phosphorescence, which has a special property in that the glow is slower after irradiation, which suggests potential applications in areas that require delayed emission, such as glowing toys, stickers, and paintings.^{7,8} Apart from photoluminescence, light-induced interconversion during isomerization is a matter of both fundamental and applied interest for other major applications, including molecular switches, photoswitchable ion transportation, photo-responsive micelles, and liquid crystals.⁹⁻¹² Photoirradiation can also be destructive, as indicated by the photodegradation of photolabile compounds or photoremovable protection groups, and can therefore be applied in photocages, sensors, synthesis, and molecular release.¹³⁻¹⁵



Scheme 1.1. Three typical photo-induced responses.

One of the major challenges in using standalone photoresponsive molecules, however, is that, to be functional, most of these molecules must be dissolved in a solution, which makes them difficult to transfer into or adjust in other systems.¹⁶ A solid solution must be found that provides rigidity, portability, and accessibility, while maintaining their intrinsic molecular properties. Porous materials can be defined as any materials that have pores, including organic, polymer, and inorganic materials, with pore sizes varying from nanometer- to millimeter-scale. A unique type of inorganic solid framework, constructed of metal ions or nodes connected via organic linkers, is the metal-organic framework (MOF), which is one candidate for incorporating photoresponsive molecules.^{17,18} MOFs possess intrinsic advantages such as porosity, a large internal void space and surface area, and an abundance of metal/ligand choices and combinations.¹⁹⁻²² When a fluorescent chromophore is incorporated with an MOF, it can either generate stronger emissions^{23,24} or glow at a different wavelength via a charge transfer process between the ligands and metal centers^{25,26} or an energy transfer process from antenna chromophores to acceptor components.²⁷ Its tunable wavelength suggests the potential use of photoemissive MOFs in applications such as luminescent sensors, light emitting devices (LEDs), and fluorescent probes for nitroaromatic explosives.²⁸⁻³⁰

Unlike photoemissive materials, light-induced isomerization makes compounds such as azobenzene (AB) derivatives a unique type of functional material. Spiropyran and diarylethene derivatives also undergo ring opening and closure upon exposure to light, usually accompanied by photochromic color change. Incorporating spiropyran into an MOF can lead to reversible framework color change,³¹ and using diarylethene derivatives as MOF struts can induce local framework movement.³²⁻³⁴ More broadly, AB can be introduced into an MOF as guest molecules, linker side chains, or backbone struts, which leads to changes in the MOF pore size,³⁵ CO₂ adsorption alternation,³⁶ or framework shrinking.³⁷ Whereas we observed no framework change

by the irradiation of AB-bipyridine-ligands-based silver complexes³⁸ or MOFs,³⁹ we did see a dramatic emission increase from that of the apo ligand. As these chromophores behave variously as linkers, linker side chains, and guest molecules, together with the different phenomena observed for different molecules, more research in this area is needed to reveal details of the process and mechanism responsible for the behavior of photoswitchable components in MOFs.

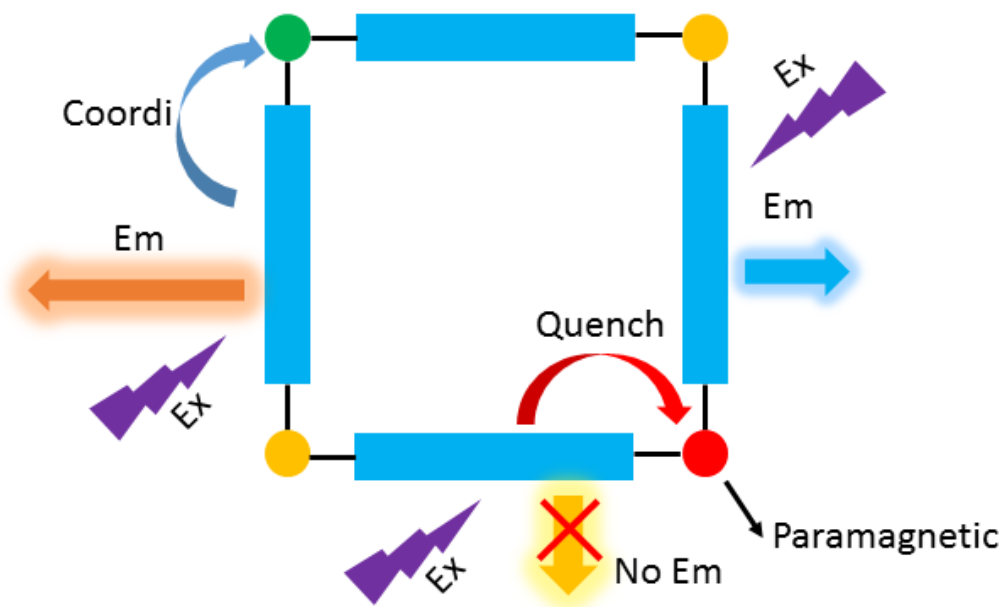
Whereas photoisomerization is non-destructive, although it can sometimes cause local framework changes, photolabile compounds undergo decomposition when exposed to light, and this property makes them excellent candidates for controlled metal release, as well as fluorescent metal probes, biochemical process sensors, and photo-switches for drug release.^{13,15,40,41} Photolabile compounds can serve as MOF linker side chains in the synthesis of novel MOF structures that cannot be easily obtained via *de novo* synthesis,^{42,43} thus providing a novel and unique method for the preparation of unapproachable MOFs. We believe that photodegradable MOFs can be constructed using ligands that decompose upon irradiation, but the lack of appropriate ligands and a solvothermal condition in MOF synthesis makes it difficult to obtain a photolabile framework. Although previous authors have reported observing a certain amount of photo-induced degradation of MOFs³⁷ and covalent organic frameworks (COFs)⁴⁴ constructed using AB derivatives, degradation induced by AB isomerization remains debatable.

Whereas there are numerous reviews of MOFs regarding their luminescence property, a comprehensive summary of photoemissive, photoswitchable, and photodegradable MOFs is lacking. In this paper, we first introduce various luminescence phenomena of emissive MOFs, including ligand-centered emission, charge-transfer-based emission, and an antenna effect. We then explore the behaviors of the photoswitchable components in MOFs. Lastly, we discuss photodegradable MOFs that comprise several photolabile compounds.

1.2. Photoemissive MOF

1.2.1. Ligand-centered Emission.

As fluorescent sensors, photoemissive MOFs always possess channels or pores with large diameters, which allows analytes diffusing in and sensed, with high sensitivity and fast response.³⁰ Even when the pores are blocked by framework interpenetration, MOF surface can still serve as interaction sites, due to its large surface area.^{45,46} Besides efficient conversion of UV radiation to visible light, emission wavelength of MOFs can be tuned by perturbing ligand electronic states via metal coordination (Scheme 1.2), making them great candidates for light emitting devices such as fluorescent lamps and plasma display panels.³⁰



Scheme 1.2. Schematic representation of ligand-centered emission in MOFs. There are three different mechanisms, solely ligand-based, metal center coordination influenced, and paramagnetic metal ion quenched. “Ex” stands for excitation, “Em” stands for emission, “Coordi” stands for coordination and “Paramagnetic” stands for paramagnetic metal ions.

The most straightforward strategy of making a luminescent MOF is to construct the framework with an emissive ligand. Linker-centered luminescent MOFs are made of conjugated organic compounds absorbing in UV and visible region, and the excitation of ligand usually happens through singlet-singlet transition.³⁰ In a typical linker-based emission, the emission energy of MOF is similar to the ligand.⁴⁷⁻⁵⁰ For example, 2,4,6-tris(4-pyridyl)-1,3,5-triazine (TPT) strongly emits a blue light at 469 nm, and four MOFs composed by this ligand emits in solid state between 465-478 nm, which can be clearly attributed to ligand-centered emission.⁵¹

While most ligand-centered MOFs emit in similar wavelength their ligand analogues, a redshift or blueshift is not uncommon, usually with a little wavelength difference.⁵²⁻⁵⁴ For example, free 1,3,5-benzenetricarboxylic acid (BTC) ligand emits at 370 nm, and two BTC MOFs (Zn and Cd) emit at longer wavelength, 410 and 405 nm, all in solid state form.⁵⁵ The redshifts can be attributed to ligand-centered electronic transitions perturbed by coordination to metal ions, and the difference emission energy between the two MOFs mentioned may be due to different coordination environment around the two metal ions. In addition, metal coordination influence can be huge if metal ions are paramagnetic such as copper(II), which can lead to a quench of the ligand-centered emission (Scheme 1.2).⁵¹ The reason could be the non-radiative decay from mixed fluorophore/metal $\pi\pi^*/dd$ state to $\pi\pi^*$ state of the organic fluorophore.⁵⁶

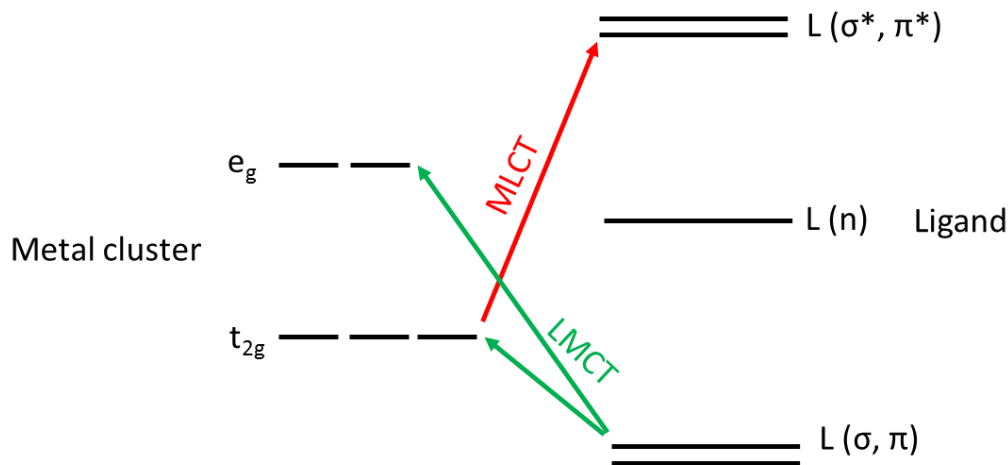
Not only small bathochromic or hypsochromic shift of emission wavelength, when fluorescent ligands are rigidified in MOFs, they also emit at similar intensity comparing to ligands. However, molecule such as tetraphenylethylene is an exception, of which the fluorescence in solution can be quenched by fast rotation of its aromatic rings and twisting of the C=C bond, while incorporating the compound into a rigid matrix can lead to strong emission, due to decreasing of non-radiative decay by restricting the rotation of the phenyl rings.²³ Interestingly, we discovered

that typically non-emissive azobenzene (AB) derivatives could be fluorescent when frozen in a solution, due to *trans-cis* isomerization (non-radiative decay) locking by strong intramolecular hydrogen bonding.⁵⁷ We further revealed embedding AB chromophores in Ag⁺ coordination polymer could dramatically enhance the degree of radiative decay and lead to a strong pinkish emission at room temperature, in which both intramolecular hydrogen bonding and metal coordination contribute.³⁸ DFT calculations in our work proves strong polymer luminescence arises from $\pi\pi^*$ excited state being stabilized below the interstitial $n\pi^*$ excited state.

1.2.2. Ligand-to-Metal-Charge-Transfer (LMCT).

While ligand-centered MOF gives similar emission as its ligand, making emission wavelength tunable is always desirable in luminescent materials, especially for their use in light emitting devices such as LEDs. Different from ligand-centered emission, in a typical ligand-to-metal-charge-transfer (LMCT) phenomenon, emission arises from a charge-transfer transition and the emission energy is always different from the ligand (Scheme 1.3).⁵⁸⁻⁶⁰ When molecular orbitals of ligand are full, charge transfer may happen from the ligand molecular orbitals to d-orbitals of metal or metal clusters, which are empty or partially filled. For example, in a MOF containing mix ligands of benzene-1,4-dicarboxylic acid (H₂BDC) and benzene-1,3,5-tricarboxylic acid (H₃BTC), the polymer's major emission redshifts from the ligands emission (370 nm) to 430 nm, while showing a shoulder peak at 370 nm. While the shoulder peak emission can be attributed to the ligand $n\leftarrow\pi^*$ emission, the major emission can be attributed to the charge-transfer transition.²⁵ In addition, the absorbance spectra show a hypsochromic shift of polymer from the two ligands, which may be attributed to metal-ligand coordination leading $\pi^*\leftarrow n$ transition perturbed by Zn²⁺. Although charge transfer emission, including an M-L or L-M emission, requires the metal center

is oxidizable or reducible, the zinc could be viewed as Zn-O cluster, qualifying it as an electron acceptor.⁶¹



Scheme 1.3. A simplified schematic electronic structure diagram showing LMCT and MLCT process in MOFs.

LMCT efficiency can be strongly affected by a second linker binding to metal, a co-crystallize compound, a counterion or a different coordination environment of metal ions. Six zinc MOFs with trimesic acid as ligand have been reported, with different amino alcohols added, either as co-crystallize solvent or a second linker.⁶² As reported, trimesic acid emits at 380 nm, and a MOF composed by this ligand and Zn^{2+} emits at 405 nm, showing LMCT phenomenon. However, three other MOFs co-crystallized with different amino alcohols show very weak emissions, which can be attributed to charge transfer process being prohibited by the presence of co-crystallize reagents, through strong hydrogen bonding interactions. More interestingly, when two different amino alcohols were coordinated to Zn^{2+} ions, one MOF showing LMCT with emission red-shifting to 430 nm, and the other MOF showing no emission at all. Although the reason is not revealed by the authors, it suggests LMCT charge transfer process can be influenced by various factors including metal-ligand coordination environment, co-crystalized solvent and different counter ions.

The emission wavelength from LMCT was found to be tuned by the number of guest water molecules. A luminescent MOF was reported showing strong fluorescence at 380 nm, redshifted from the ligand at 348 nm.⁶³ The LMCT induced redshift can be moved towards red light region gradually, with steadily loss of water molecules after being heated at different temperatures, and the emission varies from UV (380 nm) to visible light (430 nm). Different from solvatochromism of which solute showing different color in solvents with different polarity, this unique phenomenon can be caused by the absorbance of excitation UV by water molecules and anions, and LMCT process perturbed by hydrogen bonding interactions between water molecules, encapsulated BF_4^- and SiF_6^{2-} anions and MOF ligands. The original crystal has abundant lattice water and anions, the remove of which decreases hydrogen bonding interactions and thus decrease the influence on LMCT. More interestingly, re-hydration of the dehydrated MOF shifts wavelength back, indicating resumed H-bond interaction and LMCT perturbation.

As stated above, guest molecules and framework trapped ions can play a significant role in emission wavelength and efficiency during LMCT process. And it is also worth to note that LMCT and linker-centered emission are not mutually exclusive, as several literatures report the co-existence of the two mechanisms.^{25,52,64,65} LMCT was proved to be a powerful method in designing luminescent MOFs emitting in different energies; however, there are lack of researches on predicting the process. A recent report shows that LMCT can be predicted by using density functional theory (DFT).⁶⁶ In the study, the authors compared six metal nodes in UiO-66 framework and found that LMCT was only favorable in cerium-centered MOF, due to the low-lying empty Ce^{4+} 4f orbitals. They further revealed that the efficient separation of photogenerated charges through LMCT was the reason for high photocatalytic activity in Ce^{4+} MOFs. This work not only provides a novel way of foreseeing LMCT process, but also offers new method to design

efficient photocatalysts utilizing LMCT for better charge separation. Although still debated, LMCT was found to be a critical process determining the photocatalytic activity on hydrogen evolution by d^0 metal-organic frameworks, since electronic origin is the key part.⁶⁷⁻⁷⁰

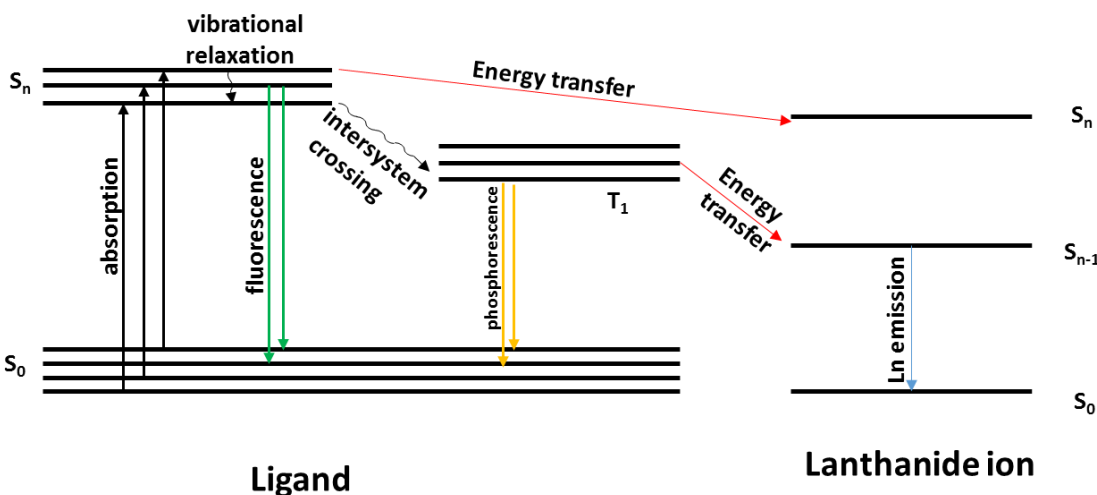
1.2.3. Metal-to-Ligand-Charge-Transfer (MLCT).

While LMCT stands for electronic transition from an organic linker-localized orbital to a metal-centered orbital, MLCT is the opposite process (Scheme 1.3), with charge transitioning from a metal-centered orbital to a ligand-centered orbital. MLCT is frequently observed in d^{10} Cu(I) and Ag(I) based MOFs. Comparing to the redshift of wavelength in LMCT, MLCT can be either blueshift or redshift. For example, a Cu(I) MOF with 4-hydroxypyridine-2,6-dicarboxylate as ligand emits at 398 and 478 nm, blueshifting from its free ligand green emission (526 nm), indicating a MLCT process from Cu-3d to O-2p and N-2p orbitals.⁷¹ Moreover, when additional metal (Ag^+) is presented in the structure, the emission shifts back to green (515 nm), suggesting a linker-centered luminescence originated from $\pi \leftarrow \pi^*$ transition of the organic linker, instead of MLCT. The reason is not specified by the authors, but the Cu-L-Ag connection could favor a charge transfer from ligand-centered orbitals to silver-center orbitals, following electronic transition from Cu(I)-centered orbitals to ligand orbitals, meaning MLCT effects could be cancelled out by the following LMCT.

A large redshift of Mn(II)-centered MOF has been reported.²⁶ Comparing to the blue emission of ligand at 440 nm, the MOF exhibits strong red fluorescence at 726 nm, which is a huge redshift caused by MLCT from Mn(II) ions to nitrogen and carboxylate-oxygen donors of imidazole ligand. Along with the long-lived emission lifetime of 0.3 ms, the system provides a new method to obtain luminescent MOFs for light-emitting diode devices. Both LMCT and MLCT can be applied for a tunable emission wavelength, making luminescent MOFs more suitable as

probes, sensors, or emitting candidates. Not like numerous researches on MLCT in rare metal complexes,⁷²⁻⁷⁵ the charge transfer process in MOFs is still undeveloped and further data is needed to better understand the process and mechanism.

1.2.4. Lanthanide Luminescence and Antenna Effect



Scheme 1.4. Schematic representation of Jablonski diagrams showing the basic photophysical processes of organic linkers, combined with energy migration and emission in lanthanide MOFs.

Strong, visible and long life-time emission, as well as large Stokes' shift, is essential for developing light-emitting devices, lasers, lighting and displays, photonic devices and biological imaging reagents. With a gradual filling of $4f$ orbitals, lanthanide ions exhibit narrow and characteristic $4f-4f$ transitions, so they can emit with a broad range, from ultraviolet (UV) to visible and near-infrared (NIR) region, which serves them as great candidates for emitting and optical applications.⁷⁶⁻⁷⁸ However, lanthanide ions suffer from weak light absorption and low quantum yields due to forbidden $f-f$ transitions implied by Laporte's parity selection rule.⁷⁹ This problem can be overcome by complexation of lanthanide ions and linkers with strong absorbing ability.⁸⁰⁻
⁸³ The coupling between linkers and metal ions allows direct energy transfer from linker excited states to metal energy levels, which is also known as sensitization or antenna effect. There are

typically three steps for lanthanide sensitization. Firstly, organic linker chromophores absorb energy and get excited. Secondly, energy is transferred to metal ions from linker excited states. Thirdly, lanthanide emits with high intensity.

For antenna effect to be effective, the lowest triplet state of organic linkers should be located at an energy level above the energy level of the lanthanide ions (Scheme 1.4). The preference of Eu(III) and Tb(III) based MOFs over other long-wavelength emissive MOFs such as Er, Gd and Nd, is determined by the intrinsic red and green color of first two, and their strong coupling to organic linkers.⁸⁴⁻⁸⁶ For example, isostructural lanthanide (Sm^{3+} , Eu^{3+} , Gd^{3+} , Tb^{3+} , Dy^{3+}) MOFs have been reported and strong emissions are only observed in Eu^{3+} and Tb^{3+} MOFs.⁸⁷

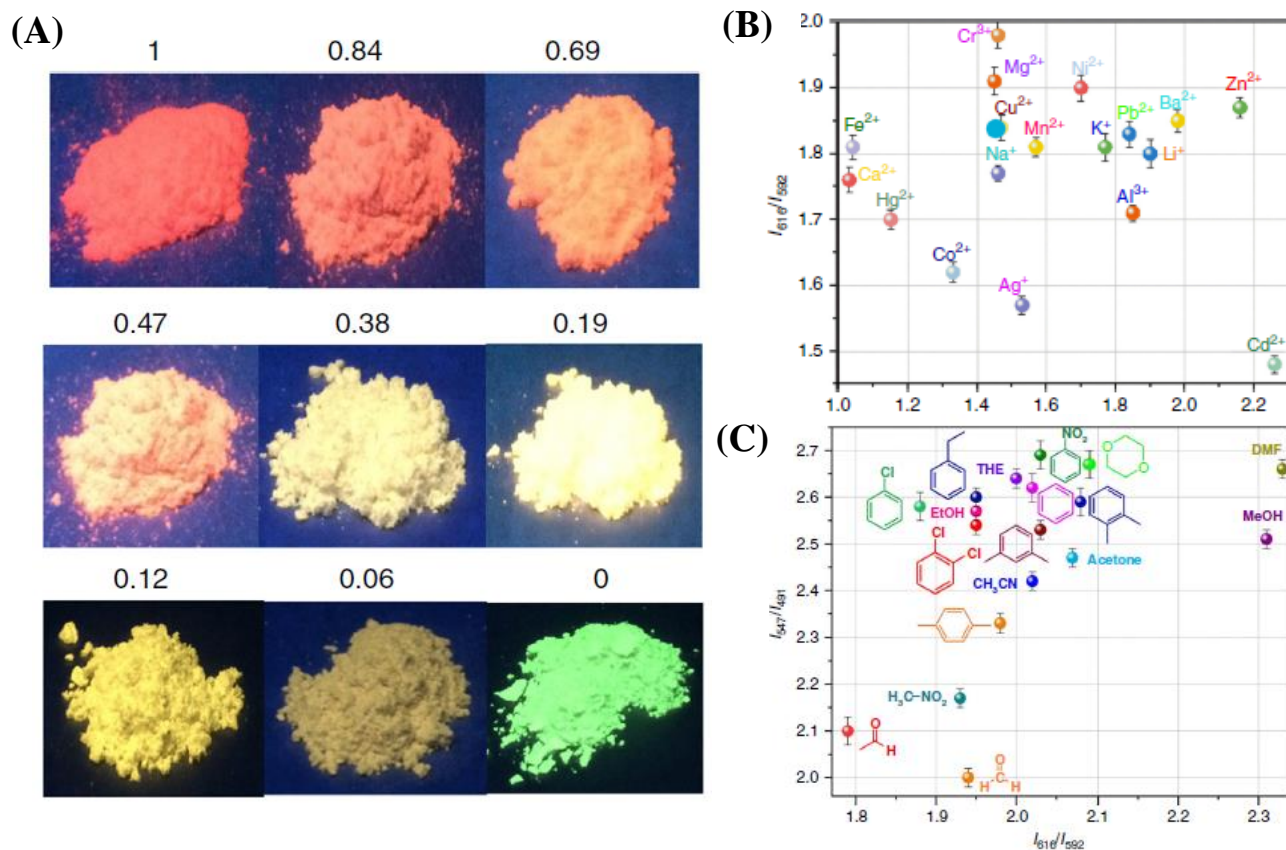


Figure 1.1. $\text{Eu}^{3+}/\text{Tb}^{3+}$ bimetallic MOFs with different ratio showing (A) colors varying from red to green, (B) decoded map for different metal ions and (C) decoded map for different VOCs. Adapted and reprinted from ref. 88.⁸⁸

Another example shows efficient sensitization has been achieved by coordinating thiophenyl-derivatized carboxylic acid to Eu^{3+} and Tb^{3+} ions and forming MOFs with intensive luminescence in visible and near-infrared region, respectively.⁸⁹

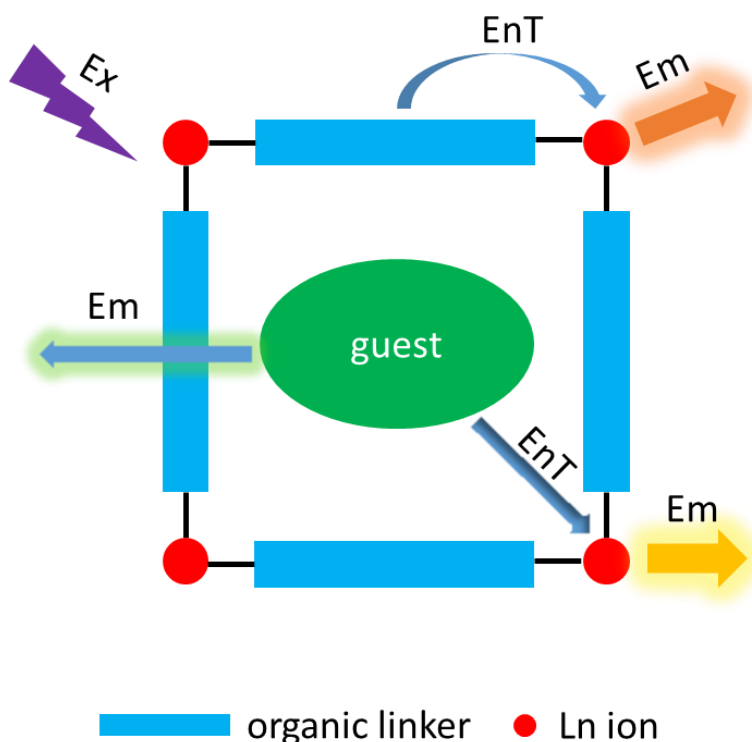
Recently, a series of bimetallic MOFs with different $\text{Eu}^{3+}/\text{Tb}^{3+}$ ratios have been reported, showing extraordinary sensing activities for both metal ions and volatile organic compounds (VOCs).⁸⁸ As shown in Figure 1.1A, emission wavelength can be tuned by adjusting the ratio of two metals, and emitting colors can be varied gradually from red to green. Moreover, $\text{Eu}_{0.47}\text{Tb}_{0.63}$ -MOF was incorporated into a polymer film and exhibited fingerprint quenching outcomes by different metal ions in aqueous solution and different VOCs in vapor. The two-dimensional decoding maps were based on different quenching performance on Eu^{3+} (616 nm) and Tb^{3+} (547 nm) emissions, as shown in Figure 1.1 B and 1.1 C.

In addition, energy transfer has also been observed between two different lanthanide ions. In hetero-lanthanide MOF containing Tb^{3+} and Eu^{3+} , Tb^{3+} can always serve as sensitizer for Eu^{3+} , leading to enhanced emission of Eu^{3+} and quenched emission of Tb^{3+} , which can be evidenced in previous reports.^{90,91} It is worth to note that in lanthanide MOFs with antenna chromophore, even though luminescence of metal ions is enhanced by the linker sensitization, the inefficiency of energy transfer process could still make the overall quantum yield low.³⁰

1.2.5. Emission from MOF Guests

Although not fully explored comparing to other luminescent MOFs, guests such as fluorescent dyes and lanthanide ions can be encapsulated into MOF channels to emit, instead of serving as MOF backbones (Scheme 1.5). This approach bypasses synthetic problems encountered

when incorporating fluorescent components as framework struts and can still serve the system as a fluorophore in solid state instead of in solution. For example, the strong emission of lanthanide ions can be easily quenched by water molecules, but encapsulating them into MOF channels via dimethylammonium cation exchange can produce emissive MOFs behaving well in aqueous system.⁹² Comparing to Ln-centered MOFs, this method not only provides a technique of making water friendly lanthanide MOFs suitable for biological environments, but also gives an easy post-synthetic approach to obtain MOFs encapsulating different lanthanide ions (Tb^{3+} , Sm^{3+} , Eu^{3+} , Yb^{3+}) and emitting various colors.



Scheme 1.5. Schematic representation of lanthanide-centered MOF emission showing antenna effect and the encapsulation of dye chromophores, along with the photophysical processes of excitation (Ex), energy transfer (EnT) and emission (Em).

In addition, by using post-synthetic cation exchange method, different lanthanide ions can be easily mixed into MOFs and mixed emission or a white light can be obtained. This has been evidenced by introducing Eu^{3+} and Yb^{3+} into a MOF with carbazole-based ligand, and by adjusting ratio of the two Ln ions a white light emission can be obtained.⁹³ Similarly, co-doping of Eu^{3+} and Yb^{3+} into a blue-emitting MOF can produce coatings on a LED light and give red, green and white emissions, by varying the ratio of two metal ions.²⁴ The energy transfer process from organic ligand sensitizer embedded in MOFs to encapsulated lanthanide ions are also proved to be efficient. Interestingly, lack of energy transfer from framework sensitizer to encapsulated Ln ions has also been observed, and the systems show discrete emissions from the framework and Ln ions, respectively.^{94,95} The authors claim no effective overlap in excitation spectra could lead to the no apparent energy transfer process.

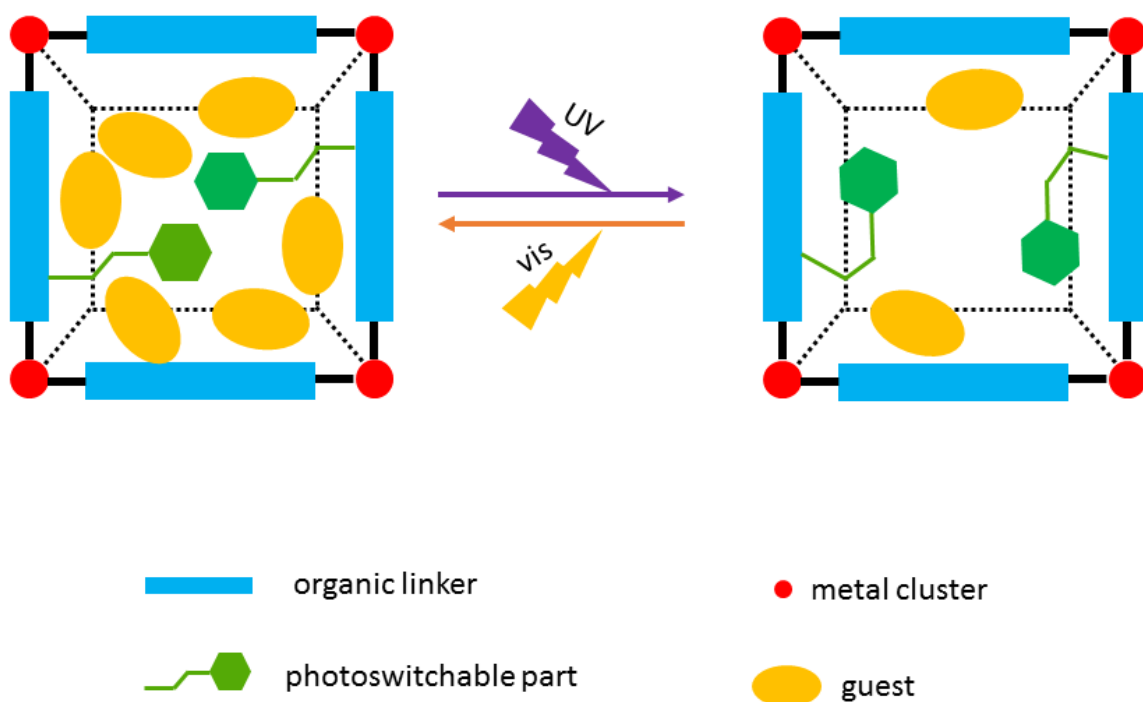
Other than physically absorbed into framework, Ln ions can also be introduced into MOFs by postsynthetic modification via coordination. Reported by a same group, MOF-253 was prepared with 2,2'-bipyridine-5,5'-dicarboxylic acid as organic linker, showing strong coordination ability at the bipyridine N sites.⁹⁶⁻⁹⁸ Eu^{3+} , Tb^{3+} , Yb^{3+} and Sm^{3+} can be brought into framework via coordination bond between Ln ions and the bipyridine, with the aid of another ligand. All of the MOFs show unique luminescence with high quantum yield.

Analogously, by encapsulating organic chromophores into MOFs can reproduce the emission of the guest molecule. A large channel ($24.5 \text{ \AA} \times 27.9 \text{ \AA}$) MOF has been prepared and the channel allows encapsulation of a large dye rhodamine 6G and emits strongly in orange-red region.⁹⁹ More interestingly, when an organic dye perylene was introduced to channels of a lanthanide MOF, emission from the dye and antenna induced Ln emission after energy transfer can be observed simultaneously.¹⁰⁰ The introducing of guest molecules into MOFs provides a more

tunable way of designing and synthesizing luminescent MOFs with different emission wavelengths, for applications in molecular recognition, guest sensing, lighting and displaying devices and biomedical imaging.

1.3. MOF with Photoswitchable Components

1.3.1. Photoswitchable Compound as Linker Sidechain



Scheme 1.6. Schematic illustration showing sidechain photoswitchable compound acting as photo-triggered switches, controlling the uptake capacity of guest molecules.

Photoisomerization can be defined as structure change of a compound induced by light irradiation. There are two types of photo-induced isomerization including *trans-cis* conversion (such as azobenzene and stilbene) and open-closed ring transition (such as spiropyran and diarylethene). Due to the reversible isomerization upon irradiation with different wavelength or

thermal treatment, photoswitchable compounds have been utilized in numerous fields, especially in molecular gates,^{12,101} photochromic switches,^{21,102} and metal ion chelators.^{103,104}

While more and more interest has been shown in MOFs as storage containers for gases and drug molecules, the demand of a photo-controllable switch on the system has surged a lot.^{35,37,105} Photoswitchable compound azobenzene (AB) and its derivatives are preferable over other photochromic compounds, since the large structural change between *trans* and *cis* isomers makes AB more suitable as molecular switches.¹⁰⁶⁻¹⁰⁸ For example, AB was coupled onto the aromatic ring of terephthalic acid, from which a framework isostructural to MOF-5 was synthesized and its CO₂ adsorption ability was characterized.³⁶ The MOF adsorbs a significant amount of CO₂ with AB in *trans* formation, and upon UV irradiation, a decreasing in CO₂ uptake is observed, due to the channel blocking by *trans*→*cis* photoisomerization (Scheme 1.6). High CO₂ uptake can be resumed when treated with heat, due to the *cis* isomer converting back to *trans*, losing channel blocking ability. In addition, the reversible alternation of MOF CO₂ uptake can be repeated many cycles, by irradiation and thermal treatment. The alteration of CO₂ adsorption capacity has also been observed on other AB MOFs.¹⁰⁹⁻¹¹¹ The dangling AB side chain provides a novel method of inserting photoswitches into MOFs, which could be utilized for other gases, such as H₂, N₂ and hydrocarbons. Similarly, larger guest molecule butanediol is loaded into a MOF channels, on top of which layers containing AB as linker side chains grow, acting as a big cap for the loaded guests.¹⁰⁵ Upon irradiation, the *trans*→*cis* isomerization allows top layer channel to open and release butanediol.

However, *trans*→*cis* isomerization does not always lead to a lower guest uptake. In a MOF reported with a large channel size, dangling AB isomerization to *cis* doesn't display blocking effects anymore, since the framework allows guest uptake in both *trans* and *cis* forms.¹¹²

Interestingly, the dipole–dipole interaction between host and guest plays an important role instead. For a more polar guest butanediol with a dipole moment of 2.58 D, the *cis* form MOF shows 20% more guest uptake comparing to *trans*. In addition, the dipole moment of AB changes from 0 D in *trans* to 3.2 D in *cis*, which suggests dipole-dipole interaction is critical. On the other hand, hexane with 0.08 D dipole moment shows no change of guest uptake upon irradiation. Furthermore, by examining several other guests with different dipole moments, the authors make a solid statement that dipole-dipole interaction is the major factor determining gas adsorption capacities.

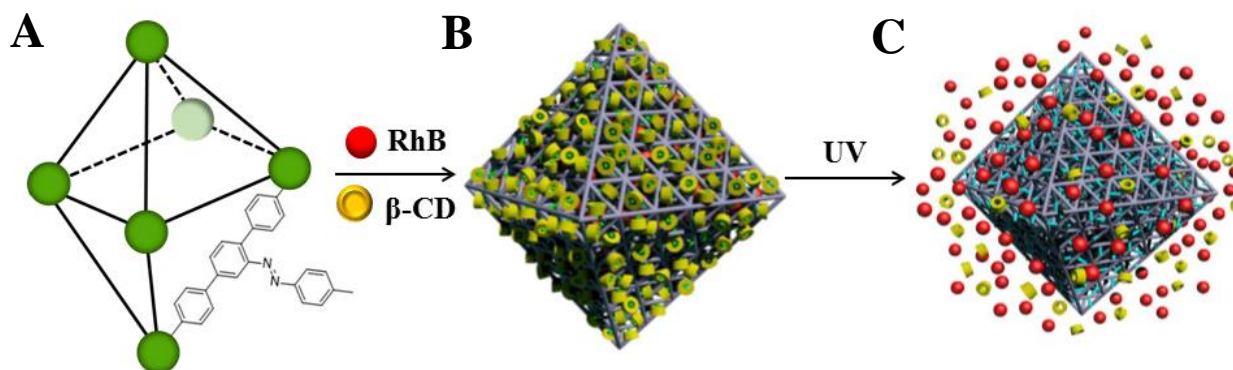


Figure 1.2. Encapsulation and photo-induced release of rhodamine B cargo from AB functionalized MOF capped by β -CD, (A) original MOF, (B) MOF loaded with rhodamine B and capped by β -CD, (C) photo-induced guest release, adapted and reproduced from ref. 108.

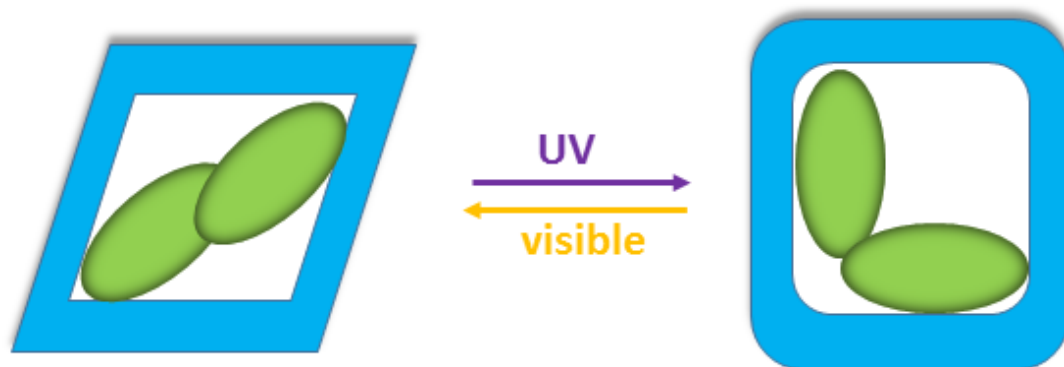
Different from *de novo* synthesis, a post-synthetic method was reported by coupling azobenzene to amine groups on a MOF ligand via covalent bond.¹¹³ Irradiation with UV leads to an increase in the CH_4 adsorption capacity and exposure to visible light shows the opposite effect. Although the authors mention the reason cannot be specified due to limited data, what they observed is not in line with the dipole-dipole interaction theory in which *cis* AB with higher dipole moment displayed less uptake of nonpolar CH_4 .¹¹² More research in this area is desired to further explore how *trans* and *cis* isomers influence uptake capacity of guest molecules. The use of AB as

gate for control release of dye molecule has also been reported.³⁵ The channel size of the MOF can be increased from 8.3 Å to 10.3 Å upon irradiation due to *trans*→*cis* conversion, allowing loaded propidium iodide dye to be released.

Similarly, rhodamine B has been loaded into a AB functionalized UiO-68 MOF capped by β-cyclodextrin (β-CD).¹⁰⁸ Surface AB can form a supramolecular complex with β-CD, which serves as a gatekeeper to prevent rhodamine B from releasing out. Since β-CD shows a much higher binding affinity toward *trans*-AB than the *cis* form, the formation of *cis* isomer upon irradiation would push β-CD away from MOF surface and open the gate to release the cargo, as shown in Figure 1.2.

Different from gating effect of AB, MOF composed by a diarylethene-based linker can display photochromic color change.²¹ The original MOF crystal is colorless when diarylethene is in ring-open form, and upon UV irradiation, the ring closes and crystal color turns to red. However, unlike diarylethene ligand displaying reversible color change between red and colorless upon irradiation in different wavelength of light, visible light irradiation cannot shift MOF crystal back to its original color. This interesting phenomenon has been explored by digesting diarylethene MOF and testing its photoactivity. The after-digesting mixture resumes its reversible photochromism, suggesting local coordination environment in framework could suppress diarylethene ring-open reaction. The same research group discovered another diarylethene MOF showing reversible photochromism between colorless and blue color, and interestingly the ring close step can be driven by UV while the ring open step can only be achieved by thermal relaxation.³³ The authors attribute the phenomenon to the formation of photo-inactive atropisomer as thiophene groups adopt a photoinactive orientation, which provides an insight local environment in MOF can play an important role in their photochromism activities.

1.3.2. Photoswitchable Compound as Guest Molecule



Scheme 1.7. Scheme showing a framework structural change is induced by *trans-cis* isomerization of encapsulated azobenzene guest molecules.

Besides being incorporated as dangling groups on MOF linkers, photoswitchable molecules can be directly encapsulated into MOF channels, a more straightforward way of introducing photoactive components. It has been reported that the isomerization of encapsulated components can induce framework structural change and alter MOF application in different directions (Scheme 1.7).¹¹⁴ For example, azobenzene was introduced into MOF structures and their isomerization ability within solid framework has been compared.¹¹⁵ Interestingly, encapsulated in the reported three MOFs upon UV irradiation, two of them show 30% *tran*→*cis* isomerization, while the third one shows no obvious *cis* isomers, according to high resolution IR spectroscopy. After comparing channel size of MOFs, the authors claim that limited *tran*→*cis* isomerization in the third MOF is attributed to the smaller MOF pore size, prohibiting azobenzene from isomerizing. Another report shows an interesting phenomenon that when a MOF is fully loaded with azobenzene molecules, no isomerization can be observed, and when part of the guest is desorbed, isomerization-induced gating effect can be seen.¹¹⁶ In addition, the gating effect is reversible upon

exposure to a different wavelength of light and can be utilized as a switch to regulate gas permeability and H₂/CO₂ separation ability, similar to gatekeeper role as MOF linker sidechains.

Although less studied, diarylethene¹¹⁷ and spiropyran¹¹⁸ molecules have also been reported encapsulating inside MOF channels. Yellowish MOF crystals can transform to red color upon UV irradiation and return to yellow upon visible light exposure, due to the photochromic property of incorporated diarylethene molecules.¹¹⁷ The presence of diarylethene inside MOF pores instead of attaching on the surface can be evidenced by the irradiated crystals showing linear dichroism. This also provides a novel way of distinguishing whether a guest molecule attaching on MOF surface or diffusing into MOF channels. In addition, trying to resolve the structure with diarylethene in the framework via SXRD doesn't work, due to inhomogeneous filling, as well as positional disorder of the guest, although residual density was observed within MOF channels. This suggests the difficulty of obtaining high quality SXRD data for MOFs capturing guest molecules, since comparing to solvent molecules, photoactive guest molecules are generally bigger and the distribution of them in MOF channels is less homogeneous than solvent guests like H₂O, methanol, or DMF. The partially filled electron densities hinders perfectly solving crystal structures.

Via a two-step post-synthetic method, spiropyran molecules have been synthesized inside MOF channels, with carboxylates coordinating to metal centers.¹¹⁸ The synthesis method using MOF as a carrier is creative, as the molecule cannot be synthesized following a typical synthetic way outside MOF. Upon irradiation or thermal treatment, reversible isomerization between spiropyran and merocyanine can be observed in MOF and UV irradiation can lead to an increasing of CO₂ uptake. This report provides a novel method of *de novo* synthesizing spiropyran molecule inside MOF channels, displaying photo-induced gas adsorption capacity change, which may inspire other light-responsive MOFs utilizing similar approaches. In addition, the synthetic method

may be applicable to other compounds which cannot be synthesized following traditional synthetic ways. Different from a post-synthetic modification, spiropyran has also been successfully embedded into different MOFs via a vapor-phase process (Figure 1.3).¹¹⁹ The report discovers that when encapsulating in three different MOFs, namely MOF-5, MIL-68(In), and MIL-68(Ga), the chromophore displays different colors, due to various polarity environments inside the three MOF channels. Upon irradiation, colors changes are observed for the MOFs, accompanied by isomerization from spiropyran to merocyanine form. In addition, colors can shift back to original upon heat treatment, making the photochromic change reversible.

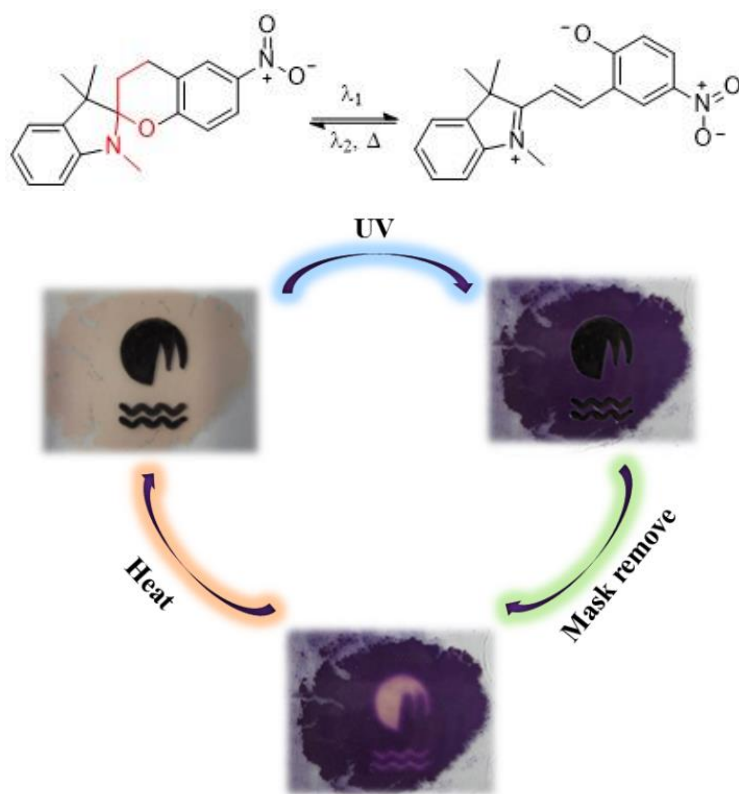
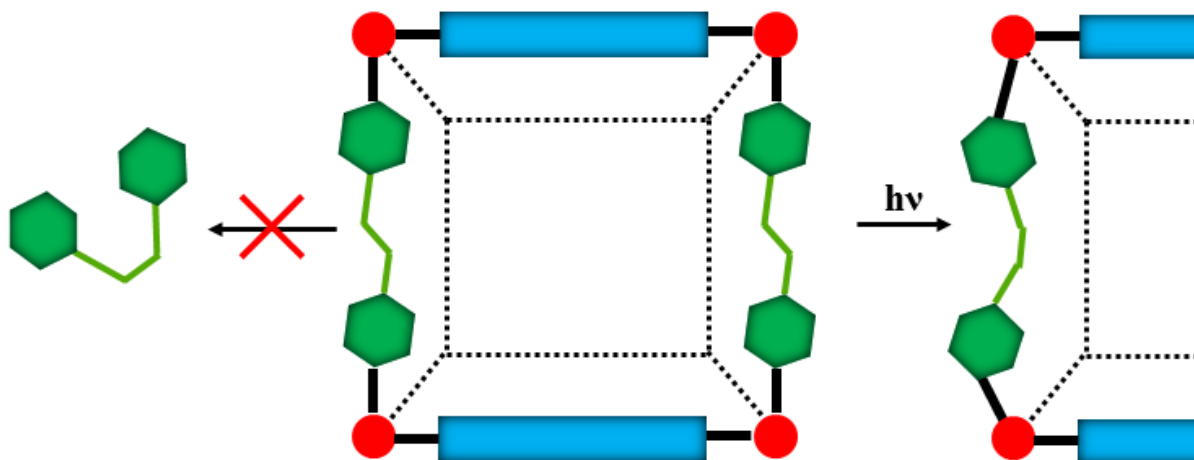


Figure 1.3. Isomerization of spiropyran and encapsulation of one spiropyran derivative in MIL-68(In), showing reversible color changes, upon irradiation or heat treatment, adapted and reproduced from ref. 119.

1.3.3. Photoswitchable Compound as Backbone Linker.



Scheme 1.8. Scheme showing unfavourability of *trans*→*cis* isomerization of AB derivatives when embedded as MOF backbone struts, and only local movements are allowed.

The isomerization of azobenzene can be restricted if additional stabilization from the structure hold the molecule in place, such as hydrogen bonding and metal complexation (Scheme 1.8).^{38,57,120} However, “breathing” behaviors were observed on MOFs composed by azobenzene derivatives.^{37,121} Hill et al. confirmed the isomerization of azobenzene moieties as metal-organic framework linkers is restricted by observing no structural change in PXRD patterns before and after irradiation. However, they have seen structural oscillations upon UV irradiation by using time-resolved FTIR spectroscopy, observing C-C-C and C-C-N bending in azo core, corresponding to peak intensity increasing at 550 cm^{-1} .³⁷ Time-resolved FTIR provides a novel way of monitoring localized structural movements within a rigid framework while PXRD or SXRD techniques are not supportive.

While it is difficult for azobenzene components to isomerize embedded in a solid framework since they must overcome framework confinement effect,^{122,123} ring open and close transformations of diarylethene molecules can be more approachable. A UV-induced buff to blue

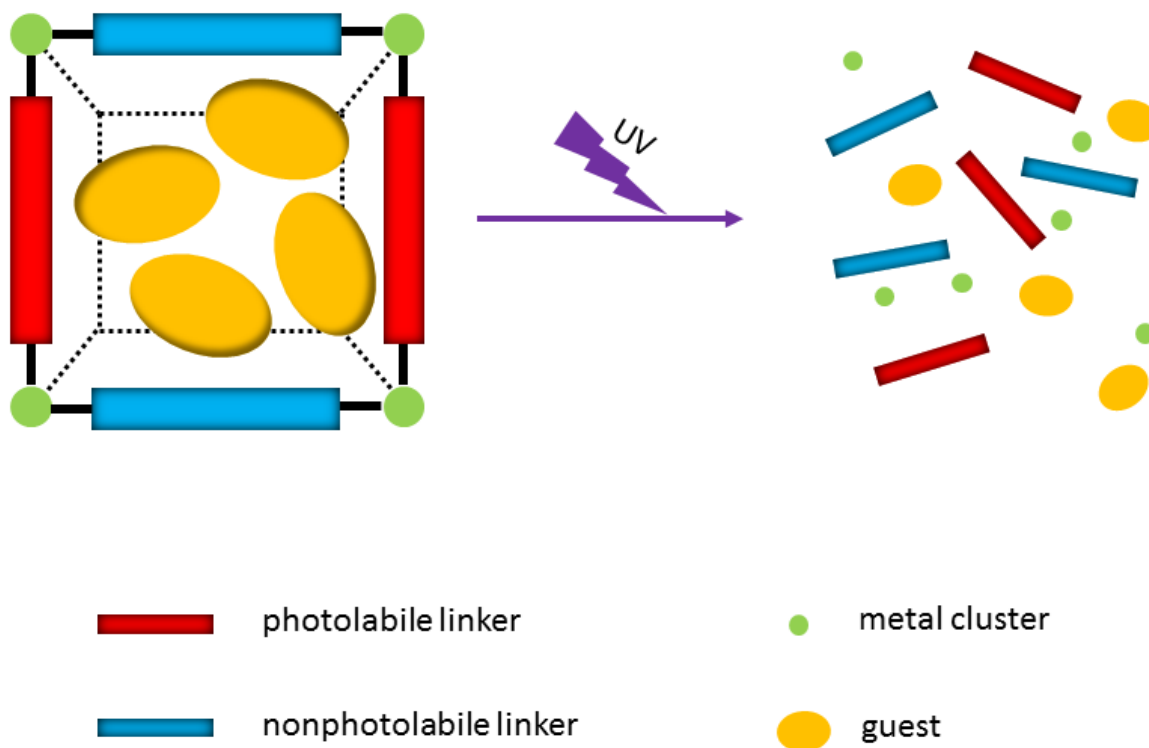
color change was observed in a dithienylethene based MOF, and the color transformed back to buff upon exposure to visible light.³⁴ The reversible MOF color change can be attributed to reversible open-ring and closed-ring transformation of the ligand, evidenced by similar absorbance change of ligand and MOF, shifting from UV to visible region upon UV irradiation. This report provides a novel way of forming photochromic MOF materials. In addition, a low-energy CO₂ release can be achieved with high CO₂ desorption capacity upon UV irradiation, and the desorption capacity can be modulated by varying irradiation wavelength. Although no other evidence provided, the authors claim the controllable CO₂ desorption behavior is attributed to local framework movements caused by transitions between open-ring and closed-ring conformers of dithienylethene ligand.

The same group reported another diarylethene metal-organic framework as a separation photo-switch for C₂H₂/C₂H₄ separation.³² Separation factor for the two gases decreases a lot upon UV irradiation, and can resume when exposed to visible light. This switchable behavior is explained by density functional theory (DFT) calculations showing host-guest interactions between MOF and guests were alternated during light irradiation. DFT calculations also suggest a local ring opening in diarylethene ligand is more achievable than alternating whole MOF skeleton.

As far as we know, spiropyran linker based MOFs have not been reported; however, amphiphilic random copolymer complex containing a spiropyran ligand was described.¹²⁴ The complex displayed reversible photochromic color change upon irradiation with different wavelength of light, and a good cycling performance was also observed.

1.4. Photodegradable MOF

As there are more and more applications incorporating photoresponsive components into metal-organic frameworks, it is rational to explore a further step that whether photo-induced transformation can achieve larger impacts by destroying local or entire framework (Scheme 1.9). On the other hand, MOFs are in great demand as drug delivery systems, due to their high drug loading ability based on high internal void space,¹²⁵⁻¹²⁷ and their big potential of forming biocomposites with enzymes, oligonucleotides, viruses and cells.¹²⁸⁻¹³⁰ However, MOF cargo delivery systems can experience slow releasing of encapsulated reagents.¹³¹⁻¹³⁴, and thus acceleration of release speed is always desired.



Scheme 1.9. Scheme showing degradation of MOF caused by photo-induced decomposition of photolabile linkers. The degradation process is irreversible.

Although local framework movement has been observed by diarylethene ring opening and closing in MOFs with diarylethene chromophores as backbone linkers,³²⁻³⁴ the framework change is minimal and MOF skeleton is retained. Azobenzene derivatives have also been inserted as MOF backbone linkers and the photo-induced isomerization can lead to MOF degradation. For example, a recent report found that cargo release speed from an azobenzene dicarboxylate based MOF could be accelerated by white light irradiation.¹³⁵ In addition, by using a higher power light source, drug release rate can be further enhanced. However, the observation of MOF degradation in dark suggests decomposition already happens in the absence of light, and more evidence is desirable to confirm photo-induced isomerization of azo core leads to MOF destructuring. A reversible local framework change was also reported due to the reversible *trans-cis* isomerization of azobenzene linker.³⁷ The authors utilized their system to test CO₂ adsorption capacity and found the reversible framework change could reversibly control the gas's capture and release. Although evidences such as FTIR was provided, azobenzene derivatives are difficult to isomerize when incorporated into a solid framework.^{57,120} Therefore, further exploration in this area is necessary to reveal whether and to what extent AB isomerization can happen in a rigid framework, and how the isomerization would affect guest capture and release performance.

MOFs were reported to be instable when exposed to acidic conditions, or strongly coordinating molecules, due to linker protonation and displacement respectively. Although this can be impediments in some fields, utilization of MOF degradation was found to be useful in drug delivery systems.¹³⁶ While many literature use natural acidic conditions in the cell cytoplasm compartments or lysosomes,^{137,138} an outside trigger can be more valuable when the natural trigger is infeasible or inefficient.

Photodecarboxylation was found to be the major mechanism of metal ion releasing from various complexes.^{139,140} However, similar phenomenon is rarely found in MOFs. A post-synthetic linker sidechain decarboxylation was reported to obtain a MOF with phenolic linker, which is not approachable by *de novo* synthesis.¹⁴¹ In the work, *ortho*-nitrobenzyl ligand was incorporated into the framework as photolabile linker, the photolysis of which yielded phenolic group. This is a significant novel method since the preparation of MOF with uncoordinated hydroxy groups is very rare due to strong coordination ability of OH groups. Although high quality crystals after irradiation cannot be obtained, NMR results and simulations confirmed the photolysis efficiency is between 55-83%. The same group has also used similar approach to prepare MOFs with hydroxy and catechol moieties using post-synthetic photo-chemical deprotection technique.⁴³ A local structural change was observed on a benzothiadiazole-derived MOF, as its non-chelated ligand wing went photo-induced decarboxylation.¹⁴² Moreover, the N₂ and NH₃ gas adsorption capacity of MOF was changed after the exposing to UV light, which provides a novel photoirradiation route of modulating MOF adsorption capacity.

The photolabile components in post-synthetic deprotection are exclusively on linker sidechains, and so far, there is no literature reporting using photolabile ligands as MOF backbone struts. It is predictable that when a backbone linker is photolabile, local or full framework decomposition can be achieved upon exposure to light. This might be less attractive from a MOF synthesis perspective; however, the approach could yield photolabile MOFs, acting as promising candidates for controlled molecule release and drug delivery systems. Revealed from a recent report, MOF MIL-88B can be encapsulated in photocleavable capsules, through the addition of modulator in MOF synthesis and the following interfacial polymerization.¹⁴³ UV-induced photolysis of photolabile *ortho*-nitrobenzyl oligomer in the polymer shell leads to gradual release

of MOF particles into outside solution, which increases the catalytic activity of tetramethylbenzidine oxidation. We envision that without sophisticated modulator addition and polymerization, a photolabile compound with modulator ability (carboxylates) can be directly attached to MOF surface by coordination to surface metal clusters.

1.5. Conclusions

Although photoresponsive MOFs have been explored extensively with regards to MOF luminescence, tuning of emission wavelength, photoswitches alternating gas adsorption capacities, reversible photochromic color change and photo-induced cargo release, various glitches remain unsolved. One of the less researched areas is fluorophore emission enhancement induced by rigidifying in a solid framework. The believed reason is chromophore motion restricted by coordination to metal ions; however, this statement is debatable and the mechanism behind is not clearly proposed or proved. Photo-induced structural change can serve MOF as photoswitches for gas adsorption and azobenzene derivatives are attractive candidates as MOF struts to initiate the structural change. Although several studies report local framework change or MOF degradation caused by AB isomerization, the evidence is not fully convincing and we observe no obvious *trans-cis* interconversion in solid frameworks. Photo-induced MOF degradation could be another hot topic which is less addressed. A photo-degradable MOF made of photolabile ligands is a more promising drug delivery system for controllable and efficient drug release.

1.6. References

- (1) Tsien, R. Y. The Green Fluorescent Protein. *Annu. Rev. Biochem* **1998**, *67*, 509-544.

- (2) Miyawaki, A.; Llopis, J.; Heim, R.; McCaffery, J. M.; Adams, J. A.; Ikura, M.; Tsien, R. Y. Fluorescent Indicators for Ca²⁺ Based on Green Fluorescent Proteins and Calmodulin. *Nature* **1997**, *388*, 882-887.
- (3) de Silva, A. P.; Gunaratne, H. Q. N.; Gunnlaugsson, T.; Huxley, A. J. M.; McCoy, C. P.; Rademacher, J. T.; Rice, T. E. Signaling Recognition Events with Fluorescent Sensors and Switches. *Chem. Rev.* **1997**, *97*, 1515-1566.
- (4) Thomas, S. W.; Joly, G. D.; Swager, T. M. Chemical Sensors Based on Amplifying Fluorescent Conjugated Polymers. *Chem. Rev.* **2007**, *107*, 1339-1386.
- (5) Hashimoto, N.; Takada, Y.; Sato, K.; Ibuki, S. Green-Luminescent (La,Ce)PO₄-Tb Phosphors for Small Size Fluorescent Lamps. *J. Lumin.* **1991**, *48-49*, 893-897.
- (6) Smets, B. M. J. Phosphors Based on Rare-Earths, a New Era in Fluorescent Lighting. *Mater. Chem. Phys.* **1987**, *16*, 283-299.
- (7) Bolton, O.; Lee, K.; Kim, H. J.; Lin, K. Y.; Kim, J. Activating Efficient Phosphorescence from Purely Organic Materials by Crystal Design. *Nat. Chem.* **2011**, *3*, 205-210.
- (8) Kohler, A.; Wilson, J. S.; Friend, R. H. Fluorescence and Phosphorescence in Organic Materials. *Adv. Mater.* **2002**, *14*, 701-707.
- (9) Andersson, J.; Li, S. M.; Lincoln, P.; Andreasson, J. Photoswitched DNA-Binding of a Photochromic Spiropyran. *J. Am. Chem. Soc.* **2008**, *130*, 11836-11837.
- (10) Irie, M. Diarylethenes for Memories and Switches. *Chem. Rev.* **2000**, *100*, 1685-1716.
- (11) Widengren, J.; Schwille, P. Characterization of Photoinduced Isomerization and Back-Isomerization of the Cyanine Dye Cy5 by Fluorescence Correlation Spectroscopy. *J. Phys. Chem. A* **2000**, *104*, 6416-6428.

- (12) Bandara, H. M. D.; Burdette, S. C. Photoisomerization in Different Classes of Azobenzene. *Chem. Soc. Rev.* **2012**, *41*, 1809-1825.
- (13) Kaplan, J. H.; Ellisdavies, G. C. R. Photolabile Chelators for the Rapid Photorelease of Divalent-Cations. *Proc. Natl. Acad. Sci. U.S.A.* **1988**, *85*, 6571-6575.
- (14) Dorman, G.; Prestwich, G. D. Using Photolabile Ligands in Drug Discovery and Development. *Trends Biotechnol.* **2000**, *18*, 64-77.
- (15) Bochet, C. G. Photolabile Protecting Groups and Linkers. *J. Chem. Soc., Perkin Trans. 1*, **2002**, 125-142.
- (16) Jones, C. L.; Tansell, A. J.; Easun, T. L. The Lighter Side of MOFs: Structurally Photoresponsive Metal-Organic Frameworks. *J. Mater. Chem. A* **2016**, *4*, 6714-6723.
- (17) Patel, D. G.; Walton, I. M.; Cox, J. M.; Gleason, C. J.; Butzer, D. R.; Benedict, J. B. Photoresponsive Porous Materials: The Design and Synthesis of Photochromic Diarylethene-Based Linkers and a Metal-Organic Framework. *Chem. Commun.* **2014**, *50*, 2653-2656.
- (18) Mukhopadhyay, R. D.; Praveen, V. K.; Ajayaghosh, A. Photoresponsive Metal-Organic Materials: Exploiting the Azobenzene Switch. *Mater. Horiz.* **2014**, *1*, 572-576.
- (19) Kreno, L. E.; Leong, K.; Farha, O. K.; Allendorf, M.; Van Duyne, R. P.; Hupp, J. T. Metal-Organic Framework Materials as Chemical Sensors. *Chem. Rev.* **2012**, *112*, 1105-1125.
- (20) Lee, J.; Farha, O. K.; Roberts, J.; Scheidt, K. A.; Nguyen, S. T.; Hupp, J. T. Metal-Organic Framework Materials as Catalysts. *Chem. Soc. Rev.* **2009**, *38*, 1450-1459.
- (21) Rosi, N. L.; Eckert, J.; Eddaoudi, M.; Vodak, D. T.; Kim, J.; O'Keeffe, M.; Yaghi, O. M. Hydrogen Storage in Microporous Metal-Organic Frameworks. *Science* **2003**, *300*, 1127-1129.

- (22) Li, H.; Eddaoudi, M.; O'Keeffe, M.; Yaghi, O. M. Design and Synthesis of an Exceptionally Stable and Highly Porous Metal-Organic Framework. *Nature* **1999**, *402*, 276-279.
- (23) Shustova, N. B.; McCarthy, B. D.; Dinca, M. Turn-on Fluorescence in Tetraphenylethylene-Based Metal-Organic Frameworks: An Alternative to Aggregation-Induced Emission. *J. Am. Chem. Soc.* **2011**, *133*, 20126-20129.
- (24) Sun, C. Y.; Wang, X. L.; Zhang, X.; Qin, C.; Li, P.; Su, Z. M.; Zhu, D. X.; Shan, G. G.; Shao, K. Z.; Wu, H.; Li, J. Efficient and Tunable White-Light Emission of Metal-Organic Frameworks by Iridium-Complex Encapsulation. *Nat. Commun.* **2013**, *4*, 2717.
- (25) Chen, W.; Wang, J. Y.; Chen, C.; Yue, Q.; Yuan, H. M.; Chen, J. S.; Wang, S. N. Photoluminescent Metal-Organic Polymer Constructed from Trimetallic Clusters and Mixed Carboxylates. *Inorg. Chem.* **2003**, *42*, 944-946.
- (26) Wei, Y. Q.; Yu, Y. F.; Wu, K. C. Highly Stable Five-Coordinated Mn(II) Polymer [Mn(Hbidc)](N) (Hbidc=1h-Benzimidazole-5,6-Dicarboxylate): Crystal Structure, Antiferromagnetic Property, and Strong Long-Lived Luminescence. *Cryst. Growth Des.* **2008**, *8*, 2087-2089.
- (27) Lee, C. Y.; Farha, O. K.; Hong, B. J.; Sarjeant, A. A.; Nguyen, S. T.; Hupp, J. T. Light-Harvesting Metal-Organic Frameworks (MOFs): Efficient Strut-to-Strut Energy Transfer in Bodipy and Porphyrin-Based MOFs. *J. Am. Chem. Soc.* **2011**, *133*, 15858-15861.
- (28) Cui, Y. J.; Yue, Y. F.; Qian, G. D.; Chen, B. L. Luminescent Functional Metal-Organic Frameworks. *Chem. Rev.* **2012**, *112*, 1126-1162.
- (29) Hu, Z. C.; Deibert, B. J.; Li, J. Luminescent Metal-Organic Frameworks for Chemical Sensing and Explosive Detection. *Chem. Soc. Rev.* **2014**, *43*, 5815-5840.

- (30) Allendorf, M. D.; Bauer, C. A.; Bhakta, R. K.; Houk, R. J. T. Luminescent Metal-Organic Frameworks. *Chem. Soc. Rev.* **2009**, *38*, 1330-1352.
- (31) Zhang, F.; Zou, X. Q.; Feng, W.; Zhao, X. J.; Jing, X. F.; Sun, F. X.; Ren, H.; Zhu, G. S. Microwave-Assisted Crystallization Inclusion of Spiropyran Molecules in Indium Trimesate Films with Antidromic Reversible Photochromism. *J. Mater. Chem.* **2012**, *22*, 25019-25026.
- (32) Fan, C. B.; Le Gong, L.; Huang, L.; Luo, F.; Krishna, R.; Yi, X. F.; Zheng, A. M.; Zhang, L.; Pu, S. Z.; Feng, X. F.; Luo, M. B.; Guo, G. C. Significant Enhancement of C₂H₂/C₂H₄ Separation by a Photochromic Diarylethene Unit: A Temperature- and Light-Responsive Separation Switch. *Angew. Chem. Int. Ed.* **2017**, *56*, 7900-7906.
- (33) Walton, I. M.; Cox, J. M.; Benson, C. A.; Patel, D. G.; Chen, Y. S.; Benedict, J. B. The Role of Atropisomers on the Photo-Reactivity and Fatigue of Diarylethene-Based Metal-Organic Frameworks. *New J. Chem.* **2016**, *40*, 101-106.
- (34) Luo, F.; Fan, C. B.; Luo, M. B.; Wu, X. L.; Zhu, Y.; Pu, S. Z.; Xu, W. Y.; Guo, G. C. Photoswitching CO₂ Capture and Release in a Photochromic Diarylethene Metal-Organic Framework. *Angew. Chem. Int. Ed.* **2014**, *53*, 9298-9301.
- (35) Brown, J. W.; Henderson, B. L.; Kiesz, M. D.; Whalley, A. C.; Morris, W.; Grunder, S.; Deng, H. X.; Furukawa, H.; Zink, J. I.; Stoddart, J. F.; Yaghi, O. M. Photophysical Pore Control in an Azobenzene-Containing Metal-Organic Framework. *Chem. Sci.* **2013**, *4*, 2858-2864.
- (36) Park, J.; Yuan, D. Q.; Pham, K. T.; Li, J. R.; Yakovenko, A.; Zhou, H. C. Reversible Alteration of CO₂ Adsorption Upon Photochemical or Thermal Treatment in a Metal-Organic Framework. *J. Am. Chem. Soc.* **2012**, *134*, 99-102.

- (37) Lyndon, R.; Konstas, K.; Ladewig, B. P.; Southon, P. D.; Kepert, C. J.; Hill, M. R. Dynamic Photo-Switching in Metalorganic Frameworks as a Route to Low-Energy Carbon Dioxide Capture and Release. *Angew. Chem. Int. Ed.* **2013**, *52*, 3695-3698.
- (38) Yan, J. J.; Wilbraham, L.; Basa, P. N.; Schüttel, M.; MacDonald, J. C.; Ciofini, I.; Coudert, F. X.; Burdette, S. C. Emissive Azobenzenes Delivered on a Silver Coordination Polymer. *Manuscript submitted* **2018**.
- (39) Yan, J. J.; Carl, A. D.; MacDonald, J. C.; Müller, P.; Grimm, R. L.; Burdette, S. C. Detection of Surface Adsorbed Guests on Emissive MOFs by X-Ray Photoelectron Spectroscopy. *Manuscript submitted* **2018**.
- (40) Han, G.; You, C. C.; Kim, B. J.; Turingan, R. S.; Forbes, N. S.; Martin, C. T.; Rotello, V. M. Light-Regulated Release of DNA and Its Delivery to Nuclei by Means of Photolabile Gold Nanoparticles. *Angew. Chem. Int. Ed.* **2006**, *45*, 3165-3169.
- (41) Kaplan, J. H.; Somlyo, A. P. Flash-Photolysis of Caged Compounds - New Tools for Cellular Physiology. *Trends Neurosci.* **1989**, *12*, 54-59.
- (42) Deshpande, R. K.; Waterhouse, G. I. N.; Jameson, G. B.; Telfer, S. G. Photolabile Protecting Groups in Metal-Organic Frameworks: Preventing Interpenetration and Masking Functional Groups. *Chem. Commun.* **2012**, *48*, 1574-1576.
- (43) Tanabe, K. K.; Allen, C. A.; Cohen, S. M. Photochemical Activation of a Metal-Organic Framework to Reveal Functionality. *Angew. Chem. Int. Ed.* **2010**, *49*, 9730-9733.
- (44) Zhang, J.; Wang, L. B.; Li, N.; Liu, J. F.; Zhang, W.; Zhang, Z. B.; Zhou, N. C.; Zhu, X. L. A Novel Azobenzene Covalent Organic Framework. *Crystengcomm* **2014**, *16*, 6547-6551.

- (45) Singh, D.; Nagaraja, C. M. A Luminescent 3D Interpenetrating Metal-Organic Framework for Highly Selective Sensing of Nitrobenzene. *Dalton Trans.* **2014**, *43*, 17912-17915.
- (46) Nagarkar, S. S.; Joarder, B.; Chaudhari, A. K.; Mukherjee, S.; Ghosh, S. K. Highly Selective Detection of Nitro Explosives by a Luminescent Metal-Organic Framework. *Angew. Chem. Int. Ed.* **2013**, *52*, 2881-2885.
- (47) Wu, W. P.; Wang, Y. Y.; Wu, Y. P.; Liu, J. Q.; Zeng, X. R.; Shi, Q. Z.; Peng, S. M. Hydro(Solvo) Thermal Synthesis, Structures, Luminescence of 2-D Zinc(II) and 1-D Copper(II) Complexes Constructed from Pyridine-2,6-Dicarboxylic Acid N-Oxide and Decarboxylation of the Ligand. *Crystengcomm* **2007**, *9*, 753-757.
- (48) Song, L.; Du, S. W.; Lin, J. D.; Zhou, H.; Li, T. A 3D Metal-Organic Framework with Rare 3-Fold Interpenetrating Dia-g Nets Based on Silver(I) and Novel Tetradentate Imidazolate Ligand: Synthesis, Structure, and Possible Ferroelectric Property. *Cryst. Growth Des.* **2007**, *7*, 2268-2271.
- (49) Du, J. L.; Hu, T. L.; Li, J. R.; Zhang, S. M.; Bu, X. H. Metal Coordination Architectures of 2,3-Bis(Triazol-1-Ylmethyl)Quinoxaline: Effect of Metal Ion and Counterion on Complex Structures. *Eur. J. Inorg. Chem.* **2008**, 1059-1066.
- (50) Ouyang, X. M.; Li, Z. W.; Okamura, T. A.; Li, Y. Z.; Sun, W. Y.; Tang, W. X.; Ueyama, N. Construction of Metal-Organic Frameworks through Coordination and Hydrogen Bonding Interactions: Syntheses, Structures and Photoluminescent Properties of Metal Complexes with Macrocyclic Ligand. *J. Solid State Chem.* **2004**, *177*, 350-360.
- (51) Li, M. X.; Miao, Z. X.; Shao, M.; Liang, S. W.; Zhu, S. R. Metal-Organic Frameworks Constructed from 2,4,6-Tris(4-Pyridyl)-1,3,5-Triazine. *Inorg. Chem.* **2008**, *47*, 4481-4489.

(52) Wang, X. L.; Bi, Y. F.; Lin, H. Y.; Liu, G. C. Three Novel Cd(II) Metal-Organic Frameworks Constructed from Mixed Ligands of Dipyrido[3,2-*d*:2',3'-*f*]quinoxaline and Benzene-dicarboxylate: From a 1-D Ribbon, 2-D Layered Network, to a 3-D Architecture. *Cryst. Growth Des.* **2007**, *7*, 1086-1091.

(53) Du, M.; Jiang, X. J.; Zhao, X. J. Molecular Tectonics of Mixed-Ligand Metal-Organic Frameworks: Positional Isomeric Effect, Metal-Directed Assembly, and Structural Diversification. *Inorg. Chem.* **2007**, *46*, 3984-3995.

(54) Chen, Z. F.; Xiong, R. G.; Zhang, J.; Chen, X. T.; Xue, Z. L.; You, X. Z. 2D Molecular Square Grid with Strong Blue Fluorescent Emission: A Complex of Norfloxacin with Zinc(II). *Inorg. Chem.* **2001**, *40*, 4075-4077.

(55) Fang, Q. R.; Zhu, G. S.; Xue, M.; Sun, J. Y.; Sun, F. X.; Qiu, S. L. Structure, Luminescence, and Adsorption Properties of Two Chiral Microporous Metal-Organic Frameworks. *Inorg. Chem.* **2006**, *45*, 3582-3587.

(56) Yang, W. J.; Chen, X. B.; Su, H. Z.; Fang, W. H.; Zhang, Y. The Fluorescence Regulation Mechanism of the Paramagnetic Metal in a Biological Hno Sensor. *Chem. Commun.* **2015**, *51*, 9616-9619.

(57) Bandara, H. M. D.; Friss, T. R.; Enriquez, M. M.; Isley, W.; Incarvito, C.; Frank, H. A.; Gascon, J.; Burdette, S. C. Proof for the Concerted Inversion Mechanism in the Trans(->)Cis Isomerization of Azobenzene Using Hydrogen Bonding to Induce Isomer Locking. *J. Org. Chem.* **2010**, *75*, 4817-4827.

(58) Tao, J.; Shi, J. X.; Tong, M. L.; Zhang, X. X.; Chen, X. M. A New Inorganic - Organic Photoluminescent Material Constructed with Helical [Zn₃(μ₃-OH)(μ₂-OH)] Chains. *Inorg. Chem.* **2001**, *40*, 6328-6330.

(59) Dai, J. C.; Wu, X. T.; Fu, Z. Y.; Cui, C. P.; Hu, S. M.; Du, W. X.; Wu, L. M.; Zhang, H. H.; Sun, R. O. Synthesis, Structure, and Fluorescence of the Novel Cadmium(II)-Trimesate Coordination Polymers with Different Coordination Architectures. *Inorg. Chem.* **2002**, *41*, 1391-1396.

(60) Dai, J. C.; Wu, X. T.; Fu, Z. Y.; Hu, S. M.; Du, W. X.; Cui, C. P.; Wu, L. M.; Zhang, H. H.; Sun, R. Q. A Novel Ribbon-Candy-Like Supramolecular Architecture of Cadmium(II)-Terephthalate Polymer with Giant Rhombic Channels: Twofold Interpenetration of the 3D 8²10-a Net. *Chem. Commun.* **2002**, *0*, 12-13.

(61) Bordiga, S.; Lamberti, C.; Ricchiardi, G.; Regli, L.; Bonino, F.; Damin, A.; Lillerud, K. P.; Bjorgen, M.; Zecchina, A. Electronic and Vibrational Properties of a MOF-5 Metal-Organic Framework: ZnO Quantum Dot Behaviour. *Chem. Commun.* **2004**, *0*, 2300-2301.

(62) Manos, M. J.; Moushi, E. E.; Papaefstathiou, G. S.; Tasiopoulos, A. J. New Zn²⁺ Metal Organic Frameworks with Unique Network Topologies from the Combination of Trimesic Acid and Amino-Alcohols. *Cryst. Growth Des.* **2012**, *12*, 5471-5480.

(63) Huang, Y. Q.; Ding, B.; Song, H. B.; Zhao, B.; Ren, P.; Cheng, P.; Wang, H. G.; Liao, D. Z.; Yan, S. P. A Novel 3D Porous Metal-Organic Framework Based on Trinuclear Cadmium Clusters as a Promising Luminescent Material Exhibiting Tunable Emissions between UV and Visible Wavelengths. *Chem. Commun.* **2006**, *0*, 4906-4908.

(64) Lan, A. J.; Han, L.; Yuan, D. Q.; Jiang, F. L.; Hong, M. C. A Blue Luminescent Inorganic-Organic Hybrid with Infinite [Cd₃(μ₃-OH)₂(μ₂-Cl)₂] Connectivity. *Inorg. Chem. Commun.* **2007**, *10*, 993-996.

- (65) Wang, Y. T.; Tang, G. M.; Qiang, Z. W. Radius-Dependent Assembly of Complexes with the Rigid Unsymmetric Ligand 5-(2-Pyridyl)-1,3,4-Oxadiazole-2-Thione: Syntheses, Structures and Luminescence Properties. *Polyhedron* **2007**, *26*, 4542-4550.
- (66) Wu, X. P.; Gagliardi, L.; Truhlar, D. G. Cerium Metal-Organic Framework for Photocatalysis. *J. Am. Chem. Soc.* **2018**, *140*, 7904-7912.
- (67) Nasalevich, M. A.; Hendon, C. H.; Santaclara, J. G.; Svane, K.; van der Linden, B.; Veber, S. L.; Fedin, M. V.; Houtepen, A. J.; van der Veen, M. A.; Walsh, A.; Gascon, J. Electronic Origins of Photocatalytic Activity in d^0 Metal Organic Frameworks. *Sci. Rep.* **2016**, *6*, 23676.
- (68) Sun, D. R.; Fu, Y. H.; Liu, W. J.; Ye, L.; Wang, D. K.; Yang, L.; Fu, X. Z.; Li, Z. H. Studies on Photocatalytic CO_2 Reduction over NH_2 -Uio-66(Zr) and Its Derivatives: Towards a Better Understanding of Photocatalysis on Metal-Organic Frameworks. *Chem. Eur. J.* **2013**, *19*, 14279-14285.
- (69) Horiuchi, Y.; Toyao, T.; Saito, M.; Mochizuki, K.; Iwata, M.; Higashimura, H.; Anpo, M.; Matsuoka, M. Visible-Light-Promoted Photocatalytic Hydrogen Production by Using an Amino-Functionalized Ti(IV) Metal-Organic Framework. *J. Phys. Chem. C* **2012**, *116*, 20848-20853.
- (70) Long, J. L.; Wang, S. B.; Ding, Z. X.; Wang, S. C.; Zhou, Y. E.; Huang, L.; Wang, X. X. Amine-Functionalized Zirconium Metal-Organic Framework as Efficient Visible-Light Photocatalyst for Aerobic Organic Transformations. *Chem. Commun.* **2012**, *48*, 11656-11658.
- (71) Zou, J. P.; Peng, Q.; Wen, Z. H.; Zeng, G. S.; Xing, Q. J.; Guo, G. C. Two Novel Metal-Organic Frameworks (MOFs) with (3,6)-Connected Net Topologies: Syntheses, Crystal Structures, Third-Order Nonlinear Optical and Luminescent Properties. *Cryst. Growth Des.* **2010**, *10*, 2613-2619.

- (72) Lumpkin, R. S.; Kober, E. M.; Worl, L. A.; Murtaza, Z.; Meyer, T. J. Metal-to-Ligand Charge-Transfer (MLCT) Photochemistry - Experimental-Evidence for the Participation of a Higher Lying MLCT State in Polypyridyl Complexes of Ruthenium(II) and Osmium(II). *J. Phys. Chem.* **1990**, *94*, 239-243.
- (73) Yam, V. W. W.; Wong, K. M. C. Luminescent Metal Complexes of d^6 , d^8 and d^{10} Transition Metal Centres. *Chem. Commun.* **2011**, *47*, 11579-11592.
- (74) Kent, C. A.; Mehl, B. P.; Ma, L. Q.; Papanikolas, J. M.; Meyer, T. J.; Lin, W. B. Energy Transfer Dynamics in Metal-Organic Frameworks. *J. Am. Chem. Soc.* **2010**, *132*, 12767-12769.
- (75) Xie, Z. G.; Ma, L. Q.; deKrafft, K. E.; Jin, A.; Lin, W. B. Porous Phosphorescent Coordination Polymers for Oxygen Sensing. *J. Am. Chem. Soc.* **2010**, *132*, 922-923.
- (76) Bunzli, J. C. G. Benefiting from the Unique Properties of Lanthanide Ions. *Acc. Chem. Res.* **2006**, *39*, 53-61.
- (77) Bunzli, J. C. G.; Piguet, C. Taking Advantage of Luminescent Lanthanide Ions. *Chem. Soc. Rev.* **2005**, *34*, 1048-1077.
- (78) Peijzel, P. S.; Meijerink, A.; Wegh, R. T.; Reid, M. F.; Burdick, G. W. A Complete $4f^n$ Energy Level Diagram for All Trivalent Lanthanide Ions. *J. Solid State Chem.* **2005**, *178*, 448-453.
- (79) Bunzli, J. C. G.; Eliseeva, S. V. Intriguing Aspects of Lanthanide Luminescence. *Chem. Sci.* **2013**, *4*, 1939-1949.
- (80) Rocha, J.; Carlos, L. D.; Paz, F. A. A.; Ananias, D. Luminescent Multifunctional Lanthanides-Based Metal-Organic Frameworks. *Chem. Soc. Rev.* **2011**, *40*, 926-940.

- (81) Cui, Y. J.; Chen, B. L.; Qian, G. D. Lanthanide Metal-Organic Frameworks for Luminescent Sensing and Light-Emitting Applications. *Coord. Chem. Rev.* **2014**, *273*, 76-86.
- (82) Peng, D.; Yin, L.; Hu, P.; Li, B.; Ouyang, Z. W.; Zhuang, G. L.; Wang, Z. X. Series of Highly Stable Lanthanide-Organic Frameworks Constructed by a Bifunctional Linker: Synthesis, Crystal Structures, and Magnetic and Luminescence Properties. *Inorg. Chem.* **2018**, *57*, 2577-2583.
- (83) Mendes, R. F.; Ananias, D.; Carlos, L. D.; Rocha, J.; Paz, F. A. A. Photoluminescent Lanthanide-Organic Framework Based on a Tetraphosphonic Acid Linker. *Cryst. Growth Des.* **2017**, *17*, 5191-5199.
- (84) Wang, J.; Jiang, M.; Yan, L.; Peng, R.; Huangfu, M. J.; Guo, X. X.; Li, Y.; Wu, P. Y. Multifunctional Luminescent Eu(III)-Based Metal-Organic Framework for Sensing Methanol and Detection and Adsorption of Fe(III) Ions in Aqueous Solution. *Inorg. Chem.* **2016**, *55*, 12660-12668.
- (85) Liu, J. J.; Sun, W.; Liu, Z. L. White-Light Emitting Materials with Tunable Luminescence Based on Steady Eu(III) Doping of Tb(III) Metal-Organic Frameworks. *RSC Adv.* **2016**, *6*, 25689-25694.
- (86) Liu, Z. F.; Wu, M. F.; Wang, S. H.; Zheng, F. K.; Wang, G. E.; Chen, J.; Xiao, Y.; Wu, A. Q.; Guo, G. C.; Huang, J. S. Eu³⁺-Doped Tb³⁺ Metal-Organic Frameworks Emitting Tunable Three Primary Colors Towards White Light. *J. Mater. Chem. C* **2013**, *1*, 4634-4639.
- (87) Chandler, B. D.; Cramb, D. T.; Shimizu, G. K. H. Microporous Metal - Organic Frameworks Formed in a Stepwise Manner from Luminescent Building Blocks. *J. Am. Chem. Soc.* **2006**, *128*, 10403-10412.

(88) Su, Y.; Yu, J. H.; Li, Y. B.; Phua, S. F. Z.; Liu, G. F.; Lim, W. Q.; Yang, X. Z.; Ganguly, R.; Dang, C.; Yang, C. L.; Zhao, Y. L. Versatile Bimetallic Lanthanide Metal-Organic Frameworks for Tunable Emission and Efficient Fluorescence Sensing. *Commun. Chem.* **2018**, *1*, 12.

(89) Eliseeva, S. V.; Pleshkov, D. N.; Lyssenko, K. A.; Lepnev, L. S.; Bunzli, J. C. G.; Kuzminat, N. P. Highly Luminescent and Triboluminescent Coordination Polymers Assembled from Lanthanide Beta-Diketonates and Aromatic Bidentate O-Donor Ligands. *Inorg. Chem.* **2010**, *49*, 9300-9311.

(90) Soares-Santos, P. C. R.; Cunha-Silva, L.; Paz, F. A. A.; Ferreira, R. A. S.; Rocha, J.; Trindade, T.; Carlos, L. D.; Nogueira, H. I. S. Photoluminescent 3D Lanthanide-Organic Frameworks with 2,5-Pyridinedicarboxylic and 1,4-Phenylenediacetic Acids. *Cryst. Growth Des.* **2008**, *8*, 2505-2516.

(91) de Lill, D. T.; de Bettencourt-Dias, A.; Cahill, C. L. Exploring Lanthanide Luminescence in Metal-Organic Frameworks: Synthesis, Structure, and Guest-Sensitized Luminescence of a Mixed Europium/Terbium-Adipate Framework and a Terbium-Adipate Framework. *Inorg. Chem.* **2007**, *46*, 3960-3965.

(92) An, J. Y.; Shade, C. M.; Chengelis-Czegany, D. A.; Petoud, S.; Rosi, N. L. Zinc-Adeninate Metal-Organic Framework for Aqueous Encapsulation and Sensitization of near-Infrared and Visible Emitting Lanthanide Cations. *J. Am. Chem. Soc.* **2011**, *133*, 1220-1223.

(93) Xie, W.; Zhang, S. R.; Du, D. Y.; Qin, J. S.; Bao, S. J.; Li, J.; Su, Z. M.; He, W. W.; Fu, Q.; Lan, Y. Q. Stable Luminescent Metal-Organic Frameworks as Dual-Functional Materials to Encapsulate Ln³⁺ Ions for White-Light Emission and to Detect Nitroaromatic Explosives. *Inorg. Chem.* **2015**, *54*, 3290-3296.

- (94) Liu, C.; Yan, B. Photofunctional Nanocomposites Based on the Functionalization of Metal-Organic Frameworks by up/down Conversion Luminescent Nanophosphors. *New J. Chem.* **2015**, *39*, 1125-1131.
- (95) Liu, C.; Yan, B. Photoactive Hybrid Polymer Films Incorporated with Lanthanide Complexes and ZIF-8 for Selectively Excited Multicolored Luminescence. *Eur. J. Inorg. Chem.* **2015**, 279-287.
- (96) Lu, Y.; Yan, B. Lanthanide Organic-Inorganic Hybrids Based on Functionalized Metal-Organic Frameworks (MOFs) for a near-UV White Led. *Chem. Commun.* **2014**, *50*, 15443-15446.
- (97) Lu, Y.; Yan, B. Luminescent Lanthanide Barcodes Based on Postsynthetic Modified Nanoscale Metal-Organic Frameworks. *J. Mater. Chem. C* **2014**, *2*, 7411-7416.
- (98) Lu, Y.; Yan, B. A Novel Luminescent Monolayer Thin Film Based on Postsynthetic Method and Functional Linker. *J. Mater. Chem. C* **2014**, *2*, 5526-5532.
- (99) Fang, Q. R.; Zhu, G. S.; Jin, Z.; Ji, Y. Y.; Ye, J. W.; Xue, M.; Yang, H.; Wang, Y.; Qiu, S. L. Mesoporous Metal-Organic Framework with Rare etb Topology for Hydrogen Storage and Dye Assembly. *Angew. Chem. Int. Ed.* **2007**, *46*, 6638-6642.
- (100) Cui, Y. J.; Song, R. J.; Yu, J. C.; Liu, M.; Wang, Z. Q.; Wu, C. D.; Yang, Y.; Wang, Z. Y.; Chen, B. L.; Qian, G. D. Dual-Emitting MOF \supset Dye Composite for Ratiometric Temperature Sensing. *Adv. Mater.* **2015**, *27*, 1420-1425.
- (101) Wang, Z. B.; Heinke, L.; Jelic, J.; Cakici, M.; Dommaschk, M.; Maurer, R. J.; Oberhofer, H.; Grosjean, S.; Herges, R.; Brase, S.; Reuter, K.; Woll, C. Photoswitching in Nanoporous, Crystalline Solids: An Experimental and Theoretical Study for Azobenzene Linkers Incorporated in MOFs. *Phys. Chem. Chem. Phys.* **2015**, *17*, 14582-14587.

- (102) Park, J.; Feng, D. W.; Yuan, S.; Zhou, H. C. Photochromic Metal-Organic Frameworks: Reversible Control of Singlet Oxygen Generation. *Angew. Chem. Int. Ed.* **2015**, *54*, 430-435.
- (103) Mabhai, S.; Dolai, M.; Dey, S.; Dhara, A.; Das, B.; Jana, A. A Novel Chemosensor Based on Rhodamine and Azobenzene Moieties for Selective Detection of Al³⁺ Ions. *New J. Chem.* **2018**, *42*, 10191-10201.
- (104) Luboch, E.; Wagner-Wysiecka, E.; Rzymowski, T. 4-Hexylresorcinol-Derived Hydroxyazobenzocrown Ethers as Chromoionophores. *Tetrahedron* **2009**, *65*, 10671-10678.
- (105) Heinke, L.; Cakici, M.; Dommaschk, M.; Grosjean, S.; Herges, R.; Brase, S.; Woll, C. Photoswitching in Two-Component Surface-Mounted Metal-Organic Frameworks: Optically Triggered Release from a Molecular Container. *ACS Nano* **2014**, *8*, 1463-1467.
- (106) Song, W. C.; Cui, X. Z.; Liu, Z. Y.; Yang, E. C.; Zhao, X. J. Light-Triggered Supramolecular Isomerism in a Self-Catenated Zn(II)-Organic Framework: Dynamic Photo-Switching CO₂ Uptake and Detection of Nitroaromatics. *Sci. Rep.* **2016**, *6*, 34870.
- (107) Gui, B.; Meng, Y.; Xie, Y.; Du, K.; Sue, A. C. H.; Wang, C. Immobilizing Organic-Based Molecular Switches into Metal-Organic Frameworks: A Promising Strategy for Switching in Solid State. *Macromol. Rapid Commun.* **2018**, *39*, 1700388.
- (108) Meng, X. S.; Gui, B.; Yuan, D. Q.; Zeller, M.; Wang, C. Mechanized Azobenzene-Functionalized Zirconium Metal-Organic Framework for on-Command Cargo Release. *Sci. Adv.* **2016**, *2*, e1600480.
- (109) Zhu, Y. L.; Zhang, W. Reversible Tuning of Pore Size and CO₂ Adsorption in Azobenzene Functionalized Porous Organic Polymers. *Chem. Sci.* **2014**, *5*, 4957-4961.

- (110) Castellanos, S.; Goulet-Hanssens, A.; Zhao, F. L.; Dikhtiarenko, A.; Pustovarenko, A.; Hecht, S.; Gascon, J.; Kapteijn, F.; Bleger, D. Structural Effects in Visible-Light-Responsive Metal-Organic Frameworks Incorporating *ortho*-Fluoroazobenzenes. *Chem. Eur. J.* **2016**, *22*, 746-752.
- (111) Huang, R. H.; Hill, M. R.; Babarao, R.; Medhekar, N. V. CO₂ Adsorption in Azobenzene Functionalized Stimuli Responsive Metal-Organic Frameworks. *J. Phys. Chem. C* **2016**, *120*, 16658-16667.
- (112) Wang, Z. B.; Grosjean, S.; Brase, S.; Heinke, L. Photoswitchable Adsorption in Metal-Organic Frameworks Based on Polar Guest-Host Interactions. *Chemphyschem* **2015**, *16*, 3779-3783.
- (113) Modrow, A.; Zargarani, D.; Herges, R.; Stock, N. Introducing a Photo-Switchable Azo-Functionality inside Cr-MIL-101-NH₂ by Covalent Post-Synthetic Modification. *Dalton Trans.* **2012**, *41*, 8690-8696.
- (114) Yanai, N.; Uemura, T.; Inoue, M.; Matsuda, R.; Fukushima, T.; Tsujimoto, M.; Isoda, S.; Kitagawa, S. Guest-to-Host Transmission of Structural Changes for Stimuli-Responsive Adsorption Property. *J. Am. Chem. Soc.* **2012**, *134*, 4501-4504.
- (115) Hermann, D.; Emerich, H.; Lepski, R.; Schaniel, D.; Ruschewitz, U. Metal-Organic Frameworks as Hosts for Photochromic Guest Molecules. *Inorg. Chem.* **2013**, *52*, 2744-2749.
- (116) Knebel, A.; Sundermann, L.; Mohmeyer, A.; Strauss, I.; Friebe, S.; Behrens, P.; Caro, J. Azobenzene Guest Molecules as Light-Switchable CO₂ Valves in an Ultrathin UIO-67 Membrane. *Chem. Mater.* **2017**, *29*, 3111-3117.

(117) Walton, I. M.; Cox, J. M.; Coppin, J. A.; Linderman, C. M.; Patel, D. G.; Benedict, J. B. Photo-Responsive MOFs: Light-Induced Switching of Porous Single Crystals Containing a Photochromic Diarylethene. *Chem. Commun.* **2013**, *49*, 8012-8014.

(118) Healey, K.; Liang, W. B.; Southon, P. D.; Church, T. L.; D'Alessandro, D. M. Photoresponsive Spiropyran-Functionalised MOF-808: Postsynthetic Incorporation and Light Dependent Gas Adsorption Properties. *J. Mater. Chem. A* **2016**, *4*, 10816-10819.

(119) Schwartz, H. A.; Olthof, S.; Schaniel, D.; Meerholz, K.; Ruschewitz, U. Solution-Like Behavior of Photoswitchable Spiroyrans Embedded in Metal-Organic Frameworks. *Inorg. Chem.* **2017**, *56*, 13100-13110.

(120) Bandara, H. M. D.; Basa, P. N.; Yan, J. J.; Camire, C. E.; MacDonald, J. C.; Jackson, R. K.; Burdette, S. C. Systematic Modulation of Hydrogen Bond Donors in Aminoazobenzene Derivatives Provides Further Evidence for the Concerted Inversion Photoisomerization Pathway. *Eur. J. Org. Chem.* **2013**, 4794-4803.

(121) Gong, L. L.; Feng, X. F.; Luo, F. Novel Azo-Metal-Organic Framework Showing a 10-Connected Bct Net, Breathing Behavior, and Unique Photoswitching Behavior toward CO₂. *Inorg. Chem.* **2015**, *54*, 11587-11589.

(122) Zhang, P.; Huo, P.; Zhang, X.; Zhu, Q. Y.; Dai, J. C-C to C=C Conversion within a Supramolecular Framework of Tetrathiafulvalene: A Confinement Effect and an Oxygen Related Dehydrogenation. *Chem. Commun.* **2018**, *54*, 7334-7337.

(123) Chen, T.; Huo, P.; Hou, J. L.; Xu, J.; Zhu, Q. Y.; Dai, J. Confinement Effects of Metal-Organic Framework on the Formation of Charge-Transfer Tetrathiafulvalene Dimers. *Inorg. Chem.* **2016**, *55*, 12758-12765.

(124) Chen, S.; Liu, H.; Cui, H. Q.; Hu, J.; Cai, H. Y. Synthesis of Spiropyran-Containing Random Copolymer by Atom Transfer Radical Polymerization and Its Complexation with Metal Ions. *Des. Monomers Polym.* **2015**, *18*, 574-582.

(125) Della Rocca, J.; Liu, D. M.; Lin, W. B. Nanoscale Metal-Organic Frameworks for Biomedical Imaging and Drug Delivery. *Acc. Chem. Res.* **2011**, *44*, 957-968.

(126) Huxford, R. C.; Della Rocca, J.; Lin, W. B. Metal-Organic Frameworks as Potential Drug Carriers. *Curr. Opin. Chem. Biol.* **2010**, *14*, 262-268.

(127) Horcajada, P.; Chalati, T.; Serre, C.; Gillet, B.; Sebrie, C.; Baati, T.; Eubank, J. F.; Heurtaux, D.; Clayette, P.; Kreuz, C.; Chang, J. S.; Hwang, Y. K.; Marsaud, V.; Bories, P. N.; Cynober, L.; Gil, S.; Ferey, G.; Couvreur, P.; Gref, R. Porous Metal-Organic-Framework Nanoscale Carriers as a Potential Platform for Drug Delivery and Imaging. *Nat. Mater.* **2010**, *9*, 172-178.

(128) Ricco, R.; Liang, W. B.; Li, S. B.; Gassensmith, J. J.; Caruso, F.; Doonan, C.; Falcaro, P. Metal-Organic Frameworks for Cell and Virus Biology: A Perspective. *ACS Nano* **2018**, *12*, 13-23.

(129) Diring, S.; Carne-Sanchez, A.; Zhang, J. C.; Ikemura, S.; Kim, C.; Inaba, H.; Kitagawa, S.; Furukawa, S. Light Responsive Metal-Organic Frameworks as Controllable CO₂-Releasing Cell Culture Substrates. *Chem. Sci.* **2017**, *8*, 2381-2386.

(130) Peng, S.; Bie, B. L.; Sun, Y. Z. S.; Liu, M.; Cong, H. J.; Zhou, W. T.; Xia, Y. C.; Tang, H.; Deng, H. X.; Zhou, X. Metal-Organic Frameworks for Precise Inclusion of Single-Stranded DNA and Transfection in Immune Cells. *Nat. Commun.* **2018**, *9*, 1293.

(131) Yu, M. F.; You, D. Q.; Zhuang, J. J.; Lin, S. Y.; Dong, L. Q.; Weng, S. T.; Zhang, B.; Cheng, K.; Weng, W. J.; Wang, H. M. Controlled Release of Naringin in Metal-Organic

Framework-Loaded Mineralized Collagen Coating to Simultaneously Enhance Osseointegration and Antibacterial Activity. *ACS Appl. Mater. Interfaces* **2017**, *9*, 19698-19705.

(132) Teplerisky, M. H.; Fantham, M.; Li, P.; Wang, T. C.; Mehta, J. P.; Young, L. J.; Moghadam, P. Z.; Hupp, J. T.; Farha, O. K.; Kaminski, C. F.; Fairen-Jimenez, D. Temperature Treatment of Highly Porous Zirconium-Containing Metal-Organic Frameworks Extends Drug Delivery Release. *J. Am. Chem. Soc.* **2017**, *139*, 7522-7532.

(133) Orellana-Tavra, C.; Marshall, R. J.; Baxter, E. F.; Lazaro, I. A.; Tao, A.; Cheetham, A. K.; Forgan, R. S.; Fairen-Jimenez, D. Drug Delivery and Controlled Release from Biocompatible Metal-Organic Frameworks Using Mechanical Amorphization. *J. Mater. Chem. B* **2016**, *4*, 7697-7707.

(134) Gao, P. F.; Zheng, L. L.; Liang, L. J.; Yang, X. X.; Li, Y. F.; Huang, C. Z. A New Type of pH-Responsive Coordination Polymer Sphere as a Vehicle for Targeted Anticancer Drug Delivery and Sustained Release. *J. Mater. Chem. B* **2013**, *1*, 3202-3208.

(135) Epley, C. C.; Roth, K. L.; Lin, S. Y.; Ahrenholtz, S. R.; Grove, T. Z.; Morris, A. J. Cargo Delivery on Demand from Photodegradable MOF Nano-Cages. *Dalton Trans.* **2017**, *46*, 4917-4922.

(136) Taylor-Pashow, K. M. L.; Della Rocca, J.; Xie, Z. G.; Tran, S.; Lin, W. B. Postsynthetic Modifications of Iron-Carboxylate Nanoscale Metal-Organic Frameworks for Imaging and Drug Delivery. *J. Am. Chem. Soc.* **2009**, *131*, 14261-14263.

(137) Lazaro, I. A.; Haddad, S.; Sacca, S.; Orellana-Tavra, C.; Fairen-Jimenez, D.; Forgan, R. S. Selective Surface Pegylation of UIO-66 Nanoparticles for Enhanced Stability, Cell Uptake, and pH-Responsive Drug Delivery. *Chem.* **2017**, *2*, 561-578.

- (138) Orellana-Tavra, C.; Haddad, S.; Marshall, R. J.; Lazaro, I. A.; Boix, G.; Imaz, I.; Maspoch, D.; Forgan, R. S.; Fairen-Jimenez, D. Tuning the Endocytosis Mechanism of Zr-Based Metal-Organic Frameworks through Linker Functionalization. *ACS Appl. Mater. Interfaces* **2017**, *9*, 35516-35525.
- (139) Mbatia, H. W.; Kennedy, D. P.; Burdette, S. C. Understanding the Relationship between Photolysis Efficiency and Metal Binding Using Argencast Photocages. *Photochem Photobiol.* **2012**, *88*, 844-850.
- (140) Klan, P.; Solomek, T.; Bochet, C. G.; Blanc, A.; Givens, R.; Rubina, M.; Popik, V.; Kostikov, A.; Wirz, J. Photoremovable Protecting Groups in Chemistry and Biology: Reaction Mechanisms and Efficacy. *Chem. Rev.* **2013**, *113*, 119-191.
- (141) Allen, C. A.; Cohen, S. M. Near-UV Photo-Induced Modification in Isoreticular Metal-Organic Frameworks. *J. Mater. Chem.* **2012**, *22*, 10188-10194.
- (142) Han, X.; Cheng, Q.; Meng, X. R.; Shao, Z. C.; Ma, K.; Wei, D. H.; Ding, J.; Hou, H. W. Unique Structural Micro-Adjustments in a New Benzothiadiazole-Derived Zn(II) Metal Organic Framework via Simple Photochemical Decarboxylation. *Chem. Commun.* **2017**, *53*, 10314-10317.
- (143) Deleu, W. P. R.; Rivero, G.; Teixeira, R. F. A.; Du Prez, F. E.; De Vos, D. E. Metal Organic Frameworks Encapsulated in Photocleavable Capsules for UV-Light Triggered Catalysis. *Chem. Mater.* **2015**, *27*, 5495-5502.

**Chapter 2 Emissive Azobenzenes Delivered on a Silver
Coordination Polymer**

2.1. Introduction

Azobenzene (AB) undergoes *trans*→*cis* isomerization when irradiated, and *cis*→*trans* isomerization thermally or upon exposure to a different wavelength of light. Since light absorption depends on the conjugated π -orbital system, ring substituents change the photoisomerization process and the optical properties of the AB chromophore. The $S_2\leftarrow S_0$ of aminoazobenzene (aAB) shifts to longer wavelengths, which typically leads to an overlap with the $S_1\leftarrow S_0$ transition.¹⁻³ As we previously reported, AzoAMoP (**1**, 2,2'-bis[*N,N'*-(2-pyridyl)methyl]diaminoazobenzene) exhibits overlapping $S_2\leftarrow S_0$ and $S_1\leftarrow S_0$ transitions with a λ_{\max} at 490 nm and 30-fold higher emission than AB at 77 K. Furthermore, AzoAMoP undergoes minimal *trans*→*cis* isomerization due to intramolecular hydrogen bonding between the anilino protons and the pyridyl and diazene nitrogen atoms.⁴ Hydrogen bonding imposes an energetic barrier that prevents the aryl rings from adopting the prerequisite collinear conformation necessary for isomerization via the concerted inversion mechanism.

To further develop the photochemistry of these unique aAB derivatives, we replaced the pyridine ligand of the aminomethylpyridine groups with a series of hydrogen bond acceptors, and changed the linker between the amine and pyridine to an ethylene.⁵ Investigations with the small library of compounds suggested that reproducing the structure-induced photophysical properties observed with AzoAMoP would be difficult with a standalone AB chromophore. This study included the report of AzoAEoP (**2**, 2,2'-bis[*N,N'*-(2-pyridyl)ethyl]diaminoazobenzene), which utilizes a pyridine ligand and an ethylene spacer. With AzoAMoP and AzoAEoP in hand, we reasoned that the using a 3-pyridyl (*meta*) or 4-pyridyl (*para*) pyridine ligand in the existing aminoazobenzene scaffold would allow retention of the hydrogen bonded anilino-hydrogen-diazene core, while orienting the pyridine nitrogen atoms on a trajectory favorable for coordinating

metal ions. Since the low temperature emission of AzoAMoP was attributed to hydrogen bonding and from being embedded in a frozen solvent glass, we hypothesized that integrating the aAB chromophore into coordination polymers would restrict non-radiative decay pathways sufficiently to produce emissive systems at ambient temperature.

2.2. Experimental Section

2.2.1. General Procedures. All reagents were purchased and used without further purification. The 2,2'-diaminoazobenzene (DAAB) synthon was prepared as previously described.⁶ Toluene, dichloromethane (CH₂Cl₂), dichloroethane (DCE) and diethylether (Et₂O) were sparged with argon and dried by passing through alumina-based drying columns. All chromatography and thin-layer chromatography (TLC) were performed on silica (200–400 mesh). TLCs were developed by using CH₂Cl₂ or solvent mixtures containing CH₂Cl₂, ethyl acetate (EtOAc), hexanes, or methanol (CH₃OH). ¹H and ¹³C NMR spectra were recorded with a 500 MHz Bruker Biospin NMR instrument. Chemical shifts are reported in ppm relative to tetramethylsilane (TMS). FT-IR spectra were recorded using Bruker Optics FT-IR spectrometer equipped with a Vertex70 attenuated total reflection (ATR) accessory by collecting 1024 scans over a scan range from 4000 to 400 cm⁻¹ at 4 cm⁻¹ resolution. Thermogravimetric analysis (TGA) measurements were carried out on a TA Instruments Hi-Res TGA 2950 Thermogravimetric Analyzer from room temperature to 800 °C under nitrogen atmosphere at a heating rate of 10 °C/min. LC/MS was carried on a Single Quadruple, Agilent Technologies 1200 series LC system. High resolution mass spectra were obtained at the University of Notre Dame mass spectrometry facility using microTOF instrument operating in positive ionization mode. Melting-point information was obtained using a Hydrothermal Mel-Temp instrument.

2,2'-Bis[N,N'-(2-pyridyl)methyl]diaminoazobenzene (1, AzoAMoP). AzoAMoP was synthesized as previously reported⁴ with minor modifications. DAAB (0.640 g, 3.02 mmol), 2-pyridinecarboxaldehyde (0.600 mL, 6.31 mmol) and 3 Å molecular sieves (0.940 g) were combined in CH₂Cl₂ (30 mL) and stirred for 24 h at room temperature. Sodium triacetoxyborohydride (NaBH(OAc)₃, 1.34 g, 6.32 mmol) was added, and the mixture was stirred at room temperature for 24 h. The reaction mixture was diluted with water (20 mL), and the product was extracted into CH₂Cl₂ (3 × 40 mL). The combined organic layers were dried over sodium sulfate (Na₂SO₄), and the solvent was removed. Flash chromatography on silica (24:1 EtOAc/MeOH) yielded an orange-red powder (387 mg, 32.5%). Analytical data matched previously reported values.⁴

2,2'-Bis[N,N'-(2-pyridyl)ethyl]diaminoazobenzene (2, AzoAEoP). AzoAEoP was synthesized as previously reported⁵ with minor modifications. DAAB (0.640 g, 3.02 mmol) and 2-vinylpyridine (316 µL, 2.93 mmol) were combined in CH₃OH (3 mL) and acetic acid (AcOH, 10 mL). The reaction mixture was stirred for 3 h at 45 °C before a second portion of 2-vinylpyridine (632 µL, 5.86 mmol) was added. After stirring for 24 h at 45 °C, the reaction mixture was cooled to room temperature, diluted with 10 mL of water, and the pH was adjusted to ~8 with ammonium hydroxide (NH₄OH). The product was extracted into EtOAc (3 × 50 mL), the combined organic materials were dried over Na₂SO₄, and the solvent was removed. Flash chromatography on silica (CH₂Cl₂/CH₃OH, 25:1) gave AzoAEoP (448 mg, 35.1%) as a dark red solid. Analytical data matched previously reported values.⁵

2,2'-Bis[N,N'-(3-pyridyl)methyl]diaminoazobenzene (3, AzoAMmP). DAAB (0.640 g, 3.02 mmol), 3-pyridinecarboxaldehyde (600 µL, 6.39 mmol) and 3 Å molecular sieves (0.940 g) were combined in DCE (30 mL) and stirred for 24 h at room temperature. NaBH(OAc)₃ (1.34 g, 6.32

mmol) was added and the reaction mixture was stirred at room temperature for 24 h. The reaction mixture was diluted with water (20 mL), and the product was extracted into CH₂Cl₂ (3 × 40 mL). The combined organic layers were dried over sodium Na₂SO₄, and the solvent was removed. Flash chromatography on silica using EtOAc/hexanes (2:1) and EtOAc/CH₃OH (20:1) yielded AzoAMmP as a dark red solid (532 mg, 44.7%). Diffusion of Et₂O into an CH₃CN solution of AzoAMmP provided orange-red blocks suitable for X-ray analysis. TLC R_f = 0.30 (silica, EtOAc/CH₃OH, 49:1). Mp = 158-159 °C. ¹H NMR (500 MHz, CDCl₃) δ 8.65 (s, 2 H), 8.53 (d, *J* = 4.9 Hz, 2 H), 8.43 (s, 2 H), 7.67 (d, *J* = 7.8 Hz, 2 H), 7.55 (dd, *J* = 8.0, 1.6 Hz, 2 H), 7.25 (t, *J* = 6.2 Hz, 2 H), 7.19 (t, *J* = 7.8 Hz, 2 H), 6.76 (t, *J* = 7.6 Hz, 2 H), 6.70 (d, *J* = 8.4 Hz, 2 H), 4.50, (s, 4 H). ¹³C NMR (125 MHz, CDCl₃) δ 149.1, 149.0, 143.0, 136.6, 134.8, 134.3, 131.7, 127.3, 123.6, 116.8, 112.0, 44.7. FT-IR (neat, cm⁻¹) 3302.0, 3062.1, 3030.0, 2991.1, 2880.2, 2617.1, 2056.7, 1498.0, 1476.3, 1465.2, 1419.9, 1309.2, 1247.5, 1199.2, 1153.9, 1122.6, 1025.9, 1041.0, 906.9, 787.0, 748.0, 706.7, 601.8. HRMS (+ESI) calculated for MH⁺ 395.1979 and observed 395.1980.

2,2'-Bis[N,N'-(4-pyridyl)methyl]diaminoazobenzene (4, AzoAMpP). DAAB (0.640 g, 3.02 mmol), 4-pyridinecarboxaldehyde (600 μL, 6.37 mmol) and 3 Å molecular sieves (0.940 g) were combined in DCE (30 mL) and stirred for 24 h at room temperature. NaBH(OAc)₃ (1.34 g, 6.32 mmol) was added and the reaction mixture was stirred at room temperature for 24 h. The reaction mixture was diluted with water (20 mL), and the product was extracted into CH₂Cl₂ (3 × 40 mL). The combined organic layers were dried over Na₂SO₄, and the solvent was removed. Flash chromatography on silica using CH₂Cl₂/CH₃OH (10:1) yielded AzoAMpP as a red orange solid (474 mg, 39.8%). Slow evaporation of chloroform (CHCl₃) provided orange-red needles suitable for X-ray analysis. TLC R_f = 0.20 (silica, CH₂Cl₂/CH₃OH, 24:1). Mp = 160-161 °C. ¹H NMR (500

MHz, CDCl₃) δ 8.58 (d, J = 5.7 Hz, 4 H), 8.55 (s, 2 H), 7.63 (dd, J = 7.9, 1.6 Hz, 2 H), 7.33 (d, J = 6.0 Hz, 4 H), 7.19 (t, J = 7.7 Hz, 2 H), 6.79 (t, J = 7.6 Hz, 2 H), 6.61 (d, J = 8.5 Hz, 2 H), 4.54 (s, 4 H). ¹³C NMR (125 MHz, CDCl₃) δ 150.2, 148.2, 143.0, 136.6, 131.8, 127.3, 122.0, 116.9, 112.1, 46.1. FT-IR (neat, cm⁻¹) 3358.0, 3111.4, 2892.3, 2130.1, 1734.2, 1652.8, 1615.2, 1528.5, 1492.4, 1415.2, 1370.5, 1312.1, 1300.9, 1244.1, 1289.1, 1206.4, 1148.1, 1124.5, 1045.8, 1016.7, 987.5, 941.5, 883.6, 804.2, 740.7, 666.3, 620.0. HRMS (+ESI) calculated for MH⁺ 395.1979 and observed 395.1985.

2,2'-Bis[N,N'-(4-pyridyl)ethyl]diaminoazobenzene (5, AzoAEpP). DAAB (0.640 g, 3.02 mmol) and 4-vinylpyridine (316 μ L, 2.96 mmol) were combined in CH₃OH (3 mL) and acetic acid (AcOH, 10 mL). The reaction mixture was stirred for 3 h at 45 °C before a second portion of 4-vinylpyridine (632 μ L, 5.91 mmol) was added. After stirring for 24 h at 45 °C, the reaction mixture was cooled to room temperature, diluted with 10 mL of water, and the pH was adjusted to ~8 with NH₄OH. The product was extracted into EtOAc (3 \times 50 mL), the combined organic materials were dried over Na₂SO₄, and the solvent was removed. Flash chromatography on silica using CH₂Cl₂/CH₃OH (15:1) yielded AzoAEpP as a red orange solid (500 mg, yield 39.1%). Slow evaporation from toluene/ethanol (1:1) provided orange-red needles suitable for X-ray analysis. TLC R_f = 0.35 (silica, DCM/CH₃OH, 10:1). Mp = 149–150 °C. ¹H NMR (500 MHz, CDCl₃) δ 8.51 (d, J = 4.4 Hz, 4 H), 8.06 (s, 2 H), 7.32 (dd, J = 8.0, 1.6 Hz, 2 H), 7.24 (t, J = 7.8 Hz, 2 H), 7.17 (d, J = 4.7 Hz, 4 H), 6.79 (d, J = 8.4 Hz, 2 H), 6.74 (t, J = 7.5 Hz, 2 H), 3.57 (q, J = 6.4 Hz, 4 H), 2.97 (t, J = 6.9 Hz, 4 H). ¹³C NMR (125 MHz, CDCl₃) δ 150.0, 148.1, 143.0, 136.4, 131.6, 127.2, 124.1, 116.3, 111.7, 42.9, 34.8. FT-IR (neat, cm⁻¹) 3205.4, 3046.8, 2917.4, 2851.4, 2171.9, 2330.4, 1601.0, 1565.1, 1509.1, 1458.6, 1321.6, 1204.0, 1147.8, 1072.3, 1042.8, 836.7, 785.9, 368.8. HRMS (+ESI) calculated for MH⁺ 423.2292 and observed 423.2270.

[[Ag(AzoAMoP)](CF₃SO₃)]_n (AgAAMoP). AzoAMoP (25.4 mg, 64.4 μmol) in toluene (1.8 mL) was added dropwise to a toluene solution (1.8 mL) of silver trifluoromethanesulfonate (AgOTf, 16.6 mg, 64.6 μmol). Upon stirring the reaction mixture for 30 min, an orange-red solid slowly precipitated. CH₃CN (1 mL) was added to re-dissolve the precipitate, and the reaction mixture was stirred at room temperature for 2 h and filtered. Slow evaporation provided orange rectangular plates suitable for X-ray analysis. FT-IR (neat, cm⁻¹) 3361.6, 3069.5, 2904.1, 2324.2, 1981.4, 1597.2, 1581.2, 1493.6, 1466.0, 1436.7, 1371.0, 1322.3, 1285.2, 1240.9, 1219.3, 1159.1, 1107.3, 1075.2, 1052.2, 1028.3, 991.5, 888.3, 823.5, 755.2, 699.3, 633.5. Elemental analysis calcd. for C₂₇H₂₅AgF₃N₇O₃S (AgAAMoP·CH₃CN): C 46.79%, H 3.61%, N 14.15%; Found: C 46.50%, H 3.90%, N 14.53%. TGA shows a 0.7% weight loss between 60-120 °C, which may correspond to absorbed solvent. Decomposition occurs at 175 °C.

[[Ag(AzoAMmP)]CF₃SO₃]]_n (AgAAMmP). AzoAMmP (25.4 mg, 64.4 μmol) in toluene (1.8 mL) was added dropwise to a toluene solution (1.8 mL) of AgOTf (16.6 mg, 64.6 μmol). Upon stirring the reaction mixture for 30 min, an orange-red solid slowly precipitated. CH₃CN (1 mL) was added to re-dissolve the precipitate, and the reaction mixture was stirred at room temperature for 2 h and filtered. Slow evaporation of the filtrate at room temperature provided crystals in orange-red blocks suitable for X-ray analysis. FT-IR (neat, cm⁻¹) 3230.2, 3076.0, 2941.6, 2889.8, 2362.8, 2314.7, 2165.8, 1982.2, 1862.7, 1739//.6, 1603.8, 1578.9, 1507.0, 1437.0, 1431.2, 1370.4, 1297.1, 1265.5, 1265.3, 1254.3, 1148.0, 1024.0, 1051.3, 941.1, 741.7, 612.6, 612.3. Elemental analysis calcd. for C₂₅H_{24.5}AgF₃N₆O_{4.5}S (AgAAMmP·1.5H₂O): C 44.29%, H 3.64%, N 12.40%; Found: C 44.01%, H 3.31%, N 12.02% The TGA shows no weight loss before decomposition at 177 °C.

[[Ag(AzoAMpP)]NO₃]]_n (AgAAMpP). AzoAMpP (10.0 mg, 25.4 μmol) was dissolved in 2.5 mL CH₃OH/CH₃CN (1:4) mixture with a few drops of DMF. The solution was added dropwise to an

CH₃CN solution (0.5 mL) containing silver nitrate (AgNO₃, 4.5 mg, 27 μmol) and tetrabutylammonium hexafluorophosphate (*n*-Bu₄PF₆, 11.0 mg, 0.0284mmol). The reaction mixture was stirred 30 min to precipitate an orange-red solid. The solid was isolated by filtration, dissolved in 2 mL of a 1:1 mixture of CH₃OH/CH₃CN, and for 2 h stirred at room temperature. The mixture was filtered and slow evaporation provided orange-red blocks suitable for X-ray analysis. FT-IR (neat, cm⁻¹) 3516.5, 3484.4, 3262.2, 2862.0, 2826.4, 1942.1, 1639.4, 1613.5, 1610.4, 1454.6, 1454.6, 1445.0, 1322.0, 1207.8, 1206.6, 1155.8, 1100.9, 1069.1, 1028.0, 963.3, 889.5, 765.7. Elemental analysis calcd. for C₂₄H₂₂N₇O₃Ag (AgAAMpP): C 51.03%, H 3.90%, N 17.37%; Found: C 50.92%, H 4.01%, N 17.43%. TGA shows a 3.6% weight loss between 60-120 °C, which may correspond to absorbed solvent. Decomposition occurs at 154 °C.

[Ag(AzoAEoP)]NO₃(AgAAEoP). AzoAEoP (30.0 mg, 71.1 μmol) in DCM (1 mL) was added dropwise into an CH₃CN solution (1 mL) of AgNO₃ (12.0 mg, 70.6 μmol) and *n*-Bu₄PF₆ (28.0 mg, 72.3 μmol). The reaction mixture was stirred 30 min to precipitate an orange solid. The solid was isolated by filtration, dissolved in 2 mL of a 1:1 mixture of CH₃OH/CH₃CN, and stirred at room temperature for 2 h. The mixture was filtered and slow evaporation provided orange-red blocks suitable for X-ray analysis. FT-IR (neat, cm⁻¹) 3247.2, 3049.8, 2911.3, 2863.4, 2324.7, 2164.5, 2051.2, 1981.6, 1903.6, 1604.1, 1566.1, 1497.9, 1482.5, 1439.3, 1423.7, 1375.0, 1322.0, 1284.7, 1249.4, 1221.3, 1177.2, 1156.4, 1129.0, 1105.9, 1084.8, 1064.8, 1044.1, 1025.4, 1004.8, 959.6, 938.5, 882.3, 846.5, 825.4, 800.5, 762.5, 752.0, 738.4, 647.8, 616.5. Elemental analysis calcd. for C₂₆H₂₇N₇O_{3.5}Ag (AgAAEoP·0.5H₂O): C 51.93%, H 4.53%, N 16.30%; Found: C 51.84%, H 4.43%, N 16.13%. The TGA shows no weight loss before decomposition at 166 °C.

{[Ag(AzoAEpP)₂]PF₆}_n (AgAAEpP). AzoAEpP (30.0 mg, 71.1 μmol) in DCM (1 mL) was added dropwise into an CH₃CN solution (1 mL) containing AgNO₃ (12.0 mg, 70.6 μmol) and *n*-Bu₄PF₆

(28.0 mg, 72.3 μmol). The reaction mixture was stirred 30 min to precipitate a yellow solid. The solid was isolated by filtration, dissolved in 2 mL of a 1:1 mixture of $\text{CH}_3\text{OH}/\text{CH}_3\text{CN}$, and stirred at room temperature for 2 h. The mixture was filtered and slow evaporation provided orange-red blocks suitable for X-ray analysis. FT-IR (neat, cm^{-1}) 3426.5, 3068.1, 2861.8, 2360.3, 2324.7, 2050.9, 1981.4, 1604.0, 1564.4, 1501.5, 1464.6, 1430.7, 1316.2, 1240.8, 1223.5, 1211.6, 1183.9, 1154.6, 1123.0, 1104.1, 1079.5, 1066.5, 1028.6, 939.4, 880.9, 847.3, 823.3, 800.0, 760.1, 740.8, 615.2. Elemental analysis calcd. for $\text{C}_{52}\text{H}_{51}\text{N}_{12}\text{F}_6\text{PAg}(\text{AgAAEP})$: C 56.89%, H 4.77%, N 15.31%; Found: C 56.72%, H 4.48%, N 15.02%. TGA shows a 0.7% weight loss between 60-120°C, which may correspond to absorbed solvent. Decomposition occurs at 197 °C.

2.2.2. Collection and Reduction of X-ray Data

X-ray Crystallography. Structural analysis was carried out in the X-Ray Crystallographic Facility at Worcester Polytechnic Institute. Crystals were glued on tip of a glass fiber or were covered in PARATONE oil on 100 μm MiTeGen polyimide micromounts and were mounted on a Bruker-AXS APEX CCD diffractometer equipped with an LT-II low temperature device. Diffraction data were collected at room temperature or at 100(2) K using graphite monochromated $\text{Mo-K}\alpha$ radiation ($\lambda = 0.71073 \text{ \AA}$) using the omega scan technique. Empirical absorption corrections were applied using the SADABS program.⁷ The unit cells and space groups were determined using the SAINT+ program.⁷ The structures were solved by direct methods and refined by full matrix least-squares using the SHELXTL program.⁸ Refinement was based on F^2 using all reflections. All non-hydrogen atoms were refined anisotropically. Hydrogen atoms on carbon atoms were all located in the difference maps and subsequently placed at idealized positions and given isotropic U values 1.2 times that of the carbon atom to which they were bonded. Hydrogen atoms bonded to oxygen atoms were located and refined with isotropic thermal parameters. Mercury 3.1 software was used

to examine the molecular structure. Relevant crystallographic information is summarized in Table 2.1 and Table 2.2, and the 50% thermal ellipsoid plot is shown in Figures 2.1-2.5.

Powder X-ray diffraction. PXRD data were collected on a Bruker-AXS D8-Advance diffractometer using Cu-K α radiation with X-rays generated at 40 kV and 40 mA. Bulk samples of crystals were placed in a 20 cm \times 16 cm \times 1 mm well in a glass sample holder, and scanned at RT from 3 $^\circ$ to 50 $^\circ$ (2 θ) in 0.05 $^\circ$ steps at a scan rate of 2 $^\circ$ /min. Simulated PXRD patterns from single crystal data were compared to PXRD patterns of experimental five AzoAXxP silver complexes, to confirm the uniformity of the crystalline samples (Figure 2.17).

2.2.3. Spectroscopy

General Spectroscopic Methods. Solution UV-Vis absorption spectra were acquired in 1.0 cm quartz cuvettes at room temperature and recorded on a Thermo Scientific Evolution 300 UV-Vis spectrometer with inbuilt Cary winUV software. Steady-state diffuse reflectance UV-Vis spectra were obtained on the same instrument with Harrick Praying Mantis diffuse reflectance accessory (Harrick Scientific Products) and referenced to magnesium sulfate. Solution emission spectra were recorded on a Hitachi F-4500 spectrophotometer with excitation and emission slit widths of 5 nm. The excitation source was 150 W Xe arc lamp (Ushio Inc.) operating at a current rate of 5 A and equipped with photomultiplier tube with a power of 400 V.

Emission and Quantum Yield Determination. Steady-state emission spectra were recorded on a Hitachi F-4500 spectrophotometer with excitation and emission slit widths of 5 nm. The excitation source was 150 W Xe arc lamp (Ushio Inc.) operating at a current rate of 5 A and equipped with photomultiplier tube with a power of 400 V. Quantum yields in the solid state were determined in triplicated following published procedures using Na₂SO₄ as the reference.^{9, 10}

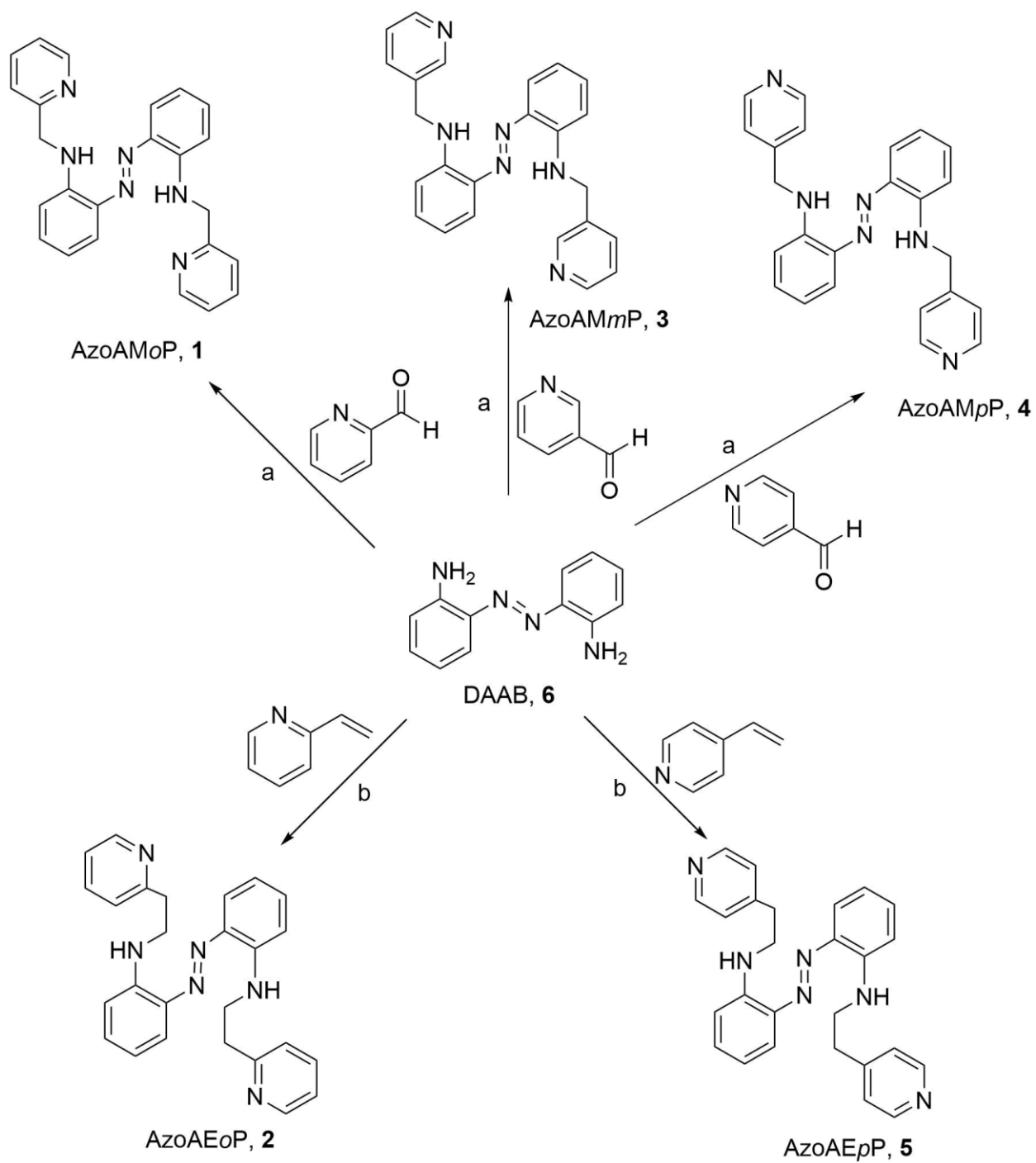
Analyte Detection by Emission. A 100 μM suspension, with respect to AzoAE*p*P units, of AgAAE*p*P in toluene (2 mL) was prepared, and the emission spectra was recorded ($\lambda_{\text{ex}} = 523 \text{ nm}$). Upon the addition of each aliquot of analyte, the mixture was equilibrated by stirring for 30 min before recording the emission spectra. The emission response to all analytes was measured by integrating the emission band between 550-800 nm. Pyridine was added from a 2 mM stock solution in toluene in three equal portions, to obtain final concentration of 33, 67, and 100 μM , and the emission was measured. After the third addition, the solvent and pyridine were removed by sparging with N_2 gas, and the resulting crystalline material was re-suspended in 2 mL of toluene and stirred for 30 min before re-measuring the emission. The emission loss and restoration steps were repeated in triplicate with single analyte additions to reach 100 μM pyridine. When excess pyridine was added (500 μM), the emission completely disappeared, and could not be restored. Measurements for *N*-methylmorpholine (NMM) were acquired using analogous procedures, were each addition provided a final concentration of 100 μM NMM. Measurements with imidazole were acquired similarly, but emission loss was irreversible. Measurements with dimethylamine (DMA) were acquired similarly except toluene was replaced with THF, and the DMA concentration after each switching cycle was 10 μM . After each DMA addition, the emission was restored by the addition of aliquots of 1.58 mM nitric acid (12.7 μL , 20.1 nmol) to achieve a final H^+ concentration of 20 μM .

2.3. Synthesis and Structure

Using the synthetic protocols for preparing AzoAM*o*P and AzoAE*o*P, we prepared three additional aAB-bipyridyl ligands AzoAM*m*P (**3**, 2,2'-bis[*N,N'*-(3-pyridyl)methyl]diaminoazobenzene), AzoAM*p*P (**4**, 2,2'-bis[*N,N'*-(4-pyridyl)methyl]diaminoazobenzene) and AzoAE*p*P (**5**, 2,2'-bis[*N,N'*-(4-

pyridyl)ethyl]diaminoazobenzene) from the common DAAB scaffold (2,2'-diaminoazobenzene, **6**) building block (Scheme 2.1). Collectively, we refer to the aABs as AzoAX_xP compounds where “X” represents the variable components. The *m*-pyridyl ligand containing the ethylene linker (AzoAEmP) has not been accessed yet owing to difficulty obtaining a stable and reactive synthon. AzoAEoP and AzoAEpP are prepared via a Michael reaction with the corresponding vinylpyridine; however, the vinyl group becomes a poor Michael acceptor with the nitrogen atom in the *meta*-position. The anilino nitrogen atom also appears to be a weak nucleophile as reactions with 3-(2-bromoethyl)-pyridine or 2-(pyridin-3-yl)ethyl 4-methylbenzenesulfonate failed to produce the desired product. Attempts to prepare AzoAEmP by reductive amination with 2-(pyridin-3-yl)acetaldehyde also proved unsuccessful owing to difficulty isolating sufficient quantities of the aldehyde precursor.

The five ligands can be viewed collectively as a library of extended bipyridine ligands where each pyridine ligand can coordinate a different metal ion to form an extended network. Fortuitously, all five AzoAX_xP ligands are highly crystalline in the solid state, and therefore could be subjected to crystallographic analysis. The two pyridine nitrogen atoms of AzoAMoP are 8.37 Å apart; however, the pyridine lone pairs engage in hydrogen bonding with the anilino hydrogen atom, which orients the potential coordination sites inward. In preliminary screenings, we observed that AzoAMoP did not appear to coordinate metal ions like Zn²⁺, presumably because the



Scheme 2.1. Synthetic protocols for preparing five AzoAXxP ligands. Reagents and conditions: (a) $\text{NaBH}(\text{OAc})_3, \text{CH}_2\text{Cl}_2$, room temperature; (b) $\text{AcOH}, \text{MeOH}, 45^\circ\text{C}$.

thermodynamic stability of the hydrogen bonds. We reasoned that a thermodynamically stable, kinetically inert metal-ligand bond could provide access to a metal complex with AzoAM o P by shifting the equilibrium from hydrogen bonding to metal ligand bonding toward complex formation. Ag⁺ appeared to be a good candidate for coordination polymer formation based on other successful investigations,¹¹⁻¹⁵ as well as the stability of Ag–pyridine bonds.¹⁶ We further speculated that the photoactivity of Ag⁺ might provide access to additional functionality in the resulting AB materials.

The other four AzoAX x P derivatives do not exhibit hydrogen bonding with the pyridine lone pairs, so ostensibly the ligands could bind metal ions more like typical bridging bipyridine derivatives. Two-coordinate metals with bridging bipyridine ligands are rare¹⁷⁻¹⁹ except for Ag⁺.^{11, 13, 20, 21} The two AzoAX x P derivatives containing methylene linkers, AzoAM m P and AzoAM p P, can rotate at the azobenzene–anilino C–N bond, anilino–methylene N–C bond and methylene–pyridine C–C bond. The two AzoAX x Ps with ethylene linkers, AzoAE o P and AzoAE p P, can also rotate about C–C ethylene bond. The multiple degrees of freedom suggest our ligands might go through noticeable reorientation during the formation of Ag⁺ complexes or polymers.

Although not absolutely predictive, the geometric structure of Ag⁺ metal organic polymer chains depends on the pyridine substitution pattern, the directionality of the pyridine lone pairs, and the conformational freedom of the ligand. Solvent and anion interactions also can impact the extended macromolecular structure. In bipyridine ligands containing *ortho* pyridine nitrogen atoms, the lone pairs tend to face inward in the apo form, but often reorient during polymerization process to minimize crowding between the side chain and the Ag⁺ binding site, which often results in zigzag silver chain structures.^{21, 22} In *meta*- and *para*-pyridine bipyridine ligands, the lone pairs tend to face outward, and therefore do not necessarily need to undergo structural rearrangement in

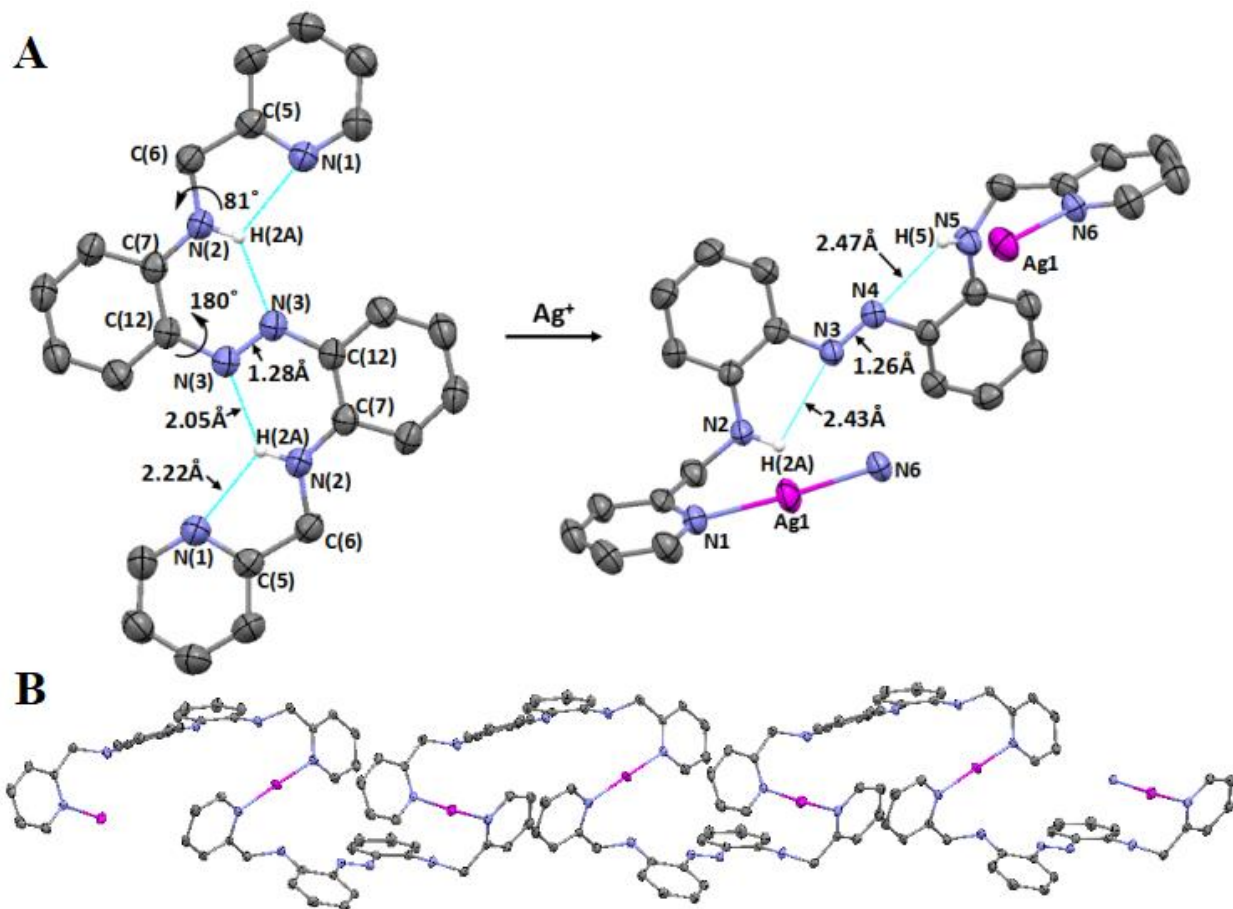


Figure 2.1A. Preparation of AgAAMoP showing the thermal ellipsoid representation diagram of AzoAMoP and AgAAMoP at the 50% probability level and selected atom labels. Hydrogen atoms except for those engaged in intramolecular hydrogen bonds are omitted for clarity. The triflate anion and a non-coordinating CH₃CN solvent molecule are omitted for clarity. AgAAMoP was prepared in toluene using AgOTf as the silver source using a slow ligand exchange process with CH₃CN. During the polymer formation, the azo N–C and anilino–methylene N–C bonds rotate by 180° and 81°, respectively. **2.1B.** Thermal ellipsoid representation diagram at the 50% probability level of the expanded helical polymer chain. Hydrogen atoms, triflate anions and CH₃CN solvent molecules are omitted for clarity.

two-coordinate Ag⁺ structures. Some *meta*-bipyridine derivatives exhibit minimal reorientation,²³ or asymmetric changes on one half of the molecule.²¹ In more rigid *meta*- and *para*-bipyridine

ligands, linear geometries are more common because of partly or completely restricted movement.^{24, 25}

Based on the structural trends with other bipy derivatives,^{21, 22} we hypothesized that the pyridine nitrogen lone pairs in AzoAMoP would flip outward to accommodate Ag⁺ coordination if the intramolecular hydrogen bonds were disrupted. We prepared the AzoAMoP complex using protocols designed to gradually deliver Ag⁺ through ligand exchange with CH₃CN.¹³ A [Ag(AzoAMoP)]⁺ complex precipitates immediately from toluene solution, but re-dissolves upon addition of CH₃CN. Slow evaporation of CH₃CN leads to nitrile–pyridine ligand exchange, and the formation of a AgAAMoP coordination polymer, which was isolated as well-defined orange crystals. Compared to the structure of the apo ligand, the azo N–C and anilino–methylene N–C bonds in the Ag⁺ polymer with AzoAMoP ligand are rotated by 180° and 81° respectively (Figure 2.1). This rearrangement orients the two pyridine rings perpendicular to the azo core but retains inward-facing pyridine nitrogen lone pairs in the formation of a helical structure where each Ag⁺ is coordinated by a pyridine nitrogen atoms from each of two different AzoAMoP ligands. Ag⁺ binding increases the length of the hydrogen bonds between the anilino hydrogen atoms and the diazene lone pairs of DAAB core by approximately 0.4 Å, and introduces a slight asymmetry in the two halves of the molecule. The core N=N bond decreases slightly from 1.28 Å to 1.26 Å owing to the decrease in hydrogen bonding (Table 2.1). Although the changes in hydrogen bonding might suggest a less rigid and therefore less emissive azobenzene chromophore, we expected that the metal complexation and crystal packing interactions would offset the loss of intramolecular forces.

Compared to AzoAMoP, AzoAMmP and AzoAMpP exhibit more conformational freedom, since both lack hydrogen bonding between the anilino hydrogen atoms and pyridine nitrogen atoms. The point-to-point distance between the two pyridine nitrogen atoms distances are 15.96 Å and 16.52 Å respectively, but unlike linear bridging analog like 4,4'-bipyridine, the effective distance obtained by projecting one pyridine nitrogen on a plane containing the other pyridine is shorter, 14.76 Å and 14.70 Å, respectively. We calculate the effective distance by combining the offset between the two pyridine ligands in the y and z direction where the x-axis is defined by a line going through one pyridine nitrogen atom through its para carbon atom, and defining the xy plane by that pyridine ring. The y and z offset distances are therefore the displacement from a linear bipyridine ligand (e.g. 4,4'-bipyridine) from the defined x-axis. So for AzoAMmP the pyridine nitrogen atoms are offset from linearity by 5.41 Å (y) and 2.12 Å (z), and AzoAMpP has more displacement along the y trajectory (6.70 Å), but a shorter deviation in the z direction (1.79 Å). In contrast to AzoAMoP, the pyridine lone pairs in both AzoAMmP and AzoAMpP point away from the diazene core to afford extended bipyridine derivatives more reminiscent of the bridging ligands found in coordination polymers. Structural changes in *meta*- and *para*-bipy derivatives are typically minimal during Ag⁺ complex formation due to limited or no orientational freedom.^{21, 23-}
²⁵ Based on these trends, we expected the AgAAMmP and AgAAMpP polymers, where the pyridine nitrogen atoms face outward in the apo ligands, would likewise undergo minimal structural changes.

AgAAMmP was synthesized by identical procedures used to prepare AgAAMoP. Due to limited solubility of AzoAMpP ligand in toluene however, the solvent was replaced with a 1:4 mixture of CH₃OH/CH₃CN and a minimal amount of DMF, and AgOTf was substituted with AgNO₃. To obtain x-ray quality crystals, anion metathesis with *n*-Bu₄PF₆ was used to replace the

NO_3^- anion with PF_6^- . Compared to the structure of the apo ligand, the azo N–C bonds in the Ag^+ polymer with *AzoAMmP* and *AzoAMpP* ligands are rotated by 180° (Figure 2.2 and Figure 2.3), which is identical to the azo N–C bond rotation observed during the formation of *AgAAMoP*. This reorients the two pyridine rings, but retains outward-facing pyridine nitrogen lone pairs in the formation of a linear or zigzag chain where each Ag^+ is coordinated by a pyridine nitrogen atoms from each of two different *AzoAMmP* or *AzoAMpP* ligands.

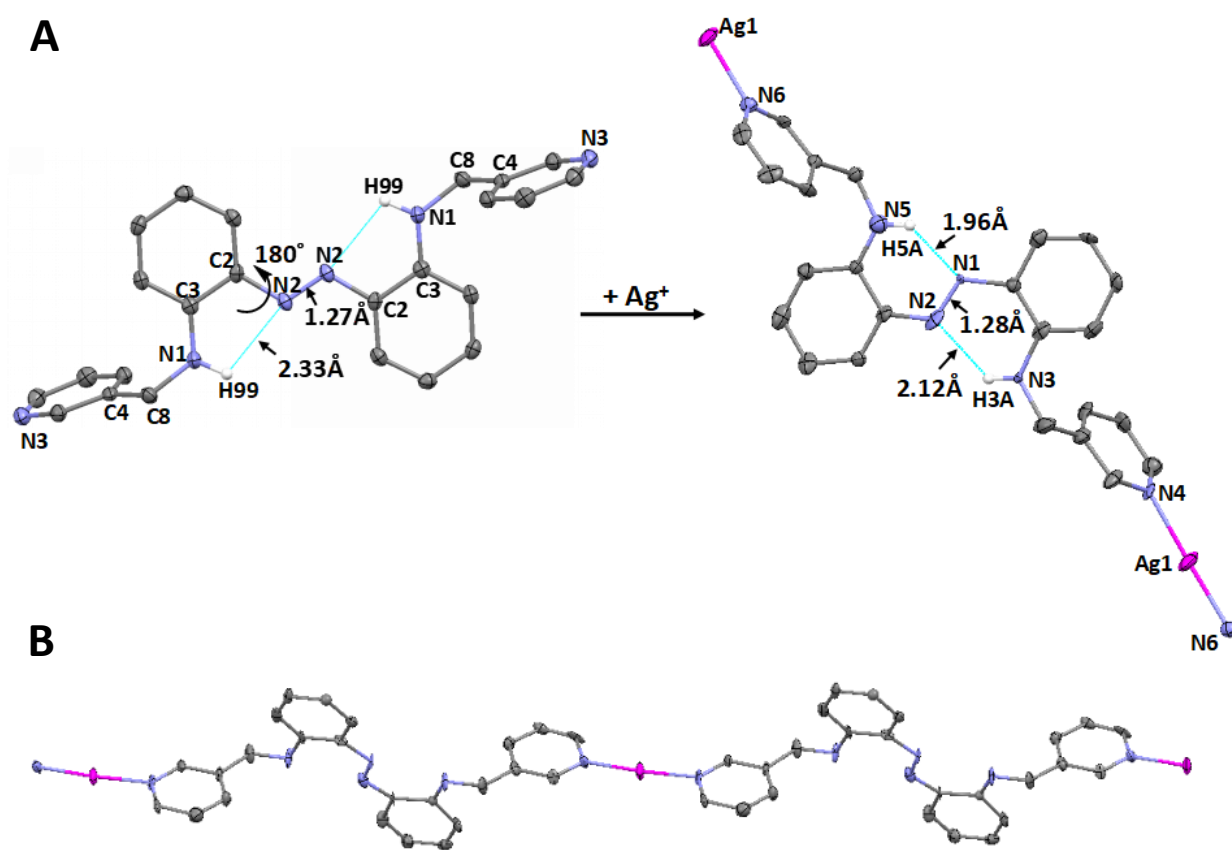


Figure 2.2A. Preparation of *AgAAMmP* showing the thermal ellipsoid representation of *AzoAMmP* and *AgAAMmP* at the 50% probability level and selected atom labels. Hydrogen atoms except for those engaged in intramolecular hydrogen bonds are omitted for clarity. The triflate anion is removed for clarity. *AgAAMmP* was prepared in toluene using AgOTf as the silver source using a slow ligand exchange process with CH_3CN . During the polymer formation, the azo N–C bonds rotate by 180° . **2.2B.** Thermal ellipsoid representation diagram at the 50% probability level of the expanded helical polymer chain. Hydrogen atoms, triflate anions are omitted for clarity.

The DAAB core in AzoAM*m*P and AzoAM*p*P exhibit nearly identical the hydrogen bond lengths, 2.33 and 2.34 Å respectively; however Ag⁺ binding produces different changes in the three derivatives containing a methylene spacer. Unlike AgAAM*o*P, the hydrogen bond length between

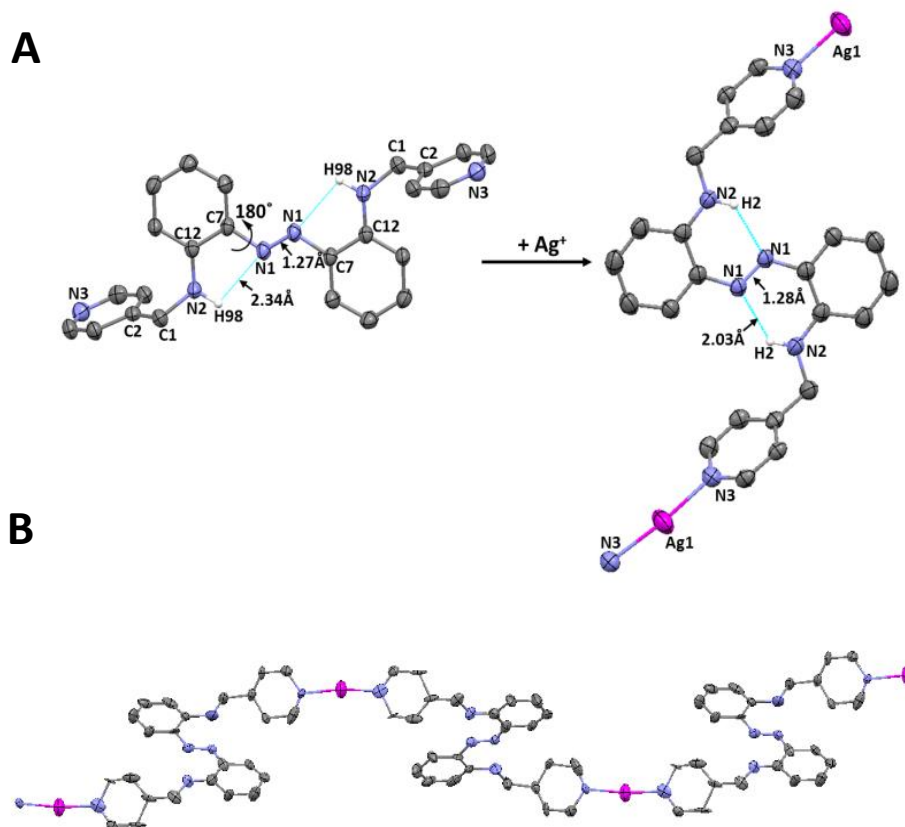


Figure 2.3A. Preparation of AgAAM*p*P showing the thermal ellipsoid representation of AzoAM*p*P and AgAAM*p*P at the 50% probability level and selected atom labels. Hydrogen atoms except for those engaged in intramolecular hydrogen bonds are omitted for clarity. The PF₆ anion is removed for clarity. AgAAM*p*P was prepared in CH₃OH/CH₃CN (1:4) using AgNO₃ as the silver source. Subsequent anion exchange with n-Bu₄PF₆ in CH₃CN provided x-ray quality crystals. During the polymer formation, the azo N–C bonds rotate by 180°. **2.3B.** Thermal ellipsoid representation diagram at the 50% probability level of the expanded zigzag polymer chain. Hydrogen atoms, PF₆ anions are omitted for clarity.

the anilino hydrogen atoms and the diazene lone pairs decreases. While the hydrogen bonds in AgAAM p P (2.02 Å) are symmetric, AgAAM m P contains a longer (2.12 Å) and shorter (1.96 Å) bond that are both contracted compared to the apo-ligand. While AgAAM o P exhibited some asymmetry in the hydrogen bond length, the difference is much more pronounced in AgAAM m P. As expected, the increased hydrogen bonding interaction results in the opposite effect on the N=N bond lengths, which increases slightly from 1.27 Å to 1.28 Å for both coordination polymers.

The pyridine nitrogen atoms of AzoAE o P are separated by 15.04 Å. While the pyridine lone pairs face inward, the length of the ethylene linkers and ligand flexibility provide no a priori reason to predict a reorientation would be required to coordinate Ag⁺. Using the identical procedure used to prepare AgAAM p P, a discrete monomeric complex was obtained (Figure 2.4). The single rotation about the azo C–N required to achieve this coordination geometry suggests kinetic trapping of a 17-membered metallacycle instead of a polymer. To the best of our knowledge, this is the largest Ag metallacycle formed from a bipy derivative to date. Large metallacycles with pyridyl donor groups are relatively uncommon. Most analogously, 13-membered-ring metallacycles of Pt and Pd,²⁶ and an 11-membered-ring metallacycle of Ag have been observed.²²

The intramolecular hydrogen bonds in AzoAE o P may be a significant factor in the preference for metallacycle formation instead of a polymeric structure. Two 2.36 Å hydrogen bonds between anilino hydrogen atom and the azo nitrogen atoms appear in apo ligand. When the ligand rotates to close the metallacycle, the hydrogen bonding between one of the anilino hydrogen and azo nitrogen is unavailable, and a new 2.07 Å hydrogen bond forms between the same proton and the other azo nitrogen atom. The hydrogen bonding in the upper half molecule remains unchanged, but the distance increases slightly from 2.36 to 2.38 Å. The shorter, stronger hydrogen bond formed in AgAAE o P may provide a thermodynamic driving force for metallacycle formation.

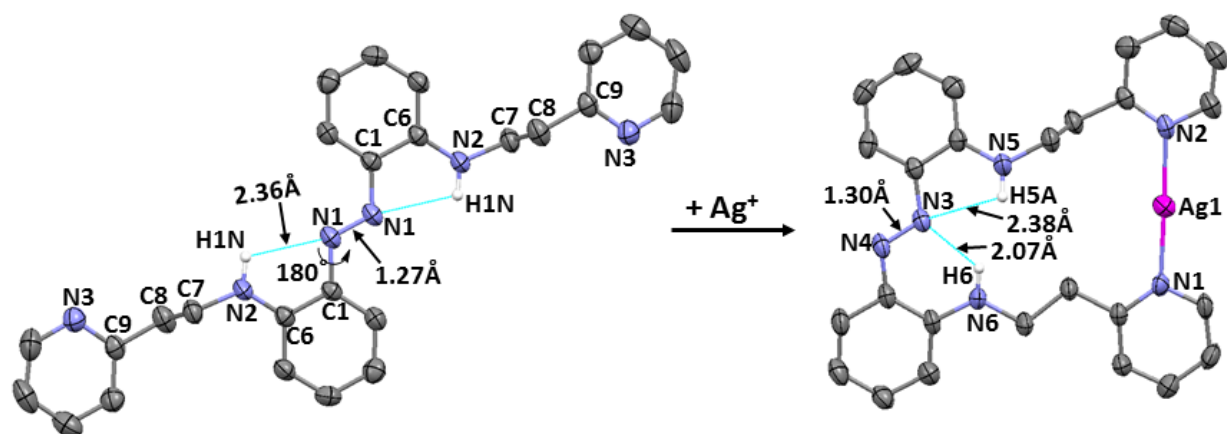


Figure 2.4. Preparation of AgAAEoP showing the thermal ellipsoid representation of AzoAEoP and AgAAEoP at the 50% probability level and selected atom labels. Hydrogen atoms except for those engaged in intramolecular hydrogen bonds are omitted for clarity. The PF_6 anion is removed for clarity. AgAAEoP was prepared in $\text{CH}_3\text{OH}/\text{CH}_3\text{CN}$ (1:4) using AgNO_3 as the silver source with added $n\text{-Bu}_4\text{PF}_6$ to provide x-ray quality crystals. During the complex formation, one azo N–C bond rotates by 180° while the other remains stationary to form a 17-membered ring. The two hydrogen bonds formed between two anilino hydrogen atoms and the same azo N atom are asymmetric with lengths of 2.07 Å and 2.38 Å respectively.

Of the five AzoAXxP ligands, AzoAEoP most closely resembles a linear bridging ligand like 4,4'-bipyridine. The point-to-point distance between the pyridine nitrogen atoms of 17.95 Å is the longest distance of all the AzoAXxP ligands, but the trajectory of the two pyridine groups is linear and the aromatic rings are coplanar in the solid state. Linear bipyridines with long nitrogen-nitrogen distances form both linear Ag^+ polymers^{25, 27} and three-dimensional networks with 4-coordinate Ag^+ sites.^{28, 29} The preference for 2-coordinate or 4-coordinate Ag^+ appears to correlate with the reorientation ability and rigidity of the ligands as well as the distance between pyridine nitrogen atoms.

Although the pyridine ligands in apo-AzoAEP are coplanar, rotation about the C–N bond in the ethylene spacers results decreases the point-to-point distance from 17.95 Å to 6.65 Å. The effective distance is obtained similarly as described above to yield y and z offset distances of 2.22

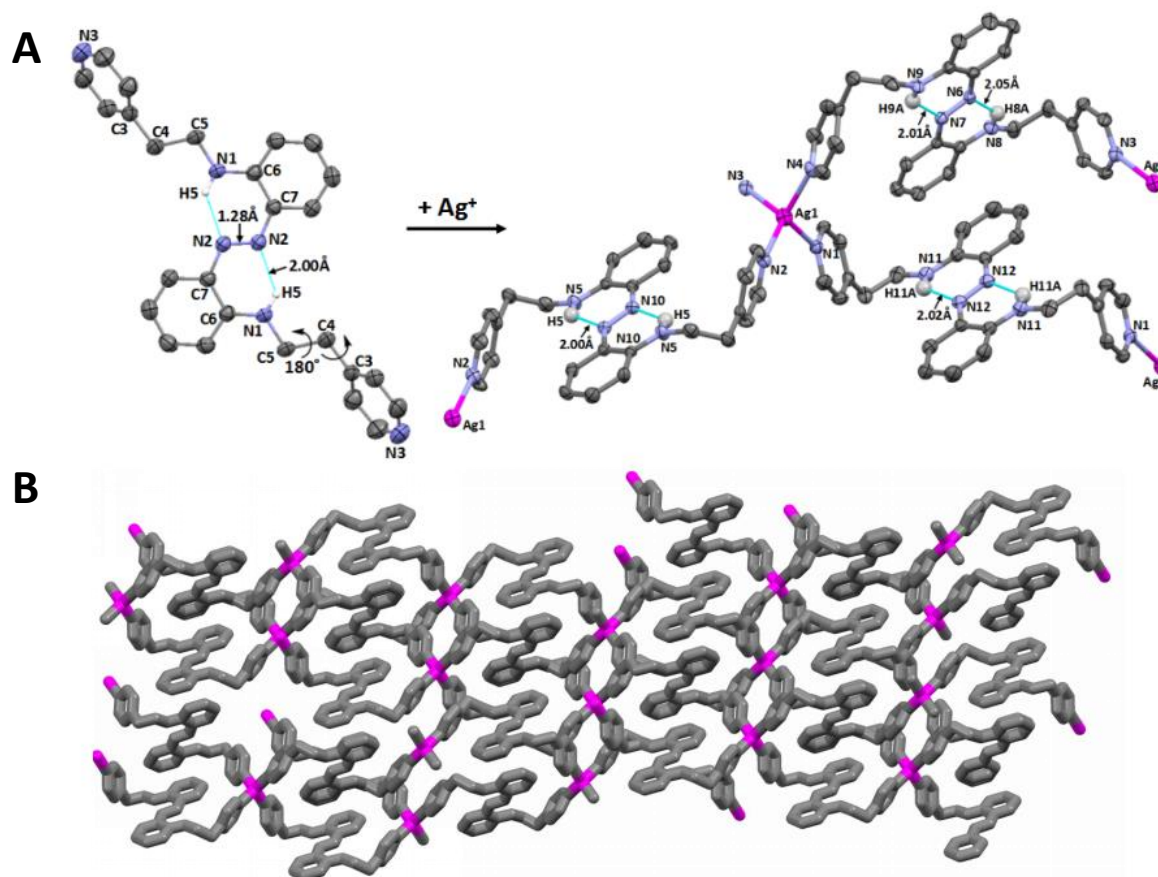


Figure 2.5A. Preparation of AgAAEP showing the thermal ellipsoid representation of AzoAEP and AgAAEP at the 50% probability level and selected atom labels. Hydrogen atoms except for those engaged in intramolecular hydrogen bonds are omitted for clarity. The PF₆ anion is removed for clarity. AgAAEP was prepared in DCM using AgNO₃ as the silver source with added n-Bu₄PF₆. The resulting precipitate was dissolved in CH₃CN to yield x-ray quality crystals from slow solvent evaporation. During the polymer formation, the ethylene C–C bonds rotate by 180° and ethylene-pyridine C–C rotates minimally. **2.5B.** Thermal ellipsoid representation at the 50% probability level of the three dimensional polymer chain. Hydrogen atoms and PF₆ anions are omitted for clarity.

and 9.09 Å, respectively. Each Ag⁺ is four-coordinate with each pyridine coming from one of four unique AzoAE*p*P ligands. We partially attribute the increased coordination to the reduced steric requirements at the donor ligand site of the *para*-pyridine isomer. Each AzoAE*p*P ligand also coordinates two separate Ag cations to form a three-dimensional infinite polymer with the distorted tetrahedral Ag⁺ sites (Figure 2.5B). The lack of steric hindrance at the coordination site of the *para*-pyridine ligands appears to be an important prerequisite for three-dimensional polymer formation with bipyridines. In previous Ag⁺ polymers and three-dimensional networks with 4-coordinate Ag⁺ sites, most of the ligands undergo minimum or no reorientation.^{25, 27, 29} Unlike these linear bipyridine ligands, AzoAE*p*P exhibits a high degree of freedom, which allows optimization of steric and electrostatic factors in Ag⁺ complex formation.

2.4. Emission

AzoAM*o*P exhibits no measurable emission at room temperature, but emits when frozen in a solvent glass at 77 K. The four additional AB compounds behave similarly. Although the wavelengths vary, all the five compounds emit with a λ_{max} between 566 nm and 610 nm (Table 2.2). Similar to AzoAM*o*P and AzoAE*p*P,^{4,5} none of the new AzoAX*x*P derivatives exhibit significant evidence for photoisomerization upon irradiation. While quantitative measurements of minimally emissive complexes are imprecise, qualitatively, AzoAE*o*P and AzoAE*p*P exhibit brighter emission than AzoAM*m*P and AzoAM*p*P. AzoAM*o*P appears to emit more weakly than the other four derivatives.

To assess the photochemistry of the Ag⁺ complexes, the emission of AgAAM*o*P, AgAAM*m*P, AgAAM*p*P, and AgAAE*p*P were evaluated in toluene as suspensions of powdered crystals. The four coordination polymers form semi-homogeneous dispersions in toluene that remain suspended for several months. Similar to the free ligands, the emission λ_{max} occurs around

600 nm for all the complexes (Table 2.2). In the solid state, the relative integrated emission intensities reveal a nearly 30-fold brighter emission for the four-coordinate *AgAAEpP* complex compared to the least emissive *AgAAMpP* complex (Figure 2.6). Complex formation redshifts the absorbance maximum of *AzoAEpP* from 502 nm to 594 nm with an emission peak centered at 641 nm (Figure 2.7). Similar to the absorbance, the emission of *AgAAEpP* redshifts 31 nm from that of free *AzoAEpP* measured at 77 K, which is a greater a change than the other three polymeric complexes. The luminescence response appears to validate the initial hypothesis that embedding the *AzoAXxP* ligand in a solid state material increases the degree of radiative decay of the AB excited state.

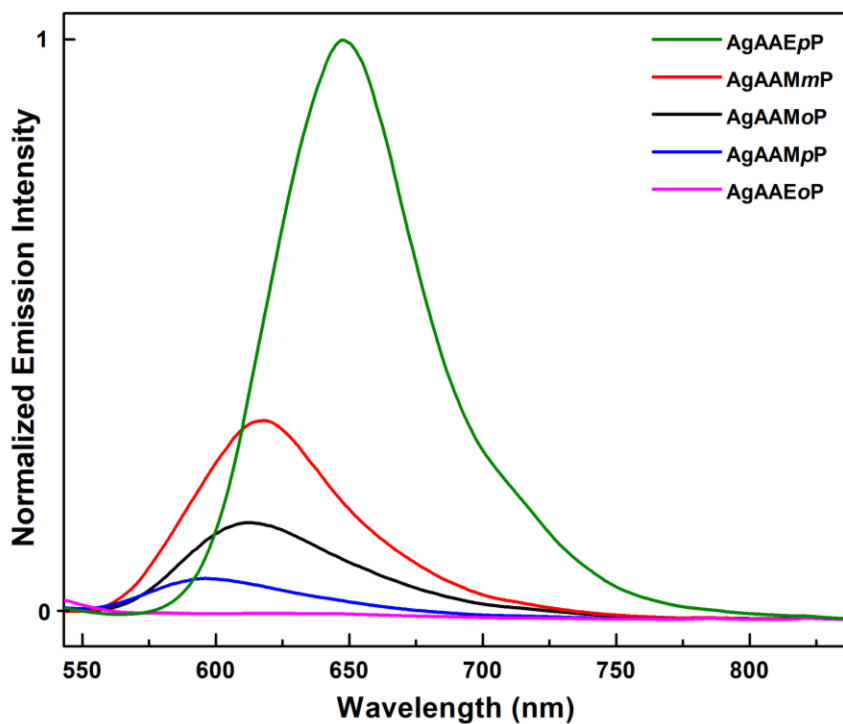


Figure 2.6. Solid state emission spectrum of the five *AzoAXxP* silver complexes (λ_{ex} 523 nm) showing the relative intensities.

The emission of AB in solution at room temperature is too weak to be detected by conventional emission instruments because efficient non-radiative pathways for the decay of the excited state exist.³⁰ In many aromatic chromophores, the emission of a photon accompanies a $S_1(\pi\pi^*) \rightarrow S_0$ transition as the excited molecule returns to the ground state. In AB however, the $S_2(\pi\pi^*) \leftarrow S_0$ absorbance has the largest extinction coefficient, but a weakly absorbing interstitial $S_1(n\pi^*)$ state is present. While the photophysical processes remain an active area of investigation,³¹⁻³³ a rapid intersystem crossing to a vibrationally excited $S_1(n\pi^*)$ state occurs after

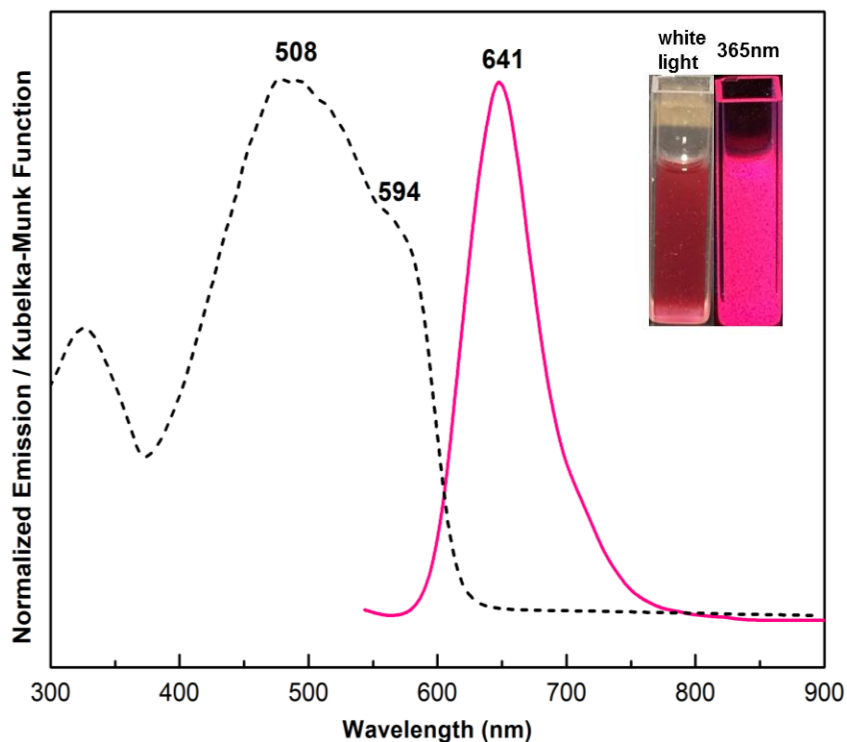


Figure 2.7. Solid state diffuse reflectance (black) and solid state emission ($\lambda_{ex}=523$ nm, pink) spectra of AgAAEP. Inset: cuvettes containing a suspension of the complex crystals in toluene ($100 \mu\text{M}$) without irradiation (left), and excited with 365 nm light (right).

$S_2(\pi\pi^*) \leftarrow S_0$ absorbance. AB isomerization occurs via the concerted inversion pathway from the S_1 state.^{34, 35} A modest increase in emission intensity can be observed in a frozen matrix when relaxation pathways involving molecular motion are impaired.

Radiative decay of AB can be increased by manipulating the frontier orbitals of the chromophore as observed in 2-borylazobenzenes.³⁶⁻³⁹ Engaging the diazene lone pair in a dative bond with a boron atom lowers the energy of the lone pair, or B–N bonding orbital, below the diazene π -bond. Thus forming the $n\pi^*$ state would require promoting an electron into the half-occupied, higher energy diazene π -orbital. The absence of the interstitial $S_1(n\pi^*)$ state removes the optically forbidden $S_1(n\pi^*) \rightarrow S_0$ transition and opens the $S_2(\pi\pi^*) \rightarrow S_0$ emission channel.

2.5. DFT Calculations

We hypothesized that introducing intramolecular hydrogen bonds between the diazene lone pair and anilino hydrogen atom might lead to a similar, albeit less drastic, change in the frontier orbitals to those observed in 2-borylazobenzenes, and therefore increase radiative decay of the excited state. This hypothesis was supported by our previous observations that an AzoAMoP derivative lacking intramolecular hydrogen bonds had significantly weaker emission at 77 K that was closer to the luminescence of AB under the same conditions.⁴ To further support the increased emission hypothesis, we interrogated the ground state electronic structure of each ligand using Density functional theory (DFT). In order to capture the structural impact of the solid-state environment on the electronic structure for each ligand, unit cell vectors and atom positions were determined using three-dimensional periodic boundary conditions before extracting a single molecule for analysing the electronic structure, an approach we have previously applied to luminescence metal-organic systems.⁴⁰ The first ten excited states were computed vertically using time-dependent DFT (TDDFT) for all the ligands.

The computational approach provides values that correlate closely with experimentally measured absorption energies. As expected, the gap between the n and π^* orbitals decreases significantly going from AB to DAAB, but the order remains unchanged (Figure 2.8). The red-

shifting of the $\pi\pi^*$ absorption maxima between AB and DAAB was calculated to be 0.95 eV, in reasonable agreement with the experimental value of 1.23 eV. Likewise, the calculated and experimental values for the five aAB showed reasonable agreement. The minimum and maximum red-shifting of the $\pi\pi^*$ transition of the five aAB ligands were measured as 0.139 eV and 0.142 eV with respect to DAAB. The equivalent red-shifts determined computationally were 0.250 eV and 0.294 eV, a similar spread to the experimental values shifted by approximately 0.1 eV.

Since our series of modified aAB ligands are significantly more emissive in a frozen matrix than AB and DAAB, we reasoned that the anilino substituent must induce further changes in the frontier orbitals. In examining the frontier orbital energies, we observed that the pyridine moieties induce a stabilization of the diazene-centered n-type orbital for the four aAB ligands (maximum 0.33 eV). This observation is in line with the expectation that the inductive effect of the pyridine substituent results in a slightly more electron rich secondary anilino nitrogen atom, leading to a slightly more stable π^* orbital and making the diazene lone pairs somewhat better hydrogen bond acceptors. AzoAMoP, which exhibits a relative orbital destabilization of approximately 0.44 eV, provides an exception to this trend. AzoAMoP shows a reduced gap between the n and π^* orbitals compared to the other four derivatives. We attribute this difference to the additional hydrogen bonding provided by the pyridine substituent, reducing the interaction between the diazene lone pair and the anilino hydrogen atom. In contrast, introducing a *meta/para* nitrogen atom within the pyridine unit or an ethylene spacer increases the distance between the nitrogen donor atom and the diazene core, rendering this interaction negligible and yielding a net stabilization of the lone pair, as is seen in the other four derivatives. The lack of emission in solution, and subsequent increase in a frozen matrix, is also consistent with hydrogen bonding as a key contributor to the emission behavior. The restricted motion at low temperature would be expected to lead to a stabilization of

the hydrogen bonds, and, in turn, the energy levels of the frontier orbitals, that would not necessarily occur in solution.

The electron donating pyridine moieties destabilize the π (HOMO) orbital for all ligands with respect to the DAAB control molecule. This destabilization exceeds the stabilization of the diazene lone pair orbital (LUMO), which results from hydrogen bonding between the diazene lone pair and the anilino hydrogen atom (maximum 0.95 eV). AzoAMoP again provides an exception, where the π^* orbitals are stabilized upon the addition of the pyridine substituents (0.52 eV). The

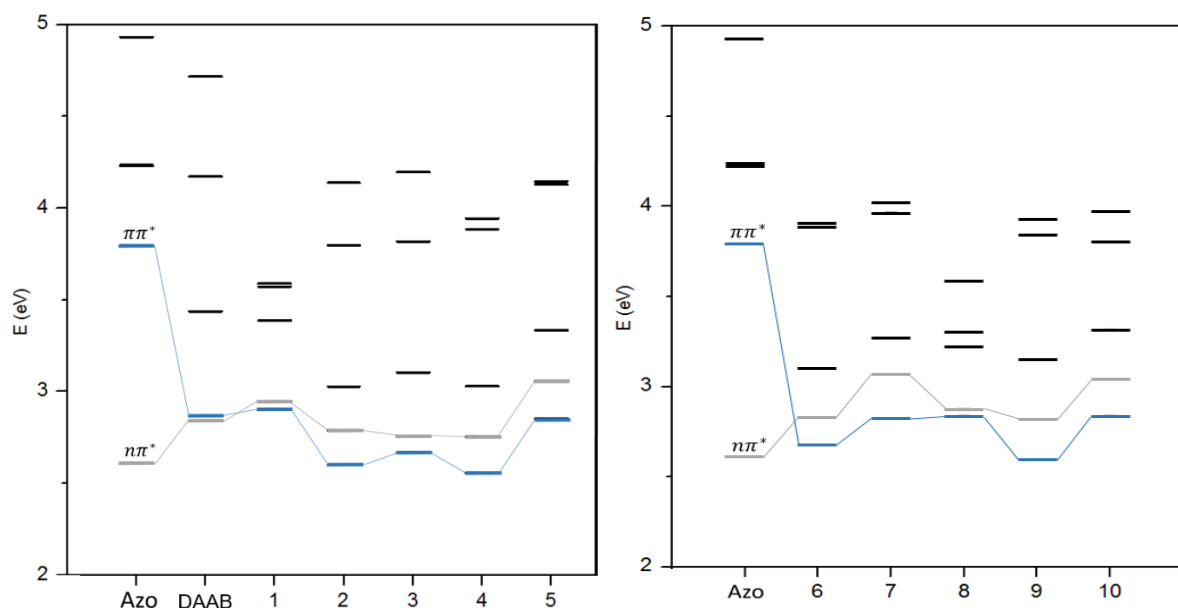


Figure 2.8. Calculated singlet excitation energies (in eV) of AB, DAAB, AzoAMoP (1), AzoAMmP (2), AzoAMpP (3), AzoAEoP (4), AzoAEpP (5) and ligands extracted from AgAAMoP (6), AgAAMmP (7), AgAAMpP (8), AgAAEoP (9), AgAAEpP (10) at PBE0/6-31+G(d,p) level of theory. The bright $\pi\pi^*$ state is shown in blue while the dark $n\pi^*$ state is in grey.

combination of these effects results in a general stabilization of the $\pi\pi^*$ excited state and destabilization of the $n\pi^*$ state (Figure 2.8), causing an inversion of the emissive $\pi\pi^*$ and non-emissive $n\pi^*$ states with respect to both AB and DAAB. As expected, this results in the removal

of the lower-lying $n\pi^*$ state as a radiationless decay channel.³⁹ Notably, the inversion of states is the least pronounced in *AzoAMoP*. In an absolute sense, the $n\pi^*$ state still lies higher in energy than the $\pi\pi^*$, but the small energy gap (0.04 eV) could permit internal conversion between these two states, accounting for the lower emission intensity of *AzoAMoP*.

To generate emission at room temperature, we hypothesized that embedding the ligands in coordination polymers would provide the requisite restrictions on molecular motion needed to stabilize the diazene lone pair-anilino hydrogen atom hydrogen bond. Our hypothesis was validated by the emission measurements on the Ag^+ systems. The 2.43 Å diazene lone pair-anilino hydrogen atom bond length in $[\text{Ag}(\text{AzoAMoP})]_n$ is the longest of the four polymeric complexes, and correlates with the lowest relative integrated emission intensity (Table 2.2). As the hydrogen bond length shortens in $[\text{Ag}(\text{AzoAMmP})]_n$ (2.12 Å) and $[\text{Ag}(\text{AzoAMpP})]_n$ (2.03 Å), the relative emission intensity increases. As our hypothesis predicts, $[\text{Ag}(\text{AzoAEpP})_2]_n$ has the brightest emission and the shortest hydrogen bonds. In order to understand the effects of the structural reorganization imposed by Ag^+ coordination on the frontier orbitals and excited states, the same computation procedures were applied to the polymeric complexes. These calculations only capture the structural effects of the Ag^+ coordination since a neutral ligand is extracted from the periodic, solid state calculations; therefore, the model does not account for the electronic effects of Ag^+ coordination.

While the trend between hydrogen bond length and emission intensity correlates as expected, the computational results predict a small energy gap between the n and π^* orbitals. Since the structural reorganization of the anilino moieties after polymer formation causes only a slight modulation in the lowest-lying excited states (Figure 2.8), the qualitative ordering of the states remains unchanged with respect to the results obtained for the crystalline ligands alone.

Interestingly, $[\text{Ag}(\text{AzoAE}p\text{P})_2]_n$ is over an order of magnitude more emissive than the other three polymeric complexes, which indicates other contributing factors to the photophysical behavior.

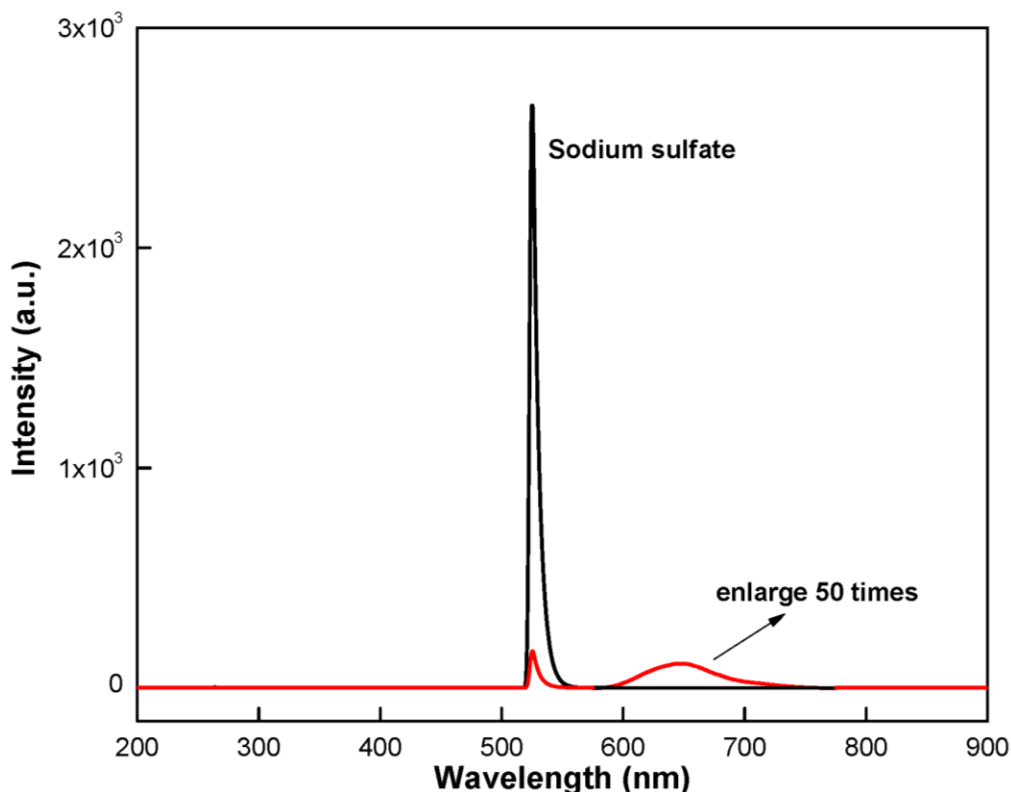


Figure 2.9. Steady-state emission and quantum yield determination of AgAAEpP. Reflectance from the sample and sodium sulfate are shown by red and black lines, respectively. Emission from the sample (enlarged by 50 times) is marked by an arrow. The excitation wavelength is 525 nm.

The calculations based on extracted ligands only capture structural effects imposed by coordination to Ag^+ ; therefore, while we are able to demonstrate a correlation between hydrogen bond length and emission behavior across the series of materials, we cannot draw any conclusions regarding the influence of Ag^+ atoms or the crystalline environment on orbital or excited state energies. Together, these results show that the enhanced luminescence observed in these azobenzene derivatives could be based on the inversion of the aforementioned electronic excited states relative to azobenzene, but no conclusions can be made concerning the differences in

emission intensity observed upon the formation of silver complexes, or the differences in luminescence intensity observed between different silver-based polymers.

2.6. Analyte Detection

AgAAEpP exhibits the brightest emission of all the Ag⁺ coordination polymers with a quantum yield of 0.8% (Figure 2.9). The other complexes have quantum yields of less than 0.1%, and therefore the exact values are not reliable. We examined the emission response to the Ag⁺-coordinating analytes pyridine, *N*-methylmorpholine, DMA and imidazole, which all have nitrogen atoms as electron donors. When 5 equivalents of pyridine with respect to AzoAEpP units is added to a suspension of AgAAEpP in toluene, no emission was detected; however, the absorbance spectrum showed the presence of AzoAEpP. When a sub-stoichiometric amount of pyridine was added, the coordination polymer emission decreased, and the absorbance spectrum showed evidence for the release of some AzoAEpP. We suspected that pyridine was displacing AzoAEpP pyridine ligands bound to the Ag⁺ sites, which would cause the loss of extended structure in the coordination polymer. The release of AzoAEpP, which is not emissive at room temperature in solution, would produce an on/off switching behavior. To provide supporting evidence for this signaling mechanism, the pyridine was removed by sparging the solution with N₂ gas. The recovery of emission after the evaporation and re-dispersion of the material in toluene suggests the reassembly of the original AgAAEpP structure. The disassembly/reassembly process also can be observed by PXRD. Upon the addition of pyridine, the diffraction pattern indicates the formation of amorphous material, and the reassembled material exhibits an identical spectrum to the original coordination polymer.

The reversible structure disassembly process can be monitored by emission spectroscopy. Initially, the emission spectrum of AgAAEpP exhibits features with maxima at 620 nm (Figure

2.10A). Upon the addition of pyridine, the peak intensity decreases gradually, and correlates with expected changes in absorbance from AzoAEpP. The pyridine removal process restores the original spectrum characteristic of AgAAEpP. This process is fairly robust, and can be repeated with minimal loss of emission, with PXRD patterns (Figure 2.17) showing structure restoring after pyridine removal and resuspension. After five cycles, the material retains 90% of the original emission intensity (Figure 2.10B), and the slight erosion of the maximum response is likely due to irreversible loss of structure, or incomplete removal of pyridine. NMM shows similar results to pyridine. The boiling points of pyridine and NMM are 115.2 °C and 116 °C, respectively, so the sparging with N₂ removes both the analyte and solvent (toluene, bp 111°C).

In contrast, when exposed to imidazole, the emission loss is not reversible. Although imidazole displaces AzoAEpP from the coordination sphere of Ag⁺ in the coordination polymer, the lack of volatility (bp 256 °C) makes removal nearly impossible. A similar response occurs upon treatment of AgAAEpP with potassium bromide. The removal of Ag⁺ through the formation of insoluble halide complexes leads to an irreversible loss of emission and a UV spectrum consistent with free AzoAEpP.

The ability to reversibly detect analytes through changes in extended structure is not limited to removal by evaporation. Addition of DMA leads to a loss of emission analogous to the response to pyridine. The addition of dilute nitric acid causes the AgAAEpP to reassemble. This process can also be repeated for multiple cycles without significant loss of absolute emission intensity (Figure 2.10C). The emission loss and restoration process by adding and removing volatile analytes like pyridine and NMM demonstrates the viability of a disassembly-reassembly process for emission detection. While physical/electrostatic interactions are more common signal transduction pathways,⁴¹⁻⁴³ our system provides an alternative sensing mechanism driven by

coordination events, but primarily demonstrates that the coordination polymer is required for the AzoAXxP ligands to be emissive at room temperature.

2.7. Conclusions

Although ABs are not typically emissive, embedding AB chromophores in a rigid coordination polymer can enhance the degree of radiative decay of the excited state. In the aAB ligands investigated, both Ag⁺ coordination and intramolecular hydrogen bonds contribute to the emission enhancement; however, the hydrogen bonding introduces the majority of the change in the frontier molecular orbitals. The stabilization of the $\pi\pi^*$ excited state below the interstitial $\pi\pi^*$ usually involved in the non-radiative decay of the excited state leads to luminescence in both solid state and crystalline samples dispersed in solvent. Our initial investigations suggest three-dimensional networks are more emissive than linear coordination polymers, however, additional examples will be required to confirm this hypothesis. The coordination polymers can be completely, or partially disassembled by the addition of Ag⁺-binding analytes such as amines, and reformed after analyte removal to provide a sensor-like system. This signal transduction mechanism differs from many polymeric sensors, and will be investigated as an alternative approach to designing practical luminescent probes.

2.8. Acknowledgement

This chapter is based on joint work with Dr. Liam Wilbraham, Dr. Ilaria Ciofini, Dr. François-Xavier Coudert from Chimie ParisTech, PSL Research University, CNRS, Institut de Recherche de Chimie Paris. All the DFT calculations on singlet excitation energies and orbital contours of AzoAXxP ligands and ligands extracted from AgAAXxP complexes were conducted by them.

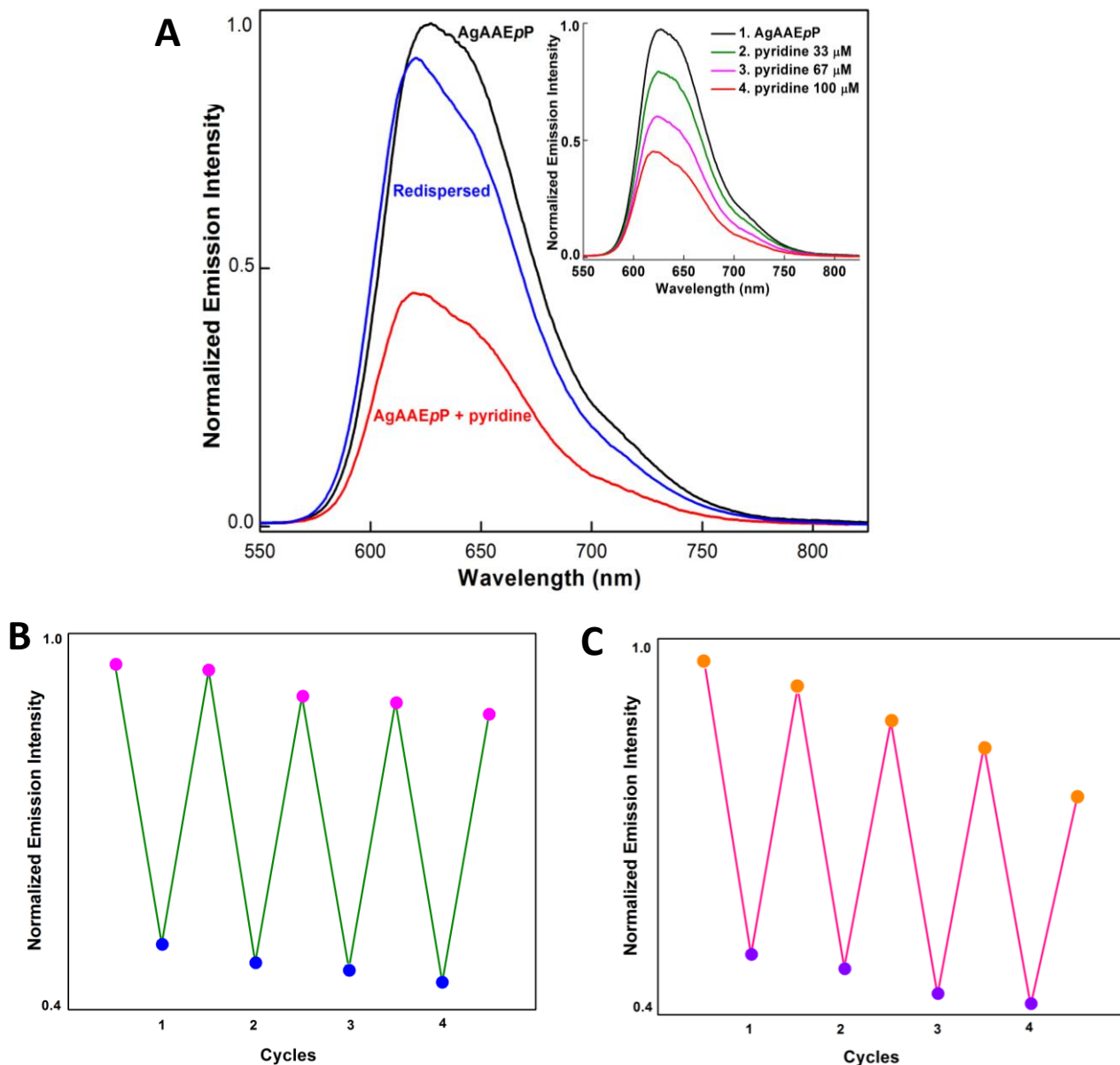


Figure 2.10A. Normalized emission response of AgAAEpP to pyridine. AgAAEpP (100 μM) was suspended in toluene (black), treated with 100 μM pyridine (red), and redispersed in toluene after removing the solvent and analyte by sparging with N_2 (blue). The response also shows stepwise decreases when incremental amounts of pyridine were added to reach final concentrations of 33 μM , 67 μM , and 100 μM . (inset). **2.10B.** Normalized emission response of AgAAEpP to multiple cycles of pyridine addition and removal. AgAAEpP (100 μM) was exposed to 100 μM of pyridine followed by a sparging and redispersion process a total of 4 times. **2.10C.** Normalized emission response of AgAAEpP to multiple cycles of DMA addition and removal. AgAAEpP (100 μM) was exposed to 10 μM of DMA followed by an addition of nitric acid to reach a final concentration of 20 μM H^+ a total of 4 times.

Table 2.1. Selected interatomic distances (Å) and angles (deg) for the five AzoAX_xP ligands.

	Selected bond lengths	Bond angles
<i>AzoAM_oP</i>	N(3)–N(3) 1.2793(15) N(3)–C(12) 1.4127(16) C(12)–N(2) 1.3573(18) N(2)–C(6) 1.4434(18)	N(3)–N(3)–C(12) 116.87(10) N(3)–C(12)–C(7) 126.89(11) N(2)–C(7)–C(12) 121.64(11) C(6)–N(2)–C(7) 123.93(11) N(2)–C(6)–C(5) 110.70(10) N(1)–C(5)–C(6) 118.15(12)
<i>AzoAM_mP</i>	N2–N2 1.268(3) C2–N2 1.414(3) C3–N1 1.373(3) C8–N1 1.444(3)	N2–N2–C2 114.9(2) N2–C2–C3 115.07(17) N1–C3–C2 119.75(18) C3–N1–C8 122.48(17) N1–C8–C4 113.39(17)
<i>AzoAM_pP</i>	N1–N1 1.265(3) C7–N1 1.415(2) C12–N2 1.373(2) C1–N2 1.449(2)	N1–N1–C7 115.08(18) N1–C7–C12 115.58(15) N2–C12–C7 119.91(15) C12–N2–C1 122.46(15) N2–C1–C2 115.93(16)
<i>AzoAE_oP</i>	N1–N1 1.267(3) C1–N1 1.408(2) C6–N2 1.354(2) C7–N2 1.446(2) C9–N3 1.340(2)	N1–N1–C1 115.48(18) N1–C1–C6 115.84(15) N2–C6–C1 120.30(16) C6–N2–C7 124.91(17) N2–C7–C8 112.68(15) N3–C9–C8 117.21(17)
<i>AzoAE_pP</i>	N2–N2 1.283(4) N2–C7 1.408(3) N1–C6 1.358(3) N1–C5 1.450(3)	N2–N2–C7 117.2(3) N2–C7–C6 127.1(2) N1–C6–C7 121.0(2) C6–N1–C5 125.0(2) N1–C5–C4 109.4(2)

Table 2.2. Photophysical properties of AzoAXxP ligands and coordination polymers.

Compound	H-bond distances NH \cdots N=N(\AA)	ϵ [$\text{M}^{-1}\text{cm}^{-1}$]	λ_{max} (nm) Abs	Em_{max} (nm)	Relative emission intensity (RT)
AzoAMoP	2.046(15)	12334	495	602 ^[a]	n.a.
AzoAMmP	2.33(3)	13729	497	607 ^[a]	n.a.
AzoAMpP	2.34(2)	13702	495	603 ^[a]	n.a.
AzoAEoP	2.36(2)	15874	501	619 ^[a]	n.a.
AzoAEpP	2.00(3)	15195	502	616 ^[a]	n.a.
AgAAMoP	2.43(3), 2.47(5)	n.a.	440	600 ^[b]	0.035
AgAAMmP	2.12(9), 1.96(2)	n.a.	440	618 ^[b]	0.067
AgAAMpP	2.02(3)	n.a.	475	590 ^[b]	0.069
AgAAEpP	2.00(3), 2.05(1), 2.01(3), 2.02(2)	n.a.	508	641 ^[b]	1.0

[a] $\lambda_{\text{ex}} = 490$ nm, [b] $\lambda_{\text{ex}} = 523$ nm

Table 2.3. Calculated orbital contours for ligands extracted from solid-state structures, as well as azobenzene. Beneath each orbital, the energy eigenvalue is shown in atomic units (isocontour value = 0.03 au).

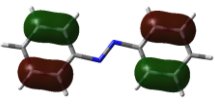
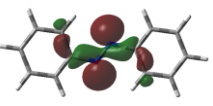
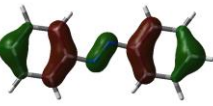

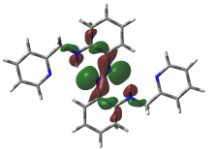
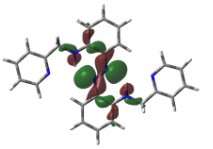
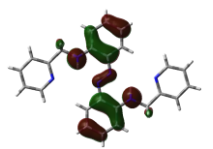
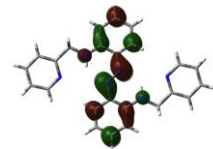
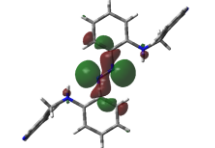
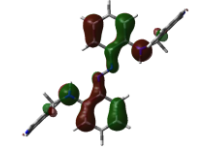
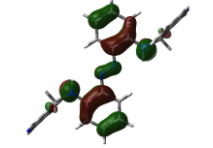
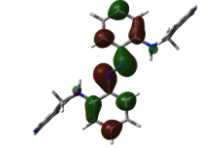
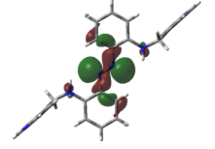
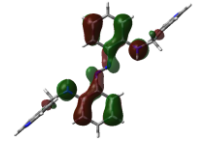
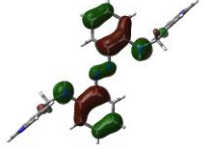
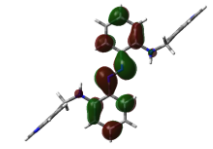
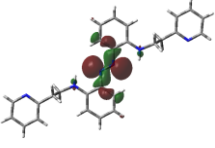
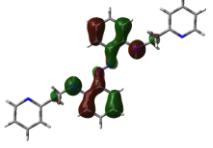
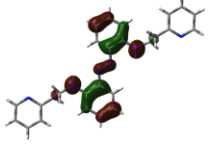
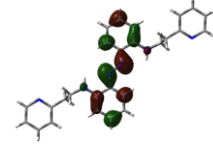
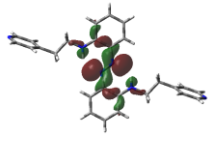
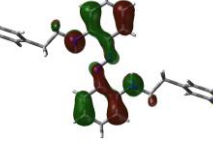
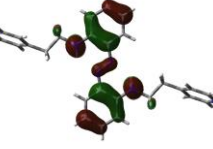
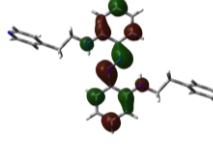
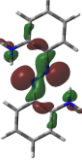
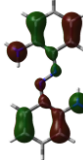
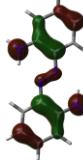
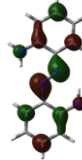
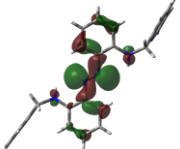
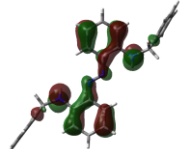
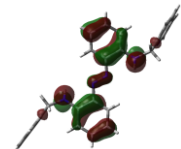

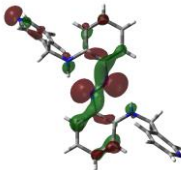
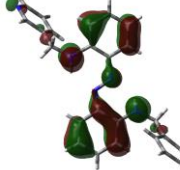
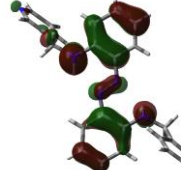
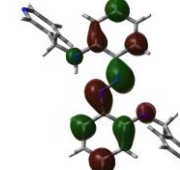
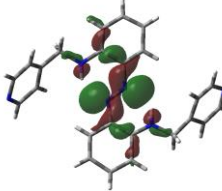
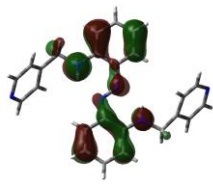
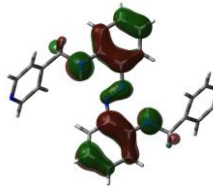
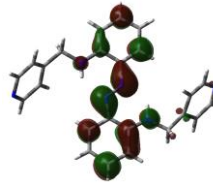
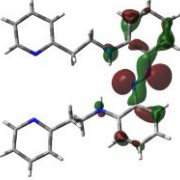
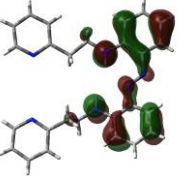
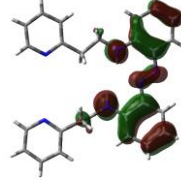
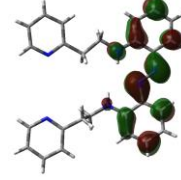
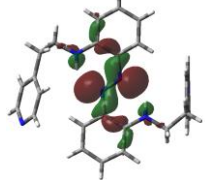
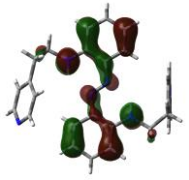
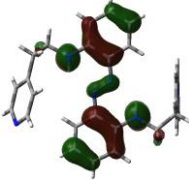
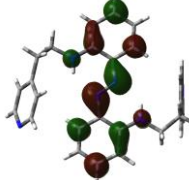
	HOMO - 2	HOMO - 1	HOMO	LUMO
Azobenzene				
	-0.27481	-0.24727	-0.24583	-0.08695
AzoAMoP				
	-0.22755	-0.20869	-0.18806	-0.05779
AzoAMmP				
	-0.25484	-0.22959	-0.20930	-0.08986
AzoAMpP				
	-0.25556	-0.23201	-0.21273	-0.09039
AzoAEoP				
	-0.24680	-0.21691	-0.19457	-0.07786
AzoAEpP				
	-0.25155	-0.22742	-0.20504	-0.07848

Table 2.4. Calculated orbital contours for ligand clusters of silver-coordinated materials, as well as DAAB. Beneath each orbital, the energy eigenvalue is shown in atomic units (isocontour value = 0.03 au).

	HOMO - 2	HOMO - 1	HOMO	LUMO
DAAB				
	-0.25003	-0.24356	-0.22518	-0.07175
AgAAMoP				
	-0.23995	-0.21831	-0.1991	-0.0752
AgAAMmP				
	-0.25483	-0.23105	-0.21061	-0.08465
AgAAMpP				
	-0.24336	-0.2253	-0.20603	-0.07837
AgAAEoP				
	-0.24099	-0.22051	-0.19963	-0.0794
AgAAEpP				

	-0.24598	-0.22157	-0.20011	-0.07313
--	----------	----------	----------	----------

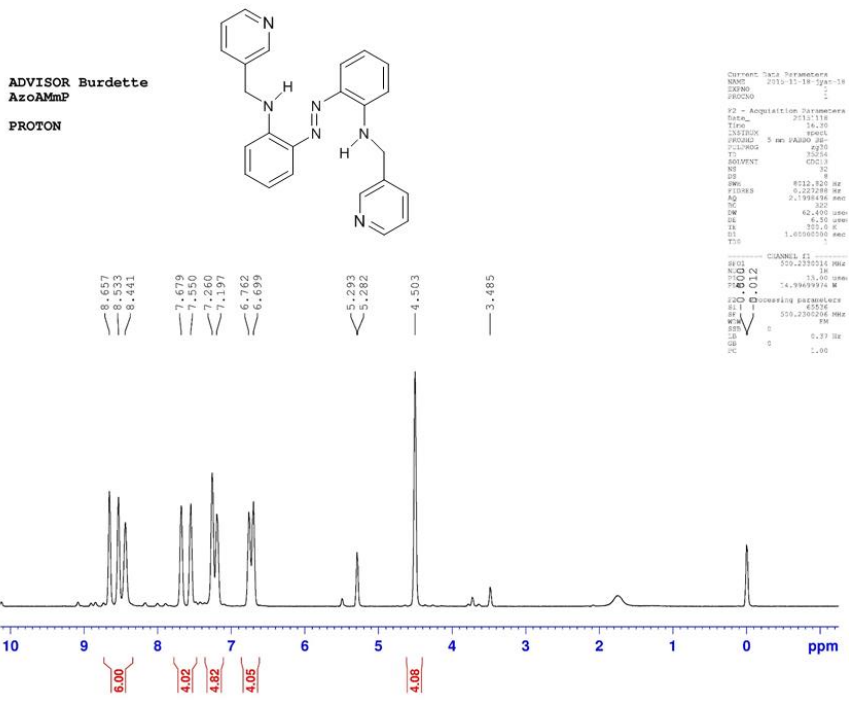


Figure 2.11. ¹H NMR of compound AzoAMmP (3).

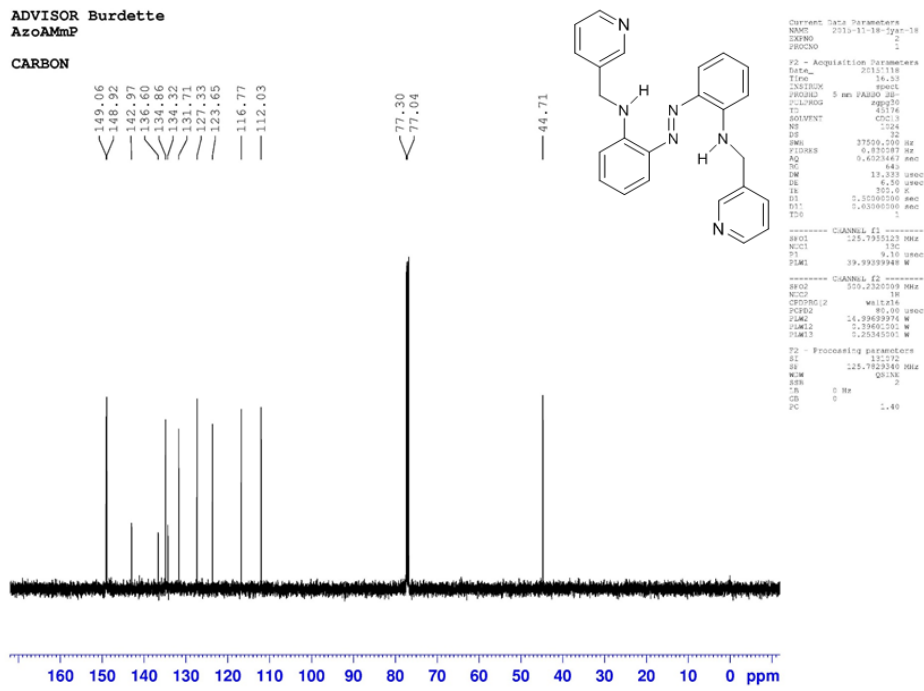


Figure 2.12. ¹³C NMR of compound AzoAMmP (3).

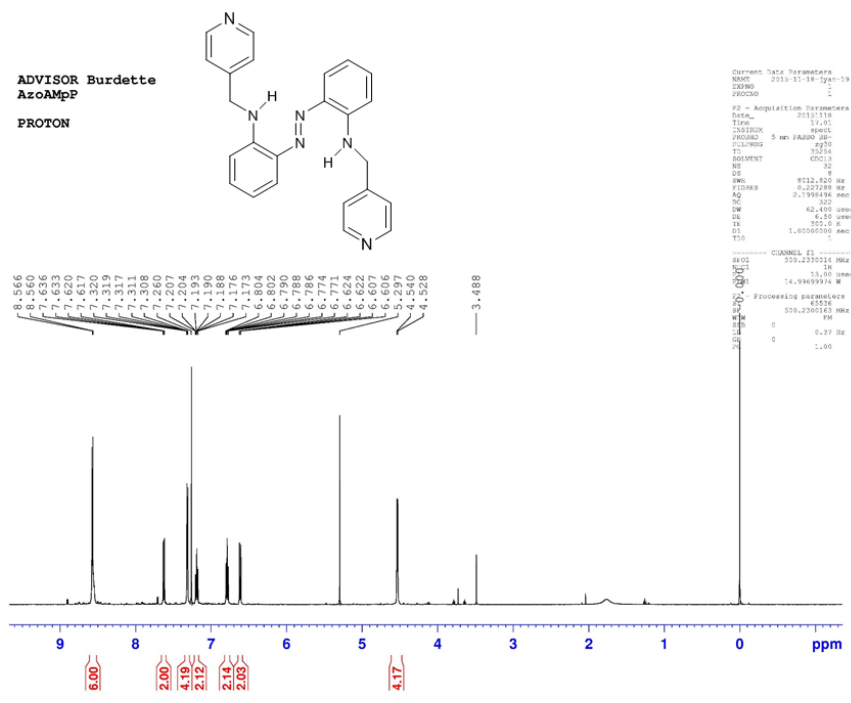


Figure 2.13. ¹H NMR of compound AzoAMpP (4).

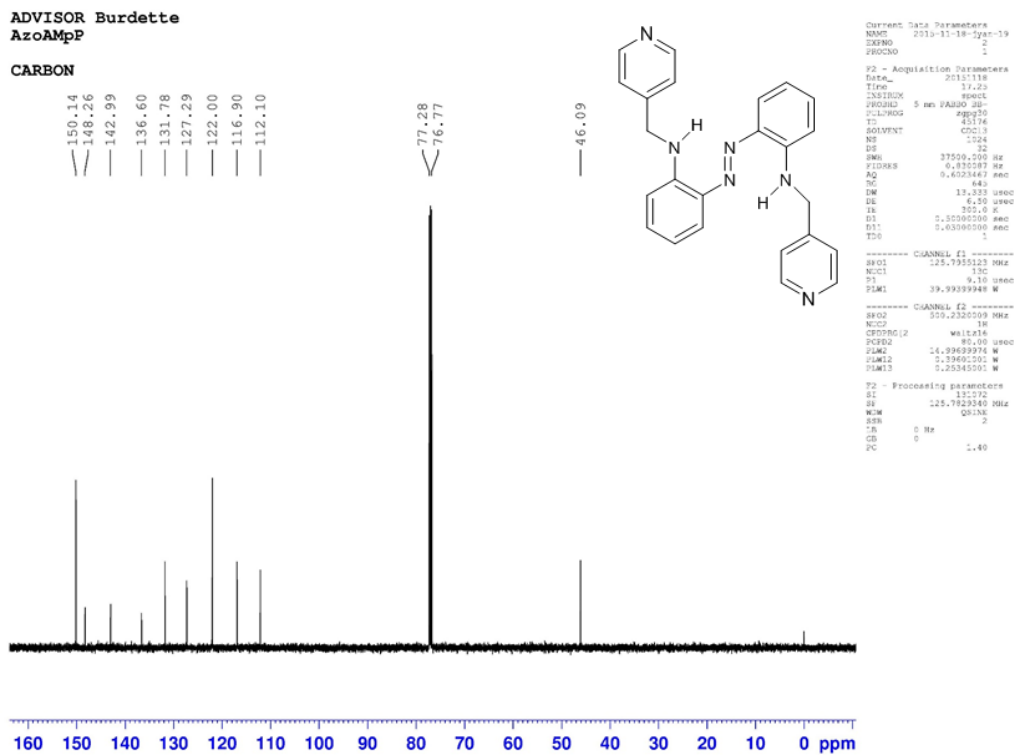


Figure 2.14. ¹³C NMR of compound AzoAMpP (4).

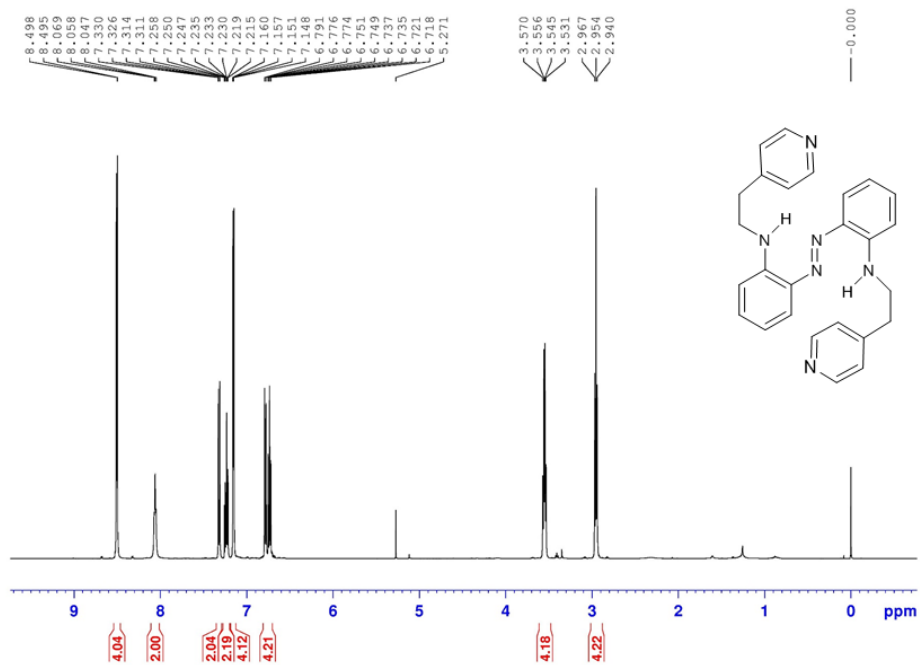


Figure 2.15. ^1H NMR of compound AzoAEpP (5).

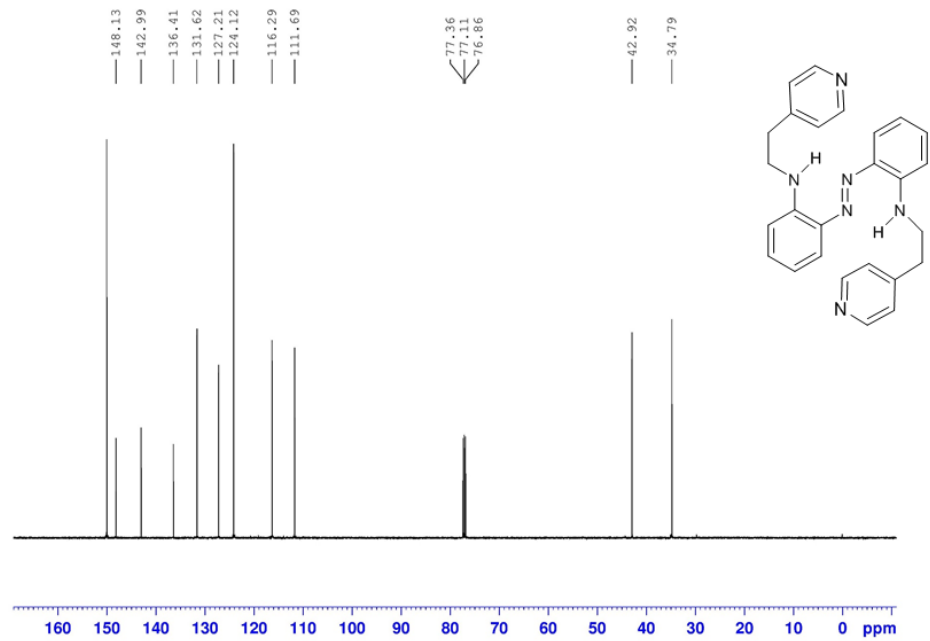


Figure 2.16. ^{13}C NMR of compound AzoAEpP (5).

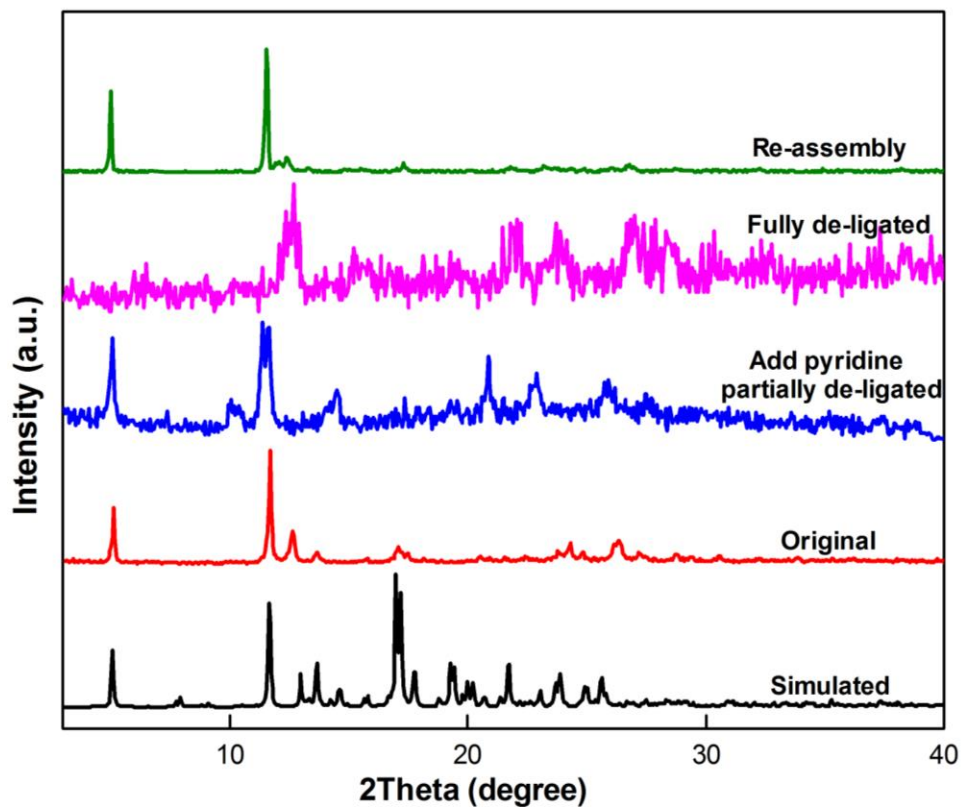


Figure 2.17. Powder X-ray diffraction patterns of AgAAEP. Both experimental (red) and simulated (black) patterns from single crystal structures are shown to confirm the phase purity. The pattern after quenching with pyridine (blue) shows polymer degradation, diffraction peaks disappearing and amorphous material forming. As more pyridine added, the material transforms to complete amorphous and polymer characteristic peaks disappear (magenta). The pattern after pyridine removal and complex re-assembly is shown in green, suggesting crystalline material with resumed polymer diffraction peaks.

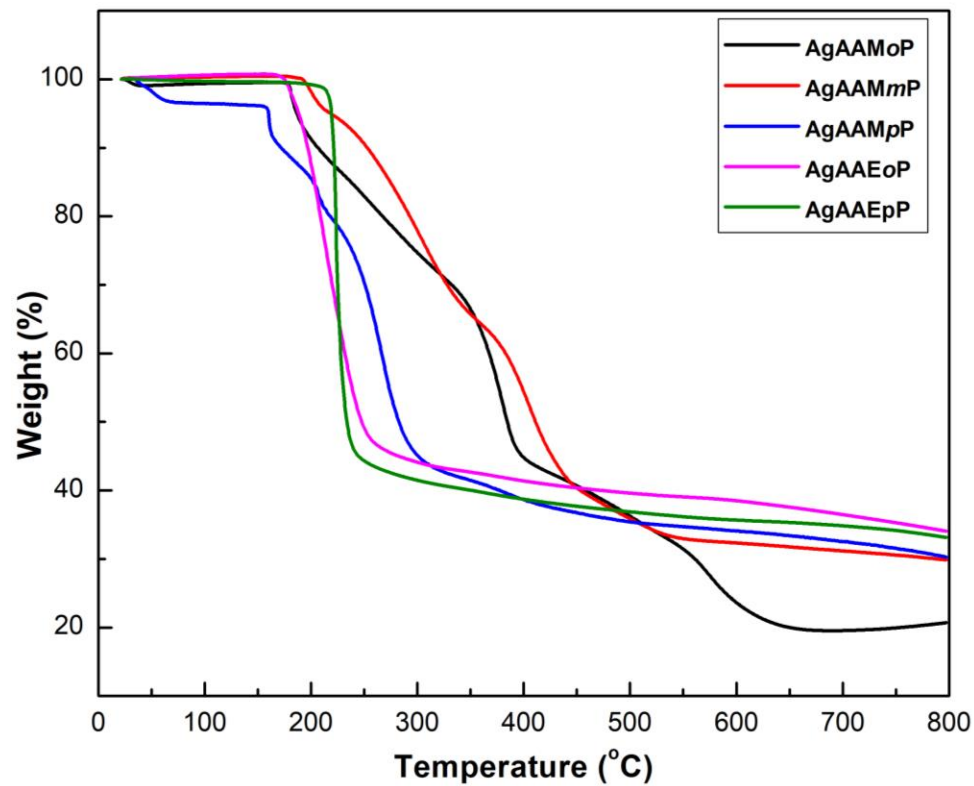


Figure 2.18. The thermogravimetric analysis (TGA) diagrams of the five aAB silver complexes.

2.9. References

- (1) Blevins, A. A.; Blanchard, G. J. Effect of positional substitution on the optical response of symmetrically disubstituted azobenzene derivatives. *J. Phys. Chem. B.* **2004**, *108*, 4962-4968.
- (2) Andersson, J. A. Thermal *cis*→*trans* isomerization of 4-hydroxyazobenzene in the vapor phase: a flash spectroscopy study. *J. Photochem.* **1983**, *22*, 255-261.
- (3) Finger, G. C.; Kruse, C. W. Aromatic fluorine compounds. VII. replacement of aromatic -Cl and -NO₂ Groups by -F^{1,2}. *J. Am. Chem. Soc.* **1956**, *78*, 6034-6037.
- (4) Bandara, H. M. D.; Friss, T. R.; Enriquez, M. M.; Isley, W.; Incarvito, C.; Frank, H. A.; Gascon, J.; Burdette, S. C. Proof for the concerted inversion mechanism in the *trans*→*cis* isomerization of azobenzene using hydrogen bonding to induce isomer locking. *J. Org. Chem.* **2010**, *75*, 4817-4827.
- (5) Bandara, H. M. D.; Basa, P. N.; Yan, J. J.; Camire, C. E.; MacDonald, J. C.; Jackson, R. K.; Burdette, S. C. Systematic modulation of hydrogen bond donors in aminoazobenzene derivatives provides further evidence for the concerted inversion photoisomerization pathway. *Eur. J. Org. Chem.* **2013**, 4794-4803.
- (6) Crank, G.; Makin, M. I. H. Oxidations of aromatic-amines by superoxide ion. *Aust. J. Chem.* **1984**, *37*, 845-855.
- (7) Sheldrick, G. M. *SADABS*, University of Göttingen: Göttingen, Germany, 1996.
- (8) Sheldrick, G. M. Crystal structure refinement with SHELXL. *Acta Crystallogr. C Struct. Chem.* **2015**, *71*, 3-8.

(9) Shustova, N. B.; McCarthy, B. D.; Dinca, M. Turn-on fluorescence in tetraphenylethylene-based metal-organic frameworks: an alternative to aggregation-induced emission. *J. Am. Chem. Soc.* **2011**, *133*, 20126-20129.

(10) Wrighton, M. S.; Ginley, D. S.; Morse, D. L. Technique for determination of absolute emission quantum yields of powdered samples. *J. Phys. Chem.* **1974**, *78*, 2229-2233.

(11) Khlobystov, A. N.; Blake, A. J.; Champness, N. R.; Lemenovskii, D. A.; Majouga, A. G.; Zyk, N. V.; Schroder, M. Supramolecular design of one-dimensional coordination polymers based on silver(I) complexes of aromatic nitrogen-donor ligands. *Coordin. Chem. Rev.* **2001**, *222*, 155-192.

(12) Robin, A. Y.; Fromm, K. M. Coordination polymer networks with O- and N-donors: What they are, why and how they are made. *Coordin. Chem. Rev.* **2006**, *250*, 2127-2157.

(13) Halper, S. R.; Do, L.; Stork, J. R.; Cohen, S. M. Topological control in heterometallic metal-organic frameworks by anion templating and metalloligand design. *J. Am. Chem. Soc.* **2006**, *128*, 15255-15268.

(14) Kaes, C.; Hosseini, M. W.; Rickard, C. E. F.; Skelton, B. W.; White, A. H. Synthesis and structural analysis of a helical coordination polymer formed by the self-assembly of a 2,2'-bipyridine-based *exo*-ditopic macrocyclic ligand and silver cations. *Angew. Chem., Int. Ed.* **1998**, *37*, 920-922.

(15) Shin, D. M.; Lee, I. S.; Lee, Y. A.; Chung, Y. K. Self-assembly between silver(I) and di- and tri-2-pyridines with flexible spacer: formation of discrete metalocycle versus coordination polymer. *Inorg. Chem.* **2003**, *42*, 2977-2982.

(16) Chen, C. Y.; Zeng, J. Y.; Lee, H. M. Argentophilic interaction and anionic control of supramolecular structures in simple silver pyridine complexes. *Inorg. Chim. Acta.* **2007**, *360*, 21-30.

(17) Qin, Z. Q.; Jennings, M. C.; Puddephatt, R. J. Alternating right- and left-handed helical loops in a self-assembled polymer: direct observation of ring-opening polymerization of a macrocyclic gold complex. *Chem. Eur. J.* **2002**, *8*, 735-738.

(18) Lin, J. C. Y.; Tang, S. S.; Vasam, C. S.; You, W. C.; Ho, T. W.; Huang, C. H.; Sun, B. J.; Huang, C. Y.; Lee, C. S.; Hwang, W. S.; Chang, A. H. H.; Lin, I. J. B. Structural, photophysical, and catalytic properties of Au(I) complexes with 4-substituted pyridines. *Inorg. Chem.* **2008**, *47*, 2543-2551.

(19) Yuan, Q.; Liu, B. Synthesis, structure and green fluorescence of a isonicotinic coordination polymer containing a silver(I) isonicotinate array and a two-coordination cadmium(II). *B. Kor. Chem. Soc.* **2006**, *27*, 150-152.

(20) Zhang, Z. Y.; Deng, Z. P.; Huo, L. H.; Zhao, H.; Gao, S. Well-designed strategy to construct helical silver(I) coordination polymers from flexible unsymmetrical bis(pyridyl) ligands: syntheses, structures, and properties. *Inorg. Chem.* **2013**, *52*, 5914-5923.

(21) Deng, Z. P.; Zhu, L. N.; Gao, S.; Huo, L. H.; Ng, S. W. Self-assembly of discrete metallocycle versus coordination polymer based on silver(I) and di-2- and di-3-pyridines with flexible spacer. *Cryst. Growth Des.* **2008**, *8*, 3277-3284.

(22) Parra, N.; Belmar, J. B.; Jimenez, C. A.; Pasan, J.; Ruiz-Perez, C. Crystal structure analysis of supramolecular arrangements in bis(1-isoquinolinecarboxamide)alkanes and their Ag(I) complexes. *CrystEngComm*. **2017**, *19*, 1076-1088.

(23) Muthu, S.; Yip, J. H. K.; Vittal, J. J. Coordination networks of Ag(I) and N,N'-bis(3-pyridine-carboxamide)-1,6-hexane: structures and anion exchange. *Dalton Trans.* **2002**, 4561-4568.

(24) Withersby, M. A.; Blake, A. J.; Champness, N. R.; Cooke, P. A.; Hubberstey, P.; Li, W. S.; Schroder, M. Silver(I)-3,6-bis(pyridin-3-yl)-1,2,4,5-tetrazine coordination polymers: a diversity of chain motifs. *Cryst. Eng.* **1999**, *2*, 123-126.

(25) Withersby, M. A.; Blake, A. J.; Champness, N. R.; Hubberstey, P.; Li, W. S.; Schroder, M. Anion control in bipyridylsilver(I) networks: a helical polymeric array. *Angew. Chem. Int. Ed.* **1997**, *36*, 2327-2329.

(26) Guerrero, M.; Pons, J.; Parella, T.; Font-Bardia, M.; Calvet, T.; Ros, J. Variable coordination behavior of new hybrid pyrazole ligand: synthesis and characterization of several Zn^{II}, Cd^{II}, Hg^{II}, Pd^{II}, Pt^{II}, and Ni^{II} complexes. *Inorg. Chem.* **2009**, *48*, 8736-8750.

(27) Blake, A. J.; Baum, G.; Champness, N. R.; Chung, S. S. M.; Cooke, P. A.; Fenske, D.; Khlobystov, A. N.; Lemenovskii, D. A.; Li, W. S.; Schroder, M. Long-range chain orientation in 1-D co-ordination polymers as a function of anions and intermolecular aromatic interactions. *Dalton Trans.* **2000**, 4285-4291.

- (28) Hirsch, K. A.; Wilson, S. R.; Moore, J. S. Coordination networks of 3,3'-dicyanodiphenylacetylene and silver(I) salts: structural diversity through changes in ligand conformation and counterion. *Inorg. Chem.* **1997**, *36*, 2960-2968.
- (29) Carlucci, L.; Ciani, G.; Proserpio, D. M. A new type of supramolecular entanglement in the silver(I) coordination polymer $[Ag_2(bpethy)_5](BF_4)_2$ [bpethy = 1,2-bis(4-pyridyl)ethyne]. *Chem. Commun.* **1999**, 449-450.
- (30) Han, M.; Hara, M. Intense fluorescence from light-driven self-assembled aggregates of nonionic azobenzene derivative. *J. Am. Chem. Soc.* **2005**, *127*, 10951-10955.
- (31) Hao, Y. W.; Wang, H. Y.; Huang, Y. J.; Gao, B. R.; Chen, Q. D.; Li, L. B.; Sun, H. B. Evidence of concerted inversion for the photon-induced molecular switching of azobenzene using rotation-free azobenzene derivatives. *J. Mater. Chem. C* **2013**, *1*, 5244-5249.
- (32) Bandara, H. M. D.; Burdette, S. C. Photoisomerization in different classes of azobenzene. *Chem. Soc. Rev.* **2012**, *41*, 1809-1825.
- (33) Tan, E. M. M.; Amirjalayer, S.; Smolarek, S.; Vdovin, A.; Zerbetto, F.; Buma, W. J. Fast photodynamics of azobenzene probed by scanning excited-state potential energy surfaces using slow spectroscopy. *Nat. Commun.* **2015**, *6*, 5860.
- (34) Rau, H.; Luddecke, E. On the rotation-inversion controversy on photo-isomerization of azobenzenes - experimental proof of inversion. *J. Am. Chem. Soc.* **1982**, *104*, 1616-1620.
- (35) Diau, E. W. G. A new *trans*-to-*cis* photoisomerization mechanism of azobenzene on the S-1(n,π^*) surface. *J. Phys. Chem. A.* **2004**, *108*, 950-956.

(36) Yoshino, J.; Furuta, A.; Kambe, T.; Itoi, H.; Kano, N.; Kawashima, T.; Ito, Y.; Asashima, M. Intensely fluorescent azobenzenes: synthesis, crystal structures, effects of substituents, and application to fluorescent vital stain. *Chem. Eur. J.* **2010**, *16*, 5026-5035.

(37) Yoshino, J.; Kano, N.; Kawashima, T. Synthesis of the most intensely fluorescent azobenzene by utilizing the B-N interaction. *Chem. Commun.* **2007**, 559-561.

(38) Yoshino, J.; Kano, N.; Kawashima, T. Fluorescence properties of simple N-substituted aldimines with a B-N interaction and their fluorescence quenching by a cyanide ion. *J. Org. Chem.* **2009**, *74*, 7496-7503.

(39) Yoshino, J.; Kano, N.; Kawashima, T. Fluorescent azobenzenes and aromatic aldimines featuring an N-B interaction. *Dalton Trans.* **2013**, *42*, 15826-15834.

(40) Wilbraham, L.; Coudert, F. X.; Ciofini, I. Modelling photophysical properties of metal-organic frameworks: a density functional theory based approach. *Phys. Chem. Chem. Phys.* **2016**, *18*, 25176-25182.

(41) Nagarkar, S. S.; Joarder, B.; Chaudhari, A. K.; Mukherjee, S.; Ghosh, S. K. Highly selective detection of nitro explosives by a luminescent metal-organic framework. *Angew. Chem., Int. Ed.* **2013**, *52*, 2881-2885.

(42) Hu, Z. C.; Pramanik, S.; Tan, K.; Zheng, C.; Liu, W.; Zhang, X.; Chabal, Y. J.; Li, J. Selective, sensitive, and reversible detection of vapor-phase high explosives via two-dimensional mapping: A new strategy for MOF-based sensors. *Cryst. Growth Des.* **2013**, *13*, 4204-4207.

(43) Lan, A. J.; Li, K. H.; Wu, H. H.; Olson, D. H.; Emge, T. J.; Ki, W.; Hong, M. C.; Li, J. A
luminescent microporous metal-organic framework for the fast and reversible detection of high
explosives. *Angew. Chem. Int. Ed.* **2009**, *48*, 2334-2338.

**Chapter 3 Detection of Surface Adsorbed Guests on Emissive
MOFs by X-ray Photoelectron Spectroscopy**

3.1. Introduction

Luminescent metal-organic frameworks (MOFs) have been used extensively as scaffolds to construct luminescent probes for many difficult-to-detect analytes including explosives.¹⁻³ While there are many approaches to induce MOF emission, constructing structures with luminescent struts is the most straightforward design strategy to achieve this goal.^{4,5} Electron-deficient compounds such as nitroaromatic molecules constitute an important class of explosive analyte targets, and typically quench ligand-centered emission.^{2,6} Charge transfer from the excited fluorophores that constitute the MOF struts to the electron deficient analytes is the most plausible quenching mechanism in most of these systems.

Emission quenching signals communication between MOF and guest, but not the specific nature of the interactions. More sophisticated measurements can establish the distance between fluorophore and quencher, as well as differentiate between inner-sphere and outer-sphere mechanisms; however, these can be complex, time-consuming experiments. Similarly UV-vis spectroscopy⁷ and vibrational spectroscopy⁸ can provide some information about host-guest interactions, but also have inherent limitations.

Both π - π stacking^{6,9} and electrostatic interactions^{2,10} have been cited to explain nitroaromatic guest-MOF interactions. Nitroaromatic molecules can be surface-absorbed in MOFs lacking porosity,^{6,10} but there are also assertions, often with limited proof, that aromatic analytes enter MOF cavities.¹¹⁻¹⁵

An X-ray crystal structure of a MOF-guest adduct would provide strong evidence for the nature of host-guest interactions; however, crystalizing supramolecular MOF complexes with well-ordered guests necessary for X-ray analysis can be difficult.^{13,14} Theoretical modeling of these

interactions can also be useful,^{16,17} but are more convincing in conjunction with direct experimental data. Thermogravimetric analysis (TGA) are used to quantitatively determining guest amount,^{11,13} but incapable of distinguish surface and internal guests. Developing a universally applicable technique to probe MOF-guest interactions would facilitate the ability to design and optimize MOF structures suitable for luminescent probes with greater selectivity and sensitivity.

X-ray photoelectron spectroscopy (XPS) possesses untapped potential to ascertain whether emission-quenching guests are adsorbed to the MOF surfaces or possibly internalized within the pores. XPS can determine metal oxidation states in MOFs^{18,19} and MOF composites,²⁰ as well as quantify catalyst decomposition due to side-reactions.²¹ XPS is sensitive to near-surface chemical environments,²² and angle-resolved XPS (ARXPS) further utilizes the attenuation of sub-surface electrons to quantify surface vs. bulk contributions to a photoelectron spectrum.²³ Given these capabilities, we envisioned developing photoelectron spectroscopic techniques to probe host-guest interactions in emissive MOF systems.

Based on our earlier studies making emissive coordination polymers with the azobenzene-based extended bipyridyl ligand AzoAEP (*(2,2'*-bis[*N,N'*-(4-pyridyl)ethyl]diaminoazobenzene),²⁴ we reasoned that we could also construct luminescent pillared paddle-wheel MOFs with standard dicarboxylate ligands and Zn²⁺. Since the emissive azobenzene fluorophore has a large surface area, we hypothesized that we might be able to access pillared paddle-wheel MOFs with unique structural features, and that various nitroaromatic guests could either π -stack with AzoAEP units, or engage in electrostatic interactions at the metal sites. Pillared paddle-wheel MOFs have paddle-wheel-type coordination of Zn(II) pairs in two dimensions with pyridyl ligand pillaring in the third. Furthermore, we expected fluorinated analogs

of nitroaromatic guests could be used to help detail the MOF-guest interactions owing to the high sensitivity of XPS for fluorine,²⁵ and the absence of interfering signals from the chosen MOF components. XPS also affords the opportunity to utilize angle-resolved techniques as well as argon-ion sputtering to desorb near-interfacial species from the MOF substrate, which could reveal the physical arrangement of the nitrophenol compounds relative to the MOF substrate (i.e. surface adsorbed guests vs bulk intercalated guests).

3.2. Experimental Section

3.2.1. General Procedures. All reagents were purchased and used without further purification. AzoAEP (2,2'-bis[N,N'-(4-pyridyl)ethyl]diaminoazobenzene) was prepared as previously described.²⁴ AzoMOF-2 was prepared and characterized analogously to AzoMOF-1, and the details can be found in the supporting information. ¹H NMR spectra were recorded with a 500 MHz Bruker Biospin NMR instrument. Elemental microanalyses for C, H, and N were performed by Micro Analysis Inc (Wilmington DE). FT-IR spectra were recorded using Bruker Vertex70 Optics FT-IR spectrometer equipped with a Specac Golden Gate attenuated total reflection (ATR) accessory by collecting 1024 scans over a scan range from 4000 to 400 cm⁻¹ at 4 cm⁻¹ resolution. Thermogravimetric analysis (TGA) measurements were carried out on a TA Instruments Hi-Res TGA 2950 Thermogravimetric Analyzer from room temperature to 700 °C under nitrogen atmosphere at a heating rate of 10 °C/min.

{Zn₂(NDC)₂(AzoAEP) • 2DMF}_n (ABMOF-1). AzoAEP (21.1 mg, 50.0 μmol), Zn(NO₃)₂ • 4H₂O (26.1 mg, 0.100 mmol) and 1,4-naphthalenedicarboxylic acid (NDC, 21.6 mg, 0.100 mmol) were combined in a sealed microwave vial in DMF/H₂O (6.8 mL/0.2 mL). After the reaction mixture was sonicated for 2 min, the clear solution was subjected to a programmed reaction cycle that involved steady, gradual heating to 100 °C over 1 h, followed by maintaining a constant

temperature for 48 h and then gradual cooling to room temperature over 6 h. The resulting orange-red blocks were harvested by filtration, and then washed and stored in DMF. NMR analysis of ABMOF-1 after digestion with D_2SO_4 in $DMSO-d_6$ was consistent with a 2:1 ratio of NDC:AzoAEP. Elemental analysis calcd. for activated ABMOF-1 $C_{50}H_{38}N_6O_8Zn_2$: C 61.12%, H 3.87%, N 8.56%; Found: C 60.46%, H 3.82%, N 8.46%. FT-IR (diamond-ATR, cm^{-1}) 3396.0, 3069.0, 2924.8, 2357.4, 2336.5, 1665.5, 1638.6, 1620.0, 1595.0, 1576.2, 1501.6, 1468.3, 1427.0, 1369.0, 1315.0, 1263.3, 1248.9, 1227.9, 1215.7, 1192.8, 1161.8, 1124.5, 1093.4, 1072.4, 1035.1, 983.4, 900.6, 863.3, 826.0, 790.6, 767.7, 747.0, 670.5, 655.8. TGA shows a 12.6% weight loss before 190 °C, corresponding to the loss encapsulated DMF, and MOF decomposition at 270 °C. No weight loss is observed if the ABMOF-1 is pretreated by drying at 80 °C for four h, and decomposition occurs at 270 °C.

$\{Zn_2(BDC)_2(AzoAEP)\}_n$ (ABMOF-2). AzoAEP (21.1 mg, 50.0 μ mol), $Zn(NO_3)_2 \cdot 4H_2O$ (26.1 mg, 0.100 mmol) and terephthalic acid (BDC, 16.6 mg, 0.100 mmol) were combined in a sealed microwave vial in DMF/ H_2O (6.8 mL/0.2 mL). After the reaction mixture was sonicated for 2 min, the clear solution was subjected to a programmed reaction cycle that involved steady gradual heating to 100 °C over 1 h, followed by maintaining a constant temperature for 48 h and gradual cooling to room temperature over 6 h. The resulting orange needles were harvested by filtration, washed and stored in DMF. NMR analysis of the MOF after digestion with D_2SO_4 in $DMSO-d_6$ is consistent with a 2:1 ratio of BDC:AzoAEP. Elemental analysis calcd. for activated ABMOF-2 $C_{42}H_{34}N_6O_8Zn_2$: C 57.22%, H 3.86%, N 9.54%; Found: C 56.95%, H 3.80%, N 9.36%. FT-R (diamond-ATR, cm^{-1}) 3235.4, 3055.0, 1681.1, 1635.7, 1598.0, 1576.6, 1501.7, 1472.2, 1431.8, 1383.8, 1316.8, 1292.5, 1244.3, 1220.3, 1161.2, 1078.1, 1032.7, 823.5, 746.0. TGA shows no mass loss in either freshly prepared or ABMOF-2 dried at 80 °C. Decomposition occurs at 207 °C.

3.2.2. Collection and Reduction of X-Ray Data

X-ray crystallography. Structural analysis was carried out in the X-Ray Crystallographic Facility at Worcester Polytechnic Institute. Crystals were glued on tip of a glass fiber and were mounted on a Bruker-AXS APEX CCD diffractometer equipped with an LT-II low temperature device. Diffraction data were collected at room temperature or 100 K using graphite monochromated Mo-K α radiation ($\lambda = 0.71073 \text{ \AA}$) using the omega scan technique. Empirical absorption corrections were applied using the SADABS program.²⁶ The unit cells and space groups were determined using the SAINT+ program.²⁶ The structures were solved by direct methods and refined by full matrix least-squares using the SHELXTL program.²⁷ Refinement was based on F² using all reflections. All non-hydrogen atoms were refined anisotropically. Hydrogen atoms on carbon atoms were all located in the difference maps and subsequently placed at idealized positions and given isotropic U values 1.2 times that of the carbon atom to which they were bonded. Hydrogen atoms bonded to oxygen atoms were located and refined with isotropic thermal parameters. Mercury 3.1 software was used to examine the molecular structure. Relevant crystallographic information is summarized in Table 3.1 and Table 3.2, and the 50% thermal ellipsoid plot is shown in Figure 3.1.

Powder X-ray Diffraction. PXRD data were collected on a Bruker-AXS D8-Advance diffractometer using Cu-K α radiation with X-rays generated at 40 kV and 40 mA. Bulk samples of crystals were placed in a 20 cm \times 16 cm \times 1 mm well in a glass sample holder, and scanned at RT from 3 $^\circ$ to 50 $^\circ$ (2 θ) in 0.05 $^\circ$ steps at a scan rate of 2 $^\circ$ /min. Simulated PXRD patterns from single crystal data were compared to PXRD patterns of ABMOF-1, to confirm the uniformity of the crystalline sample.

3.2.3. Spectroscopy

General Spectroscopic Methods. Solution UV-vis absorption spectra were acquired in 1.0 cm quartz cuvettes at room temperature and recorded on a Thermo Scientific Evolution 300 UV-vis spectrometer with inbuilt Cary winUV software. Steady-state diffuse reflectance UV-vis spectra were obtained on the same instrument with a Harrick Praying Mantis diffuse reflectance accessory (Harrick Scientific Products) and referenced to MgSO_4 .⁴ Solution emission spectra were recorded on a Hitachi F-4500 spectrophotometer with excitation and emission slit widths of 5 nm. The excitation source was a 150 W Xe arc lamp (Ushio Inc.) operating at a current of 5 A and equipped with photomultiplier tube with a power of 400 V. Analytes screened included 2,4-dinitrophenol (2,4-DNP), chlorobenzene (CB), 1,3-dinitrobenzene (1,3-DNB), 1,4-dinitrobenzene (1,4-DIB), 2-nitrophenol (2-NP), 4-nitrophenol (4-NP), and 2,6-dinitro-4-trifluoromethyl phenol (2,6-DNP-4- CF_3).

Emission and Quantum Yield Determination. Steady-state emission were recorded on a Hitachi F-4500 spectrophotometer with excitation and emission slit widths of 5 nm. The excitation source was a 150 W Xe arc lamp (Ushio Inc.) operating at a current of 5 A and equipped with photomultiplier tube at 400 V. Quantum yields in the solid state were determined in triplicated using published procedures with Na_2SO_4 as the reference.^{4,28}

Analyte Detection by Emission. A 2 mL suspension of 40 μM ABMOF-1 in DMF was prepared from a 2 mM stock solution and the emission spectra was recorded ($\lambda_{\text{ex}} = 523$ nm). For each emission assay, three 40 μL aliquots from 2 mM stock solutions were added successively to obtain the response to 1-10 equivalents of the analyte (1 eq with respect to AzoAEP units) to the ABMOF-1 suspension. After each aliquot addition, the mixture was equilibrated by stirring for 30 min before the emission spectrum was recorded. The emission response to all analytes was

measured by integrating the emission band between 530-800 nm. All spectroscopic experiments were performed in triplicate.

3.2.4. X-ray Photoelectron Spectroscopy

Analyte–MOF samples for XP spectroscopy were specifically limited to the 2,6-DNP-4-CF₃ guest and to ABMOF-1 crystals with 4 mm × 4 mm faces. Washing three times in DMF and overnight air drying followed MOF exposure to the DNP–CF₃. A PHI5600 XPS with a third-party acquisition system (RBD Instruments, Bend Oregon) acquired all photoelectron spectra as described previously.²⁹ Analysis chamber base pressures were $<1 \times 10^{-9}$ torr. For certain experiments, argon-ion sputtering removal of near-interfacial species preceded XPS acquisition. With the MOF/analyte sample in the XPS analysis chamber, sputter conditions utilized a differentially pumped ion gun source at 25 mA electron emission, 3.5 kV beam voltage, and $\sim 1.5 \times 10^{-4}$ Torr of research-grade argon. Sputtering lasted for 6 s during which the ion gun rastered the beam across the sample over an area that was aligned with and somewhat larger than the sampling area of the analyzer. A hemispherical energy analyzer that was positioned at 90° with respect to the incoming X-ray flux collected photoelectrons at angles of 30°, 45°, and 60° with respect to the MOF surface normal angle. For the large-faced samples under study, photoelectron acquisition at higher angles with respect to the surface normal demonstrated increased surface sensitivity as compared to acquisition at smaller angles.²³ Survey spectra utilized a pass energy of 117 eV, a 0.5 eV step size, and a 50 ms per step dwell time. High-resolution XP spectra employed a 23.5 eV pass energy, 25 meV step size, and a 50 ms dwell time per step. A low-energy electron gun provided charge neutralization. Neutralization power and energy were optimized to minimize fwhm peak widths rather than to position a peak at a specific binding energy. With features ascribed to adventitious carbon between 283.5–285.0 eV under this neutralization methodology,

spectra were linearly shifted to position the adventitious carbon feature at 284.8 eV in the data analysis phase. Data for the Zn 2p_{3/2} photoelectron region were fit with a Shirley-type background,³⁰ and Gaussian-Lorentzian (pseudo-Voigt) GL(30)-style peak shapes.³¹ Universal Tougaard-style backgrounds,³² and GL(30)-style peak shapes described photoelectron features for the C 1s, O 1s, and F 1s regions. Fits that employ multiple peaks within a spectral region utilized identical fwhm values for each peak to minimize mathematically optimized but potentially chemically unrealistic fits.

3.3. Synthesis and Structure

Our previous investigations with silver coordination polymers indicated that AzoAEP can behave like a rigid, linear bipyridine ligand despite an increased size and flexibility.²⁴ Like many other bipyridine ligands, we did not observe the formation of discrete, well-defined crystalline materials with AzoAEP and Zn²⁺;³³ however, when used in conjunction with dicarboxylate ligands, AzoAEP forms pillared paddle-wheel MOFs. Benzene 1,4-dicarboxylic acid (BDC) and 1,4-naphthalenedicarboxylic acid (NDC) form similar pillared paddle-wheel structures. In {Zn₂(NDC)₂(AzoAEP)•2DMF}_n (ABMOF-1), each dinuclear Zn²⁺ site is bridged by a carboxylate from each of four NDC ligands to form paddle-wheel complexes with the second carboxylate from each NDC ligand connecting to an independent Zn²⁺ paddle-wheel unit (Figure 3.1 A). The paddle-wheel coordination polymer sheets are in turn pillared with AzoAEP ligands to form a three-dimensional framework. The basic structure, as well as the accompanying paddle wheel geometry and bond distances are comparable to those found in other pillared paddle-wheel MOFs.³⁴⁻³⁶ The coordination chemistry in {Zn₂(BDC)₂(AzoAEP) • 2DMF}_n (ABMOF-2) is identical to that of ABMOF-1.

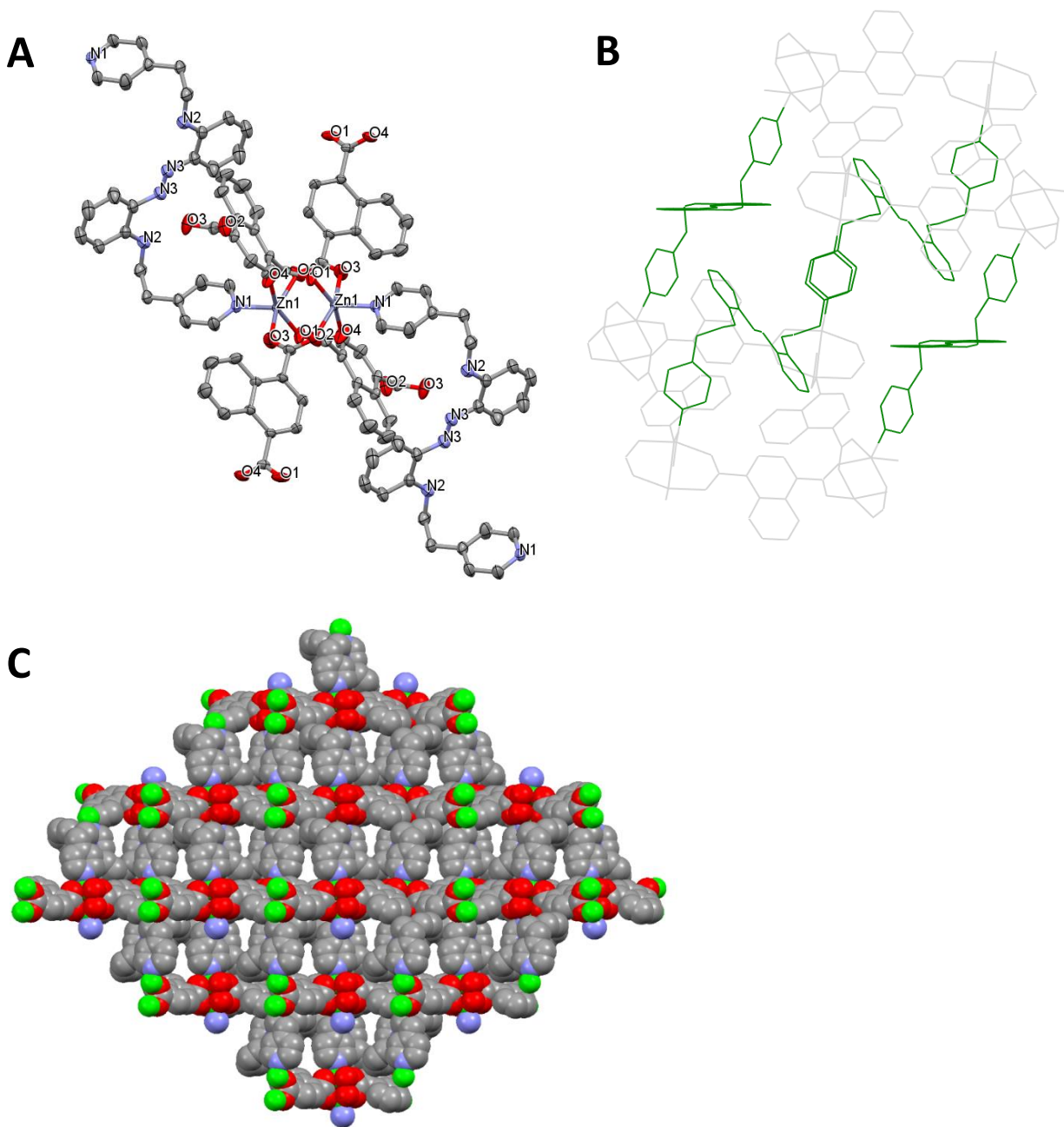


Figure 3.1A. ORTEP plot of ABMOF-1 showing 50% thermal ellipsoids and selected atom labels. Hydrogen atoms are omitted for clarity. **3.1B.** Wireframe diagram of ABMOF-1 showing primitive cubic nets with four AzoAEpP ligand pillars in green. **3.1C.** Space-filling diagram of ABMOF-1 showing crystal packing of the non-interpenetrated MOF structure showing the pore structure. Zn = green, N = blue, O = red, and C = gray. Hydrogen atoms and DMF molecules have been omitted for clarity.

Unlike linear bipyridine ligands like 4,4'-bipyridine, AzoAEP can reorient by rotation of the phenyl-azo C-N bonds, anilino-ethylene N-C bonds, ethylene-pyridine C-C bonds and/or the ethylene bonds C-C. The multiple degrees of freedom enable AzoAEP to adopt structures that differ from those accessible with rigid ligands. Owing to the nonlinear shape of AzoAEP, the ABMOF-1 framework forms a tilted primitive cubic net (Figure 3.1B), in contrast to the frequently observed vertical³³ or semi-vertical cubic nets.³⁴ The use of extended dicarboxylate ligands or bidentate pillars often leads to multiply interpenetrated frameworks since large voids formed by long linkers may allow interpenetration to happen.^{34,37} ABMOF-2 forms a 3-fold interpenetrated framework, with a vertical primitive cubic net whereas ABMOF-1 forms a non-interpenetrated framework with permanent porosity. Although the dicarboxylate span of NDC and BDC is similar, the point-to-point distance between the two pyridine nitrogen atoms of AzoAEP in ABMOF-1 and ABMOF-2 frameworks is quite different, 13.0 Å and 19.3 Å respectively. Furthermore, the effective distance in ABMOF-1 obtained by projecting one pyridine nitrogen on a plane containing the other pyridine is even shorter, 7.1 Å in ABMOF-1 compared to 19.3 Å in ABMOF-2 where the pyridine ligands are collinear. The linear conformation in AzoAEP in ABMOF-2 opens enough void space to permit 3-fold interpenetration. Compared to the structure of the apo ligand, in ABMOF-1, the azo N-C bonds rotate by 180°, anilino-ethylene N-C bonds rotate by 65°, and ethylene-pyridine C-C rotates 71°, resulting in the lone pairs pointing toward the diazene core as opposed to outward in the free ligand. This results in a primitive cubic net where framework interpenetration is blocked by the ligands occupying the void space.

Examination of ABMOF-1 crystal structure reveals one-dimensional pores along *c* axis of with an average size of $4.5 \times 1.9 \text{ \AA}^2$, after removing DMF guest molecules (Figure 3.1C). PLATON analysis using SQUEEZE³⁸ shows an average solvent accessible size of $4.5 \times 1.8 \text{ \AA}^2$, with the void

space occupies 26.2% of total volume. The pore-size cannot be calculated by Platon software precisely in ABMOF-2 due to crystallographic disorder in the azobenzene ligand (Figure 3.16); however, the pores are smaller and interpenetration further restricts the void space. The pores in ABMOF-1 are relatively small, especially for a non-interpenetrated network. Interpenetrated pillared paddlewheel MOFs tend to contain pores with dimensions not much larger than 5 Å,^{39,40} whereas non-interpenetrated pillared paddlewheel MOFs contain larger pores with dimensions between 11–40 Å.^{41–43} Non-interpenetrated MOFs with large pores can encapsulate large molecules such as ibuprofen,⁴⁴ benzene,⁴⁵ or toluene,⁴⁶ whereas interpenetrated MOFs are usually limited to small molecules such as CO₂⁴⁷ and other gases.⁴⁸ Despite having a non-interpenetrated structure, the small pores in ABMOF-1 preclude the inclusion of large guest molecules such as 2,4-dinitrophenol (2,4-DNP), as an explosive chemical, but also a safer substitute for more explosive trinitroaromatic compounds. The size exclusion phenomenon has also been shown in other luminescent MOF based detecting systems.^{2,6,10}

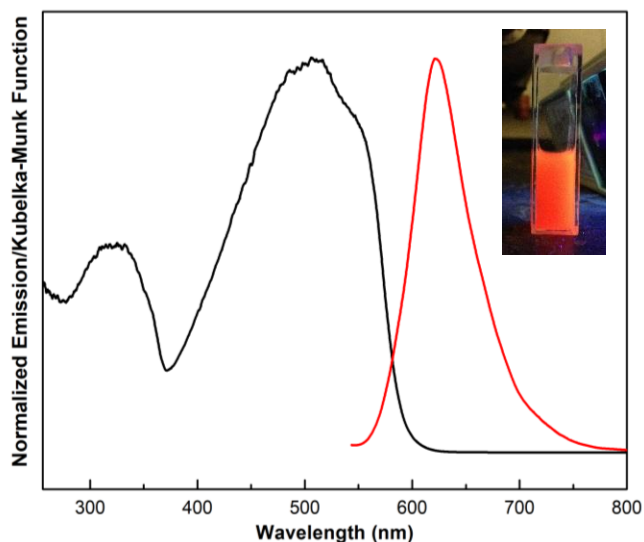


Figure 3.2. Solid state diffuse reflectance (black) and solid state emission ($\lambda_{\text{ex}} = 523$ nm, red) spectra of ABMOF-1. Inset: cuvettes containing a suspension of the complex crystals in DMF (40 μM) excited with 365 nm light (right).

3.4. Photophysical Properties of ABMOF-1 and Guest Molecule Detection

ABMOF-1 exhibits maximum absorbance at 500 nm with a broad emission centered at 610 nm (Figure 3.2), which are similar to the optical properties observed for Ag⁺ metal organic polymers containing the AzoAEP ligand.²⁴ Our investigations also demonstrated that AzoAEP emits with a λ_{max} at 605 nm when frozen in a solvent glass at 77 K, therefore, we attribute the emission observed in ABMOF-1 to the AzoAEP ligand, since NDC ligand emits at 480 nm. Although the quantum yield is low ($\phi = 0.4\%$), the emission is clearly visible when ABMOF-1 is dispersed in solvent (Figure 3.2, inset). Both ABMOF-1 and ABMOF-2 show strong emission at room temperature, but the latter was not responsive to guest molecules, so additional studies focused exclusively on ABMOF-1. While the lack of any other significant differences between the two MOFs suggests the interpenetration leads to the contrasting luminescence response, the emission of other interpenetrated MOFs can be quenched by nitro aromatics,^{49,50} so no definitive conclusion can be made based on all of our experiments.

When dispersed in DMF, powdered ABMOF-1 forms a semi-homogeneous suspension that persists indefinitely without any evidence of decomplexation even after 2 h of sonication. Based on previous studies of emissive MOF quenching,^{2,9} we chose 6 analytes – chlorobenzene (CB), 1,3-dinitrobenzene (1,3-DNB), 1,4-dinitrobenzene (1,4-DNB), 2-nitrophenol (2-NP), 4-nitrophenol (4-NP) and 2,4-dinitrophenol (2,4-DNP) based on electron withdrawing and electrostatic interaction ability – to probe the host-guest chemistry of ABMOF-1. All the aryl guest molecules can potentially π -stack with the aromatic MOF struts, but only the phenolic analytes can engage in electrostatic interactions with charged MOF components. Electron-deficient aromatic compounds readily quench MOF emission, so guests were also chosen to probe the scope of this behavior. The aromatic substituents range from inductively withdrawing halides

to nitro groups, which are strongly electron withdrawing by resonance. Trinitroaromatics, which are typically the strongest quenching guests, were not screened owing to safety concerns.

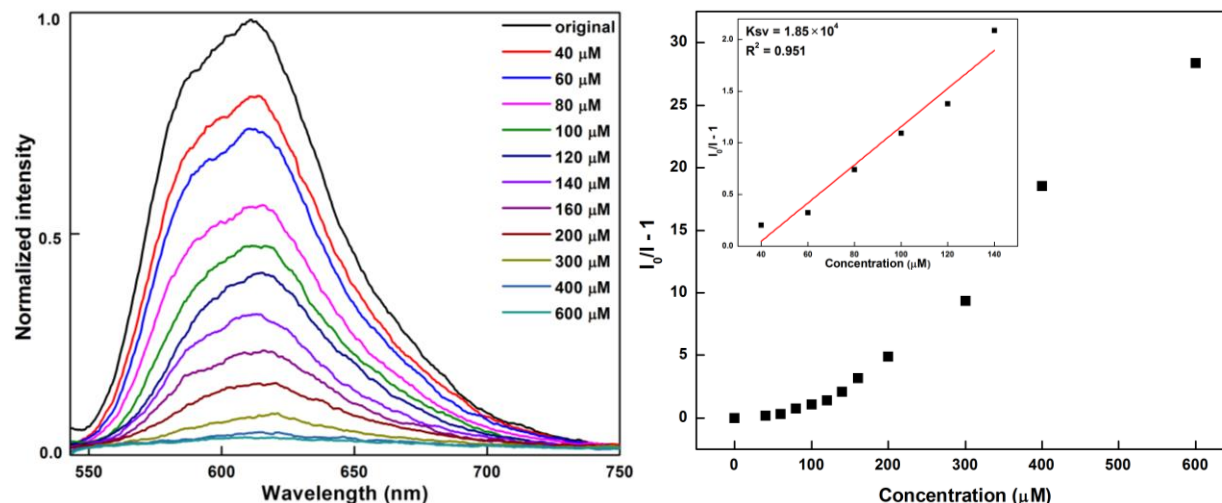


Figure 3.3A. Normalized emission response of ABMOF-1 to 2,4-DNP ($\lambda_{\text{ex}} = 500 \text{ nm}$). ABMOF-1 ($40 \mu\text{M}$) was suspended in DMF (black) and treated with 2,4-DNP in DMF to obtain final concentration of $40 \mu\text{M}$, $80 \mu\text{M}$, $120 \mu\text{M}$, $160 \mu\text{M}$, $200 \mu\text{M}$, until $600 \mu\text{M}$. Solutions were equilibrated for 30 min before each measurement. **3.3B.** Stern-Volmer plot for ABMOF-1 with the addition of 2,4-DNP (insert: enlarged view of a selected area) using the SV equation $I_0/I = 1 + K_{\text{sv}}[A]$, where I_0 is the initial fluorescence intensity at 610 nm , I is the fluorescence intensity after adding 2,4-DNP, $[A]$ is the molar concentration of analyte, and K_{sv} is the quenching constant (M^{-1}).

Of all the guests screened, only 2,4-DNP quenched ABMOF-1 emission significantly (Figure 3.3 and Figure 3.5). We attribute this response primarily to the proximity of the analyte to chromophores on or near the MOF surface since the size of 2,4-DNP ($6.1 \text{ \AA} \times 4.7 \text{ \AA}$) is larger than the pores in ABMOF-1. Nitroaromatic compounds typically quench emission by an electron transfer process from an electronically excited chromophore coming into a low-lying empty orbital on the nitro compound, which is also true of MOFs.⁴⁹⁻⁵¹ Although we cannot completely exclude energy-transfer quenching mechanisms observed in some MOF systems^{2,52} the lack of spectral overlap between emission spectra of ABMOF-1 and absorption spectra of the guest molecules

suggests the contributions from these alternative pathways is minimal. The absence of emission peak shifting characteristic of energy transfer also support this conclusion.

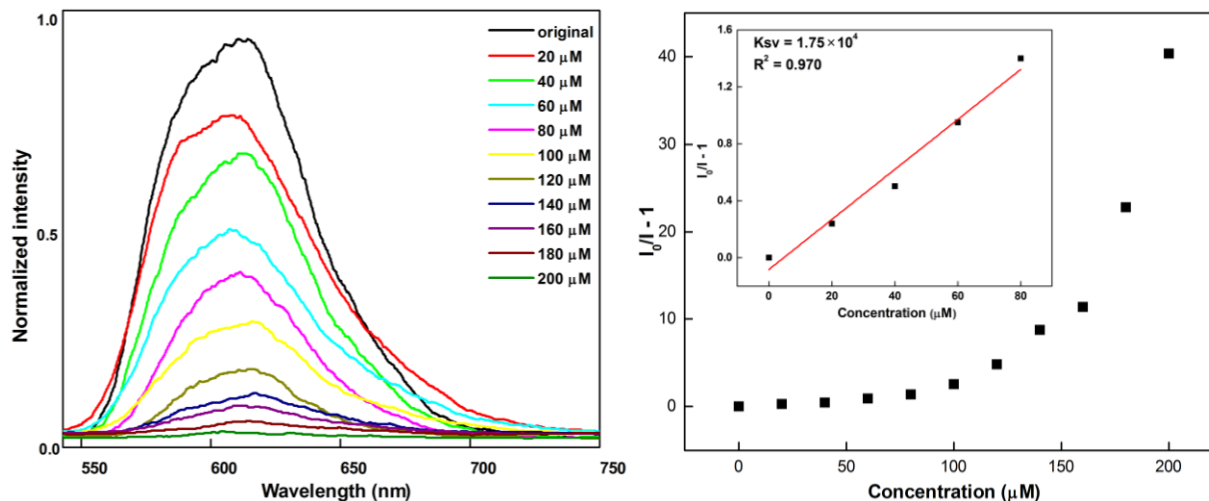


Figure 3.4A. Normalized emission response of ABMOF-1 to 2,6-DNP-4-CF₃ ($\lambda_{ex} = 523$ nm). ABMOF-1 (40 μ M) was suspended in DMF (black) and treated with 2,6-DNP-4-CF₃ in DMF to obtain final concentration of 20 μ M, 40 μ M, 60 μ M, 80 μ M, until 200 μ M. Solutions were equilibrated for 30 min before each measurement. **3.4B.** Stern-Volmer plot for ABMOF-1 with the addition of 2,6-DNP-4-CF₃ (insert: enlarged view of a selected area) using the SV equation $I_0/I = 1 + K_{sv}[A]$, where I_0 is the initial fluorescence intensity at 610 nm, I is the fluorescence intensity after adding 2,6-DNP-4-CF₃, $[A]$ is the molar concentration of analyte, and K_{sv} is the quenching constant (M^{-1}).

Achieving a significant emission response in ABMOF-1 requires a strong quencher with a low lying LUMO, and a phenol to decrease the distance between fluorophore and quencher, which is consistent with the proposed electron transfer quenching mechanism. In ABMOF-1, the quenching response to 2-NP (approximately 20% reduction in integrated emission) and 4-NP (approximately 25%) is minimal, whereas 2,4-DNP quenches almost completely (97%) (Figure 3.5). The lack of emission with 1,3-DNB, suggests the hydroxyl of 2,4-DNP anchors the guest to the MOF surface either through an interaction with surface-exposed Zn²⁺ ions, carboxylic acids or pyridine groups. A preliminary examination of the Stern-Volmer relationship suggests a shift from

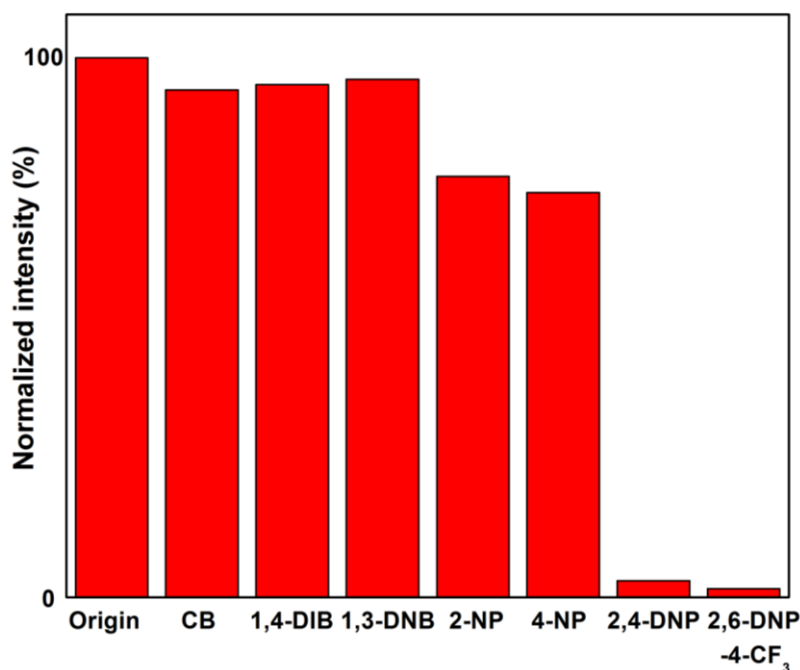


Figure 3.5. Normalized fluorescence intensity of 40 μM ABMOF-1 suspension in 2 mL DMF (original), and after adding 10 eq of different analytes, after each adding the suspension was stirring for 30 min before measuring. The excitation wavelength is 500 nm and the area under the emission spectra was integrated over a wavelength range of 540-800 nm.

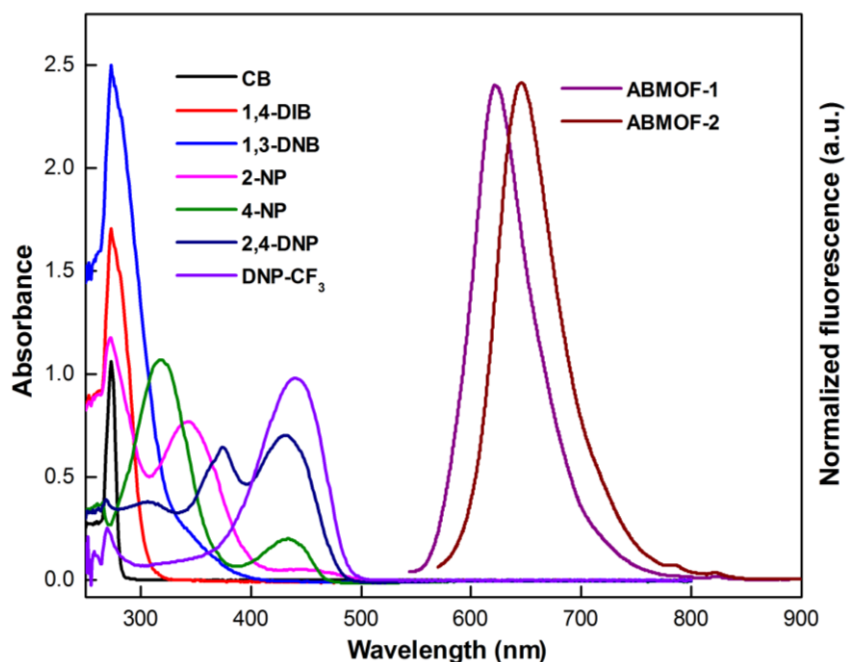


Figure 3.6. Absorbance spectra of 0.1 mM DMF solutions of CB, 1,4-DIB, 1,3-DNB, 2-NP, 4-NP, 2,4-DNP and 2,6-DNP-4-CF₃, showing no obvious overlap with the emission spectra of ABMOF-1 and ABMOF-2 suspended in DMF (40 μM).

dynamic to static quenching as the 2,4-DNP concentration increases. These observations are indicative of a distance-sensitive process like electron transfer, and the quenching properties of 2,4-DNP. Any metal bond to or salt bridge with the weakly coordinating 2,4-DNP anion would be weak and require high concentrations to drive the binding equilibrium. The stronger response to the most electron deficient analyte also supports the conclusion that electron transfer from the electronically excited MOF to a low-lying empty guest orbital dominates the quenching mechanism.

The narrow channels in ABMOF-1 restrict the host-guest behavior to surface interactions, but obtaining direct evidence to clearly confirm surface adsorption remains difficult. In MOFs with larger pores distinguishing between internalized guests internalized in pores and surface interaction imposes an even greater challenge. In ABMOF-1 internalized DMF molecules are observed in the X-ray structure, but surface molecules are outside the detection window, even if those molecules were densely populated, strongly adhered, and sufficiently ordered for crystallography. MOF emission can be quenched at significantly less than total theoretical pore occupancy,^{53,54} which excludes detection by single crystal analysis. In contrast, PXRD is sensitive to sample crystallinity changes, but detailed MOF structural information is both difficult to extrapolate, and neither internalized nor surface adhered guests necessarily perturb the crystal form.^{49,50}

In contrast to other X-ray techniques, our XPS measurements were readily able to elucidate interactions between the guest molecules and ABMOF-1. For an ABMOF-1 sample (4 mm × 4 mm) that was exposed to 10 eq. (regarding to AzoAEP) of 2,4-DNP for 0.5 h, wash three times with DMF and overnight air drying, the XPS spectra (Figure 3.7) revealed no features above a

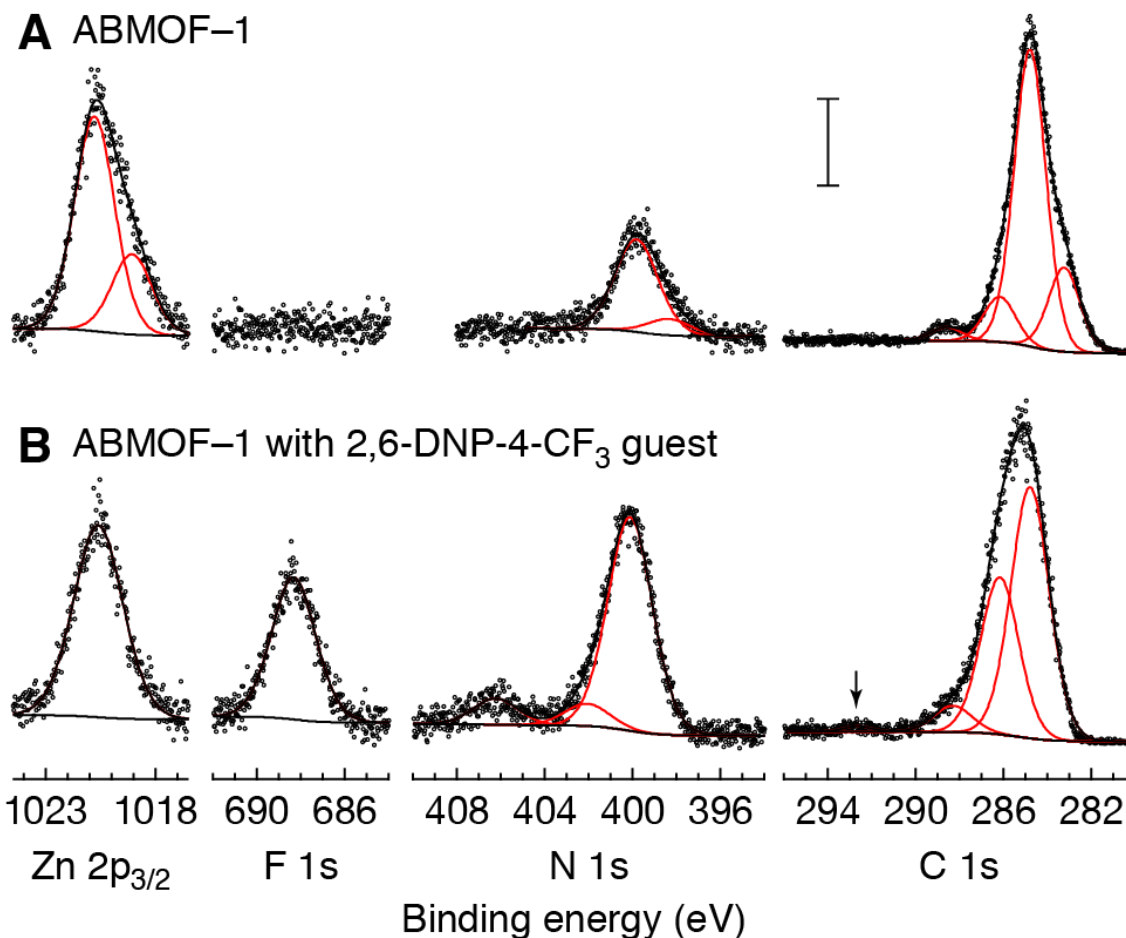


Figure 3.7. XPS spectra of representative ABMOF-1 samples both (A) with no guest exposure, and (B) following exposure to the 2,6-dinitro-4-trifluoromethyl-phenol (2,6-DNP-4-CF₃) guest. The F 1s region demonstrates no visible features for a non-exposed sample and strong features ascribed to fluorine in the CF₃ group for the ABMOF-1 following 2,6-DNP-4-CF₃ guest exposure. Additional features in frame B include a N 1s feature ascribed to a nitro species at 406.5 eV and a C 1s feature due to carbon in a CF₃ group at 292.5 eV (arrow). The vertical scale bar represents 100 counts per second (cps) for the Zn 2p_{3/2}, F 1s, and N 1s regions, and 300 cps for the C 1s regions in both frames. We attribute to the satellite fits in frame A to non-homogeneous charge neutralization of the insulating MOF sample.

background signal in the portion of the N 1s region that would be ascribable to the nitro groups of the guest. Separately, we observed rapid sublimation of 2,4-DNP under analogous vacuum conditions similar to those encountered in the XPS load lock. The rapid sublimation 2,4-DNP, and

the of lack of observable, unique chemical states for 2,4-DNP-treated ABMOF-1 implies only weak physisorption of the guest but cannot provide insight into adsorption vs intercalation behavior. As the 2,4-DNP did not demonstrate sufficiently strong interactions with the ABMOF-1 substrate, we explored other emission-quenching guest molecules with unique chemical features for photoelectron analyses.

Unlike 2,4-DNP, the fluorinated 2,6-DNP-4-CF₃ guest does not desorb from ABMOF-1 under vacuum and is detectable with photoelectron spectroscopy. Like 2,4-DNP however, 2,6-DNP-4-CF₃ quenches ABMOF-1 emission as presented and does not perturb the ABMOF-1 structure as determined by PXRD. By inducing a similar luminescent response while containing three fluorine atoms per molecule that impart an intense and chemically distinct signal in photoelectron spectra,²⁵ 2,6-DNP-4-CF₃ provides a convenient and attractive guest molecule to probe adsorption vs intercalation interactions with ABMOF-1.

The high-resolution XP spectra of ABMOF-1 in the absence or presence of 2,6-DNP-4-CF₃ exhibit distinct peaks characteristic of the elemental composition (Figure 3.7). Each spectrum displays the experimentally measured peaks corresponding to electrons originating from the Zn 2p_{3/2}, F 1s, N 1s, and C 1s regions (black) and the modeled fits of the data (red). Spectra of guest-free ABMOF-1 reveal features attributed to Zn²⁺ at ~1021 eV, the azo nitrogen atoms at ~400 eV, and carboxylate carbon atoms at ~289 eV; whereas, only non-fittable background signal were observed in the F 1s region (Figure 3.7A). Each of the largest fitted peaks corresponding to the Zn 2p_{3/2}, N 1s, and C 1s regions also possess a smaller satellite feature at an approximately 3 eV lower binding energy with comparable area ratios to each of the large fitted peaks. We ascribe each of these satellites to an artifact of non-homogeneous charging on the ABMOF-1 surface that results in a similarly non-homogeneous charge compensation by the neutralizer. Therefore, the satellite

features do not represent distinct chemical features in the photoelectron spectra. Both the aromatic carbon atoms and adventitiously adsorbed carbon species contribute to the large feature in the C 1s region in a manner that prohibits rigorous interpretation.

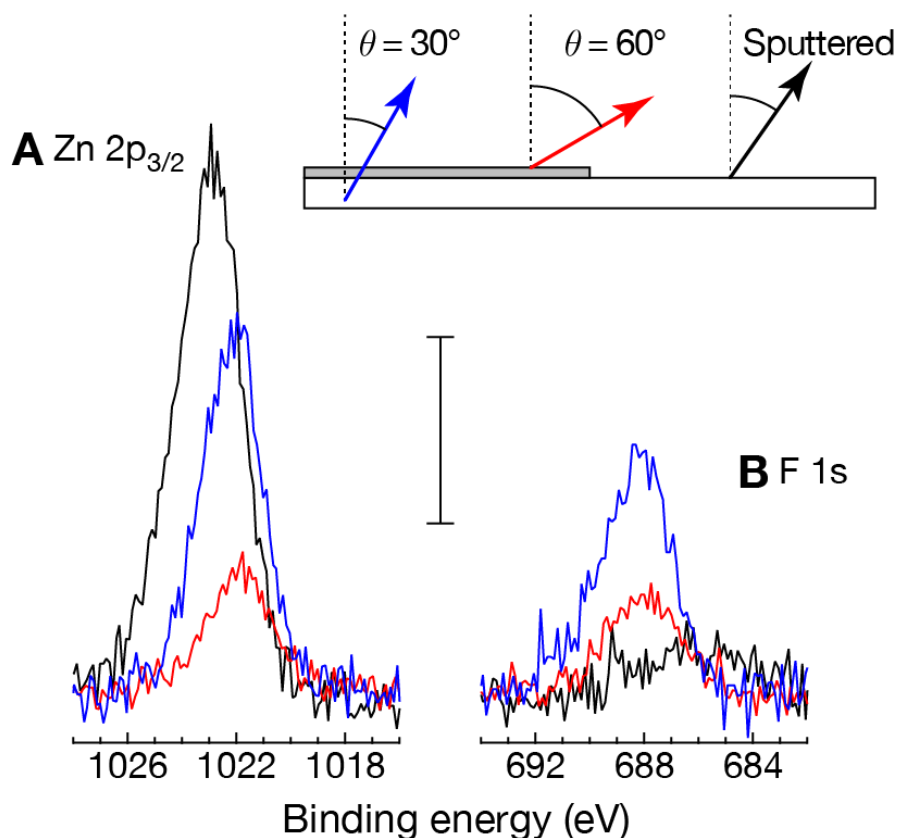


Figure 3.8. XP spectra of the (A) Zn $2p_{3/2}$, and (B) F $1s$ regions for ABMOF-1 samples exposed to 2,6-DNP-4- CF_3 . In both frames, the blue traces correspond to photoelectron take-off angles of 30° with respect to the surface normal that is a comparatively bulk-sensitive angle. The red traces correspond to photoelectron take-off angles of 60° , which is a more surface-sensitive angle as compared to the 30° results. Lastly, the black traces correspond to photoelectron signals following a brief argon-ion sputter to remove near-interfacial species. This combination of results demonstrates that the signals due to fluorine are present closer to the sample surface relative to the signals due to Zn^{2+} . We interpret the more surface-localized nature of the fluorine signals to result from 2,6-DNP-4- CF_3 that is adsorbed onto rather than intercalated into the ABMOF-1 substrate. The scale bar represents 100 cps for both frames.

Upon the introduction of 2,6-DNP-4-CF₃, the spectra of ABMOF-1 no longer contains the charging artifacts present in the guest-free spectra; however, the spectra do exhibit features ascribable to the guest molecule (Figure 3.7B). Specifically, the F 1s region shows a strong feature due to photoelectron emission from the three fluorine atoms on the trifluoromethyl group of the guest molecule. Similarly, the N 1s spectrum reveals a feature towards higher binding energy at ~406.5 that we assign to the nitro-group nitrogen atoms of 2,6-DNP-4-CF₃. In addition to these new features, the fluorine atoms in the -CF₃ moiety shift the photoelectron emission corresponding to that carbon atom towards higher binding energy as revealed by the small feature at approximately 292.5 eV in the C 1s spectrum. Collectively, these results demonstrate an association between the 2,6-DNP-4-CF₃ guest and the ABMOF-1 substrate; however, further photoelectron analyses are required to elucidate the adsorption vs intercalation nature of the guest-MOF interaction.

Both the Zn 2p_{3/2} and F 1s regions in the spectra of 2,6-DNP-4-CF₃-exposed ABMOF-1 change noticeably due to collection of the photoelectrons at different angles, and following argon-ion sputtering. Figure 3.8 shows spectra that are representative of acquisitions on multiple 2,6-DNP-4-CF₃-exposed ABMOF-1 samples. The blue traces in both frames represent photoelectron signals collected at 30° with respect to the surface normal angle while the red traces represent signals collected at 60° for 2,6-DNP-4-CF₃-exposed ABMOF-1 samples. Since the probability for photoelectron escape (5-10 nm)²³ –given by an attenuation length that is related to the inelastic mean free path–decreases exponentially with depth below the sample surface, the electrons generated more deeply in the sample have a decreased probability of reaching the detector relative to electrons generated at shallow depths.²³ When photoelectrons are collected at higher angles with respect to the surface normal, they must travel through more material to escape and have a

decreased probability of escape relative to electrons collected at angles closer to the surface normal. Thus, the spectra collected at 30° are more sensitive to content of the bulk material when compared to spectra that are collected at 60°, which are more surface sensitive. Considering a ratio of area intensities for the F 1s that is a proxy for the 2,6-DNP-4-CF₃ guest and the Zn 2p_{3/2} intensity that is a proxy for ABMOF-1, an $I_{\text{F } 1s}/I_{\text{Zn } 2p_{3/2}}$ ratio would demonstrate no angle dependence for homogeneously intercalated guests while the ratio would increase with increasing angle for surface-adsorbed guests. The photoelectron spectra collected at 30° in Fig. 5 (blue) demonstrate $I_{\text{F } 1s}/I_{\text{Zn } 2p_{3/2}} = 857 \text{ cps} / 1178 \text{ cps} = 0.73$, while the spectra collected at 60° (red) demonstrate $I_{\text{F } 1s}/I_{\text{Zn } 2p_{3/2}} = 403 \text{ cps} / 382 \text{ cps} = 1.1$. The increase in the F 1s-to-Zn 2p_{3/2} peak area ratio at 60° relative to 30° indicates that the fluorine atoms are physically situated closer to the sample surface relative to the Zn²⁺ atoms.

Photoelectron scans following argon-ion sputtering further reveal the physical relationship between the fluorine atoms and the Zn²⁺ atoms (Figure 3.8). Sputter conditions yield a sample bombardment of 3.5 keV Ar⁺ ions for six seconds. Calibration studies from our lab indicate that these sputtering conditions remove approximately 2–5 monolayers of adsorbed species on substrates under study. The resulting Zn 2p_{3/2} trace (black) following Ar⁺ sputtering demonstrates a significantly larger intensity compared to the Zn 2p_{3/2} features collected at either 30° or 60° in the absence of sputter cleaning. In contrast to the Zn 2p_{3/2} signals, the resulting F 1s signals following sputtering are greatly attenuated relative to the F 1s data collected at 30° or 60° in the absence of sputtering. The increase of the Zn 2p_{3/2} suggests the removal of species above the layer that contains the Zn²⁺ atoms, which had attenuated the Zn 2p_{3/2} signals before sputtering. The decrease of the F 1s signal indicates the fluorine atoms were principally localized in the top 2–5 monolayers of species that were sputtered away due to Ar⁺ bombardment; therefore, the

combination of angle-resolved XPS and argon-ion sputtering results reveal that the fluorine atoms are localized in the near interfacial layers of the sample, while the Zn^{2+} atoms are localized in the bulk material. A model consistent with the photoelectron data is the surface adsorption of 2,6-DNP-4- CF_3 guest on the ABMOF-1 substrate. If the guest molecule had intercalated into the ABMOF-1 network, we would have observed no relative change in the Zn^{2+} to fluorine signals.

3.5. Conclusions

Embedding azobenzene struts into rigid MOF structures can lead to emission from the chromophore instead of dissipation of excitation energy via non-radiative pathways. ABMOF-1 and ABMOF-2 are the first emissive MOFs containing azobenzene fluorophores, but only ABMOF-1 responds significantly to various nitroaromatic analytes. Based on the similarity of the emission response to other luminescent MOF systems and the pore sizes that preclude guest encapsulation, we reasoned that ABMOF-1 would be a valuable test case to evaluate XPS as an analytical technique to detect surface adsorbed species. Different from optical spectroscopies and other techniques, the interfacial sensitivity of XPS can elucidate the presence specific chemical species and states on a material surface with a sub-monolayer limit of detection. Although we are conducting additional studies understand the atomic level interactions at the surface, an association between the guest and the ABMOF-1 substrate has been demonstrated by high-resolution XPS showing strong features of guest-associated fluorine atoms, as well as the energy level shifting of nitrogen and carbon photoelectron emission, sustaining as a novel way to characterize surface-associated nitroaromatic guests on MOFs. Angle-resolved and argon-ion sputtering XPS further indicate guests are physically situated closer to the sample surface. The study of MOF-guest interaction by collecting XPS data at different angles and sputtering several surface monolayers provide a new method to study host-guest interaction on MOF or other coordination polymers.

3.6. Acknowledgement

This chapter is based on joint work with Dr. Ronald L. Grimm and Alexander D. Carl at Department of Chemistry and Biochemistry, Worcester Polytechnic Institute. The X-ray photoelectron spectroscopy (XPS) of ABMOF-1 before and after quenching, and the XP spectra at different angles and after argon-ion sputtering were done by Alexander D. Carl with the guidance of Dr. Ronald L. Grimm.

The solving and refinement of ABMOF-2 crystal structure was accomplished with the assistance from Dr. Peter Müller at X-Ray Diffraction Facility, Chemistry Department, Massachusetts Institute of Technology (MIT).

Table 3.1. Crystal data and structure refinements for ABMOF-1.

Compound	$\{\text{Zn}_2(\text{NDC})_2(\text{AzoAE}p\text{P}) \cdot 2\text{DMF}\}_n$
Formula	$\text{C}_{56}\text{H}_{52}\text{N}_8\text{O}_{10}\text{Zn}_2$
Formula weight (g mol ⁻¹)	1127.84
Crystal size	1.00 × 0.75 × 0.15
Crystal system	Monoclinic
Color	Orange-red
Space group	P2 ₁ /c
a/Å	12.1475
b/Å	15.602
c/Å	14.578
α/°	90.00
β/°	99.566
γ/°	90.00
Volume/Å ³	2724.5
Z	4
Temp, K	296 (2)
ρ _{calc} /cm ³	1.375
Radiation	Mo Kα (λ = 0.71073 Å)
2θ range for data collection/°	4.82 to 66.26
Index ranges	-18 ≤ h ≤ 18, -23 ≤ k ≤ 23, -19 ≤ l ≤ 22
Reflections collected	39345
Independent reflections	10334
Observed reflections	8084
R	0.0403
wR2	0.1439
no. of parameters	345
Goodness-of-fit on F2	1.056

Table 3.2. Crystal data and structure refinements for ABMOF-2.

Compound	$\{\text{Zn}_2(\text{BDC})_2(\text{AzoAE}p\text{P})\}_n$
Formula	$\text{C}_{50}\text{H}_{40}\text{N}_6\text{O}_8\text{Zn}$
Formula weight (g mol^{-1})	918.25
Crystal size	$0.25 \times 0.18 \times 0.01$
Crystal system	Monoclinic
Color	Orange
Space group	$C 1 2/m 1$
$a/\text{\AA}$	15.730(3)
$b/\text{\AA}$	15.100(3)
$c/\text{\AA}$	10.023(2)
$\alpha/^\circ$	90.00
$\beta/^\circ$	119.21(3)
$\gamma/^\circ$	90.00
Volume/ \AA^3	2078.0(9)
Z	2
Temp, K	100 (2)
$\rho_{\text{calc}}/\text{cm}^3$	1.468
Radiation	Mo $K\alpha$ ($\lambda = 0.71073\text{\AA}$)
2θ range for data collection/ $^\circ$	4.92 to 46.36
Index ranges	$-20 \leq h \leq 20$, $-16 \leq k \leq 19$, $-12 \leq l \leq 12$
Reflections collected	11989
Independent reflections	2357
Observed reflections	1825
R	0.0521
wR2	0.1397
no. of parameters	344
Goodness-of-fit on F2	1.090

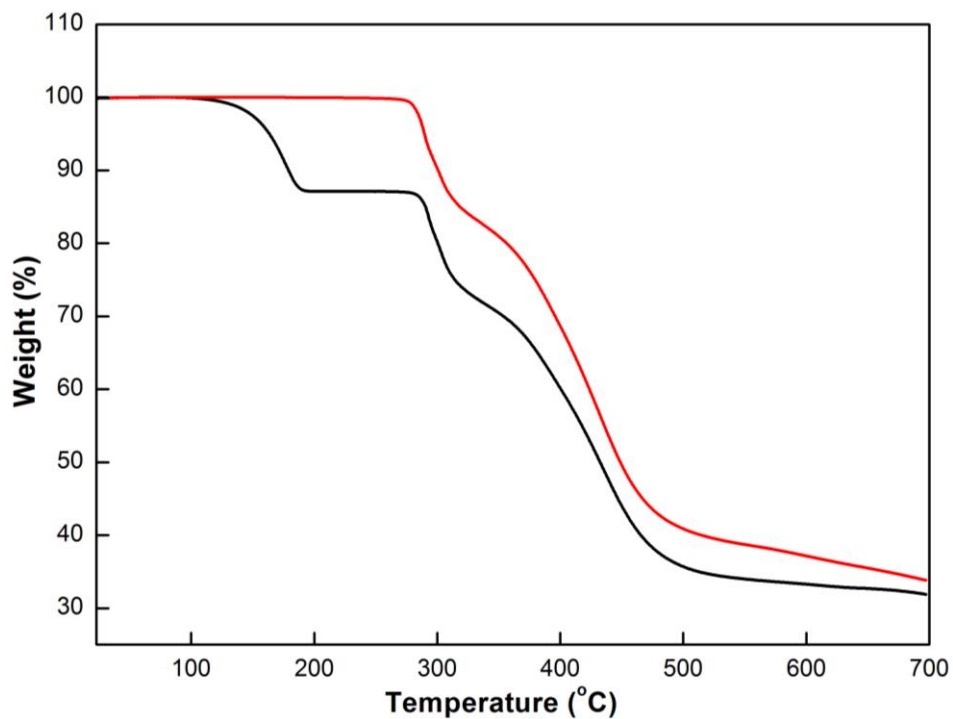


Figure 3.9. Thermogravimetric analysis (TGA) diagrams of fresh prepared (black) and activated (red) ABMOF-1.

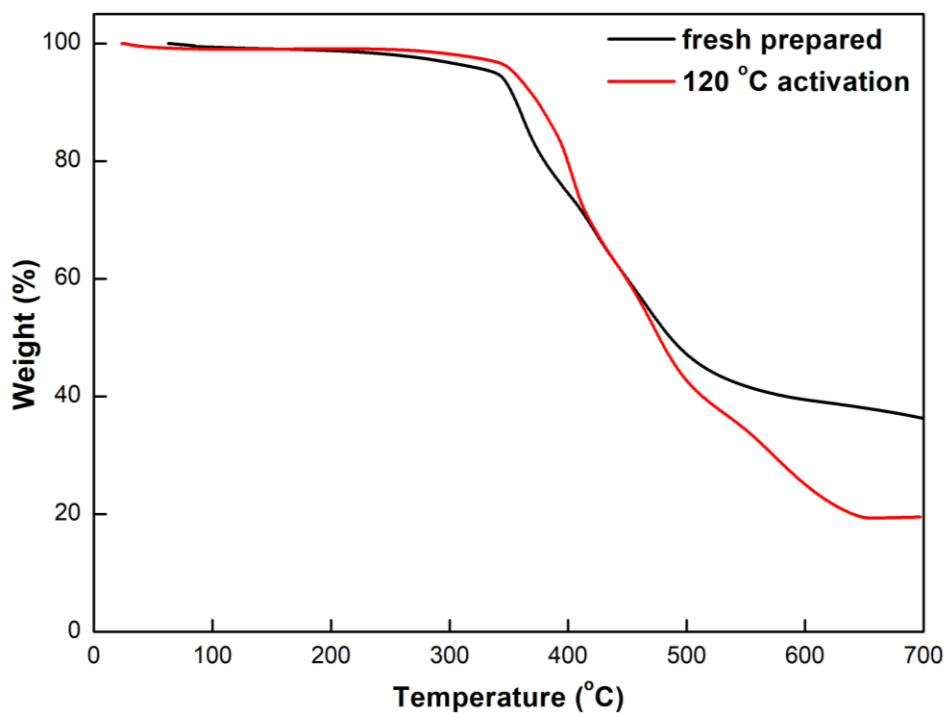


Figure 3.10. Thermogravimetric analysis (TGA) diagrams of fresh prepared (black) and activated (red) ABMOF-2.

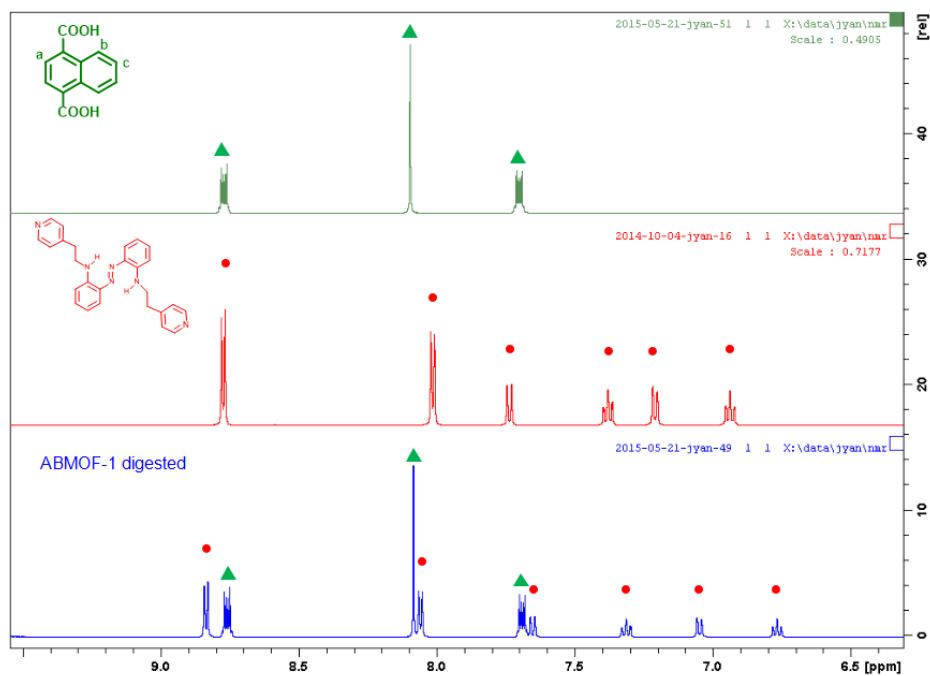


Figure 3.11. Digested NMR of ABMOF-1, comparing with original ligands NDC and AzoAEpP.

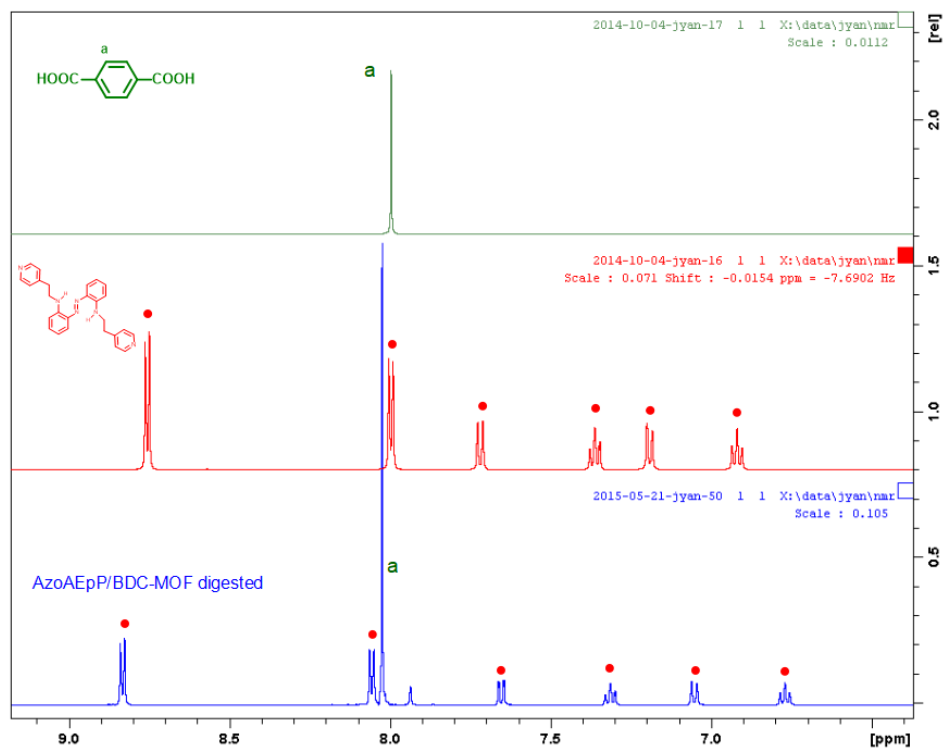


Figure 3.12. Digested NMR of ABMOF-2, comparing with original ligands BDC and AzoAEpP.

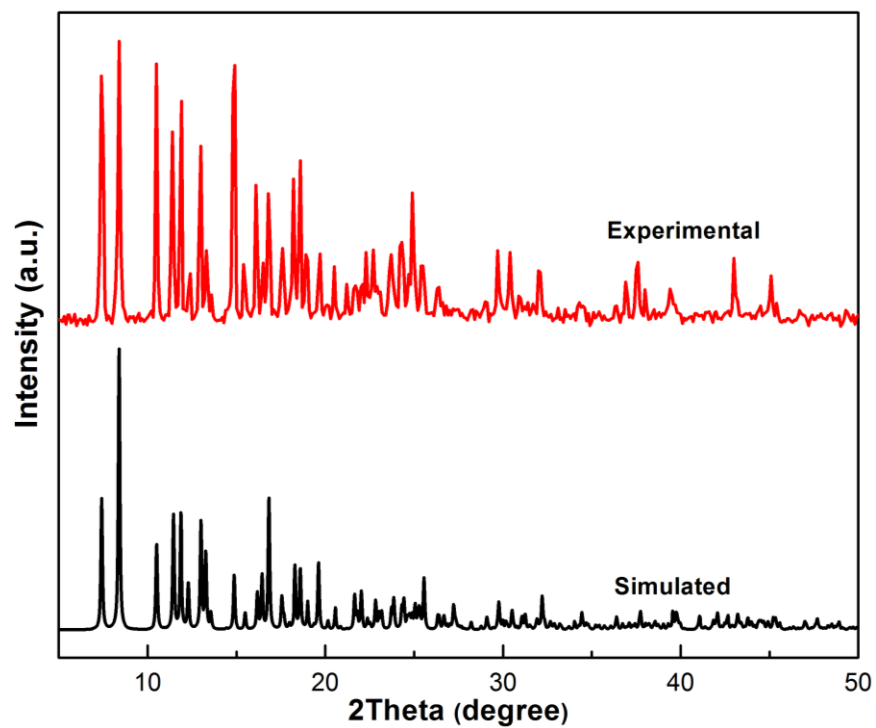


Figure 3.13. Powder X-ray diffraction patterns of ABMOF-1. Both experimental and simulated patterns from single crystal structures are shown to confirm the phase purity.

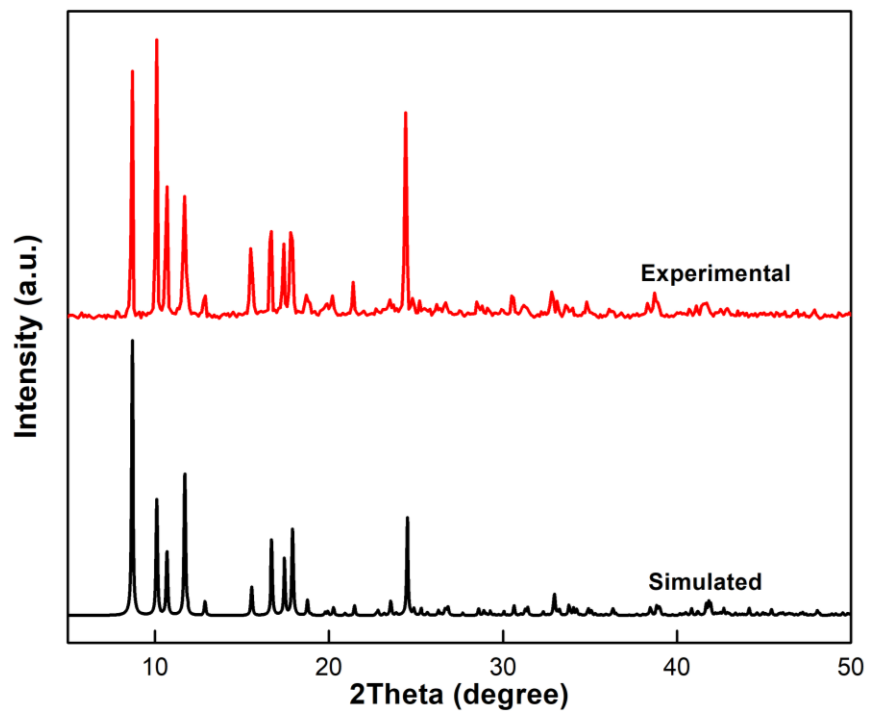


Figure 3.14. Powder X-ray diffraction patterns of ABMOF-2. Both experimental and simulated patterns from single crystal structures are shown to confirm the phase purity.

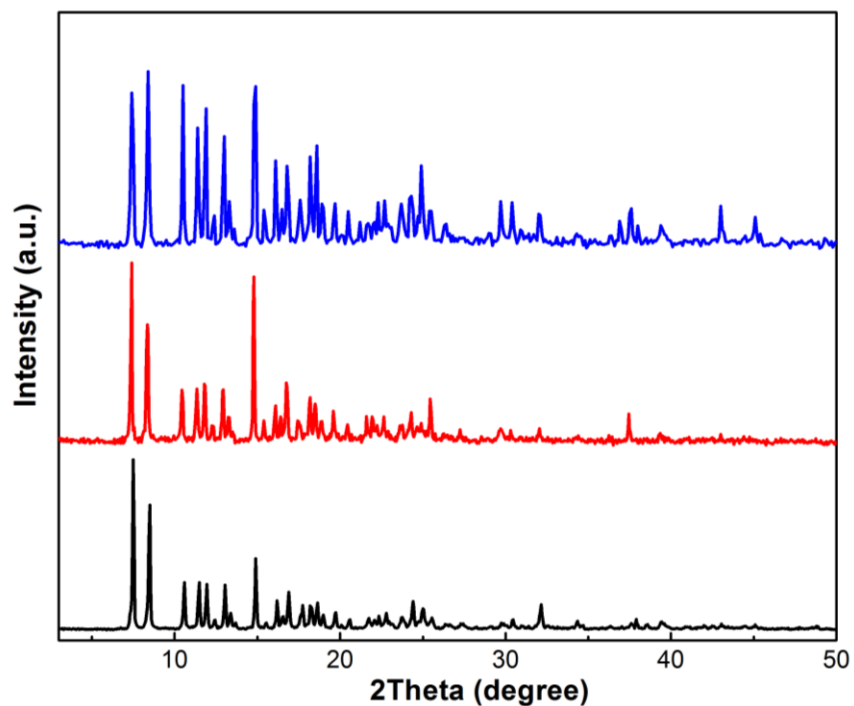


Figure 3.15. PXRD diffraction patterns of ABMOF-1 (black) and after quenching with 2,4-DNP (red) and 2,6-DNP-4-CF₃ (blue). The nearly identical patterns confirm no significant change of MOF structure after quenching.

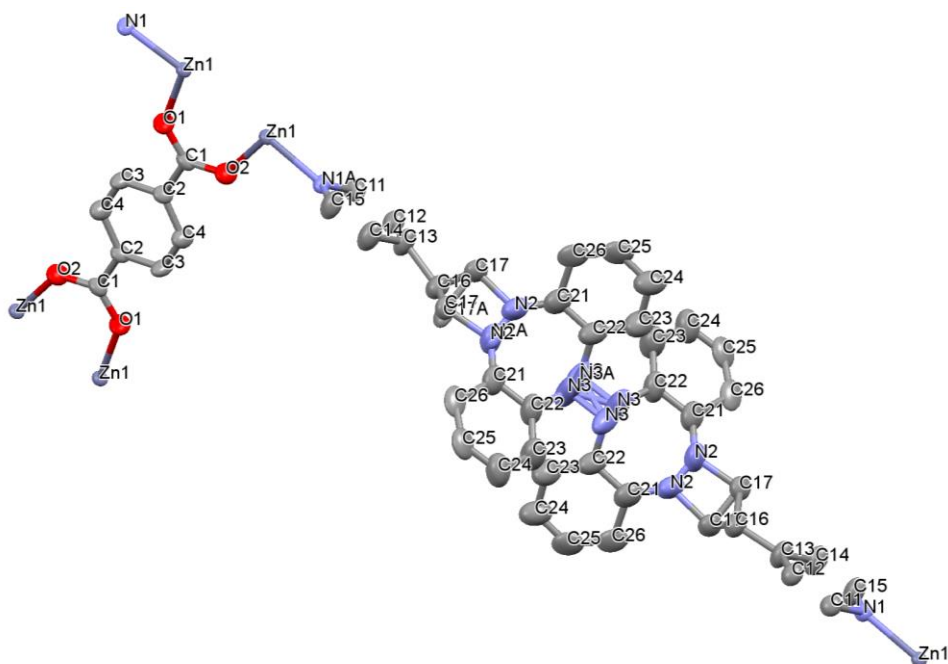


Figure 3.16. Completely labeled ORTEP plot of 50% thermal ellipsoids for ABMOF-2, showing highly disordered on the AzoAEP ligand.

3.7. References

- (1) Lan, A. J.; Li, K. H.; Wu, H. H.; Olson, D. H.; Emge, T. J.; Ki, W.; Hong, M. C.; Li, J. A Luminescent Microporous Metal-Organic Framework for the Fast and Reversible Detection of High Explosives. *Angew. Chem., Int. Ed.* **2009**, *48*, 2334-2338.
- (2) Nagarkar, S. S.; Joarder, B.; Chaudhari, A. K.; Mukherjee, S.; Ghosh, S. K. Highly Selective Detection of Nitro Explosives by a Luminescent Metal-Organic Framework. *Angew. Chem., Int. Ed.* **2013**, *52*, 2881-2885.
- (3) Hu, Z. C.; Deibert, B. J.; Li, J. Luminescent Metal-Organic Frameworks for Chemical Sensing and Explosive Detection. *Chem. Soc. Rev.* **2014**, *43*, 5815-5840.
- (4) Shustova, N. B.; McCarthy, B. D.; Dinca, M. Turn-on Fluorescence in Tetraphenylethylene-Based Metal-Organic Frameworks: An Alternative to Aggregation-Induced Emission. *J. Am. Chem. Soc.* **2011**, *133*, 20126-20129.
- (5) Lee, C. Y.; Farha, O. K.; Hong, B. J.; Sarjeant, A. A.; Nguyen, S. T.; Hupp, J. T. Light-Harvesting Metal-Organic Frameworks (MOFs): Efficient Strut-to-Strut Energy Transfer in Bodipy and Porphyrin-Based MOFs. *J. Am. Chem. Soc.* **2011**, *133*, 15858-15861.
- (6) Gole, B.; Bar, A. K.; Mukherjee, P. S. Fluorescent Metal-Organic Framework for Selective Sensing of Nitroaromatic Explosives. *Chem. Commun.* **2011**, *47*, 12137-12139.
- (7) Lu, Z. Z.; Zhang, R.; Li, Y. Z.; Guo, Z. J.; Zheng, H. G. Solvatochromic Behavior of a Nanotubular Metal-Organic Framework for Sensing Small Molecules. *J. Am. Chem. Soc.* **2011**, *133*, 4172-4174.
- (8) Zou, X. Q.; Zhu, G. S.; Hewitt, I. J.; Sun, F. X.; Qiu, S. L. Synthesis of a Metal-Organic Framework Film by Direct Conversion Technique for VOCs Sensing. *Dalton Trans.* **2009**, 3009-3013.

- (9) Zhang, Z. J.; Xiang, S. C.; Rao, X. T.; Zheng, Q. A.; Fronczek, F. R.; Qian, G. D.; Chen, B. L. A Rod Packing Microporous Metal-Organic Framework with Open Metal Sites for Selective Guest Sorption and Sensing of Nitrobenzene. *Chem. Commun.* **2010**, *46*, 7205-7207.
- (10) Tian, D.; Li, Y.; Chen, R. Y.; Chang, Z.; Wang, G. Y.; Bu, X. H. A Luminescent Metal-Organic Framework Demonstrating Ideal Detection Ability for Nitroaromatic Explosives. *J. Mater. Chem. A* **2014**, *2*, 1465-1470.
- (11) Shimomura, S.; Horike, S.; Matsuda, R.; Kitagawa, S. Guest-Specific Function of a Flexible Undulating Channel in a 7,7,8,8-Tetracyano-*p*-quinodimethane Dimer-Based Porous Coordination Polymer. *J. Am. Chem. Soc.* **2007**, *129*, 10990-10991.
- (12) Alaerts, L.; Kirschhock, C. E. A.; Maes, M.; van der Veen, M. A.; Finsy, V.; Depla, A.; Martens, J. A.; Baron, G. V.; Jacobs, P. A.; Denayer, J. E. M.; De Vos, D. E. Selective Adsorption and Separation of Xylene Isomers and Ethylbenzene with the Microporous Vanadium(IV) Terephthalate MIL-47. *Angew. Chem., Int. Ed.* **2007**, *46*, 4293-4297.
- (13) Lin, X.; Blake, A. J.; Wilson, C.; Sun, X. Z.; Champness, N. R.; George, M. W.; Hubberstey, P.; Mokaya, R.; Schroder, M. A Porous Framework Polymer Based on a Zinc(II) 4,4'-Bipyridine-2,6,2',6'-Tetracarboxylate: Synthesis, Structure, and "Zeolite-Like" Behaviors. *J. Am. Chem. Soc.* **2006**, *128*, 10745-10753.
- (14) Takashima, Y.; Martinez, V. M.; Furukawa, S.; Kondo, M.; Shimomura, S.; Uehara, H.; Nakahama, M.; Sugimoto, K.; Kitagawa, S. Molecular Decoding Using Luminescence from an Entangled Porous Framework. *Nat. Commun.* **2011**, *2*, 168.
- (15) Zhao, Z. X.; Li, X. M.; Huang, S. S.; Xia, Q. B.; Li, Z. Adsorption and Diffusion of Benzene on Chromium-Based Metal Organic Framework MIL-101 Synthesized by Microwave Irradiation. *Ind. Eng. Chem. Res.* **2011**, *50*, 2254-2261.

- (16) Greathouse, J. A.; Ockwig, N. W.; Criscenti, L. J.; Guilinger, T. R.; Pohl, P.; Allendorf, M. D. Computational Screening of Metal-Organic Frameworks for Large-Molecule Chemical Sensing. *Phys. Chem. Chem. Phys.* **2010**, *12*, 12621-12629.
- (17) Gao, G. H.; Li, S. J.; Li, S.; Wang, Y. D.; Zhao, P.; Zhang, X. Y.; Hou, X. H. A Combination of Computational - Experimental Study on Metal-Organic Frameworks MIL-53(Al) as Sorbent for Simultaneous Determination of Estrogens and Glucocorticoids in Water and Urine Samples by Dispersive Micro-Solid-Phase Extraction Coupled to UPLC-MS/MS. *Talanta* **2018**, *180*, 358-367.
- (18) Zhao, X. L.; Liu, S. L.; Tang, Z.; Niu, H. Y.; Cai, Y. Q.; Meng, W.; Wu, F. C.; Giesy, J. P. Synthesis of Magnetic Metal-Organic Framework (MOF) for Efficient Removal of Organic Dyes from Water. *Sci. Rep.* **2015**, *5*, 11849.
- (19) Duke, A. S.; Dolgoplova, E. A.; Galhenage, R. P.; Ammal, S. C.; Heyden, A.; Smith, M. D.; Chen, D. A.; Shustova, N. B. Active Sites in Copper-Based Metal-Organic Frameworks: Understanding Substrate Dynamics, Redox Processes, and Valence-Band Structure. *J. Phys. Chem. C* **2015**, *119*, 27457-27466.
- (20) Taher, A.; Kim, D. W.; Lee, I. M. Highly Efficient Metal Organic Framework (MOF)-Based Copper Catalysts for the Base-Free Aerobic Oxidation of Various Alcohols. *Rsc. Adv.* **2017**, *7*, 17806-17812.
- (21) Shi, L.; Wang, T.; Zhang, H. B.; Chang, K.; Meng, X. G.; Liu, H. M.; Ye, J. H. An Amine - Functionalized Iron(III) Metal-Organic Framework as Efficient Visible-Light Photocatalyst for Cr(VI) Reduction. *Adv. Sci.* **2015**, *2*, 1500006.
- (22) Ebel, M. F. Determination of Reduced Thickness D-Lambda of Thin-Layers by means of X-Ray Photoelectron-Spectroscopy. *J. Electron. Spectrosc. Relat. Phenom.* **1978**, *14*, 287-322.

- (23) Fadley, C. S. Solid State– and Surface–Analysis by means of Angular-Dependent X-Ray Photoelectron Spectroscopy. *Prog. Solid State Chem.* **1976**, *11*, 265-343.
- (24) Yan, J. J.; Wilbraham, L.; Basa, P. N.; Shuettel, M.; MacDonald, J. C.; Ciofini, I.; Coudert, F. X.; Burdette, S. C. Emissive Azobenzenes Delivered on a Silver Coordination Polymer. *Manuscript submitted* **2018**.
- (25) Moulder, J. F.; Stickle, W. F.; Sobol, P. E.; Bomben, K. D. *Handbook of X-Ray Photoelectron Spectroscopy*; Physical Electronics Division: Perkin-Elmer Corporation: Eden Prairie, MN, 1993.
- (26) Sheldrick, G. M. *Sadabs*; University of Göttingen: Göttingen, Germany, 1996.
- (27) Sheldrick, G. M. Crystal Structure Refinement with SHELXL. *Acta Crystallogr. C Struct. Chem.* **2015**, *71*, 3-8.
- (28) Wrighton, M. S.; Ginley, D. S.; Morse, D. L. Technique for Determination of Absolute Emission Quantum Yields of Powdered Samples. *J. Phys. Chem.* **1974**, *78*, 2229-2233.
- (29) Carl, A. D.; Kalan, R. E.; Obayemi, J. D.; Kana, M. G. Z.; Soboyejo, W. O.; Grimm, R. L. Synthesis and Characterization of Alkylamine-Functionalized Si(111) for Perovskite Adhesion with Minimal Interfacial Oxidation or Electronic Defects. *Acs Appl. Mater. Interfaces* **2017**, *9*, 34377-34388.
- (30) Shirley, D. A. High-Resolution X-Ray Photoemission Spectrum of Valence Bands of Gold. *Phys. Rev. B* **1972**, *5*, 4709-4714.
- (31) Fairley, N. Peak Fitting in XPS. http://www.casaxps.com/help_manual/manual_updates/peak_fitting_in_xps.pdf (accessed May 18 2017).
- (32) Tougaard, S. Universality Classes of Inelastic Electron Scattering Cross-Sections. *Surf. Interface Anal.* **1997**, *25*, 137-154.

- (33) Ma, B. Q.; Mulfort, K. L.; Hupp, J. T. Microporous Pillared Paddle-Wheel Frameworks Based on Mixed-Ligand Coordination of Zinc Ions. *Inorg. Chem.* **2005**, *44*, 4912-4914.
- (34) Chen, B. L.; Ma, S. Q.; Hurtado, E. J.; Lobkovsky, E. B.; Zhou, H. C. A Triply Interpenetrated Microporous Metal-Organic Framework for Selective Sorption of Gas Molecules. *Inorg. Chem.* **2007**, *46*, 8490-8492.
- (35) Gadzikwa, T.; Farha, O. K.; Mulfort, K. L.; Hupp, J. T.; Nguyen, S. T. A Zn-Based, Pillared Paddlewheel MOF Containing Free Carboxylic Acids via Covalent Post-Synthesis Elaboration. *Chem. Commun.* **2009**, 3720-3722.
- (36) Bury, W.; Fairen-Jimenez, D.; Lalonde, M. B.; Snurr, R. Q.; Farha, O. K.; Hupp, J. T. Control over Catenation in Pillared Paddlewheel Metal-Organic Framework Materials via Solvent-Assisted Linker Exchange. *Chem. Mater.* **2013**, *25*, 739-744.
- (37) Kesanli, B.; Cui, Y.; Smith, M. R.; Bittner, E. W.; Bockrath, B. C.; Lin, W. B. Highly Interpenetrated Metal-Organic Frameworks for Hydrogen Storage. *Angew. Chem., Int. Ed.* **2005**, *44*, 72-75.
- (38) Spek, A. L. Single-Crystal Structure Validation with the Program Platon. *J. Appl. Crystallogr.* **2003**, *36*, 7-13.
- (39) Chen, B. L.; Liang, C. D.; Yang, J.; Contreras, D. S.; Clancy, Y. L.; Lobkovsky, E. B.; Yaghi, O. M.; Dai, S. A Microporous Metal-Organic Framework for Gas-Chromatographic Separation of Alkanes. *Angew. Chem., Int. Ed.* **2006**, *45*, 1390-1393.
- (40) Chen, B. L.; Ma, S. Q.; Zapata, F.; Lobkovsky, E. B.; Yang, J. Hydrogen Adsorption in an Interpenetrated Dynamic Metal-Organic Framework. *Inorg. Chem.* **2006**, *45*, 5718-5720.

- (41) Horcajada, P.; Serre, C.; Vallet-Regi, M.; Sebban, M.; Taulelle, F.; Ferey, G. Metal-Organic Frameworks as Efficient Materials for Drug Delivery. *Angew. Chem., Int. Ed.* **2006**, *45*, 5974-5978.
- (42) Chun, H.; Dybtsev, D. N.; Kim, H.; Kim, K. Synthesis, X-Ray Crystal Structures, and Gas Sorption Properties of Pillared Square Grid Nets Based on Paddle-Wheel Motifs: Implications for Hydrogen Storage in Porous Materials. *Chem.-Eur. J.* **2005**, *11*, 3521-3529.
- (43) Shultz, A. M.; Farha, O. K.; Hupp, J. T.; Nguyen, S. T. A Catalytically Active, Permanently Microporous MOF with Metalloporphyrin Struts. *J. Am. Chem. Soc.* **2009**, *131*, 4204-4205.
- (44) Hartlieb, K. J.; Ferris, D. P.; Holcroft, J. M.; Kandela, I.; Stern, C. L.; Nassar, M. S.; Botros, Y. Y.; Stoddart, J. F. Encapsulation of Ibuprofen in Cd-MOF and Related Bioavailability Studies. *Mol. Pharm.* **2017**, *14*, 1831-1839.
- (45) Santra, A.; Francis, M.; Parshamoni, S.; Konar, S. Nanoporous Cu(I) Metal-Organic Framework: Selective Adsorption of Benzene and Luminescence Sensing of Nitroaromatics. *Chemistryselect* **2017**, *2*, 3200-3206.
- (46) Qin, W. P.; Cao, W. X.; Liu, H. L.; Li, Z.; Li, Y. W. Metal-Organic Framework MIL-101 Doped with Palladium for Toluene Adsorption and Hydrogen Storage. *Rsc. Adv.* **2014**, *4*, 2414-2420.
- (47) Ugale, B.; Dhankhar, S. S.; Nagaraja, C. M. Interpenetrated Metal-Organic Frameworks of Cobalt(II): Structural Diversity, Selective Capture, and Conversion of CO₂. *Cryst. Growth Des.* **2017**, *17*, 3295-3305.
- (48) Cai, J. F.; Yu, J. C.; Xu, H.; He, Y. B.; Duan, X.; Cui, Y. J.; Wu, C. D.; Chen, B. L.; Qian, G. D. A Doubly Interpenetrated Metal-Organic Framework with Open Metal Sites and Suitable Pore

Sizes for Highly Selective Separation of Small Hydrocarbons at Room Temperature. *Cryst. Growth Des.* **2013**, *13*, 2094-2097.

(49) Asha, K. S.; Bhattacharyya, K.; Mandal, S. Discriminative Detection of Nitro Aromatic Explosives by a Luminescent Metal-Organic Framework. *J. Mater. Chem. C* **2014**, *2*, 10073-10081.

(50) Li, X.; Yang, L.; Zhao, L.; Wang, X. L.; Shao, K. Z.; Su, Z. M. Luminescent Metal-Organic Frameworks with Anthracene Chromophores: Small-Molecule Sensing and Highly Selective Sensing for Nitro Explosives. *Cryst. Growth Des.* **2016**, *16*, 4374-4382.

(51) Song, X. Z.; Song, S. Y.; Zhao, S. N.; Hao, Z. M.; Zhu, M.; Meng, X.; Wu, L. L.; Zhang, H. J. Single-Crystal-to-Single-Crystal Transformation of a Europium(III) Metal-Organic Framework Producing a Multi-Responsive Luminescent Sensor. *Adv. Funct. Mater.* **2014**, *24*, 4034-4041.

(52) Nagarkar, S. S.; Desai, A. V.; Ghosh, S. K. A Fluorescent Metal-Organic Framework for Highly Selective Detection of Nitro Explosives in the Aqueous Phase. *Chem. Commun.* **2014**, *50*, 8915-8918.

(53) Zhang, M. H.; Zhang, L. L.; Xiao, Z. Y.; Zhang, Q. H.; Wang, R. M.; Dai, F. N.; Sun, D. F. Pentiptycene-Based Luminescent Cu (II) MOF Exhibiting Selective Gas Adsorption and Unprecedentedly High-Sensitivity Detection of Nitroaromatic Compounds (NACs). *Sci. Rep.* **2016**, *6*, 20672.

(54) Banerjee, D.; Hu, Z. C.; Li, J. Luminescent Metal-Organic Frameworks as Explosive Sensors. *Dalton Trans.* **2014**, *43*, 10668-10685.

**Chapter 4 MOF Decomposition and Introduction of
Repairable Defects Using a Photodegradable Strut**

4.1. Introduction

The large void spaces and high surface areas within metal-organic frameworks (MOFs) make them appealing for a wide variety of storage, sequestration and separation applications;^{1,2} however, most MOFs are permanent structures incapable of responding to external stimuli. To overcome these limitations, photoactive MOF components have been explored. By incorporating azobenzene ligands onto the side chains of MOF struts, *cis*←*trans* photoisomerization can open and close access to channels;³ however, azobenzene isomerization is nearly^{4,5} or completely^{6,7} restricted in rigid materials. Moreover, photochromic diarylethene derivatives have been incorporated as MOF struts, and local framework movement can be achieved by diarylethene ring opening and closing⁸⁻¹⁰ but the framework change is minimal and MOF skeleton is retained. Alternatively, photolabile protecting groups on side chains can be removed to change the channel structure.^{11,12}

MOFs are susceptible to degradation under acidic conditions, or when exposed to strongly coordinating molecules, due to linker protonation and displacement respectively. Although these and other processes of structural breakdown are impediments in some fields, MOF decomposition can be exploited for molecular release in applications such as drug delivery.¹³ Most MOFs designed for drug delivery are engineered to respond to the acidic compartments in the cell cytoplasm or in lysosomes.^{14,15} In the absence of pH changes however, the options for triggered release of guest from MOFs are more limited.

Light degradable materials have been studied extensively,¹⁶⁻¹⁸ but there are limited examples of MOF photodecomposition. While complexes that release metal ions in response to light are somewhat common^{19,20} including photocaged complexes that release zinc upon decarboxylation,²¹ the analogous photochemistry has not been explored in MOFs.

Photodecarboxylation in a benzothiadiazole-derived MOF led to detectable structural changes and differences in gas adsorption although the experimental data for the proposed behavior not definitive,²² and an azobenzene-containing MOF reportedly degrades upon irradiation;²³ however, irradiation only accelerates the basal rate of decomposition. Local and dynamic structural modulation upon irradiation has been reported with MOFs⁴ and COFs⁵ containing photoswitchable struts; however, direct evidence for the changes are limited. Inspired by our earlier studies on molecule release triggered by photodecarboxylation of a capping on MOF surface,²⁴ we envisioned incorporating photolabile dicarboxylates as struts to facilitate photodegradation of MOFs.

4.2. Experimental Section

4.2.1. General Procedures

All reagents were purchased and used without further purification. Thin-layer chromatography (TLC) was performed on silica (200-400 mesh). TLCs were developed by using mixture of dichloromethane (DCM) and methanol (MeOH). ¹H and ¹³C NMR spectra were recorded with a 500 MHz Bruker Biospin NMR instrument. FT-IR spectra were recorded using Bruker Vertex70 Optics FT-IR spectrometer equipped with a Specac Golden Gate attenuated total reflection (ATR) accessory by collecting 256 scans over a scan range from 4000 to 600 cm⁻¹ at 4 cm⁻¹ resolution. Elemental microanalyses for C, H, and N were performed by Micro Analysis Inc. (Wilmington DE). Thermogravimetric analysis (TGA) measurements were carried out on a TA Instruments Hi-Res TGA 2950 Thermogravimetric Analyzer from room temperature to 800 °C under nitrogen atmosphere at a heating rate of 10 °C/min. LC/MS was carried on a Single Quadruple, Agilent Technologies 1200 series LC system. High resolution mass spectra were obtained at the University of Notre Dame mass spectrometry facility using microTOF instrument operating in positive

ionization mode. Melting-point information was obtained using a Hydrothermal Mel-Temp instrument.

2-Nitro-1,4-phenylenediacetic acid (NPDAC, 2). Concentrated sulfuric acid (5 mL) and *p*-phenylenediacetic acid (0.300 g, 1.54 mmol) were combined at 0 °C, and concentrated nitric acid (0.5 mL) was added dropwise to the mixture. After stirring in the dark for 1 h, the reaction mixture was added dropwise to ice (200 g), and the product was extracted into EtOAc (2 × 100 mL). The combined organic layers were washed with saturated NaCl (2 × 100 mL), dried over Na₂SO₄ and the solvent was removed to yield the product as a light-yellow powder without further purification (0.280 g, 76.1% yield). TLC R_f = 0.41 (silica, 6.5:1, DCM/MeOH). Mp = 246-248 °C. ¹H NMR (500 MHz, DMSO-*d*₆) δ 12.55 (s, 2 H), 8.01 (s, 1 H), 7.59 (d, *J* = 7.88 Hz, 1 H), 7.48 (d, *J* = 7.88 Hz, 1 H), 3.97 (s, 2 H), 3.75 (s, 2 H). ¹³C NMR (125 MHz, DMSO-*d*₆) δ 172.6, 171.9, 148.8, 136.5, 135.5, 133.9, 129.3, 126.1. FT-IR (diamond-ATR, cm⁻¹) 2966.7, 2647.5, 2549.6, 1696.4, 1529.3, 1409.8, 1351.7, 1289.7, 1231.6, 1202.9, 1144.8, 1079.5, 916.3, 887.0, 825.6, 810.6, 763.6, 738.1, 676.8. HRMS (+ESI) calculated for MNa⁺ 262.0322, observed 262.0341.

[Zn(PDAC)(4,4'-dipyridyl)•CH₃OH]_n (PDAC-MOF). PDAC-MOF was prepared at room temperature by modifying the reported solvothermal synthesis.²⁵ Sodium hydroxide (8.00 mg, 0.200 mmol) was added to a solution of *p*-phenylenediacetic acid (19.4 mg, 0.100 mmol) and 4,4'-dipyridine (15.6 mg, 0.100 mmol) in 1 mL of MeOH/H₂O (4:1). The solution was layered with MeOH (5 mL) to induce slow mixing with a third layer of MeOH (1 mL) containing zinc nitrate tetrahydrate (Zn(NO₃)₂ • 6H₂O 226.1 mg, 0.100 mmol) for 5 d to yield colorless needles (33.0 mg, yield 74.1%). Anal. Calc. for C₂₁H₂₀N₂O₅Zn: C, 56.53; H, 4.49; N, 6.28. Found: C, 56.21; H, 4.62; N, 6.35%. FT-IR (diamond-ATR, cm⁻¹) 3433.9, 3348.6, 3034.5, 2922.3, 1652.6, 1586.2, 1562.8, 1514.0, 1490.6, 1435.9, 1402.8, 1324.6, 1297.2, 1277.7, 1217.2, 1201.6, 1170.3, 1145.1, 1103.9,

1072.6, 1047.4, 1031.7, 1008.3, 953.6, 863.7, 844.4, 818.9, 770.1, 732.9, 703.7, 664.6, 631.5. TGA shows a 15.7% weight loss between 23-40 °C, which may correspond to absorbed MeOH co-crystallized in the framework. Decomposition occurs at 135 °C.

[Zn(NPDAC)(4,4'-dipyridyl)•CH₃OH]_n (NPDAC-MOF). NPDAC (215 mg, 0.900 mmol) and NaOH (72.0 mg, 1.80 mmol) were dissolved in 10 mL MeOH to prepare a 0.090 M NPDAC sodium salt solution. Crystalline PDAC-MOF (20.0 mg, 45.0 μmol) was immersed in 5 mL MeOH, and 5 mL of NPDAC sodium salt solution (0.090 M) was added. The mixture was kept in dark for 7 d to yield colorless needles suitable for X-ray analysis (16.7 mg, yield 83.2%). FT-IR (diamond-ATR, cm⁻¹) 2918.2, 2683.5, 1629.2, 1609.7, 1580.5, 1527.6, 1494.5, 1416.3, 1342.3, 1269.9, 1219.1, 1146.9, 1072.6, 1047.4, 1014.3, 924.4, 897.0, 863.7, 811.0, 783.7, 721.1, 690.1, 637.2. The ligand composition of the resulting MOF crystals was determined by ¹H NMR after digesting the crystals with D₂SO₄ in DMSO-d₆, showing PDAC was replaced by NPDAC. TGA shows a 16.5% weight loss between 23-46 °C, which may correspond to co-crystallized MeOH in the framework. Decomposition occurs at 112 °C.

NPDAC30-MOF. PDAC-MOF crystals (20.0 mg, 45.0 μmol) were immersed in 5 mL MeOH, and combined with 1.5 mL of NPDAC sodium salt solution (0.090 M) and 3.5 mL additional MeOH. The mixture was kept in dark for 7 d to induce linker exchange. The ligand composition of the resulting MOF crystals was determined by ¹H NMR after digesting the crystals with D₂SO₄ in DMSO-d₆, which show approximately 30% of the original PDAC was replaced by NPDAC.

4.2.2. Collection and Reduction of X-ray Data

X-ray Crystallography. Structural analysis was carried out in the X-Ray Crystallographic Facility at Worcester Polytechnic Institute. Crystals were glued on tip of a glass fiber or were covered in

PARATONE oil on 100 μm MiTeGen polyimide micromounts and were mounted on a Bruker-AXS APEX CCD diffractometer equipped with an LT-II low temperature device. Diffraction data were collected at room temperature using graphite monochromated Mo-K α radiation ($\lambda = 0.71073 \text{ \AA}$) using the omega scan technique. Empirical absorption corrections were applied using the SADABS program.²⁶ The unit cells and space groups were determined using the SAINT+ program.²⁷ The structures were solved by direct methods and refined by full matrix least-squares using the SHELXTL program.²⁸ Refinement was based on F^2 using all reflections. All non-hydrogen atoms were refined anisotropically. Hydrogen atoms on carbon atoms were all located in the difference maps and subsequently placed at idealized positions and given isotropic U values 1.2 times that of the carbon atom to which they were bonded. Hydrogen atoms bonded to oxygen atoms were located and refined with isotropic thermal parameters. Mercury 3.1 software and Diamond Version 3.1d were used to examine the molecular structure. Relevant crystallographic information is summarized in Table 4.1, and the 50% thermal ellipsoid plots are shown in Figure 4.2.

Powder X-ray Diffraction. PXRD data were collected on a Bruker-AXS D8-Advance diffractometer using Cu-K α radiation with X-rays generated at 40 kV and 40 mA. Bulk samples of crystals were placed in a 20 cm \times 16 cm \times 1 mm well in a glass sample holder, and scanned at RT from 3 $^\circ$ to 50 $^\circ$ (2θ) in 0.05 $^\circ$ steps at a scan rate of 2 $^\circ$ /min. Simulated PXRD patterns from single crystal data were compared to PXRD patterns of PDAC-MOF and NPDAC-MOF to confirm the uniformity of the crystalline samples.

4.2.3. Spectroscopy

General Spectroscopic Methods. All aqueous solutions were prepared from Millipore (Biopak™ Ultrafiltration Cartridge) water. All organic solutions were prepared using spectroscopic grade solvents. UV-vis absorption spectra were obtained by taking sample solutions in 1.0 cm quartz cuvette at 23 °C with total volumes kept at 2 mL or 3 mL, and recorded on Thermo Scientific Evolution 300 UV-vis spectrometer with inbuilt Cary winUV software. Photolysis was carried at 23 °C in 1.0 cm quartz cuvette illuminated by 3 W UV LED (Mouser Electronics, 365 nm, 200 mW) powered by a 700 mA LuxDrive FlexBox using a variable DC source set at 12 VDC. Rate of photolysis and photoproducts were analyzed using LC/MS (Single Quadrupole, Agilent Technologies) by monitoring at changes at 277 nm.

Quantum Efficiency and Photoproducts Determination. A 2 mL solution of NPDAC (15 mM) in MeOH (5% H₂O) was prepared from a 45 mM stock solution and exposed to a LED UV irradiation for 60, 180, 360, and 600 s. A fresh 2 mL solution was used for each time interval irradiation, and 100 µL of ketoprofen in MeOH (100 mM) was added as internal standard before subjecting samples to LC-MS analysis. The quantum efficiency was calculated following established procedures.²⁹ The photoproducts were confirmed using HPLC and ¹H NMR analysis. All the samples were eluted using an isocratic mixture of 95:5 CH₃CN:H₂O containing 0.1% formic acid at a flow rate of 0.3 mL/min. The identity of individual peaks that are labeled from **2-5** in the HPLC traces in Figure 4.1 were identified by m/z values in the mass spectrum. Bulk photolysis of NPDAC was carried out by dissolving NPDAC (23.9 mg, 0.100 mmol) in 2 mL D₂O containing NaOH (8.0 mg, 0.20 mmol). The solution was irradiated with 365 nm light for 35 min. The D₂O mixture was analyzed by ¹H NMR spectroscopy, and then extracted successively with 2

mL hexanes and 2 mL DCM, and the combined organic phase was removed. The combined organic-soluble extracts were dissolved in CDCl_3 and the ^1H NMR was recorded.

4.2.4. Photolysis of NPDAC-MOF

NPDAC-MOF (5.00 mg, 11.2 μmol) was immersed in MeOH (2 mL), kept in dark for 2 h, and UV-vis absorption spectra was recorded. The mixture was exposed to 365 nm of light for 2 h in total, the first 1 h without stirring and the second hour with stirring. After 10 min of irradiation, the mixture was removed to the dark for 30 min before measuring the absorbance of the supernatant liquid. This process was repeated after total irradiation times of 20, 30, 45 and 60 min (3.5 h elapsed). After irradiation, the solution was filtered through glass wool, and LC-MS analysis was performed on the filtrate using ketoprofen as an internal standard. The sample was eluted using an isocratic mixture of 95:5 $\text{CH}_3\text{CN}:\text{H}_2\text{O}$ containing 0.1% formic acid at a flow rate of 0.3 mL/min, and the absorbance at 277 nm was monitored.

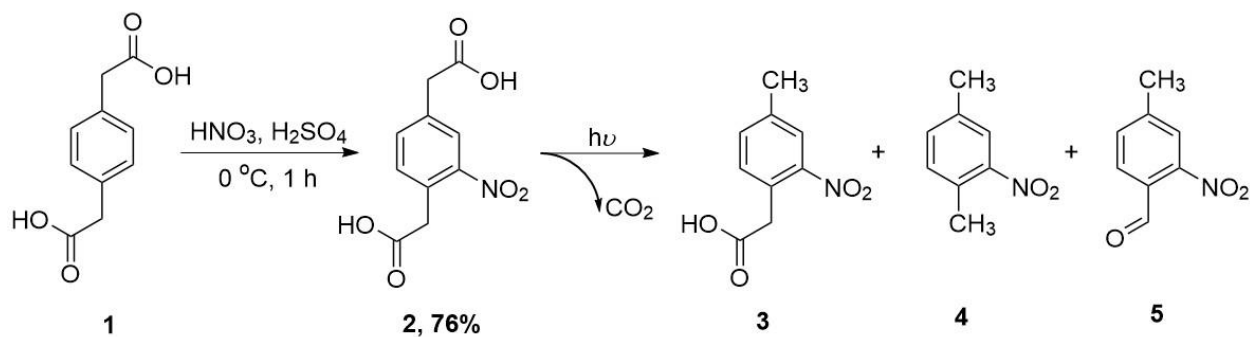
4.2.5. Defects Creation and MOF Repair

NPDAC30-MOF (20 mg) was as immersed in MeOH (2 mL). The mixture was irradiated (365 nm) with stirring for 2 h. The resulting material was isolated, rinsed with MeOH, and divided into two equal portions. The two samples were immersed in 5 mL MeOH containing 135 μmol PDAC or 1.5 mL NPDAC sodium salt solution (0.090 M) combined with 3.5 mL MeOH for 1 d. The materials were isolated and crystallinity was verified by PXRD. The ligand composition of the resulting MOF crystals was determined by ^1H NMR after digesting the crystals with D_2SO_4 in DMSO-d_6 .

4.3. Design and Structural Considerations

Developing photoswitchable MOF components has often outpaced exploration of MOFs containing photolabile building blocks possibly due to the latter being more susceptible to decomposition during standard solvothermal MOF syntheses. Since multicarboxylates, specifically dicarboxylate struts like terephthalic acid, are nearly ubiquitous in MOFs, we envisioned designing a light-reactive dicarboxylate ligand, as well as the corresponding approach necessary to incorporate these components into MOFs under facile conditions. We recently exploited the photoreactivity of *meta*-nitrophenylacetic acid derivatives to design zinc photocages²¹ and photocapping groups,²⁴ so we hypothesized that a similar functional group could be adapted to construct a photoreactive MOF strut.

Although less common than terephthalic acid, *p*-phenylenediacetic acid (PDAC) has been used to construct MOFs with^{30,31} and without dipyridine groups.²⁵ We anticipated that a



Scheme 4.1. The synthetic route of **2** and its photolysis reaction, showing three possible major photoproducts, 4-methyl-2-nitrophenylacetic acid (**3**), 2-nitro-*p*-xylene (**4**) and 4-methyl-2-nitrobenzaldehyde (**5**).

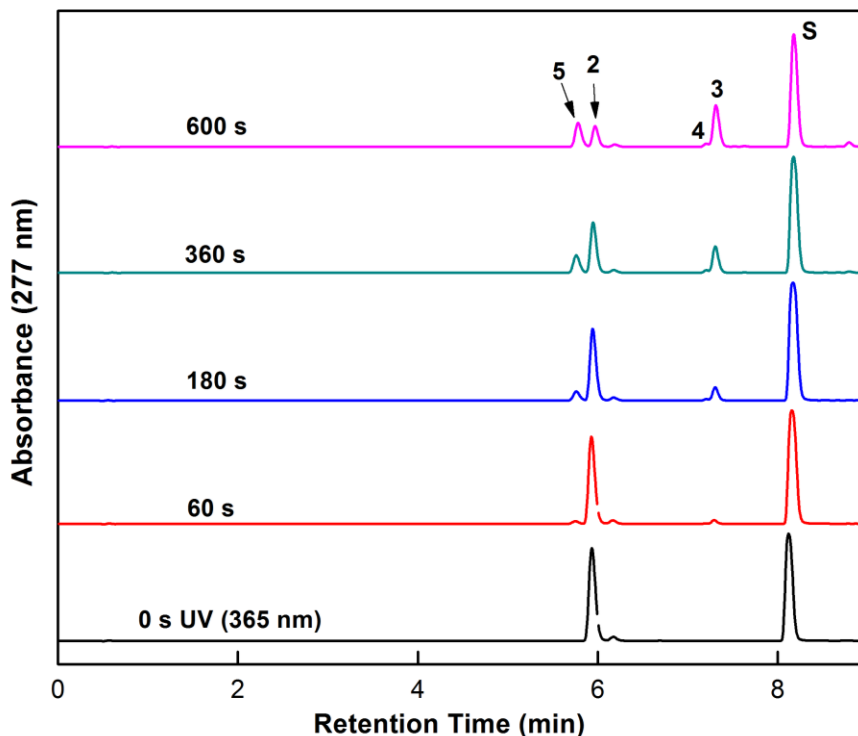
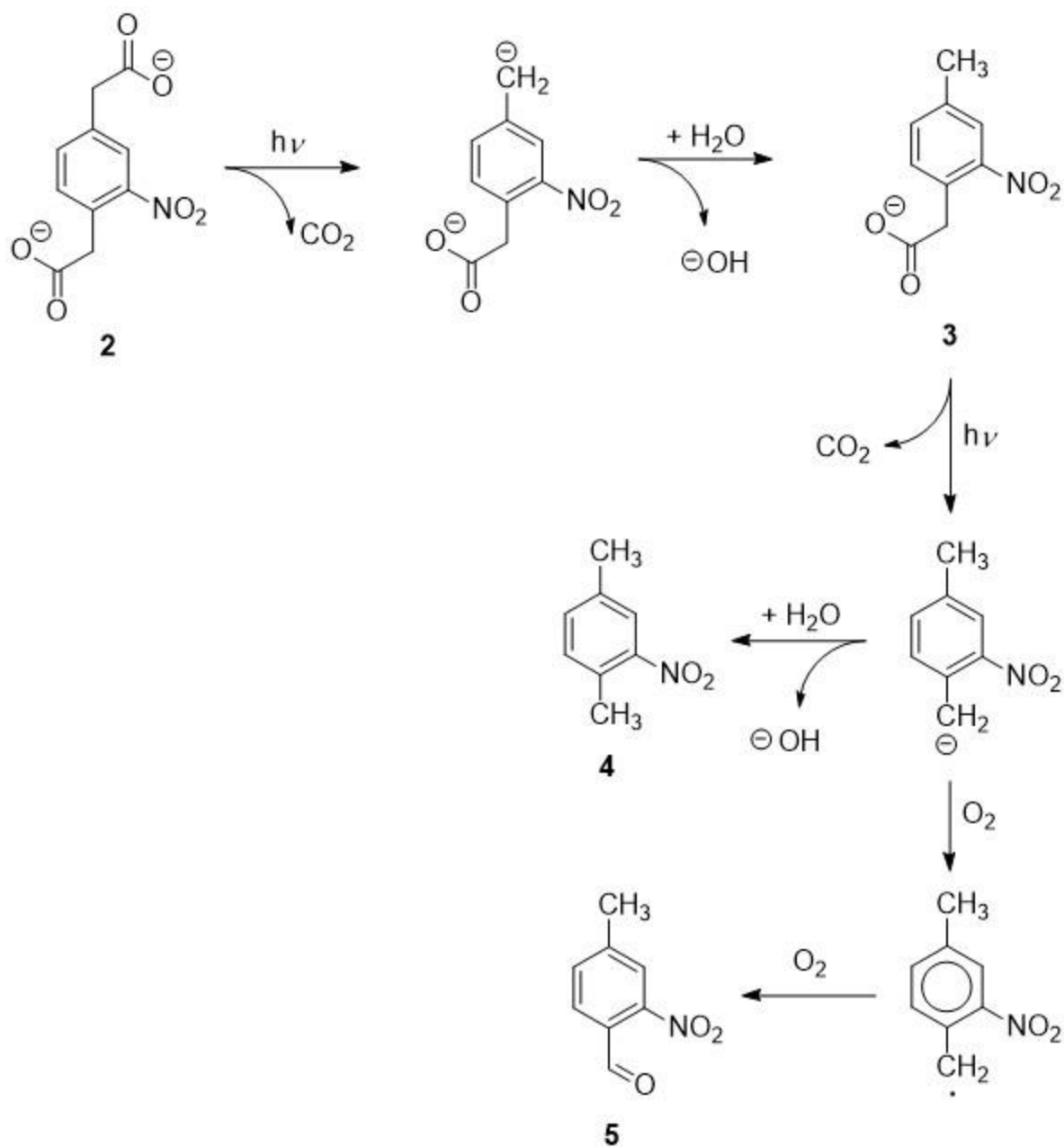


Figure 4.1. HPLC analysis of the photolysis of NPDAC (15 mM) in MeOH (5% H₂O), ketoprofen was used as internal standard (S). A decrease in the intensity of NPDAC (**2**) and an increase in the intensities of photoproducts 4-methyl-2-nitrophenylacetic acid (**3**) with m/z 194.1, 2-nitro-*p*-xylene (**4**) with m/z 302.0 as dimer fragment, and 4-methyl-2-nitrobenzaldehyde (**5**) with m/z 164.0 upon UV (LED, 365 nm) exposure (0 to 10 min) was observed.

nitroaromatic analog might be thermally unstable, so we designed a solvent layering technique to prepare PDAC-MOF crystals as an alternative to the reported solvothermal synthesis.^{25,30} The PDAC-MOF framework we obtained at room temperature shows an identical semi-pillared paddle-wheel (sppw) structure as previously reported, but with an improved R value.³⁰

4.4. Photolabile Strut and MOF Synthesis

Nitration of PDAC yields the desired photolabile linker NPDAC in high yield since mono-nitration deactivates the ring to further electrophilic aromatic substitution reactions (Scheme 4.1). Upon



Scheme 4.2. Proposed pathway to the formation of photoproducts from NPDAC (2) photolysis. The three detected photoproducts are 4-methyl-2-nitrophenylacetic acid (3), 2-nitro-*p*-xylene (4) and 4-methyl-2-nitrobenzaldehyde (5). The mechanistic pathway to the formation of 5 is unclear, but is consistent with the reaction chemistry of other phenylacetic acid derivatives under similar conditions.

exposure to light, NPDAC decomposes to provide a mixture of photoproducts that includes 4-methyl-2-nitrophenylacetic acid (3) with m/z 194.1, 2-nitro-*p*-xylene (4) with m/z 302.0 as a dimer

ion, and 4-methyl-2-nitrobenzaldehyde (**5**) with m/z 164.0, as determined by LCMS analysis (Figure 4.1), which was verified by NMR. Bulk photolysis of NPDAC in D_2O was monitored by 1H NMR (Figure 4.5, 4.6). After 35 min of irradiation, the 1H NMR shows a mixture of NPDAC and one major photoproduct 4-methyl-2-nitrophenylacetic acid (**3**), which is produced by the photodecarboxylation characteristic of *meta*-nitrophenylacetate compounds.^{32,33} Several minor unidentifiable photoproducts are also observed. During the irradiation, the clear yellowish solution became opaque, indicating the possible formation of hydrophobic photoproducts. After extracting the mixture with hexane and then DCM, two additional photoproducts were recovered. Photoproduct **4** corresponds to a second photodecarboxylation at the *ortho* position (Scheme 4.2). While decarboxylation *ortho*-nitrophenylacetate was anticipated,³² the exact pathway that leads to the aldehyde **5** remains unclear. Under aerobic conditions however, *ortho*- and *para*-nitrotoluene derivatives are susceptible to oxidation, and the photolysis conditions are amenable to radical formation, which could account for the observed photoproduct.³⁴⁻³⁷ Phenylacetic acids can also be converted directly to benzaldehyde derivatives with various reagents,³⁸⁻⁴⁰ so the presence of **5** is unremarkable. A photolysis quantum yield ($\Phi_{\text{photolysis}}$) of 33% was calculated by quantifying the disappearance of NPDAC over the course of the reaction.

Although the NPDAC exhibited the desired photodecarboxylation chemistry, neither solvothermal conditions nor room temperature reactions analogous to the synthesis used to prepare PDAC-MOF provided crystalline materials. We therefore explored post-synthetic linker exchange (PSLE) as an alternative synthetic strategy to obtain a photoactive MOF. PSLE has been applied successfully to prepare MOFs that resist *de novo* syntheses,⁴¹⁻⁴³ and as a strategy to prevent framework interpenetration.^{44,45} When introduced to a concentrated solution of the new ligand,

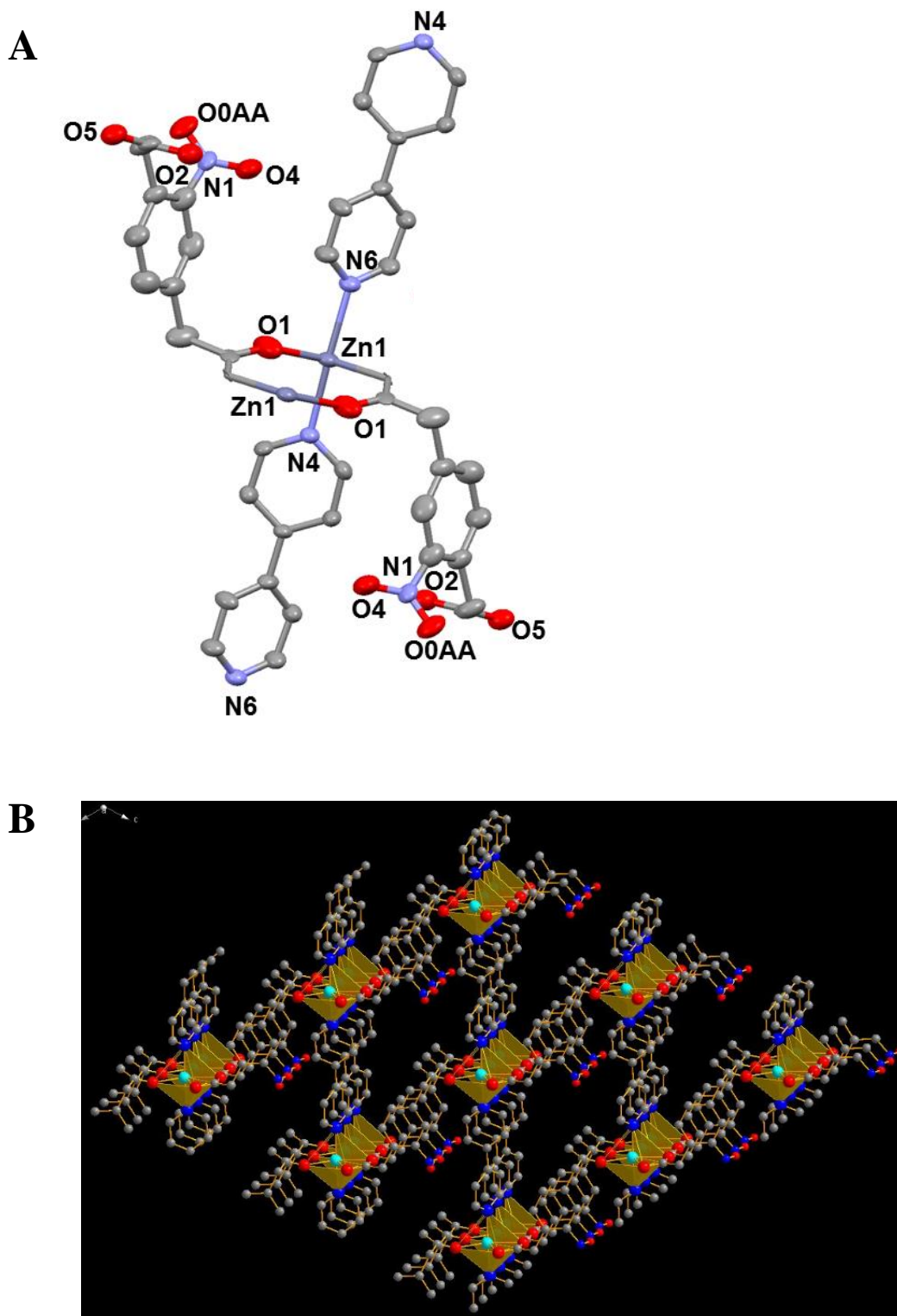


Figure 4.2A. ORTEP diagrams showing the structure of NPDAC-MOF, showing of 50% thermal ellipsoids with labels for non C, H atoms. Hydrogen atoms and MeOH guest molecule are omitted for clarity. **4.2B.** Two-dimensional layer showing the crystal packing, with bright yellow octahedral showing Zn^{2+} atoms are coordinated by four oxygen atoms and two nitrogen atoms.

small energy differences between the two different linker analogues in the heterogeneous reaction create dynamic equilibrium necessary for interconversion.

Exposure of PDAC-MOF to a ten-fold excess of NPDAC with respect to PDAC resulted in the isolation colorless needles of NPDAC-MOF after 7 days. Single crystal x-ray analysis revealed nearly identical cell parameters for PDAC-MOF and NPDAC-MOF. Like PDAC-MOF, the framework of NPDAC-MOF adopts a sppw structure (Figure 4.2A). Unlike typical pillared-paddle wheel structures, the two carboxylates are not in the same plane, forming a tilted paddle wheel with one NPDAC ligand facing up and the other facing down. In addition, each Zn^{2+} is 6-coordinated instead of five, coordinated by two pyridine ligands and three carboxylate groups. An extended three-dimensional structure is shown in Figure 4.2 B, with yellow octahedral representing six coordination of Zn^{2+} atoms by four oxygen and two nitrogen atoms. The X-ray reveals MeOH guest molecules, which upon removal by modeling reveal pores with dimensions of $1.18 \text{ \AA} \times 1.10 \text{ \AA} \times 0.89 \text{ \AA}$. The nitro group on each of the dicarboxylate ligand is disordered in the X-ray, however, the digested 1H NMR and LCMS experiments indicate a complete replacement of PDAC by NPDAC.

4.5. MOF Photolysis and Reassembly

NPDAC-MOF appears to be stable indefinitely in the absence of light while stored in MeOH. Upon exposure to UV light however, several photoproducts were detectable by UV-vis spectroscopy and LCMS (Figure 4.3). The increase in absorbance centered at 240 nm corresponds to 4,4'-dipyridine, which is consistent with fragmentation of the paddle wheel sheets and release of the pillars. Like NPDAC ligand, three new peaks appear in the LC trace, corresponding to same three products of photodecarboxylation with the addition of a peak consistent with 4,4'-dipyridine

(Scheme 4.3). Irradiation of PDAC-MOF under identical conditions reveals no evidence of decomposition.

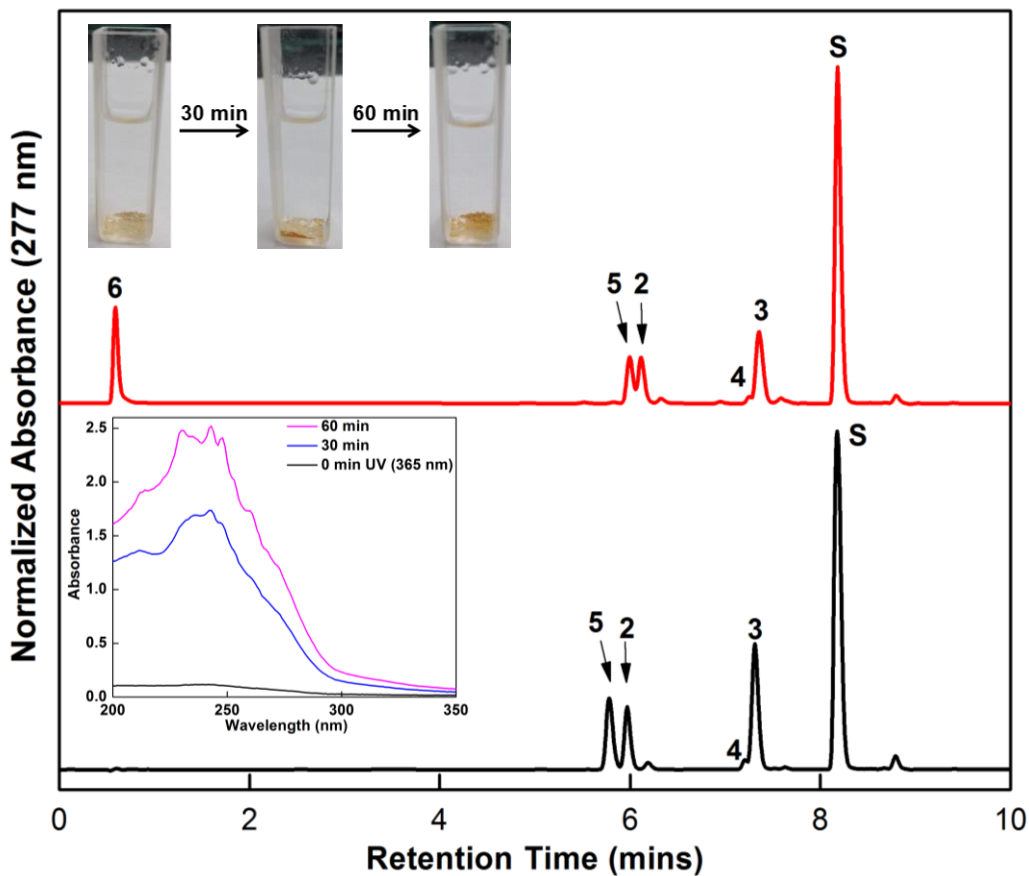
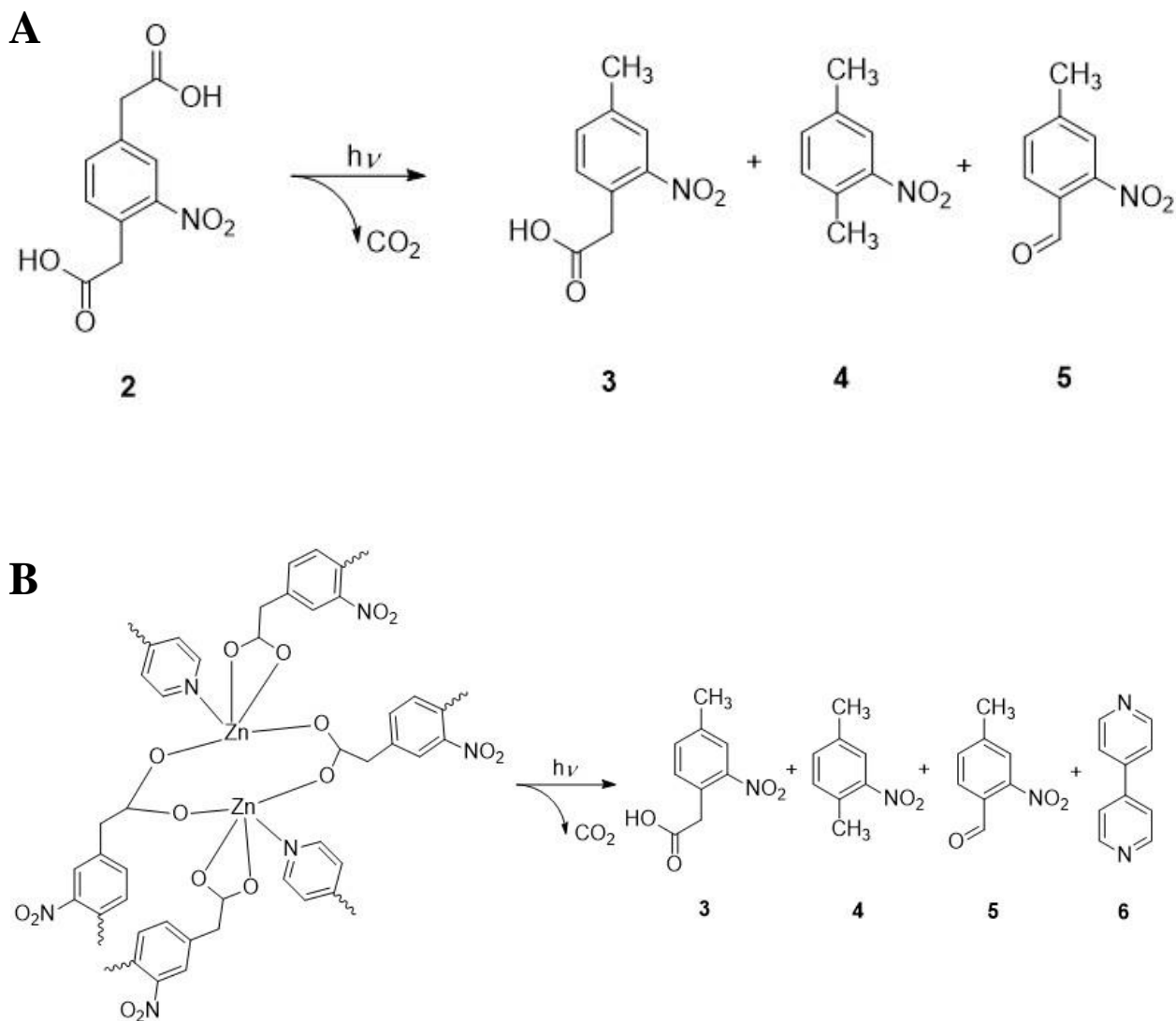
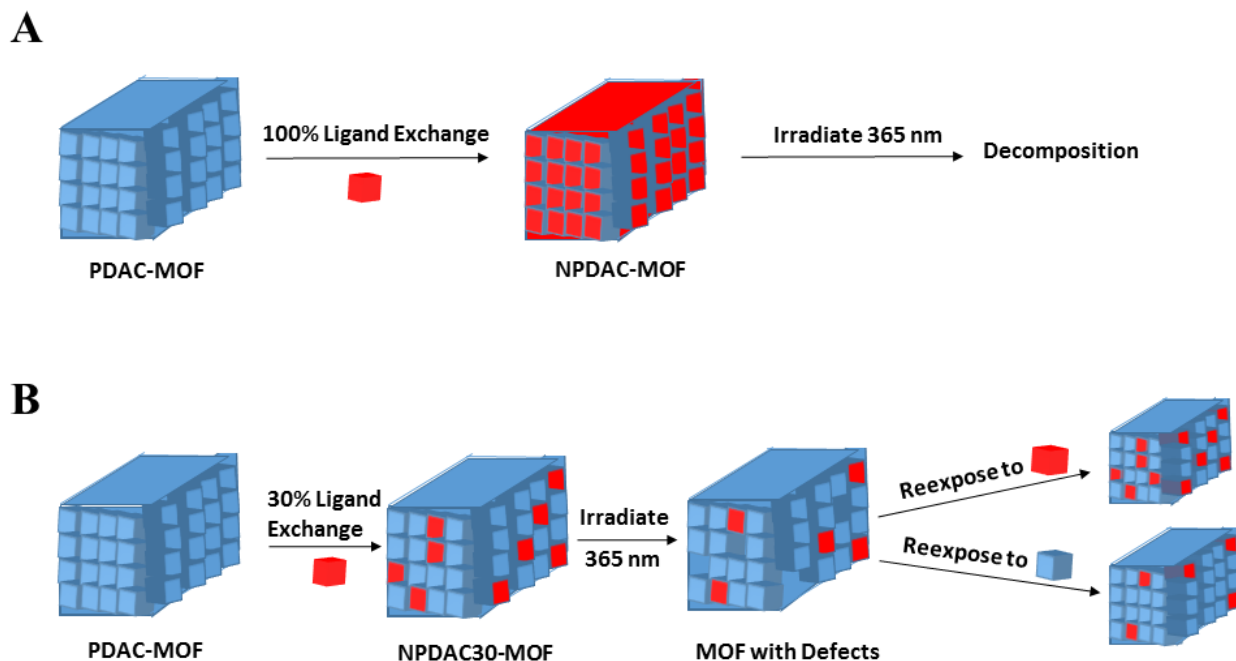


Figure 4.3. Stacking HPLC traces of photolysis product of NPDAC-MOF after irradiation 1 h (red), comparing with the ligand photolysis product after irradiation 10 min (black). Ketoprofen was used as internal standard (S), and starting material NPDAC is marked as (2), possible photoproducts are marked as 4-methyl-2-nitrophenylacetic acid (3), 2-nitro-*p*-xylene (4) and 4-methyl-2-nitrobenzaldehyde (5), together with the released 4,4'-dipyridine (6) from decomposition of NPDAC-MOF. Upper inset photos show the crystal color changes from light yellow to dark yellow as irradiated with 365 nm light. Lower inset UV-Vis spectroscopy shows the absorbance of 5 mg NPDAC-MOF in 2 mL MeOH irradiating with 365 nm LED in a period of 1 h.



Scheme 4.3. Proposed photolysis reactions of NPDAC and NPDAC-MOF. Both have three detected products, which are 4-methyl-2-nitrophenylacetic acid (**3**), 2-nitro-*p*-xylene (**4**) and 4-methyl-2-nitrobenzaldehyde (**5**). Pillar ligand 4,4'-bipyridine (**6**) also shows up after NPDAC-MOF degradation.

Obtaining detailed structural information about MOF defects is difficult. While wide-ranging defects can introduce cracks through desolvation⁴⁶ or spiral growth associated with screw dislocations that can be observed by microscopic imaging techniques,⁴⁷ random defects are often imperceptible. Alternatively, powder X-ray diffraction is a widely used technique to investigate



Scheme 4.4A. Fully linker exchange will result NPDAC-MOF, which decomposes completely after 365 nm irradiation for 2 h. **4.4B.** Partially linker exchange will result NPDAC30-MOF, which undergoes decomposing and forming MOF defects. MOF structure can be restored after re-exposing defected MOF into NPDAC or PDAC ligands.

the creation of defects or amorphous phases, by monitoring the intensity, shape or position change of Bragg diffraction peaks.^{48,49} Comparison of the PXRD pattern of NPDAC-MOF with the pattern simulated from single crystal structure shows good agreement with predicted reflections. After 1 h of irradiation the disappearance of Bragg diffraction at 2θ between $7\text{-}13^\circ$ and $15\text{-}25^\circ$, along with the broadening of diffraction peaks, suggests decreasing crystallinity and increasing amorphization. All the Bragg diffraction peaks disappear after 2 h of irradiation, and two broad diffraction peaks at $2\theta = 5\text{-}10^\circ$ and $15\text{-}30^\circ$ appear, which indicates of complete phase change from crystalline to amorphous (Figure 4.4).

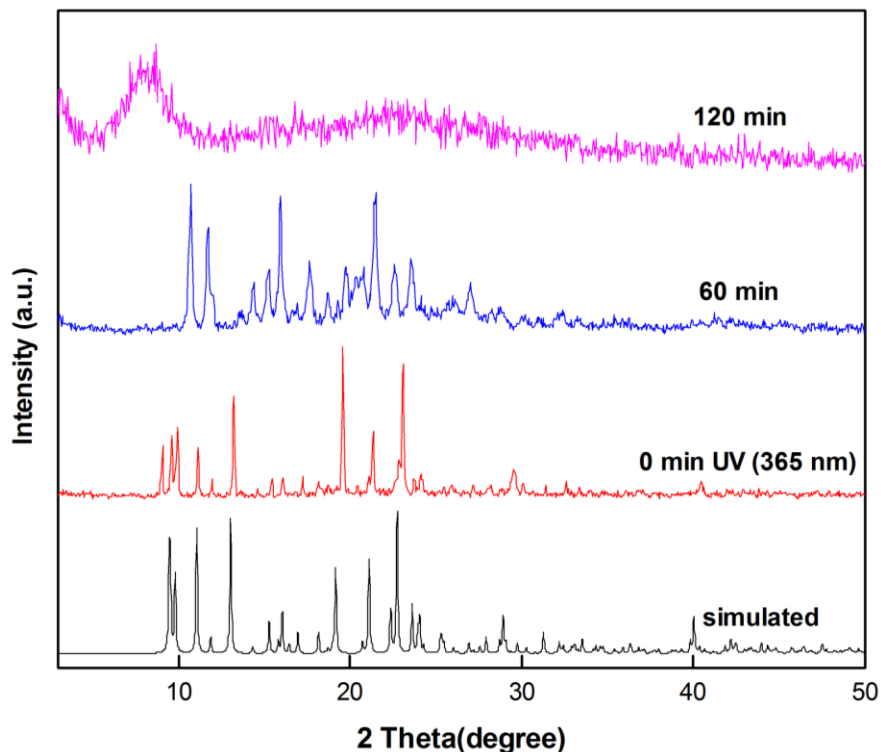


Figure 4.4. Powder X-ray diffraction patterns of simulated and experimental NPDAC-MOF, and upon 365 nm LED irradiation for 60 min and 120 min.

A light-digestible MOF has many possible intriguing applications such as a delivery vehicle for chemical reagents or therapeutic agents, but we also envisioned using the strategy to semi-rationally modify the contents of an assembled MOF. By reducing the amount of NPDAC in the PSLE reaction from a 10-fold excess to a 3-fold excess, the digested ^1H NMR suggests approximately 30% replacement of PDAC in the MOF (NPDAC30-MOF). Unlike NPDAC-MOF, long-term irradiation of NPDAC30-MOF did not result in the formation of amorphous material as determined by PXRD; however, the digested NMR revealed the NPDAC content decreased from 30% to 16%. With nearly half of introduced NPDAC ligand lost to photodecomposition, a crystalline MOF containing multiple defects was obtained. Defect sites can be probed by TGA⁵⁰ or potentiometric titrations,^{51,52} but the TGA method has deficiencies,⁵³ and titrations are based on the hypothesis that the missing linkers have been replaced by specific ligand or solvent molecules.

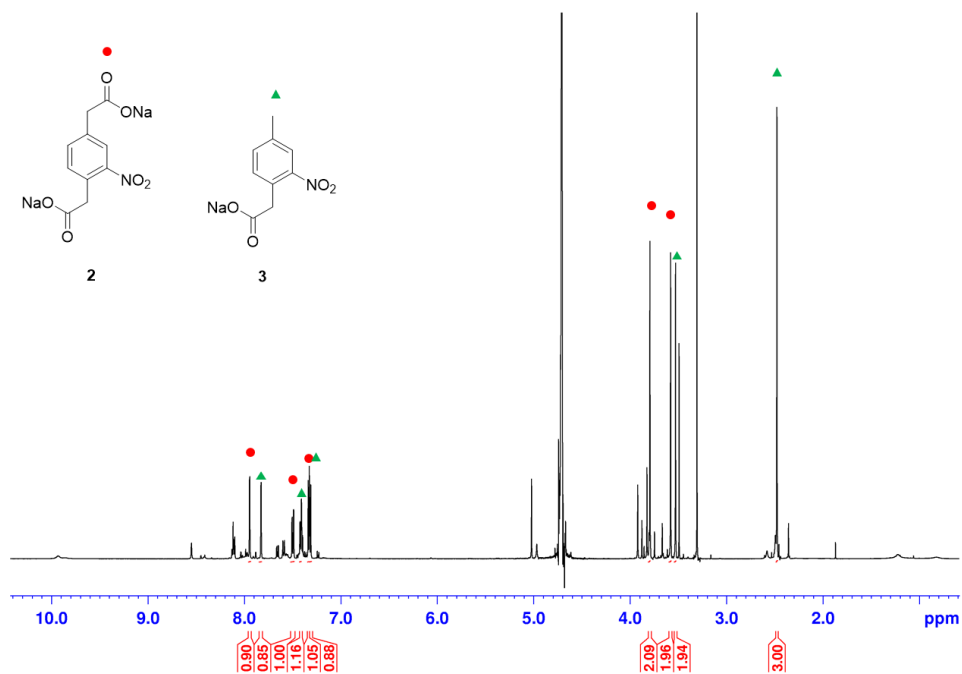


Figure 4.5. ¹H NMR spectroscopy NPDAC sodium salt in D₂O (2 mL, 50 mM) after irradiation with 365 nm (LED, 3 Wcm⁻²) for 35 mins, showing major compounds including starting material (2) and one major photoproduct (3).

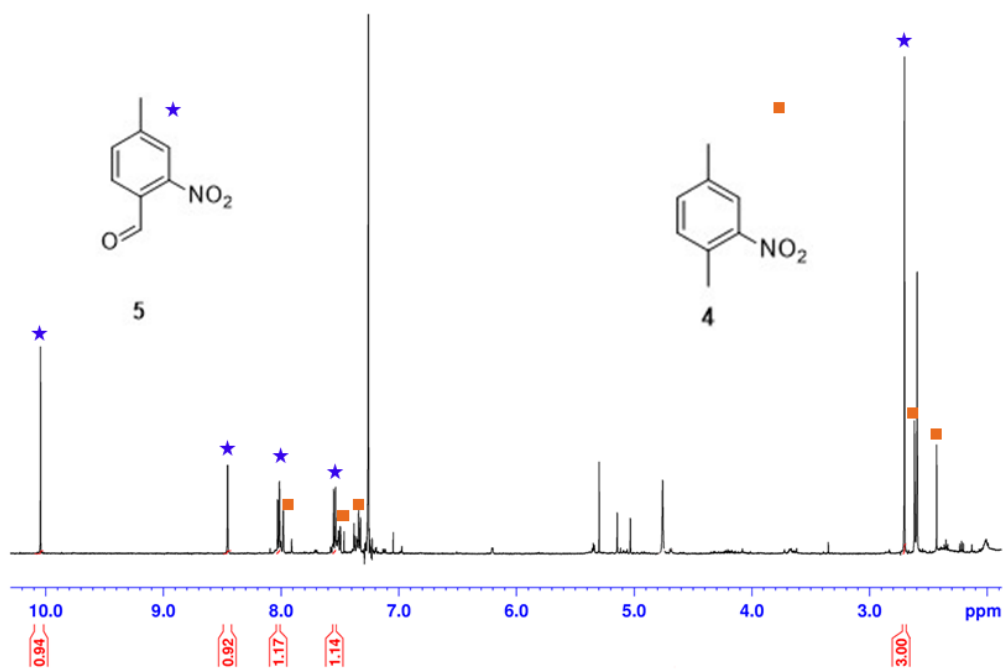


Figure 4.6. ¹H NMR spectroscopy NPDAC sodium salt in D₂O (2 mL, 50 mM) after irradiation with 365 nm (LED, 3 Wcm⁻²) for 35 mins and extract with 2 mL hexanes and 2 mL DCM. Solvent removal of the organic phase and NMR in CDCl₃ shows photoproducts (4) and (5).

Since photolysis permanently degrades the organic linker, digesting our MOF in acid and analyzing the contents by NMR spectroscopy provides a convenient alternative to quantify the amount, if not the location, of MOF defects.

While defects might produce adverse effects in crystalline materials, defects also can be an advantage in functional materials such as MOFs, where defects usually result from ligand or metal center vacancies. While chemical defects in semiconductors and surface defects on nanocomposites are critical for their intrinsic properties, defects in MOFs can impart catalytic activity,^{54,55} facilitate adsorbate diffusion,^{56,57} increase photoluminescence^{58,59} and improve performance in separations.⁶⁰ MOFs generally contain a variety of defects;^{61,62} however, artificial defects can be introduced to MOFs by *de novo* synthesis or post-synthetic modification, either on metal nodes or ligand sites.^{63,64} Incomplete assembly caused by rapid crystallization,⁶⁵ and linker vacancies introduced by using a mixed linker approach^{66,67} or modulator addition^{53,55,68} are typical ways to introduce defects by *de novo* synthesis. In addition, post-synthetic modification by treating with acid or water,^{69,70} partial thermal degradation,⁷¹⁻⁷³ or PSLE⁷⁴ can lead to missing ligands or metal nodes. Although *de novo* syntheses are more straightforward, post-synthetic modification on “perfectly” formed crystals can be used to introduce defects in a controlled manner.⁶²

While the chemical impacts of MOF defects have been explored, fewer studies have explored defect repair. Missing linkers can be replaced by exposure to the original ligands, but so far the examples have been limited.^{68,75} Our approach provides a general method to introduce and repair defects cleanly, since photolysis does not require external reagents or harsh conditions to

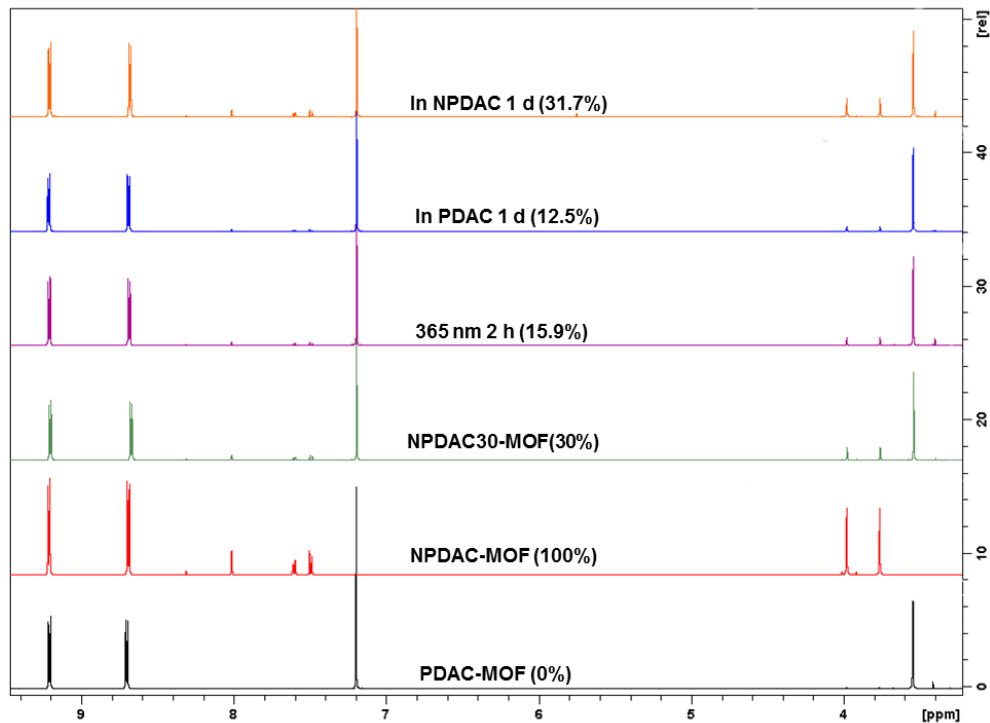


Figure 4.7. Digested ^1H NMR of PDAC-MOF, NPDAC-MOF, NPDAC30-MOF, irradiation of NPDAC30-MOF with 365 nm LED for 2 h, expose the irradiated material to PDAC 1 d, and expose the irradiated material to NPDAC for 1 d. The percentage shows the percent of NPDAC ligand. The chemical shifts show up at 3.58 and 7.21 ppm for PDAC ligand, and 3.78, 4.01, 7.50, 7.61 and 8.02 ppm for NPDAC ligand. The chemical shifts at 8.72 and 9.21 ppm belong to 4,4'-dipyridine ligand.

initiate defect formation. To investigate MOF repair, an irradiated sample of NPDAC30-MOF was divided into two equivalent portions, which were then immersed in solutions containing either 3-fold excess PDAC or NPDAC for 1 d. Digested ^1H NMR shows the NPDAC content in the first portion is 32% and in the second portion is 13% (Figure 4.7). These experiments demonstrate that a photolyzed NPDAC30-MOF can be efficiently reconstituted under facile conditions since the amount of NPDAC present after repair is identical to that found in the original NPDAC30-MOF sample within experimental error (32% vs 30%). The decreased NPDAC (13% vs 30%) and increased PDAC content after repairing irradiated NPDAC30-MOF with PDAC further supports

the repair model (Scheme 4.4B). The NPDAC percentage in both portions corresponds the theoretical content if all the defect sites were filled by one of the two ligands.

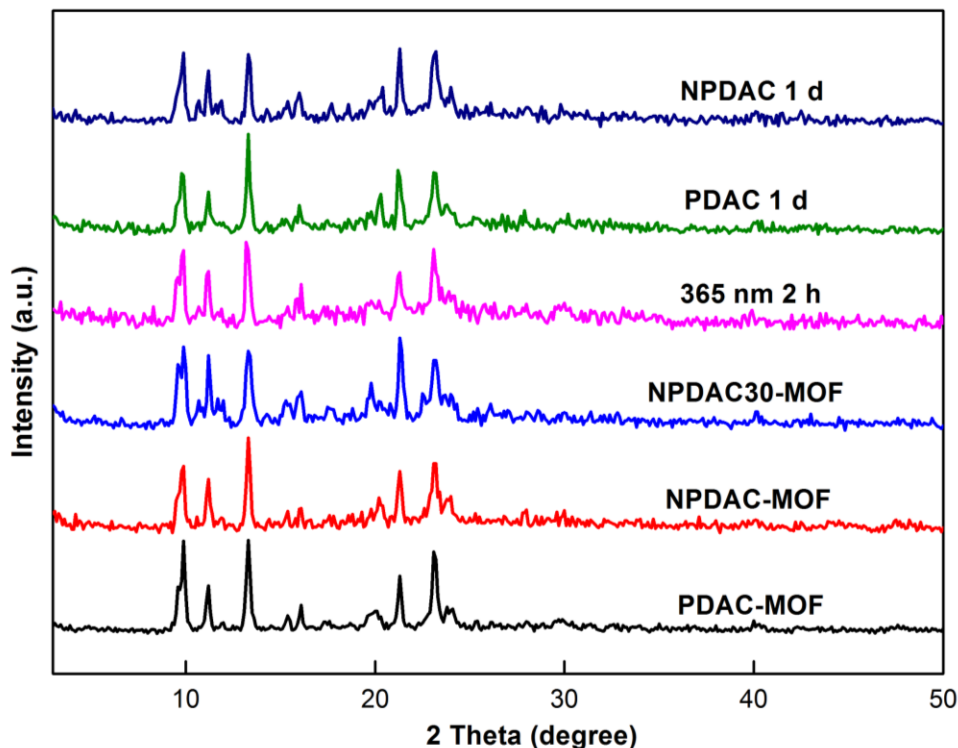


Figure 4.8. Powder X-ray diffraction patterns of PDAC-MOF, NPDAC-MOF, NPDAC30-MOF, irradiation of NPDAC30-MOF with 365 nm LED for 2 h, expose the irradiated material to PDAC 1 d, and expose the irradiated material to NPDAC for 1 d.

4.6. Conclusion

Utilizing a photolabile ligand as MOF strut can make a framework undergo full or partial decomposition upon irradiation. For the first time, a nitrophenylacetate derivative has been incorporated into MOF as a backbone linker via PLSE method. The photo-induced decarboxylation of the NPDAC-MOF represents a novel way of degrading a MOF, which provides an innovative approach to formulating photoresponsive porous materials with potential applications in molecular release and drug delivery. When photoactive linker is mixed with non-

photolabile linker via partial PLSE, the MOF structure can be retained after irradiation, but with the introduction of multiple defects, offering a new method to create vacancies in MOFs. Defect repair can be achieved by treatment with replacement ligands, the scope of which is an interesting area for developing customizable MOF contents. The use of carboxylate struts capable of undergoing photodecarboxylation may lead to a general approach introducing MOF defects for a variety of new applications, and will be the subject of further investigations.

Table 4.1. Crystal data and structure refinements for NPDAC-MOF.

Compound	NPDAC-MOF
Formula	$C_{22}H_{20}N_{2.13}O_{4.25}Zn$
Formula weight ($g\ mol^{-1}$)	447.52
Crystal size	$0.55 \times 0.15 \times 0.08$
Crystal system	Triclinic
Color	Colorless
Space group	P-1
$a/\text{\AA}$	9.620(6)
$b/\text{\AA}$	10.724(7)
$c/\text{\AA}$	11.122(7)
$\alpha/^\circ$	116.790(15)
$\beta/^\circ$	105.111(16)
$\gamma/^\circ$	95.384(16)
Volume/ \AA^3	958.6(11)
Z	2
Temp, K	296 (2)
ρ_{calc}/cm^3	1.550
Radiation	Mo K α ($\lambda = 0.71073\text{\AA}$)
2θ range for data collection/ $^\circ$	4.36 to 45.02
Index ranges	$-10 \leq h \leq 10, -11 \leq k \leq 11, -12 \leq l \leq 12$
Reflections collected	17759
Independent reflections	2588
Observed reflections	2255
R	0.0506
wR2	0.1494
no. of parameters	291
Goodness-of-fit on F2	1.013

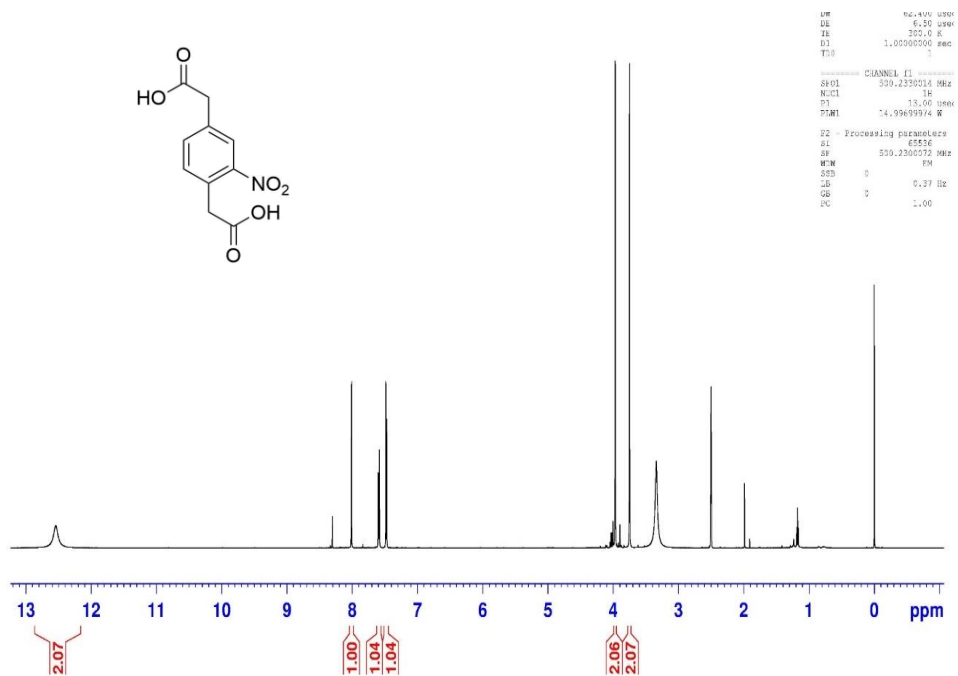


Figure 4.9. ^1H NMR of NPDAC ligand.

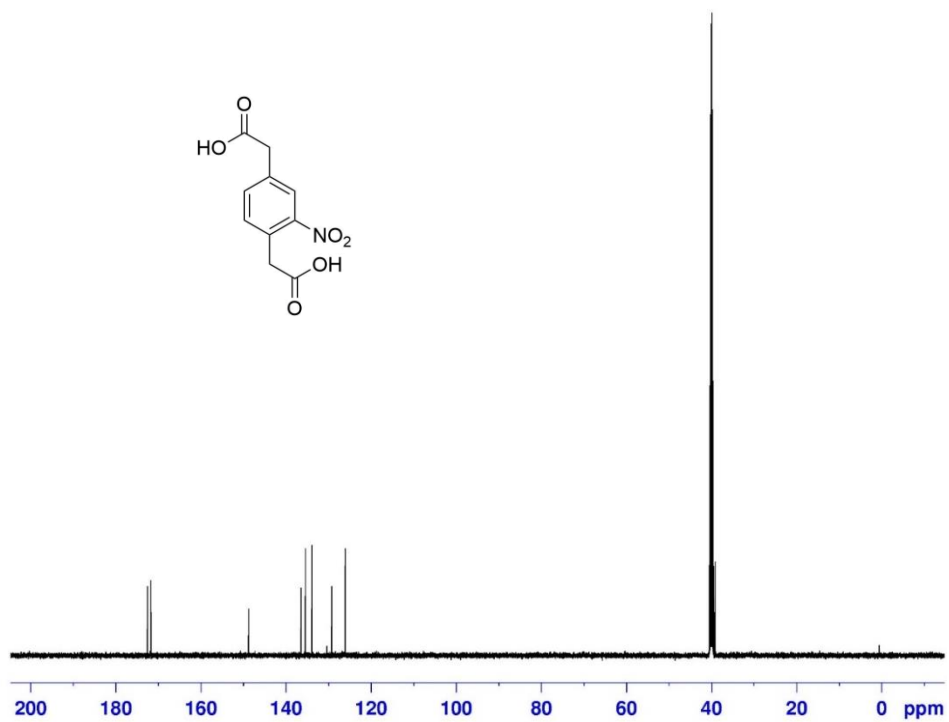


Figure 4.10. ^{13}C NMR of NPDAC ligand.

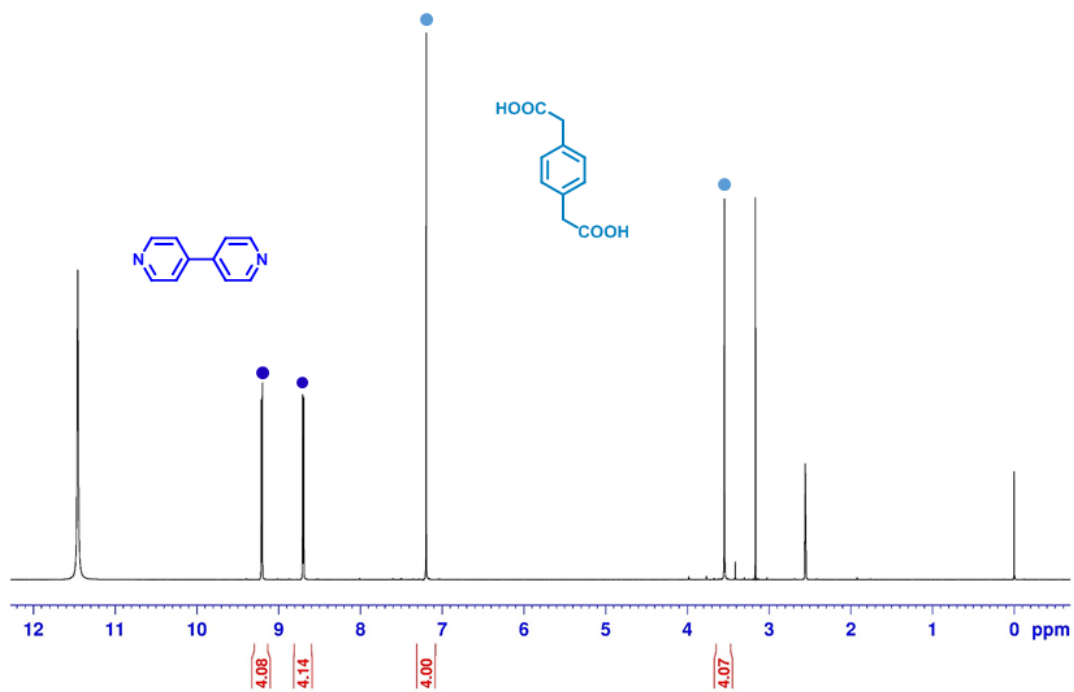


Figure 4.11. Digested ^1H NMR of PDAC-MOF with D_2SO_4 , showing a consistent 1:1 ratio of PDAC : 4,4'-bipyridine.

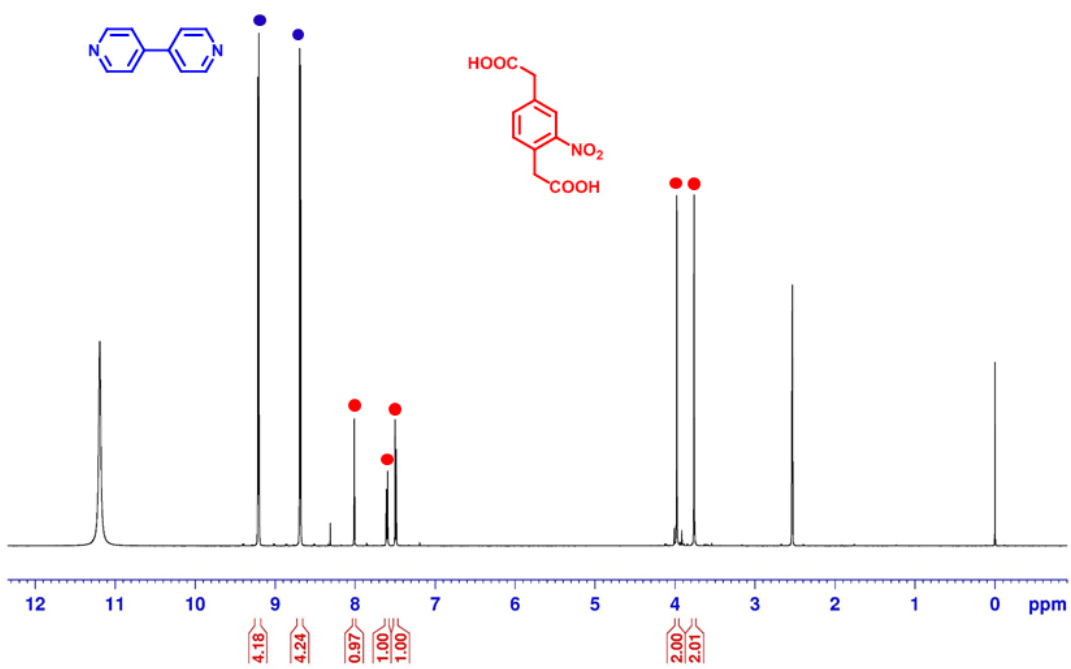


Figure 4.12. Digested ^1H NMR of NPDAC-MOF with D_2SO_4 , showing a consistent 1:1 ratio of NPDAC : 4,4'-bipyridine.

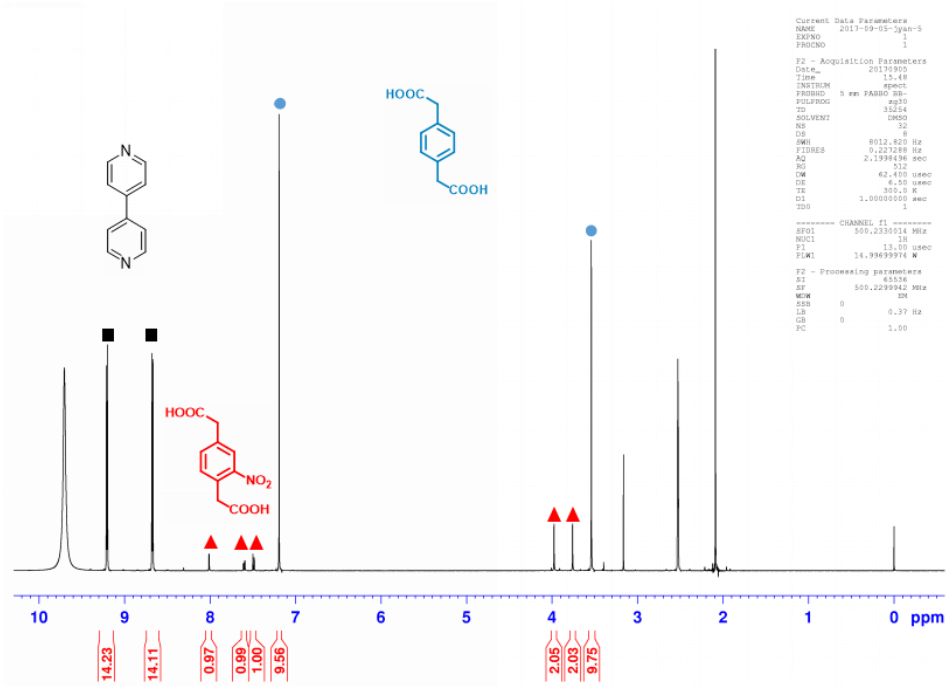


Figure 4.13. Digested ^1H NMR of NPDAC30-MOF, showing 30% of the PDAC ligand has been replaced by the NPDAC ligand.

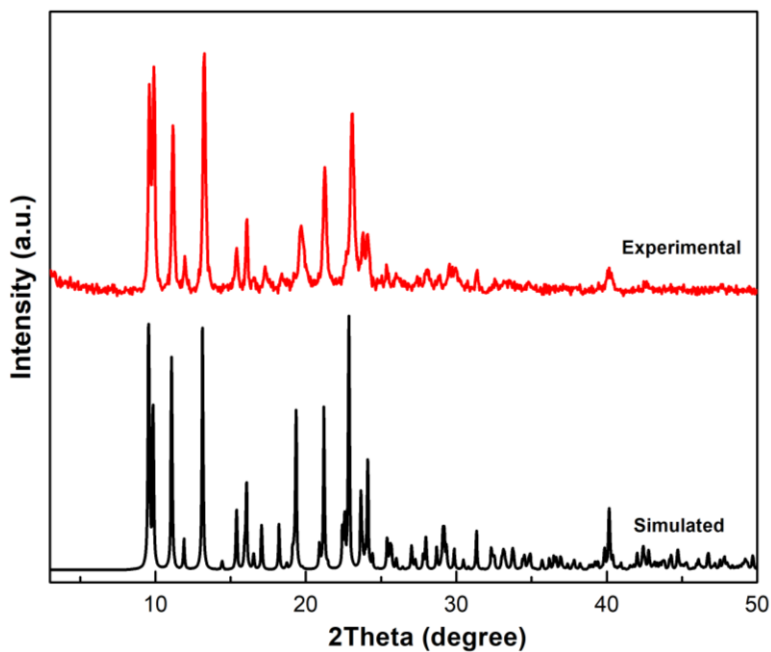


Figure 4.14. Powder X-ray diffraction patterns of PDAC-MOF. Both experimental and simulated patterns from single crystal structures are shown to confirm the phase purity.

4.7. References

- (1) L. E. Kreno, K. Leong, O. K. Farha, M. Allendorf, R. P. Van Duyne, J. T. Hupp, *Chem. Rev.* **2012**, *112*, 1105-1125.
- (2) S. L. James, *Chem. Soc. Rev.* **2003**, *32*, 276-288.
- (3) J. Park, D. Q. Yuan, K. T. Pham, J. R. Li, A. Yakovenko, H. C. Zhou, *J. Am. Chem. Soc.* **2012**, *134*, 99-102.
- (4) R. Lyndon, K. Konstas, B. P. Ladewig, P. D. Southon, C. J. Kepert, M. R. Hill, *Angew. Chem. Int. Ed.* **2013**, *52*, 3695-3698.
- (5) J. Zhang, L. B. Wang, N. Li, J. F. Liu, W. Zhang, Z. B. Zhang, N. C. Zhou, X. L. Zhu, *Crystengcomm* **2014**, *16*, 6547-6551.
- (6) J. J. Yan, L. Wilbraham, P. N. Basa, M. Schüttel, J. C. MacDonald, I. Ciofini, F. X. Coudert, S. C. Burdette, *Manuscript submitted* **2018**.
- (7) J. J. Yan, A. D. Carl, J. C. MacDonald, P. Müller, R. L. Grimm, S. C. Burdette, *Manuscript submitted* **2018**.
- (8) C. B. Fan, L. Le Gong, L. Huang, F. Luo, R. Krishna, X. F. Yi, A. M. Zheng, L. Zhang, S. Z. Pu, X. F. Feng, M. B. Luo, G. C. Guo, *Angew. Chem. Int. Ed.* **2017**, *56*, 7900-7906.
- (9) F. Luo, C. B. Fan, M. B. Luo, X. L. Wu, Y. Zhu, S. Z. Pu, W. Y. Xu, G. C. Guo, *Angew. Chem. Int. Ed.* **2014**, *53*, 9298-9301.
- (10) I. M. Walton, J. M. Cox, C. A. Benson, D. G. Patel, Y. S. Chen, J. B. Benedict, *New J. Chem.* **2016**, *40*, 101-106.
- (11) R. K. Deshpande, G. I. N. Waterhouse, G. B. Jameson, S. G. Telfer, *Chem. Commun.* **2012**, *48*, 1574-1576.
- (12) C. A. Allen, S. M. Cohen, *J. Mater. Chem.* **2012**, *22*, 10188-10194.

- (13) K. M. L. Taylor-Pashow, J. Della Rocca, Z. G. Xie, S. Tran, W. B. Lin, *J. Am. Chem. Soc.* **2009**, *131*, 14261-14263.
- (14) C. Orellana-Tavra, S. Haddad, R. J. Marshall, I. A. Lazaro, G. Boix, I. Imaz, D. Maspoch, R. S. Forgan, D. Fairen-Jimenez, *ACS Appl. Mater. Interfaces* **2017**, *9*, 35516-35525.
- (15) I. A. Lazaro, S. Haddad, S. Sacca, C. Orellana-Tavra, D. Fairen-Jimenez, R. S. Forgan, *Chem.* **2017**, *2*, 561-578.
- (16) J. Xiang, F. J. Ge, B. Yu, Q. Yan, F. Shi, Y. Zhao, *ACS Appl. Mater. Interfaces* **2018**, *10*, 20790-20800.
- (17) T. C. Zhao, P. Y. Wang, Q. Li, A. A. Al-Khalaf, W. N. Hozzein, F. Zhang, X. M. Li, D. Y. Zhao, *Angew. Chem. Int. Ed.* **2018**, *57*, 2611-2615.
- (18) G. Liu, C. M. Dong, *Biomacromolecules* **2012**, *13*, 1573-1583.
- (19) P. Klan, T. Solomek, C. G. Bochet, A. Blanc, R. Givens, M. Rubina, V. Popik, A. Kostikov, J. Wirz, *Chem. Rev.* **2013**, *113*, 119-191.
- (20) H. W. Mbatia, D. P. Kennedy, S. C. Burdette, *Photochem. Photobiol.* **2012**, *88*, 844-850.
- (21) P. N. Basa, S. Antala, R. E. Dempski, S. C. Burdette, *Angew. Chem. Int. Ed.* **2015**, *54*, 13027-13031.
- (22) X. Han, Q. Cheng, X. R. Meng, Z. C. Shao, K. Ma, D. H. Wei, J. Ding, H. W. Hou, *Chem. Commun.* **2017**, *53*, 10314-10317.
- (23) C. C. Epley, K. L. Roth, S. Y. Lin, S. R. Ahrenholtz, T. Z. Grove, A. J. Morris, *Dalton Trans.* **2017**, *46*, 4917-4922.
- (24) J. J. Yan, R. Homan, C. Boucher, P. N. Basa, R. L. Grimm, J. C. MacDonald, S. C. Burdette, *in preparation* **2018**.

- (25) Liu, T. F.; Lu, J.; Shi, L. X.; Guo, Z. G.; Cao, R. Conformation Control of a Flexible 1,4-Phenylenediacetate Ligand in Coordination Complexes: A Rigidity-Modulated Strategy. *Crystengcomm* **2009**, *11*, 583-588.
- (26) Sheldrick, G. M. *SADABS: Empirical Absorption Corrections Program*; University of Göttingen: Göttingen, Germany, **1997**.
- (27) *SAINT-Plus*; Bruker Analytical X-ray System: Madison, WI, **1999**.
- (28) Sheldrick, G. M. Crystal Structure Refinement with *SHELXL*. *Acta Crystallogr. C* **2015**, *71*, 3-8.
- (29) Bandara, H. M. D.; Kennedy, D. P.; Akin, E.; Incarvito, C. D.; Burdette, S. C. Photoinduced Release of Zn²⁺ with ZinClev-1: A Nitrobenzyl-Based Caged Complex. *Inorg. Chem.* **2009**, *48*, 8445-8455.
- (30) G. P. Yang, Y. Y. Wang, W. H. Zhang, A. Y. Fu, R. T. Liu, E. K. Lermontova, Q. Z. Shi, *Crystengcomm* **2010**, *12*, 1509-1517.
- (31) G. G. Sezer, O. Z. Yesilel, H. Erer, O. Sahin, *J. Solid State Chem.* **2016**, *233*, 463-470.
- (32) J. D. P. Margerum, C. T., *J. Am. Chem. Soc.* **1969**, *91*, 2467-2472.
- (33) J. M. Mewes, K. Neumann, M. K. Verhoefen, G. Wille, J. Wachtveitl, A. Dreuw, *Chemphyschem* **2011**, *12*, 2077-2080.
- (34) R. Lechner, S. Kummel, B. König, *Photochem. Photobiol. Sci.* **2010**, *9*, 1367-1377.
- (35) A. Itoh, T. Kodama, S. Inagaki, Y. Masaki, *Org. Lett.* **2000**, *2*, 331-333.
- (36) Y. Maki, M. Sako, I. Oyabu, T. Murase, Y. Kitade, K. Hirota, *J. Chem. Soc., Chem. Commun.* **1989**, 1780-1782.
- (37) H. Koshima, *Mol. Cryst. Liq. Cryst.* **2005**, *440*, 207-214.
- (38) Y. Wei, P. Hu, M. Zhang, W. P. Su, *Chem. Rev.* **2017**, *117*, 8864-8907.

- (39) H. T. Song, W. Ding, Q. Q. Zhou, J. Liu, L. Q. Lu, W. J. Xiao, *J. Org. Chem.* **2016**, *81*, 7250-7255.
- (40) Q. Feng, Q. L. Song, *J. Org. Chem.* **2014**, *79*, 1867-1871.
- (41) O. Karagiari, W. Bury, J. E. Mondloch, J. T. Hupp, O. K. Farha, *Angew. Chem. Int. Ed.* **2014**, *53*, 4530-4540.
- (42) K. K. Tanabe, S. M. Cohen, *Angew. Chem. Int. Ed.* **2009**, *48*, 7424-7427.
- (43) H. H. Fei, J. F. Cahill, K. A. Prather, S. M. Cohen, *Inorg. Chem.* **2013**, *52*, 4011-4016.
- (44) W. Bury, D. Fairen-Jimenez, M. B. Lalonde, R. Q. Snurr, O. K. Farha, J. T. Hupp, *Chem. Mater.* **2013**, *25*, 739-744.
- (45) K. L. Mulfort, O. K. Farha, C. L. Stern, A. A. Sarjeant, J. T. Hupp, *J. Am. Chem. Soc.* **2009**, *131*, 3866-3868.
- (46) L. Carlucci, G. Ciani, M. Moret, D. M. Proserpio, S. Rizzato, *Angew. Chem. Int. Ed.* **2000**, *39*, 1506-1510.
- (47) M. Moret, S. Rizzato, *Cryst. Growth Des.* **2009**, *9*, 5035-5042.
- (48) Z. F. Xin, X. S. Chen, Q. Wang, Q. Chen, Q. F. Zhang, *Microporous Mesoporous Mater.* **2013**, *169*, 218-221.
- (49) T. D. Bennett, J. C. Tan, Y. Z. Yue, E. Baxter, C. Ducati, N. J. Terrill, H. H. M. Yeung, Z. F. Zhou, W. L. Chen, S. Henke, A. K. Cheetham, G. N. Greaves, *Nat. Commun.* **2015**, *6*, 8079.
- (50) L. Valenzano, B. Civaleri, S. Chavan, S. Bordiga, M. H. Nilsen, S. Jakobsen, K. P. Lillerud, C. Lamberti, *Chem. Mater.* **2011**, *23*, 1700-1718.
- (51) M. R. DeStefano, T. Islamoglu, J. T. Hupp, O. K. Farha, *Chem. Mater.* **2017**, *29*, 1357-1361.

- (52) R. C. Klet, Y. Y. Liu, T. C. Wang, J. T. Hupp, O. K. Farha, *J. Mater. Chem. A* **2016**, *4*, 1479-1485.
- (53) H. Wu, Y. S. Chua, V. Krungleviciute, M. Tyagi, P. Chen, T. Yildirim, W. Zhou, *J. Am. Chem. Soc.* **2013**, *135*, 10525-10532.
- (54) H. Furukawa, U. Muller, O. M. Yaghi, *Angew. Chem. Int. Ed.* **2015**, *54*, 3417-3430.
- (55) F. Vermoortele, B. Bueken, G. Le Bars, B. Van de Voorde, M. Vandichel, K. Houthoofd, A. Vimont, M. Daturi, M. Waroquier, V. Van Speybroeck, C. Kirschhock, D. E. De Vos, *J. Am. Chem. Soc.* **2013**, *135*, 11465-11468.
- (56) B. Bueken, H. Reinsch, N. Reimer, I. Stassen, F. Vermoortele, R. Ameloot, N. Stock, C. E. A. Kirschhock, D. De Vos, *Chem. Commun.* **2014**, *50*, 10055-10058.
- (57) J. Park, Z. Y. U. Wang, L. B. Sun, Y. P. Chen, H. C. Zhou, *J. Am. Chem. Soc.* **2012**, *134*, 20110-20116.
- (58) A. K. Cheetham, T. D. Bennett, F. X. Coudert, A. L. Goodwin, *Dalton Trans.* **2016**, *45*, 4113-4126.
- (59) W. Huang, M. Zhang, S. D. Huang, D. Y. Wu, *Inorg. Chem.* **2017**, *56*, 6768-6771.
- (60) Y. D. Chiang, S. Bhattacharyya, K. C. Jayachandrababu, R. P. Lively, S. Nair, *ACS Sustainable Chem. Eng.* **2018**, *6*, 7931-7939.
- (61) E. J. Mittemeijer, *Fundamentals of Materials Science, The Crystal Imperfection; Lattice Defects*, Springer Berlin, Heidelberg, **2011**.
- (62) Z. L. Fang, B. Bueken, D. E. De Vos, R. A. Fischer, *Angew. Chem. Int. Ed.* **2015**, *54*, 7234-7254.
- (63) D. S. Sholl, R. P. Lively, *J. Phys. Chem. Lett.* **2015**, *6*, 3437-3444.

- (64) S. E. Dissegna, K. Epp, W. R. Heinz, G. Kieslich, R. A. Fischer, *Adv. Mater.* **2018**, *30*, 1704501.
- (65) U. Ravon, M. Savonnet, S. Aguado, M. E. Domine, E. Janneau, D. Farrusseng, *Microporous Mesoporous Mater.* **2010**, *129*, 319-329.
- (66) D. N. Bunck, W. R. Dichtel, *Chem. Eur. J.* **2013**, *19*, 818-827.
- (67) X. Q. Kong, H. X. Deng, F. Y. Yan, J. Kim, J. A. Swisher, B. Smit, O. M. Yaghi, J. A. Reimer, *Science* **2013**, *341*, 882-885.
- (68) O. V. Gutov, M. G. Hevia, E. C. Escudero-Adan, A. Shafir, *Inorg. Chem.* **2015**, *54*, 8396-8400.
- (69) F. Vermoortele, R. Ameloot, L. Alaerts, R. Matthessen, B. Carlier, E. V. R. Fernandez, J. Gascon, F. Kapteijn, D. E. De Vos, *J. Mater. Chem.* **2012**, *22*, 10313-10321.
- (70) B. B. Tu, Q. Q. Pang, D. F. Wu, Y. N. Song, L. H. Weng, Q. W. Li, *J. Am. Chem. Soc.* **2014**, *136*, 14465-14471.
- (71) P. Valvekens, D. Jonckheere, T. De Baerdemaeker, A. V. Kubarev, M. Vandichel, K. Hemelsoet, M. Waroquier, V. Van Speybroeck, E. Smolders, D. Depla, M. B. J. Roeffaers, D. De Vos, *Chem. Sci.* **2014**, *5*, 4517-4524.
- (72) B. Bueken, N. Van Velthoven, A. Krajnc, S. Smolders, F. Taulelle, C. Mellot-Draznieks, G. Mali, T. D. Bennett, D. De Vos, *Chem. Mater.* **2017**, *29*, 10478-10486.
- (73) S. Gadipelli, Z. X. Guo, *Chem. Mater.* **2014**, *26*, 6333-6338.
- (74) P. A. Szilagyi, P. Serra-Crespo, J. Gascon, H. Geerlings, B. Dam, *Front. Energy Res.* **2016**, *4*, 9.
- (75) X. R. Wang, L. Z. Zhai, Y. X. Wang, R. T. Li, X. H. Gu, Y. Di Yuan, Y. H. Qian, Z. G. Hu, D. Zhao, *ACS Appl. Mater. Interfaces* **2017**, *9*, 37848-37855.

**Chapter 5 On-Demand Guest Release from MOF-5 Sealed
with Nitrophenylacetate Photocapping Groups**

5.1. Introduction

Storage and transport of sensitive, volatile and reactive materials represents a significant challenge in a broad range of chemical research fields.¹⁻⁵ The blending of large void spaces and high surface areas impart metal organic frameworks (MOFs) with attractive properties for engineering storage systems for gases like H₂^{4,6} and CO₂.^{7,8} Trapping these gases, however, requires the MOFs to be contained within pressure vessels,⁹ so the primary benefits derive from van der Waals forces that increases the density of gas within the storage volume. Alternatively, intermolecular forces such as electrostatic interactions,^{10,11} hydrogen bonding,^{12,13} and π - π stacking^{14,15} can impart additional stabilization between MOFs and larger guests such as dye molecules; however, guests can leach out of the MOFs when the concentration gradient changes.¹⁶⁻

18

MOFs can also be conscripted for drug delivery, but storing and releasing therapeutic payloads in a constructive manner is limited by the same host-guest interactions. With weaker interactions, drug molecules leach from MOF pores passively, which might be exploited for gradual delivery, but could also squander valuable pharmaceuticals with premature release.¹⁸⁻²⁰ With strong interactions, drug molecules might be released more slowly than the rate of MOF excretion from the body.²¹⁻²³

The desired equilibrium between encapsulation and liberation might be achievable by manipulating intermolecular forces between MOFs and guests, but a triggered release mechanism would impart the necessary control for MOFs to be used more universally as delivery vehicles. Additive chelators have been used to control MOF crystal size,²⁴⁻²⁶ but fewer examples of MOFs with rationally modified surfaces exist. Post-synthetic MOF surface modifications have been used

to introduce fluorescent monolayers²⁷ and induce aggregation of crystals,²⁸ but the potential to trap guests in pores had not been explored until recently.

In recent investigations with MOF-5 ($\text{Zn}_4\text{O}(\text{BDC})_3$, BDC: 1,4-benzodicarboxylate), we demonstrated that introducing triphenylacetic acid (TPAA) capping groups effectively trap the large organic dye crystal violet (CV) within the MOF crystals. The observations were consistent with surface-bound TPAA groups blocking the MOF pores, which prevents the encapsulated dye from diffusing back into solution. Liberating the TPAA from the surface by protonation can reverse guest trapping, but acidic conditions can also degrade the MOF by extruding the carboxylate struts,^{29,30} so the pH must be controlled carefully to prevent unwanted decomposition. In parallel efforts, we have been exploring photodecarboxylation as a strategy to control the temporal and spatial release of metal ions in biology.³¹ We hypothesized that an analogous strategy could be used to engineer a MOF capping group that could be used to release guest molecules with light.

5.2. Experimental Section

5.2.1. General Procedures

All reagents were purchased and used without further purification, and reactions were carried out under an inert atmosphere. Previously reported procedures were used to prepare 1-bromomethyl-3-nitro-benzene (**1**)³² and methyl (2S) aminophenyl ethanoate (**2**).³¹ The capping group 3-nitrophenylacetic acid (**PC2, PhotoCap-2**) was purchased from Acros Organics. MOF-5 was synthesized following established procedures,³³ and its PXRD pattern was compared to simulated patterns from single crystal to confirm the uniformity of the crystalline sample. Acetonitrile (CH_3CN), diethylether (Et_2O) and tetrahydrofuran (THF) were sparged with argon and dried by passing through alumina-based drying columns. All chromatography and thin-layer

chromatography (TLC) were performed on silica (200-400 mesh). TLCs were developed by using CH₂Cl₂ or solvent mixtures containing CH₂Cl₂, hexanes, or diethyl ether (Et₂O). ¹H and ¹³C NMR spectra were recorded with a 500 MHz Bruker Biospin NMR instrument. Chemical shifts are reported in ppm relative to tetramethylsilane (TMS). FT-IR spectra were recorded using Bruker Vertex70 Optics FT-IR spectrometer equipped with a Specac Golden Gate attenuated total reflection (ATR) accessory by collecting 256 scans over a scan range from 4000 to 600 cm⁻¹ at 4 cm⁻¹ resolution. LC/MS was carried on a Single Quadruple, Agilent Technologies 1200 series LC system. GC/MS spectra were obtained from a Single Quadruple, Agilent Technologies 7890B GC system. Thermogravimetric analysis (TGA) measurements were carried out on a TA Instruments Hi-Res TGA 2950 Thermogravimetric Analyzer from room temperature to 800 °C under nitrogen atmosphere at a heating rate of 10 °C/min. High resolution mass spectra were obtained at the University of Notre Dame mass spectrometry facility using microTOF instrument operating in positive ionization mode. Melting-point information was obtained using a Hydrothermal Mel-Temp instrument.

[Bis-(3-nitro-benzyl)-amino]-phenyl-acetic acid methyl ester (3). Methyl (2S) aminophenyl ethanoate (**2**) (0.490 g, 2.95 mmol) was combined with 1-bromomethyl-3-nitro-benzene (1.29 g, 5.97 mmol), potassium carbonate (0.410 g, 2.97 mmol) and sodium iodide (0.134 g, 0.894 mmol) in dry CH₃CN (9 mL). After refluxing for 1 h, additional 1-bromomethyl-3-nitro-benzene (0.642 g, 2.97 mmol) and potassium carbonate (0.410 g, 2.97 mmol) was added to the reaction before refluxing for another 6 h, and stirred for an additional 16 h at 45 °C. Removal of precipitates by filtration and solvent removal provided the crude product as a yellow oil. Flash chromatography on silica (5:4 CH₂Cl₂/hexanes) yielded light yellow oil (0.675 g, 52.2%). TLC R_f = 0.57 (silica, 5:2 DCM/Hexanes). ¹H NMR (500 MHz, CDCl₃) δ 8.13 (s, 2 H), 8.07 (d, *J* = 8.12 Hz, 2 H), 7.63

(d, $J = 7.7$ Hz, 2 H), 7.46 (t, $J = 7.9$ Hz, 2 H), 7.32-7.42 (m, 5 H), 4.60 (s, 1 H), 3.94 (d, $J = 14.5$ Hz, 2 H), 3.85 (d, $J = 14.4$ Hz, 2H), 3.81 (s, 3 H); ^{13}C NMR (125 MHz) δ 172.1, 148.4, 141.4, 135.5, 134.6, 129.4, 128.9, 128.6, 123.5, 122.4, 66.91, 54.38, 51.9. FT-IR (diamond-ATR, cm^{-1}) 3084.4, 3065.6, 3032.4, 2957.0, 2928.8, 2849.0, 1738.6, 1602.4, 1527.1, 1498.8, 1456.8, 1437.9, 1353.2, 1282.3, 1207.5, 1169.9, 1136.6, 1075.7, 1004.8, 915.7, 854.2, 746.2, 699.1, 638.2. HRMS (+ESI) calculated for MH^+ 436.1503 and observed 436.1524.

[Bis-(3-nitro-benzyl)-amino]-phenyl-acetic acid (4). Compound **3** (0.100 g, 230 μmol) was dissolved in a mixture of MeOH (5 mL) and THF (2 mL), and sonicated for 5 min. Potassium hydroxide (KOH, 0.129 g, 2.30 mmol) was dissolved in MeOH (0.5 mL) and deionized water (0.5 mL). The KOH solution was added to the solution of compound **3** solution dropwise over 10 min at room temperature, and the sealed reaction vessel was placed in the dark for 36 h. After solvent removal, 2 g of crushed ice was added, and the pH was adjusted to ~ 5 with dilute HCl. The product was extracted into EtOAc (2 \times 25 mL), washed with saturated NaCl, and dried over Na_2SO_4 . Solvent removal yielded a brown powder without additional purification (66.0 mg, 68.1%). TLC $R_f = 0.68$ (silica, 5:2 Et₂O/hexanes); mp = 143-144 $^\circ\text{C}$. ^1H NMR (500 MHz, CD_3CN) δ 8.12 (s, 2 H), 7.97 (d, $J = 8.2$ Hz, 2 H), 7.67 (d, $J = 7.6$ Hz, 2 H), 7.50 (d, $J = 7.3$ Hz, 2 H), 7.43 (t, $J = 7.9$ Hz, 2 H), 7.38 (t, $J = 7.5$ Hz, 2 H), 7.30 (m, 1 H), 4.55 (s, 1 H), 4.00 (d, $J = 14.6$ Hz, 2 H), 3.83 (d, $J = 14.6$ Hz, 2 H); ^{13}C NMR (125 MHz) δ 173.6, 149.6, 143.3, 137.4, 136.4, 130.7, 130.6, 130.0, 129.7, 127.8, 123.3, 69.0, 56.0. FT-IR (diamond-ATR, cm^{-1}) 3078.3, 3036.5, 2921.3, 2851.7, 1711.7, 1587.3, 1522.6, 1448.7, 1347.1, 1213.5, 1185.8, 1135.2, 1089.0, 1028.7, 982.5, 927.1, 890.2, 858.1, 802.7, 733.7, 696.7, 669.0. HRMS (+ESI) calculated for MH^+ 422.1347 and observed 422.1325.

[Bis-(3-nitro-benzyl)-amino]-(3-nitro-phenyl)-acetic acid (5, PC1). Compound **4** (66.0 mg, 0.157 mmol) was dissolved in concentrated sulfuric acid (3.00 mL, 55.2 mmol) using sonication.

Concentrated nitric acid (0.100 mL, 1.17 mmol) was added drop wise to the mixture at 0 °C, and the sealed reaction vessel was placed in the dark for 1 h at 0 °C. The resultant reaction mixture was added dropwise to ice (50 g), and the product was extracted into EtOAc (2×50 mL). The combined organics were washed with saturated NaCl (15 mL), dried over Na₂SO₄, and the solvent was removed to yield an orange powder without additional purification (66.7 mg, 91.3 % yield). TLC R_f = 0.27 (silica, 5:2 Et₂O/hexanes); mp 117-118 °C dec. ¹H NMR (500 MHz, CDCl₃) δ 8.29 (s, 1 H), 8.24 (d, *J* = 8.2 Hz, 1 H), 8.17 (s, 2 H), 8.12 (d, *J* = 8.1 Hz, 2H), 7.77 (d, *J* = 7.8 Hz, 1 H), 7.61-7.69 (m, 3 H), 7.53 (t, *J* = 7.9 Hz, 2 H), 4.74 (s, 1 H), 4.00 (d, *J* = 14.4 Hz, 2 H), 3.87 (d, *J* = 14.3 Hz, 2 H); ¹³C NMR (125 MHz) δ 173.2, 148.5, 140.2, 137.0, 135.0, 135.6, 130.0, 129.8, 123.8, 123.6, 123.5, 122.9, 65.7, 54.4. FT-IR (diamond-ATR, cm⁻¹) 3087.5, 2925.6, 2851.7, 1739.4, 1619.9, 1531.9, 1458.0, 1347.1, 1310.2, 1273.2, 1227.6, 1195.0, 1167.2, 1135.2, 1098.3, 1042.9, 1010.3, 908.6, 839.6, 807.6, 728.8, 687.5, 673.4. HRMS (+ESI) calculated for MH⁺ 467.1197 and observed 467.1174.

5.2.2. Powder X-ray Diffraction

PXRD data were collected on a Bruker-AXS D8-Advance diffractometer using Cu-K α radiation with X-rays generated at 40 kV and 40 mA. Freshly prepared MOF-5 crystals were washed with a few drops of ethanol (EtOH) and blotted dry with a filter paper. A layer of parafilm was placed on the sample holder before the crystals were placed, a few drops of EtOH were added to prevent crystals from degradation. The sample was scanned at RT from 3° to 50° (2 θ) in 0.05° steps at a scan rate of 2°/min. Simulated PXRD patterns from single crystal data were compared to PXRD patterns of MOF-5, to confirm the uniformity of the crystalline sample.

5.2.3. Spectroscopy

General Spectroscopic Methods. All aqueous solutions were prepared from Millipore Biopak™ Ultrafiltration Cartridge purified water. All organic solutions were prepared using spectroscopic grade solvents. UV-vis absorption spectra were obtained by taking sample solutions in 1.0 cm quartz cuvette at 23 °C with total volumes kept at 2 mL or 3 mL and recorded on Thermo Scientific Evolution 300 UV-vis spectrometer with inbuilt Cary winUV software. Photolysis was carried at 23 °C in 1.0 cm quartz cuvette illuminated by 3 W UV LED (Mouser Electronics, 365 nm, 200 mW) powered by a 700 mA LuxDrive FlexBox using a variable DC source set at 12 VDC. Rate of photolysis and photoproducts were analyzed using LC/MS (Single Quadrupole, Agilent Technologies) by monitoring at changes at 277 nm. GC/MS spectra were obtained from a Single Quadrupole, Agilent Technologies 7890B GC system.

Quantum Efficiency and Photoproducts Determination. A 2 mL solution of **PC1** (2.50 mM) or **PC2** (4.76 mM) in MeOH containing 2.5% H₂O were prepared from 15 mM stock solutions and irradiated for 30, 60, 120, 300, 420, and 600 s. A separate 2 mL solution was used for each data collection. Samples were subjected to LC-MS analysis with ketoprofen (5 mM), as internal standard. The quantum efficiency was calculated using established procedures.³⁴ All samples were eluted with an isocratic mixture of 95:5 H₂O:CH₃CN containing 5 mM NH₄HCO₃ for **PC1**, or 0.5% formic acid for **PC2** at a flow rate of 0.3 mL/min. The compounds corresponding to the individual peaks in the LC of both compounds were identified by m/z values.

5.2.4. Guest Loading, Trapping and Release.

CVMOF. Freshly prepared MOF-5 (75.0 mg, 97.4 μmol) was washed with EtOH, blotted dry with filter paper and transferred into an EtOH solution of crystal violet (CV) (4 mL, 65.3 mM, 90% saturated). The mixture was kept in dark for 1 d at room temperature before the crystals were isolated and blotted dry with filter paper.

MOF Capacity Determination. CV loading amount was quantified using the following protocol: in to a vial was charged with 20 mL EtOH and 2.0 mg CV loaded MOF-5, with the addition of 10 μL concentrated HCl. Absorbance of digested solution at 580 nm was recorded and CV concentration was calculated using a calibration curve. Three trials gave an average loading capacity of 100 mg/g MOF (10 wt%).

CVMOF@PC1. CVMOF (25 mg) was added to 5 mL of DMF solution of [bis-(3-nitro-benzyl)-amino]-(3-nitro-phenyl)-acetic acid (**PC1**) (15.4 mg, 0.0330 mmol), with the addition of *N,N*-diisopropylethylamine (DIPEA) (6.3 μL , 0.036 mmol), zinc nitrate hexahydrate (20.0 mg, 0.0672 mmol), and CV (10.0 mg, 0.0245 mmol). The mixture was placed in dark at room temperature for 48 h, before the crystals were blotted dry with filter paper, quickly washed with small amount of EtOH, and transferred into EtOH solution for future use.

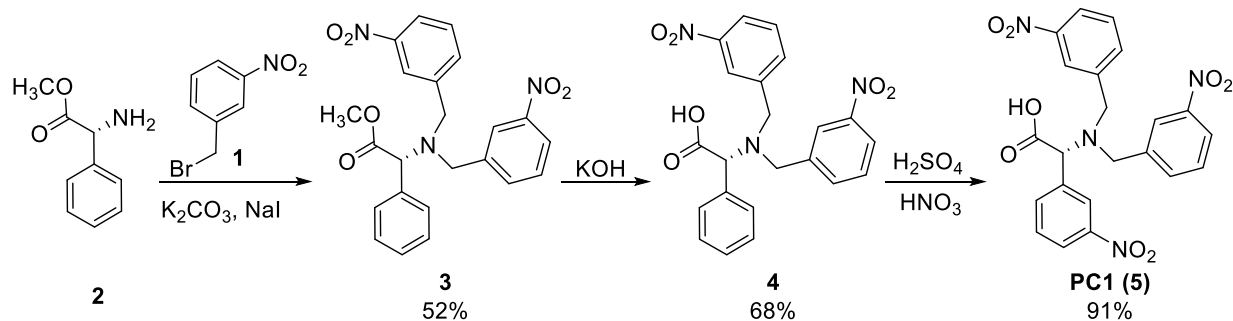
CVMOF@PC2. Guest loading and trapping with 3-nitrophenylacetic acid (**PC2**) (6.00 mg, 0.0331 mmol) was carried out analogously as CVMOF@**PC1** except the mixture was heated to 100 $^{\circ}\text{C}$ at 1 $^{\circ}\text{C}/\text{min}$, kept at 100 $^{\circ}\text{C}$ for 48 h, and cooled to room temperature at 0.25 $^{\circ}\text{C}/\text{min}$, and without the addition of DIPEA.

CVMOF@TPAA and CVMOF@DBA. Guest loading and trapping with TPAA (9.54 mg, 0.0331 mmol) and dibenzylamine (DBA) (6.53 mg, 0.0331 mmol) were carried out analogously as CVMOF@PC2.

CV Release from Capped Systems. Capped crystals (0.7 mg) were dispersed in 2.5 mL EtOH and the absorbance (450–650 nm) was recorded at 10 min increments for 90 min in the dark, and then at 10 min increments while continuously irradiating for 90 min. The supernatant was decanted and replaced with 2.5 mL EtOH and irradiation was continued for 30 min and the absorbance recorded. Under continuous irradiation, the decanting and replenishment procedure were repeated three times until no further absorbance increase was observed. Experiments were performed in triplicate.

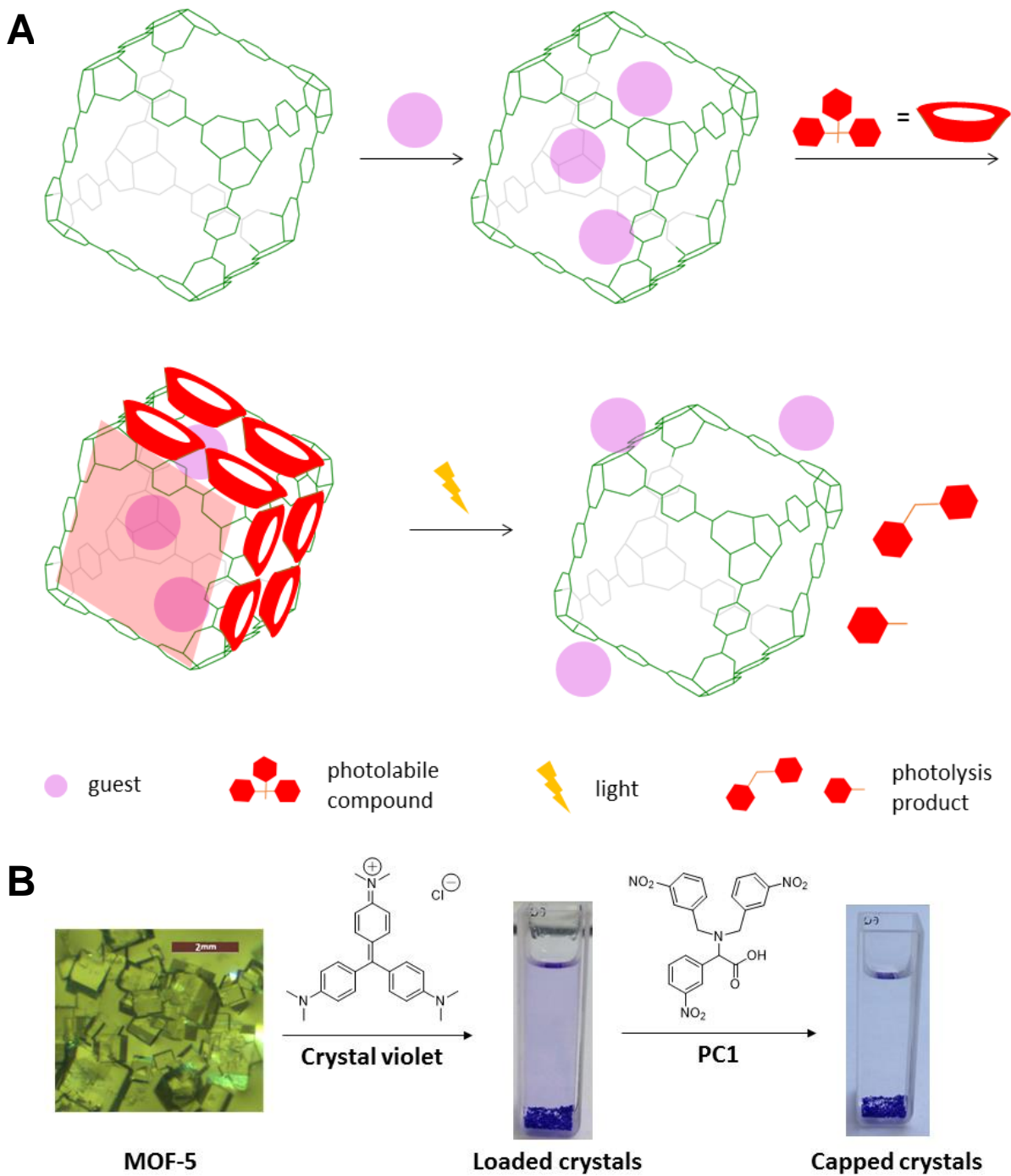
5.3. Guest Trapping Strategy and Photolabile Capping Group Synthesis and Characterization

MOF-5 contains an internal void cavity sphere with diameter of 18.5 Å as calculated by Cerius³⁵ formed by the Zn₄O nodes and BDC struts.^{33,35} The 7.6 Å spherical radius of CV,³⁶ the dye utilized in our previous studies, lies near the upper size limit of guests that MOF-5 can accommodate. Early results from molecular dynamics simulations suggest that TPAA capping groups bound to surface Zn₄O nodes can associate with adjacent capping groups. A critical result of these interactions is a decrease in the accessible area between these capping groups that may limit the exit of any guest with a radius larger than 2.7 Å. Smaller carboxylate capping groups also prevent CV leakage to varying degrees, which suggests either differing modes of capping group coordination to the MOF surface, or that trapping a guest as large as CV does not require a bulky capping group. Additional simulations and experiments with implications for pore capping, guest trapping, and interfacial MOF chemistry are the subject of ongoing investigations.



Scheme 5.1. The synthetic route of photolabile compound **PC1**.

Since TPAA most effectively prevented CV release, we rationalized that a TPAA derivative capable of undergoing photodecarboxylation would be the ideal candidate to test our light-driven guest release hypothesis. Attempts to nitrate TPAA directly provided an inseparable mixture of products due to non-specific nitration at *ortho*-, *meta*- and *para*-positions on all three phenyl rings, so a new target was designed. Our Zn^{2+} photocage is based on a phenylglycine framework, and the compounds undergo stereoselective nitration at the *meta*-position.³¹ The α -amine can also be alkylated using a variety of electrophiles. We reasoned that alkylating the amine with deactivated benzylic groups would not only provide a capping group with the necessary steric bulk, but also yield a compound where a single phenyl group could be nitrated cleanly. By treating phenylglycine methyl ester with 3-nitrobenzyl bromide, we obtained **3** in reasonable yield (Scheme 5.1). After saponification, the carboxylic acid **4** was nitrated to yield pure **PC1 (PhotoCap-1)** in 32% overall yield for the three-step reaction sequence.



Scheme 5.2A. Guest molecule loading into MOF-5 channels, encapsulating by surface coordination of capping reagents, and light induced guest release. **5.2B.** Photos taken of MOF-5 crystals before and after CV loading, and soaking in EtOH before light induced release.

The photoactivity of **PC1** was assessed by LCMS and GCMS analysis after photolysis with 365 nm light. Upon irradiation, two new peaks appeared in the LC trace corresponding to bis(*m*-nitrobenzyl)amine and *m*-nitrobenzaldehyde (Figure 5.1, Scheme 5.3). A 28% photolysis quantum yield ($\Phi_{\text{photolysis}}$) was calculated by monitoring the disappearance of **PC1**. **PC2** is less sterically demanding than **PC1**, but we still anticipated would efficient blocking the MOF-5 pores for larger guests. Earlier investigations demonstrated that although a large capping group like TPAA efficiently trap CV in MOF-5, smaller carboxylate ligands could also prevent CV release to varying degrees. As the smallest possible *m*-nitrophenylacetic acid derivative, analysis of the trapping efficiency and guest release with **PC2** would help establish thresholds necessary to trap CV in MOF-5. The photoactivity of **PC2** was analyzed analogously to **PC1** (Figure 5.2, Scheme 5.4), and the primary photoproduct detected was 3-nitrotoluene with $\Phi_{\text{photolysis}}$ of 9.5%.

5.4. Guest Molecule Loading and Release

MOF-5 encapsulates 10 wt% CV (**CVMOF**), which is comparable to CV loading in CuBTC MOF, which contains either 11.9 wt% or 27.5 wt% CV depending on the preparation method.³⁷ MOF-5 can absorb up to 59.2 wt% capsaicin, 31.5 wt% 5-fluorouracil,³⁸ or 20 wt% benzene.³⁹ The loading capacity can be rationalized on the relative size of each guest, and although capsaicin is large in one dimension, CV has a larger diameter and is more spherical than cylindrical compared to capsaicin. In the absence of a capping group, rapid CV release from **CVMOF** is evident upon visual inspection, which suggests CV slowly leaks from inside the MOF into the EtOH solution. Equilibrium is reached after 2 h with approximately 45% of the internalized CV having been released (Figure 5.3). After three cycles that involve decanting the supernatant and replacement with fresh EtOH, almost 60% of the total CV can be recovered. Some residual CV remains permanently associated with the MOF barring treatment with acid or other harsh

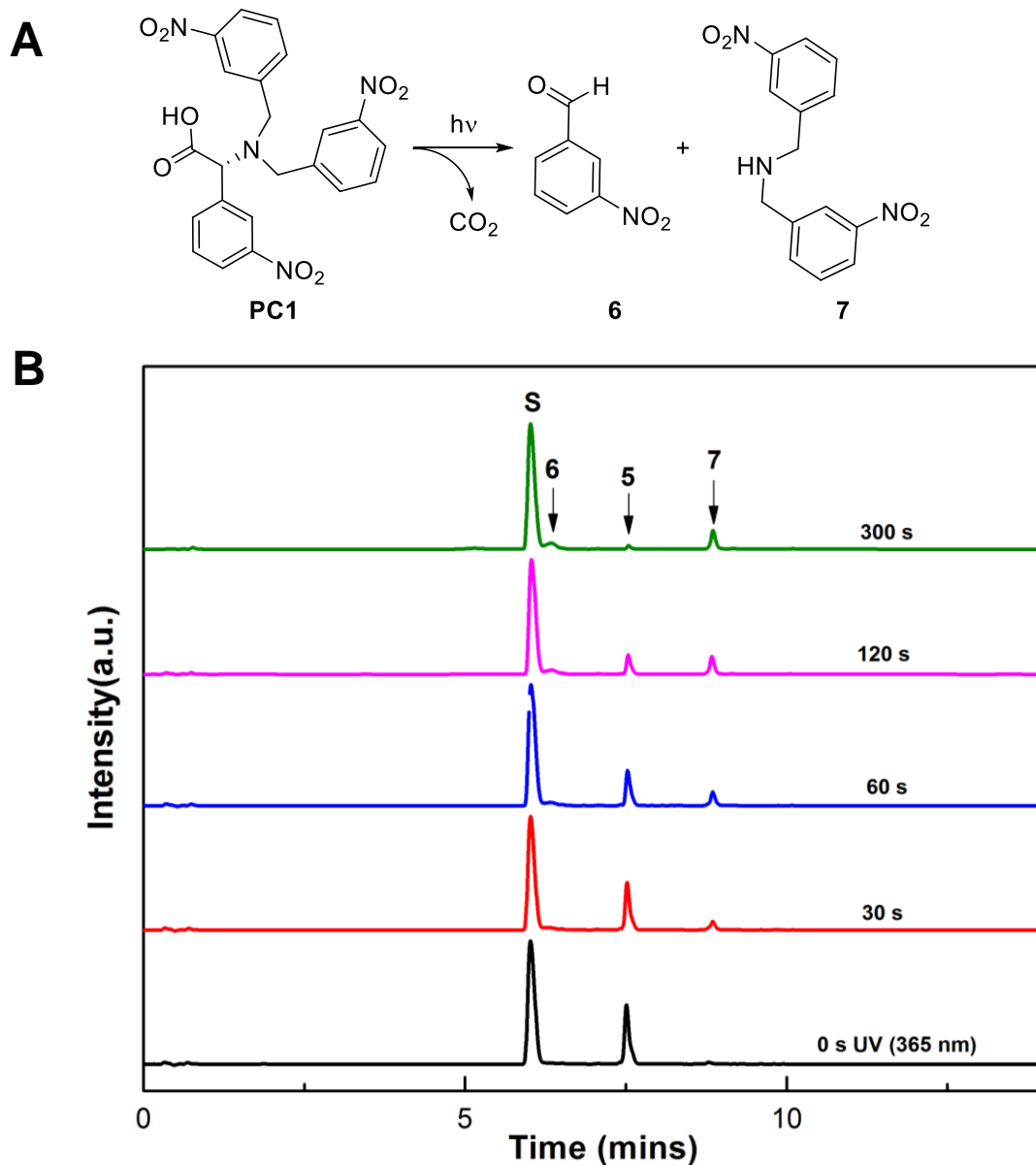


Figure 5.1A. The possible photolysis route of **PC1** undergoing photodecarboxylation. **5.1B.** HPLC analysis of the photolysis of **PC1** in MeOH (2.5% water), ketoprofen was used as internal standard (S). A decrease in the intensity of **PC1** (**5**) and an increase in the intensities of photoproducts including *m*-nitrobenzaldehyde (**6**), and bis(*m*-nitrobenzyl)amine (**7**), upon UV (LED, 365 nm) exposure (0 to 5 min) was observed.

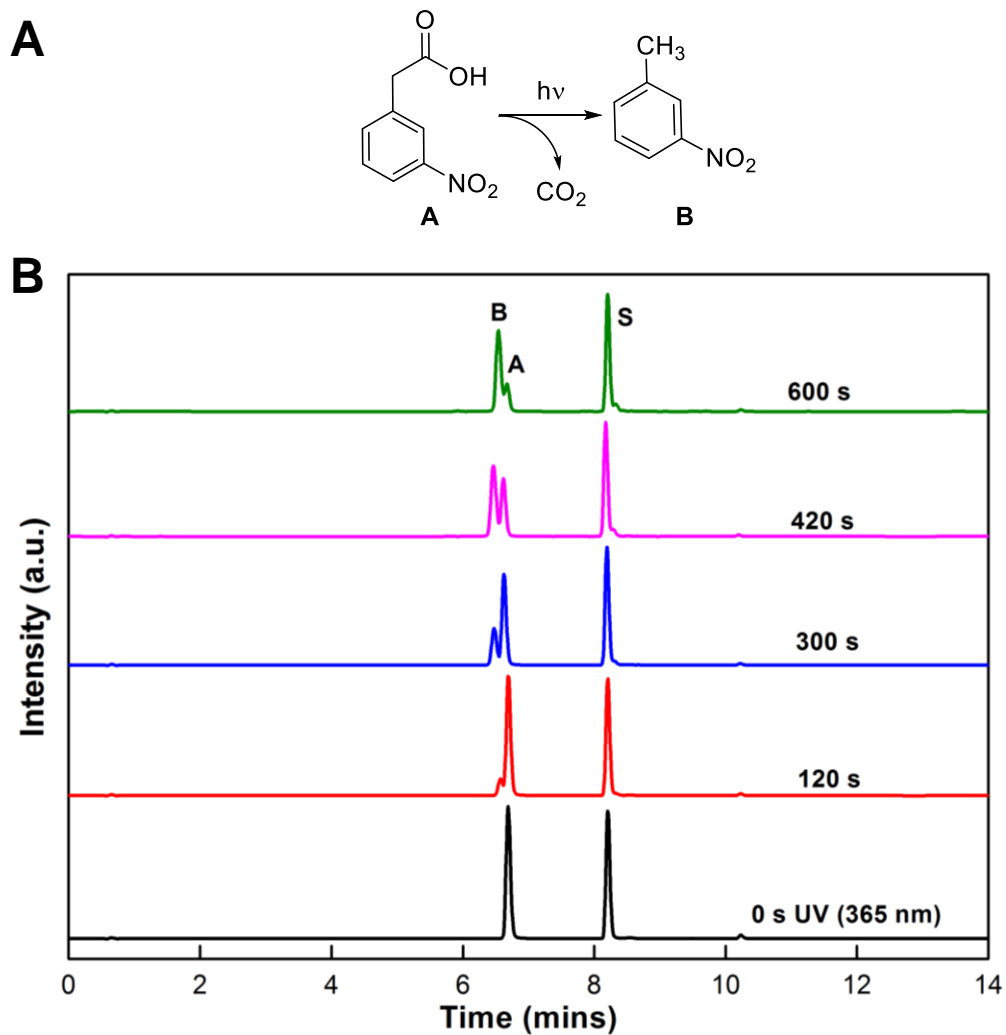
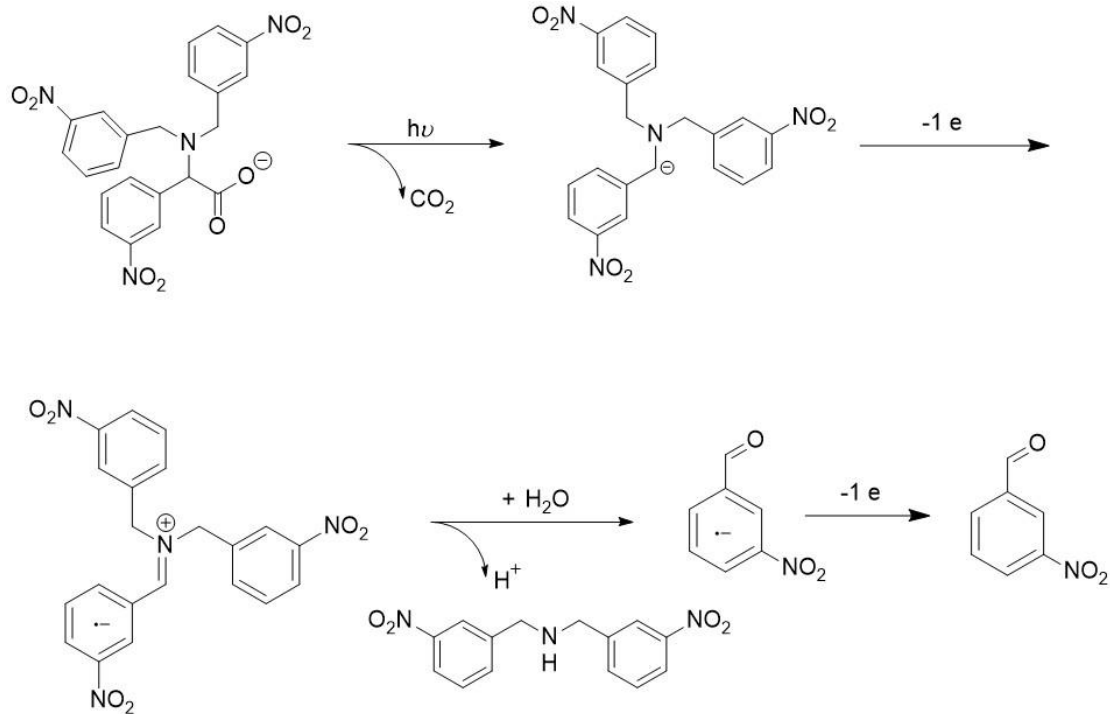
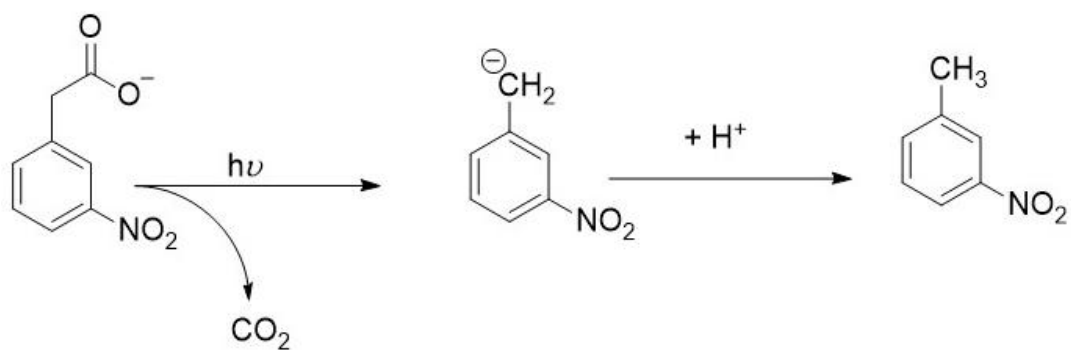


Figure 5.2A. The possible photolysis route of PC2 undergoing photodecarboxylation. **5.2B.** HPLC analysis of the photolysis of PC2 in MeOH (2.5% water), ketoprofen was used as internal standard (S). A decrease in the intensity of PC2 (A) and an increase in the intensities of photoproduct 3-nitrotoluene (B) upon UV (LED, 365 nm) exposure (0 to 10 min) was observed.



Scheme 5.3. Proposed mechanism for the photolysis of PC1. There are two major products after decarboxylation and hydrolysis, bis(*m*-nitrobenzyl)amine and *m*-nitrobenzaldehyde. The probable oxidant is dissolved oxygen.



Scheme 5.4. Proposed mechanism of photolysis of PC2. The major photolysis product is 3-nitrotoluene.

conditions that compromise the macromolecular structure. These results are similar to the amount of CV released from mechano-synthesized CuBTC MOF (52%),³⁷ which can be attributed to the similarity in pore sizes and internal surface chemistry.⁴⁰ The persistence of some CV in both MOF-5 and CuBTC MOF suggests the strong π - π stacking interactions that prevent complete guest release. The plateauing of CV release may also indicate there are steric barriers to releasing large guests if they penetrate deeply into the MOF that are not present with smaller guests like capsaicin and 5-fluorouracil that are released more efficiently (>70%).³⁸

CVMOF@TPAA. While uncapped ***CVMOF*** rapidly releases CV until an apparent equilibrium is reached, introducing TPAA can effectively trap CV within the MOF crystals. After subjecting ***CV@MOF*** to a capping procedure, ***CVMOF@TPAA*** shows negligible loss of CV over extended periods of time (Figure 5.4, black curve). This suggests the dye remains internalized due to surface-bound TPAA groups blocking the MOF pores. Although CV can be released after treatment with strong acid, this approach is susceptible to degrading the MOF structure in addition to releasing the CV guest, and lacks the desired degree of finesse for applications in controlled release.

CVMOF@PC1 and CVMOF@PC2. The TPAA capping groups originally were introduced to MOF-5 using additional Zn^{2+} and temperatures analogous to solvothermal conditions used to prepare MOF-5. Owing to the thermal instability of ***PC1***, a modified room temperature synthesis of ***CVMOF@PC1*** was devised. In contrast to solvothermal conditions where DMF or DEF decomposition releases amines to serve as bases,⁴¹ the room temperature synthesis requires the addition of a base to buffer the protons from the ligand. DIPEA (*N,N*-diisopropylethylamine) is sufficiently basic to deprotonate the carboxylate ligands, but cannot interact strongly with the MOF

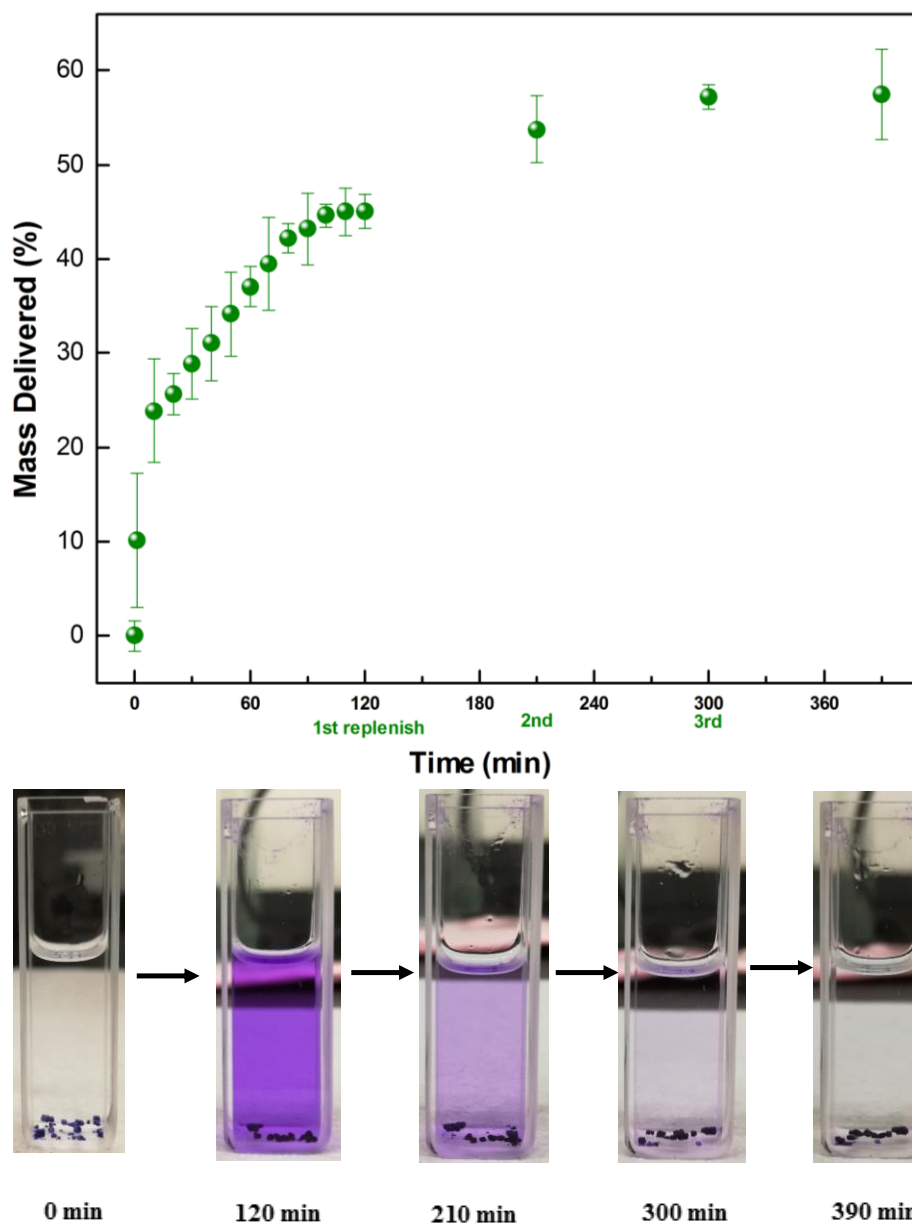


Figure 5.3A. CV release profile from CVMOF without capping. Details: UV cuvette was charged with 0.7 mg of crystals and filled with 2.5 mL EtOH, the absorbance of which was monitored by UV-Vis instrument at 580 nm. The system was kept in dark for 120 min until equilibrium reached, and supernatant was decanted and replenished with 2.5 mL fresh EtOH, with absorbance recorded after 90 min. Three replenishment cycles were conducted until no further releasing was observed. **5.3B.** Photos taken in the CV release process. Experiments were performed in triplicates.

surface owing to the steric congestion provided by the alkyl substituents. **CVMOF@PC2** can be prepared by analogous solvothermal conditions used to prepare capped **CVMOF@TPAA**. Both capping protocols were successful as indicated by the transformation of the MOF-5 from clear to purple crystals where the coloration persists when the MOF crystals are immersed in EtOH for 24 h (Scheme 5.2B).

PC1 was designed to mimic the steric requirements of TPAA, and **CVMOF@PC1** exhibits a lack of CV release similar to **CVMOF@TPAA** under light-free conditions (Figure 5.4, red curve). When light is introduced however, a dramatic increase in CV absorbance is measured in the solution containing the **CVMOF@PC1** crystals. Equilibrium is reached after 1 h of irradiation after approximately 20% of the CV has been released. Following four cycles that involve decanting the supernatant, replacing the CV-containing solvent with fresh EtOH, and irradiating for additional time periods, over 30% of the originally internalized dye can be recovered. Our previous investigations demonstrated that amines can also seal CV inside MOF channels, so we hypothesize the bis(*m*-nitrobenzyl)amine photoproduct (**7**) from **PC1** photolysis blocks MOF pores after photolysis. The control compound DBA, a structural analog of **7**, was used to prepare **CVMOF@DBA**, and capping experiments suggests MOF pores are partially blocked in the presence of diamines of this size.

To test the size-dependence of the pore blocking, **PC2** was used to prepare **CVMOF@PC2**. **PC2** is the smallest possible nitrophenylacetic acid derivative that will undergo photodecarboxylation. Similar to both TPAA and **PC1**, **PC2** traps CV in MOF-5 (Figure 5.4, blue curve) with only slightly higher leaking of the dye into solution after capping. This suggests large guests like CV may not require bulky capping groups to achieve guest trapping whereas this might not be sufficient to contain smaller guests. Consistent with our hypothesis and model studies with

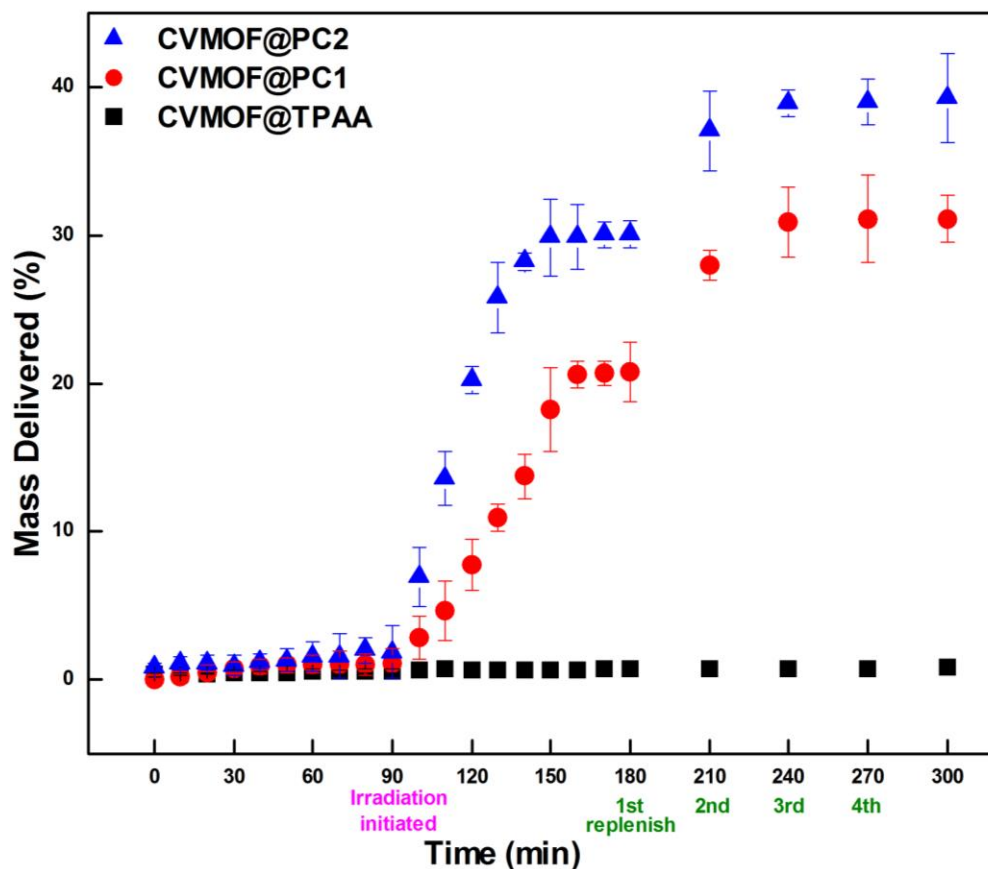


Figure 5.4. In dark and photo-triggered CV release profile of CVMOF@PC1, CVMOF@PC2 and CVMOF@TPAA. Details: UV cuvette was charged with 0.7 mg of capped crystals and filled with 2.5 mL EtOH, the absorbance of which was monitored by UV-Vis instrument at 580 nm. The system was kept in dark for 90 min, and irradiated for 90 min of allowing equilibrium reached, before replenishing with 2.5 mL fresh EtOH and irradiation for another 30 min. Four replenishments and irradiation cycles were conducted, and no further CV releasing was observed. Experiments were performed in triplicates.

diamine trapping, 30% of the initial CV is released from CVMOF@PC2 after only 1 h of irradiation since the 3-nitrotoluene photoproduct cannot bind to the MOF surface (Figure 5.4). Following four cycles of solvent replacement almost 40% of the CV can be recovered. The reduced leaching of CV compared to CVMOF may indicate that the smaller PC2 photocapping group can enter the MOF channels where the photodecarboxylation reaction is inhibited.

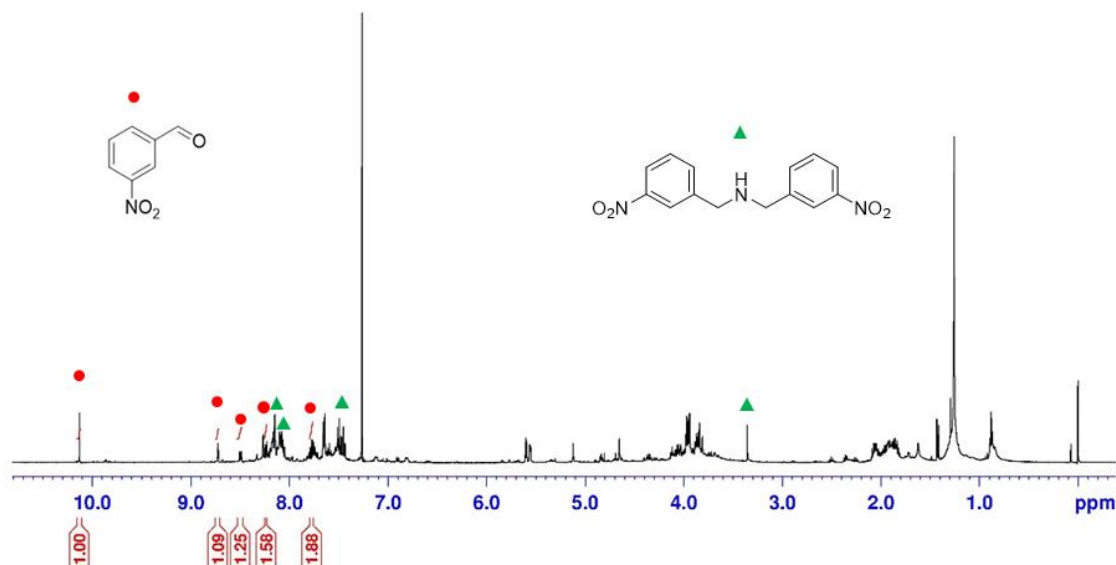


Figure 5.5. ^1H NMR spectroscopy of PC1 in MeOH containing 2.5% H_2O (2 mL, 15 mM) after irradiation with 365 nm (LED, 3 W cm^{-2}) for 20 mins. Solvent removal and NMR in CDCl_3 shows photoproducts *m*-nitrobenzaldehyde (6) and bis(*m*-nitrobenzyl)amine (7).

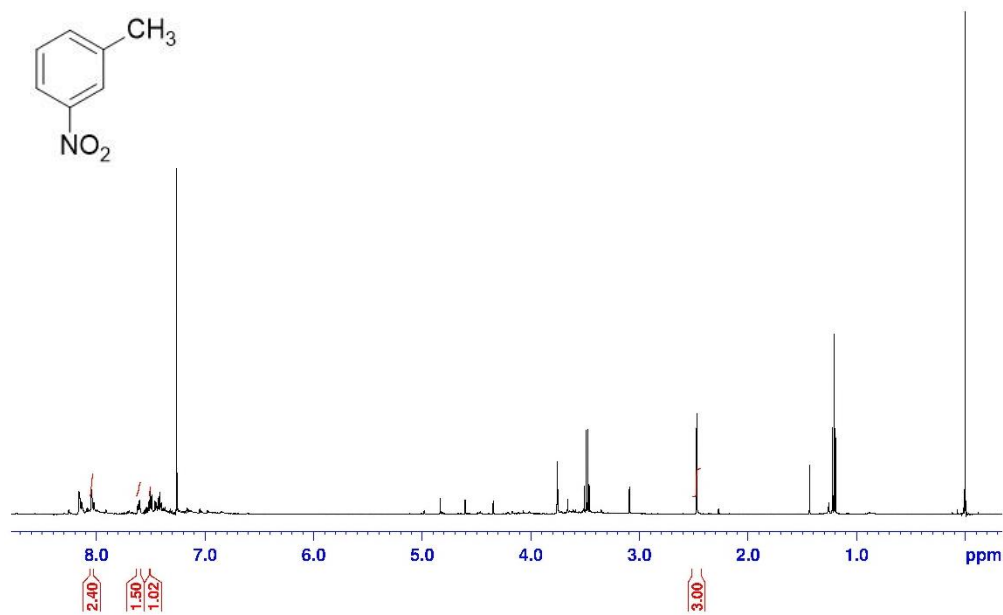


Figure 5.6. ^1H NMR of photoproducts after PC2 photolysis. The major product 3-nitrotoluene can be clearly observed.

5.5. Conclusions

Photocapping reagents have been introduced to the surface of MOF-5 to trap CV, which can be only liberated upon irradiation. This approach provides a novel process for introducing trapped MOF guests with light that can be developed for a variety of applications that require encapsulation and controlled release of small molecules. Despite the size discrepancy, both **PC1** and **PC2**, exhibit similar trapping and releasing properties when used in conjunction with a large guest like CV. Correlating trapping and releasing abilities with the sizes of caps and guest will require a systematic investigation that will also include probing the nature of the capping group–MOF surface interaction. Our current efforts are focused on both understanding the relationship between different capping groups and various guests, as well as exploring whether analytical techniques such as X-ray photoelectron spectroscopy can provide insight into how these carboxylic acid groups interact with the MOF surface. As we explore MOF-5 as well as other three-dimensional coordination polymers, we anticipate this approach will lead to a more general approach to exploiting MOFs for the storage and delivery of guest molecules.

5.6. Acknowledgement

This chapter is based on joint work with Dr. John C. MacDonald at Department of Chemistry and Biochemistry, Worcester Polytechnic Institute. This on-demand photo-induced crystal violet release project is derived from previous unpublished results in Dr. John C. MacDonald's group, on the investigation of crystal violet sealing and releasing from MOF-5 with different capping reagents. I would also like to thank REU student Rick Homan from MacDonald group doing many experiments on MOF preparation and CV releasing, and REU student Corrianna Boucher and Katherine Fossum at Burdette group doing capping reagent PC1 and MOF-5 synthesis work.

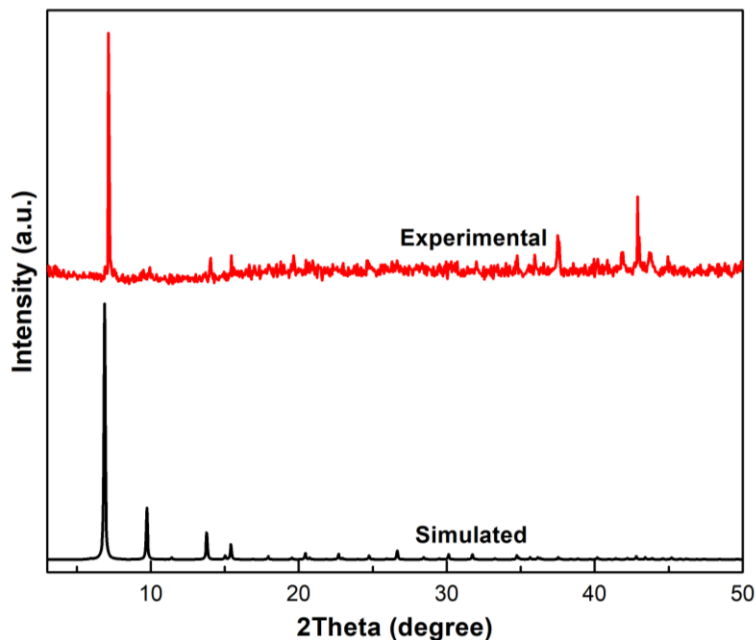


Figure 5.7. Powder X-ray diffraction patterns of MOF-5. Both experimental and simulated patterns from single crystal structures are shown to confirm the phase purity.

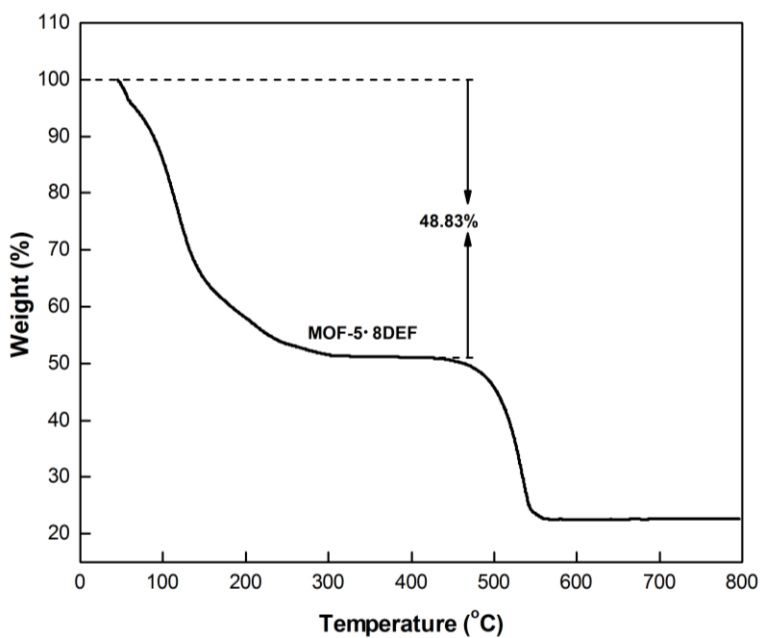


Figure 5.8. The thermogravimetric analysis (TGA) diagram of fresh prepared MOF-5. The solvent weight loss is calculated to 48.83%, and by using the formula $Zn_4O(C_8H_4O_4)_3 \cdot X(C_5H_{11}O)$, X can be calculated to be 8, meaning there are 8 DEF molecules per MOF unit cell. The curve also suggests MOF-5 can persist to 400 °C, which is a typical range for MOF-5.

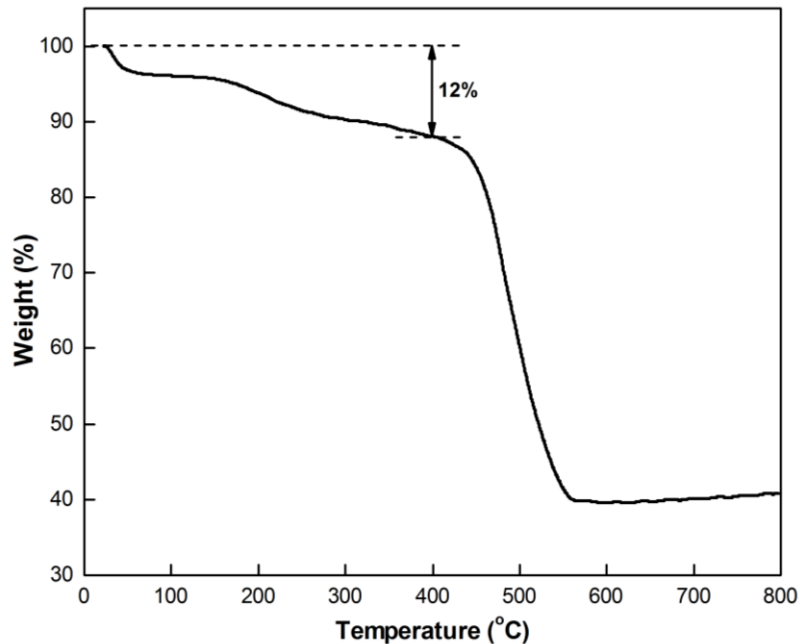


Figure 5.9. The thermogravimetric analysis (TGA) diagram of CVMOF after heated in 60 °C oven for 1 h. The weight loss before 400 °C can be attributed to the weight of loaded CV, which is 12%.

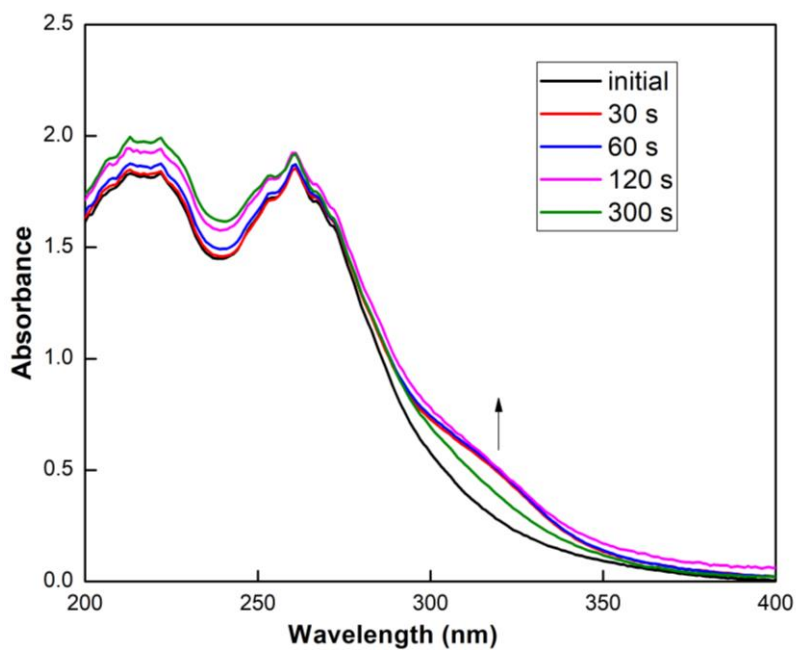
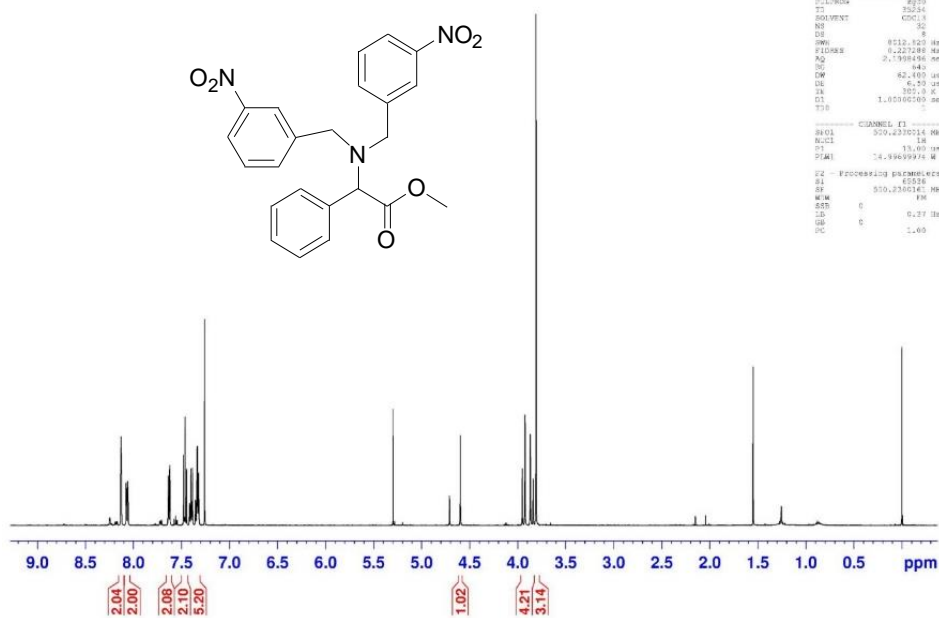


Figure 5.10. UV-Vis absorbance spectra showing photolysis of PC1 (100 μ M) in MeOH (2.5% water). Irradiation at 365 nm leads to the new bands forming in the absorption range from 300 to 350 nm, indicating the forming of photoproducts.

ADVISOR Burdette
Disubstituted product after column

PROTON



```

Current Data Parameters
NAME: 2511-05-04-19en-6E
EXPNO: 2
PROCNO: 1
F2 - Acquisition Parameters
Date_ 20150804
Time 25.03
INSTRUM spect
PROBHD 5 mm EASY-13C
P1 12.00000000
T1 300.2
SOLVENT CDCl3
NS 8
DS 4
SWH 812.823 Hz
FIDRES 0.227288 Hz
AQ 0.1709156 sec
RG 640
AQ 0.1709156 sec
DE 4.40
WDW EM
SSB 0
GB 0
PC 1.00
===== CHANNEL f1 =====
NUC1 13C
PULPROG zgpg30
PC 19.00
SFO1 125.7603500 MHz
===== CHANNEL f2 =====
F2 - Processing parameters
SI 65536
SF 500.1360400 MHz
WDW EM
SSB 0
GB 0
PC 1.00

```

Figure 5.11. ¹H NMR of [bis-(3-nitro-benzyl)-amino]-phenyl-acetic acid methyl ester (3).

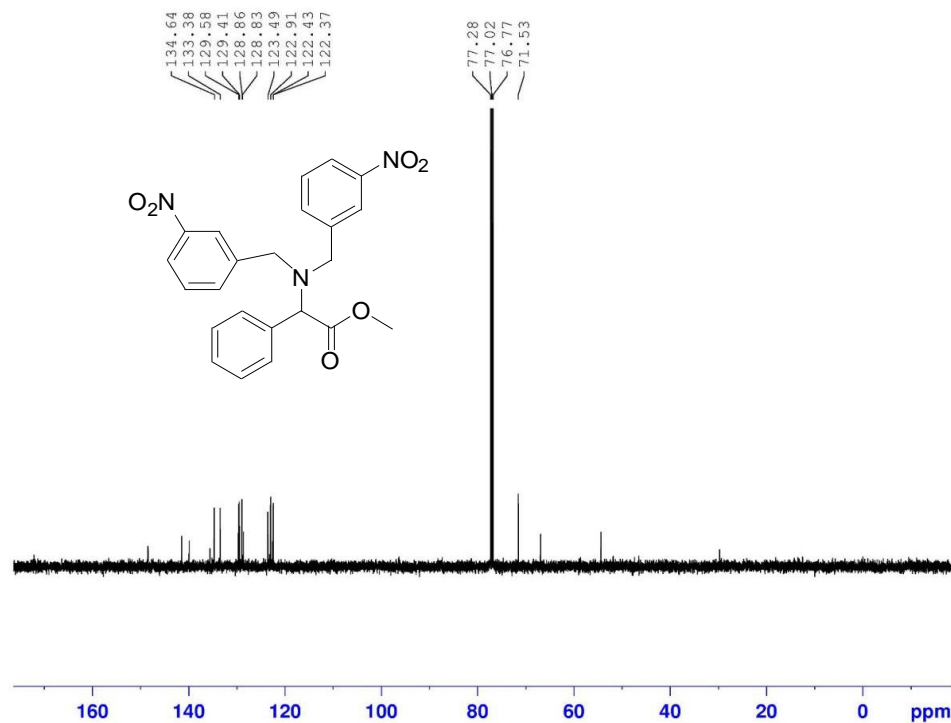
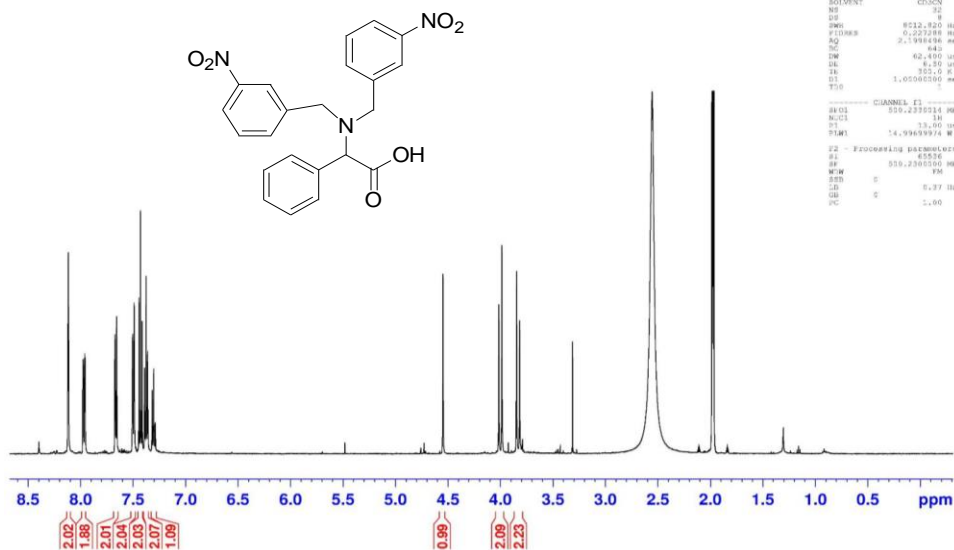


Figure 5.12. ¹³C NMR of [bis-(3-nitro-benzyl)-amino]-phenyl-acetic acid methyl ester (3).

ADVISOR Burdette
Hydrolysis product
PROTON

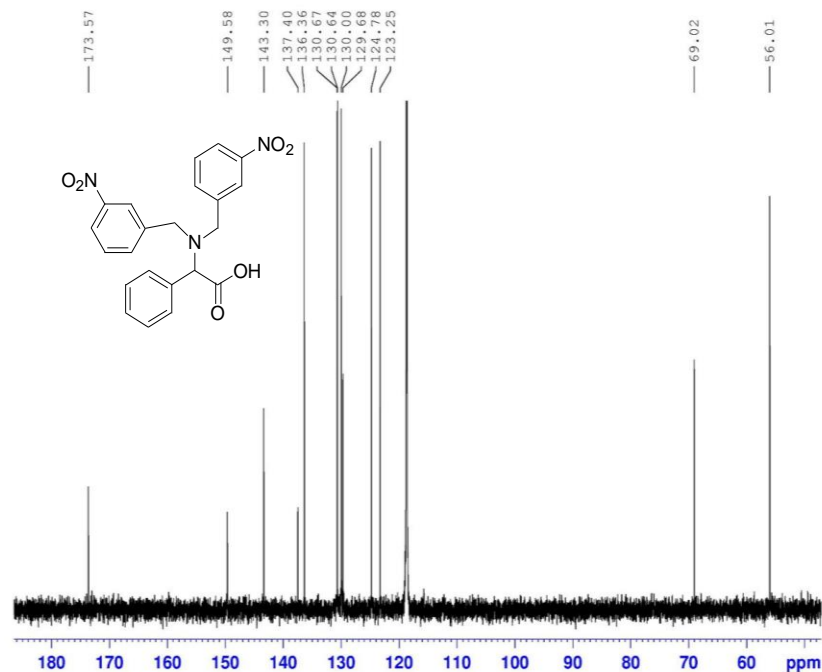


```

Current Data Parameters
NAME      2017-01-10-01-conduct
EXPNO    1
PROCNO   1
F2 - Acquisition Parameters
Date_    20170110
Time     11:12
INSTRUM  spect
PROBHD   5 mm F400
PULPROG  zgpg30
TD       65536
SOLVENT  CDCl3
NS       124
DS       2
SWH      8032.850 Hz
FIDRES   0.227288 Hz
AQ       3.198436 sec
RG        440
DW       62.490 usec
DE       8.10 usec
TE       302.0 K
D1       1.0500000 sec
TD0      1
----- CHANNEL f1 -----
NUC1     13C
P1       13.00 usec
PL1      14.9949974 W
F2 - Processing parameters
SI       65536
SF       500.2305500 MHz
WDW      EM
SSB      0
GB       0
PC       1.00
  
```

Figure 5.13. ¹H NMR of [bis-(3-nitro-benzyl)-amino]-phenyl-acetic acid (4).

ADVISOR Burdette
Hydrolysis product without extraction
CARBON



```

Current Data Parameters
NAME      2017-01-01-conduct
EXPNO    2
PROCNO   1
F2 - Acquisition Parameters
Date_    20170102
Time     11:26
INSTRUM  spect
PROBHD   5 mm F400
PULPROG  zgpg30
TD       65536
SOLVENT  CDCl3
NS       124
DS       2
SWH      37500.200 Hz
FIDRES   0.832587 Hz
AQ       0.6023447 sec
RG        440
DW       13.333 usec
DE       6.50 usec
TE       302.0 K
D1       0.2500000 sec
D11      0.0500000 sec
TD0      1
----- CHANNEL f1 -----
NUC1     13C
P1       9.10 usec
PL1      39.9939948 W
----- CHANNEL f2 -----
NUC2     13C
P2       13.00 usec
PL2      14.9949974 W
PL3      0.2534500 W
F2 - Processing parameters
SI       65536
SF       125.7627624 MHz
WDW      EM
SSB      0
GB       0
PC       1.00
  
```

Figure 5.14. ¹³C NMR of [bis-(3-nitro-benzyl)-amino]-phenyl-acetic acid (4).

ADVISOR Burdette
Nitration product in CDCl3
PROTON

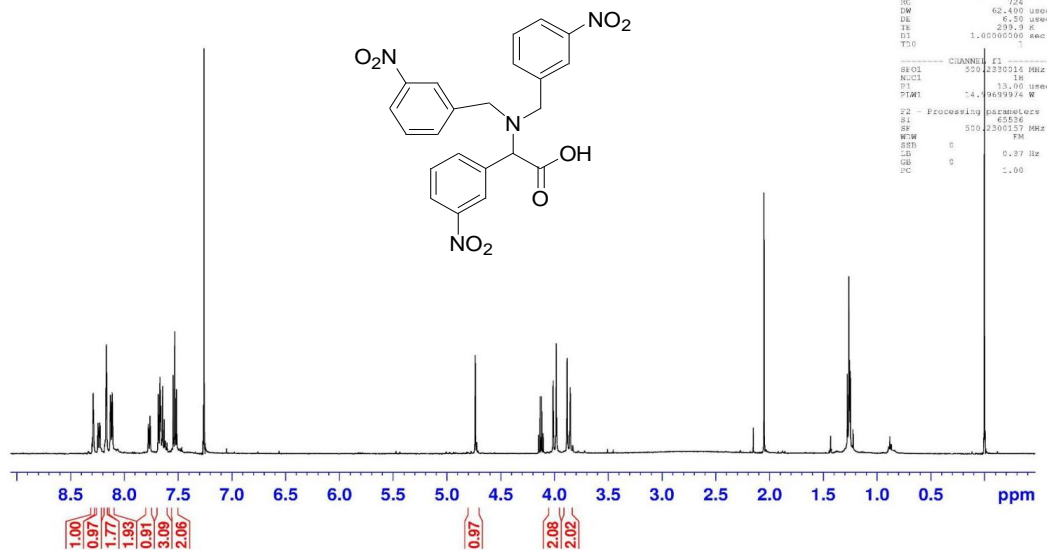


Figure 5.15. ¹H NMR of [bis-(3-nitro-benzyl)-amino]-(3-nitro-phenyl)-acetic acid (PC1).

ADVISOR Burdette
Final product c13 NMR
CARBON

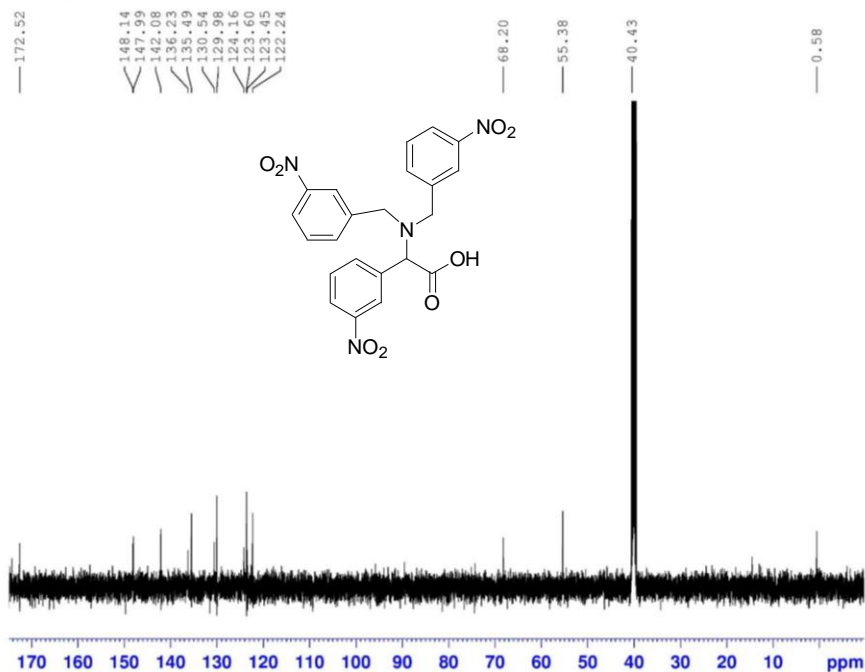


Figure 5.16. ¹³C NMR of [bis-(3-nitro-benzyl)-amino]-(3-nitro-phenyl)-acetic acid (PC1).

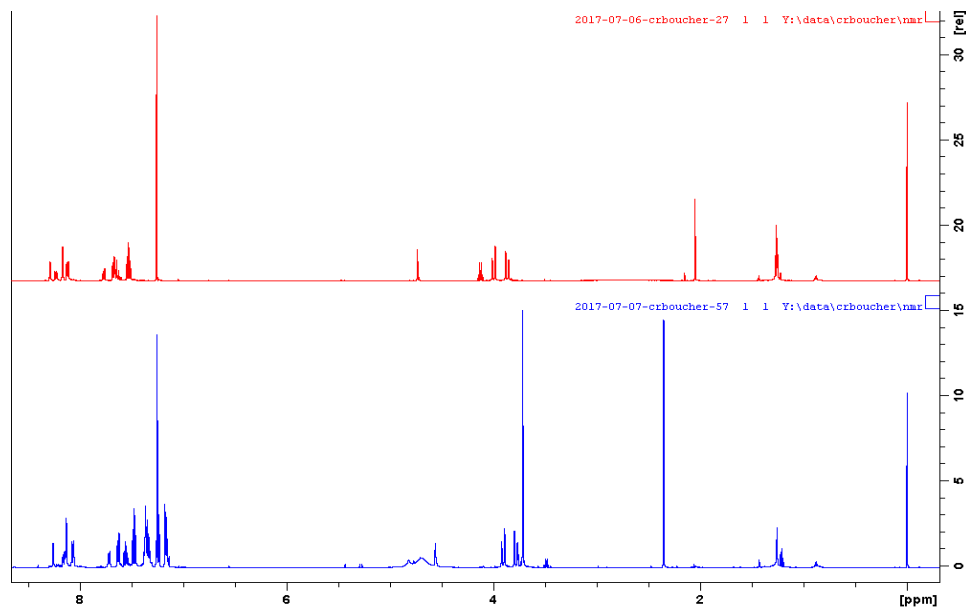


Figure 5.17. ¹H NMR spectroscopy showing thermal decomposition of compound **PC1**. Upper (red) spectrum is the original compound, and lower (blue) spectrum is after heating at 80 °C for 24 h. New peaks coming out after heating could belong to **PC1** degradation products.

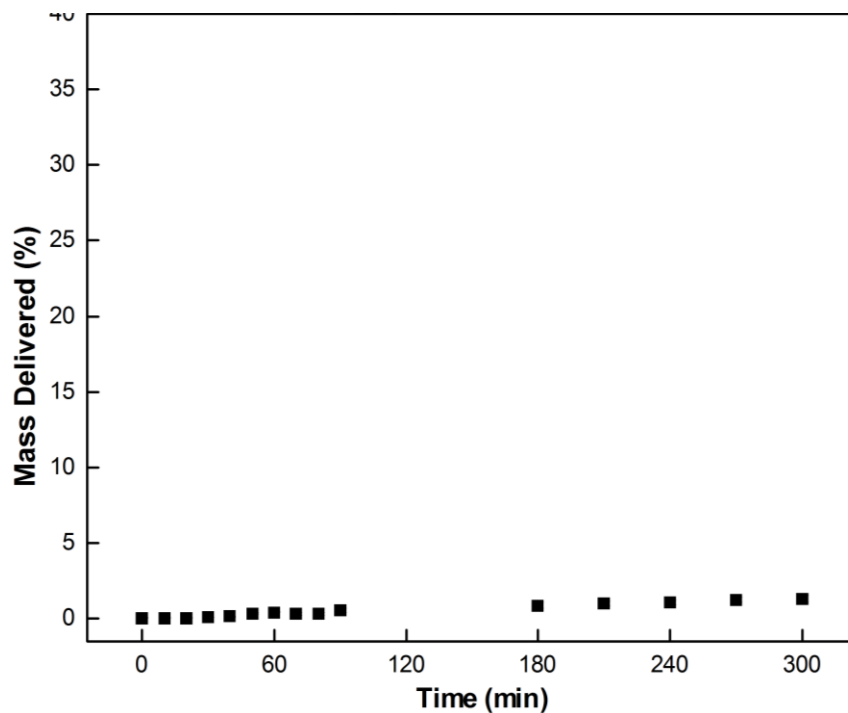


Figure 5.18. CV release profile from CVMOF@DBA. Details: UV cuvette was charged with 0.7 mg of capped crystals and filled with 2.5 mL EtOH. The absorbance was monitored by UV-Vis at 580 nm.

5.7. References

- (1) Rosi, N. L.; Eckert, J.; Eddaoudi, M.; Vodak, D. T.; Kim, J.; O'Keeffe, M.; Yaghi, O. M. Hydrogen Storage in Microporous Metal-Organic Frameworks. *Science* **2003**, *300*, 1127-1129.
- (2) Zhang, S.; Liu, X. Y.; Yang, Q.; Su, Z. Y.; Gao, W. J.; Wei, Q.; Xie, G.; Chen, S. P.; Gao, S. L. A New Strategy for Storage and Transportation of Sensitive High-Energy Materials: Guest-Dependent Energy and Sensitivity of 3D Metal-Organic-Framework-Based Energetic Compounds. *Chem. Eur. J.* **2014**, *20*, 7906-7910.
- (3) Yang, J.; Sudik, A.; Wolverton, C.; Siegel, D. J. High Capacity Hydrogen Storage Materials: Attributes for Automotive Applications and Techniques for Materials Discovery. *Chem. Soc. Rev.* **2010**, *39*, 656-675.
- (4) Schlapbach, L.; Zuttel, A. Hydrogen-Storage Materials for Mobile Applications. *Nature* **2001**, *414*, 353-358.
- (5) Duren, T.; Sarkisov, L.; Yaghi, O. M.; Snurr, R. Q. Design of New Materials for Methane Storage. *Langmuir* **2004**, *20*, 2683-2689.
- (6) Murray, L. J.; Dinca, M.; Long, J. R. Hydrogen Storage in Metal-Organic Frameworks. *Chem. Soc. Rev.* **2009**, *38*, 1294-1314.
- (7) Britt, D.; Furukawa, H.; Wang, B.; Glover, T. G.; Yaghi, O. M. Highly Efficient Separation of Carbon Dioxide by a Metal-Organic Framework Replete with Open Metal Sites. *Proc. Natl. Acad. Sci. U.S.A.* **2009**, *106*, 20637-20640.
- (8) Millward, A. R.; Yaghi, O. M. Metal-Organic Frameworks with Exceptionally High Capacity for Storage of Carbon Dioxide at Room Temperature. *J. Am. Chem. Soc.* **2005**, *127*, 17998-17999.

- (9) Czaja, A. U.; Trukhan, N.; Muller, U. Industrial Applications of Metal-Organic Frameworks. *Chem. Soc. Rev.* **2009**, *38*, 1284-1293.
- (10) Yang, J. M.; Ying, R. J.; Han, C. X.; Hu, Q. T.; Xu, H. M.; Li, J. H.; Wang, Q.; Zhang, W. Adsorptive Removal of Organic Dyes from Aqueous Solution by a Zr-Based Metal-Organic Framework: Effects of Ce(III) Doping. *Dalton Trans.* **2018**, *47*, 3913-3920.
- (11) Haque, E.; Lo, V.; Minett, A. I.; Harris, A. T.; Church, T. L. Dichotomous Adsorption Behaviour of Dyes on an Amino-Functionalised Metal-Organic Framework, Amino-MIL-101(Al). *J. Mater. Chem. A* **2014**, *2*, 193-203.
- (12) Wu, S. C.; You, X.; Yang, C.; Cheng, J. H. Adsorption Behavior of Methyl Orange onto an Aluminum-Based Metal Organic Framework, MIL-68(Al). *Water Sci. Technol.* **2017**, *75*, 2800-2810.
- (13) Wu, Z. B.; Yuan, X. Z.; Zhong, H.; Wang, H.; Zeng, G. M.; Chen, X. H.; Wang, H.; Zhang, L.; Shao, J. G. Enhanced Adsorptive Removal of *p*-Nitrophenol from Water by Aluminum Metal-Organic Framework/Reduced Graphene Oxide Composite. *Sci. Rep.* **2016**, *6*, 25638.
- (14) Choi, I. H.; Bin Yoon, S.; Huh, S.; Kim, S. J.; Kim, Y. Photophysical Properties of Cationic Dyes Captured in the Mesoscale Channels of Micron-Sized Metal-Organic Framework Crystals. *Sci. Rep.* **2018**, *8*, 9838.
- (15) DeFuria, M. D.; Zeller, M.; Genna, D. T. Removal of Pharmaceuticals from Water Via Pi-Pi Stacking Interactions in Perfluorinated Metal-Organic Frameworks. *Cryst. Growth Des.* **2016**, *16*, 3530-3534.
- (16) Orellana-Tavra, C.; Marshall, R. J.; Baxter, E. F.; Lazaro, I. A.; Tao, A.; Cheetham, A. K.; Forgan, R. S.; Fairen-Jimenez, D. Drug Delivery and Controlled Release from

Biocompatible Metal-Organic Frameworks Using Mechanical Amorphization. *J. Mater. Chem B* **2016**, *4*, 7697-7707.

(17) Agostoni, V.; Horcajada, P.; Noiray, M.; Malanga, M.; Aykac, A.; Jicsinszky, L.; Vargas-Berenguel, A.; Semiramoth, N.; Daoud-Mahammed, S.; Nicolas, V.; Martineau, C.; Taulelle, F.; Vigneron, J.; Etcheberry, A.; Serre, C.; Gref, R. A "Green" Strategy to Construct Non-Covalent, Stable and Bioactive Coatings on Porous MOF Nanoparticles. *Sci. Rep.* **2015**, *5*, 7925.

(18) Rojas, S.; Colinet, I.; Cunha, D.; Hidalgo, T.; Salles, F.; Serre, C.; Guillou, N.; Horcajada, P. Toward Understanding Drug Incorporation and Delivery from Biocompatible Metal-Organic Frameworks in View of Cutaneous Administration. *ACS Omega* **2018**, *3*, 2994-3003.

(19) Hartlieb, K. J.; Ferris, D. P.; Holcroft, J. M.; Kandela, I.; Stern, C. L.; Nassar, M. S.; Botros, Y. Y.; Stoddart, J. F. Encapsulation of Ibuprofen in Cd-MOF and Related Bioavailability Studies. *Mol. Pharm.* **2017**, *14*, 1831-1839.

(20) Chen, Q.; Chen, Q. W.; Zhuang, C.; Tang, P. P.; Lin, N.; Wei, L. Q. Controlled Release of Drug Molecules in Metal-Organic Framework Material HKUST-1. *Inorg. Chem. Commun.* **2017**, *79*, 78-81.

(21) Rangaraj, P.; Parshamoni, S.; Konar, S. MOF as a Syringe Pump for the Controlled Release of Iodine Catalyst in the Synthesis of Meso-Thienyl Dipyrrromethanes. *Chem. Commun.* **2015**, *51*, 15526-15529.

(22) Jia, Y. M.; Wei, B. M.; Duan, R. X.; Zhang, Y.; Wang, B. Y.; Hakeem, A.; Liu, N. N.; Ou, X. W.; Xu, S. F.; Chen, Z. F.; Lou, X. D.; Xia, F. Imparting Biomolecules to a Metal-Organic Framework Material by Controlled DNA Tetrahedron Encapsulation. *Sci. Rep.* **2014**, *4*, 5929.

(23) Horcajada, P.; Serre, C.; Maurin, G.; Ramsahye, N. A.; Balas, F.; Vallet-Regi, M.; Sebban, M.; Taulelle, F.; Ferey, G. Flexible Porous Metal-Organic Frameworks for a Controlled Drug Delivery. *J. Am. Chem. Soc.* **2008**, *130*, 6774-6780.

(24) Sakata, Y.; Furukawa, S.; Kondo, M.; Hirai, K.; Horike, N.; Takashima, Y.; Uehara, H.; Louvain, N.; Meilikhov, M.; Tsuruoka, T.; Isoda, S.; Kosaka, W.; Sakata, O.; Kitagawa, S. Shape-Memory Nanopores Induced in Coordination Frameworks by Crystal Downsizing. *Science* **2013**, *339*, 193-196.

(25) Diring, S.; Furukawa, S.; Takashima, Y.; Tsuruoka, T.; Kitagawa, S. Controlled Multiscale Synthesis of Porous Coordination Polymer in Nano/Micro Regimes. *Chem. Mater.* **2010**, *22*, 4531-4538.

(26) Hermes, S.; Witte, T.; Hikov, T.; Zacher, D.; Bahnmüller, S.; Langstein, G.; Huber, K.; Fischer, R. A. Trapping Metal-Organic Framework Nanocrystals: An *in-Situ* Time-Resolved Light Scattering Study on the Crystal Growth of MOF-5 in Solution. *J. Am. Chem. Soc.* **2007**, *129*, 5324-5325.

(27) Kondo, M.; Furukawa, S.; Hirai, K.; Kitagawa, S. Coordinatively Immobilized Monolayers on Porous Coordination Polymer Crystals. *Angew. Chem. Int. Ed.* **2010**, *49*, 5327-5330.

(28) Yanai, N.; Sindoro, M.; Yan, J.; Granick, S. Electric Field-Induced Assembly of Monodisperse Polyhedral Metal-Organic Framework Crystals. *J. Am. Chem. Soc.* **2013**, *135*, 34-37.

(29) Zheng, C. C.; Wang, Y.; Phua, S. Z. F.; Lim, W. Q.; Zhao, Y. L. ZnO-DOX@ZIF-8 Core-Shell Nanoparticles for Ph-Responsive Drug Delivery. *ACS Biomater. Sci. Eng.* **2017**, *3*, 2223-2229.

- (30) Zhuang, J.; Kuo, C. H.; Chou, L. Y.; Liu, D. Y.; Weerapana, E.; Tsung, C. K. Optimized Metal-Organic-Framework Nanospheres for Drug Delivery: Evaluation of Small-Molecule Encapsulation. *ACS Nano* **2014**, *8*, 2812-2819.
- (31) Basa, P. N.; Antala, S.; Dempksi, R. E.; Burdette, S. C. A Zinc(II) Photocage Based on a Decarboxylation Metal Ion Release Mechanism for Investigating Homeostasis and Biological Signaling. *Angew. Chem. Int. Ed.* **2015**, *54*, 13027-13031.
- (32) Shaikh, M. H.; Subhedar, D. D.; Nawale, L.; Sarkar, D.; Khan, F. A. K.; Sangshetti, J. N.; Shingate, B. B. 1,2,3-Triazole Derivatives as Antitubercular Agents: Synthesis, Biological Evaluation and Molecular Docking Study. *Med. Chem. Commun.* **2015**, *6*, 1104-1116.
- (33) Li, H.; Eddaoudi, M.; O'Keeffe, M.; Yaghi, O. M. Design and Synthesis of an Exceptionally Stable and Highly Porous Metal-Organic Framework. *Nature* **1999**, *402*, 276-279.
- (34) Bandara, H. M. D.; Kennedy, D. P.; Akin, E.; Incarvito, C. D.; Burdette, S. C. Photoinduced Release of Zn²⁺ with ZinCleave-1: A Nitrobenzyl-Based Caged Complex. *Inorg. Chem.* **2009**, *48*, 8445-8455.
- (35) Eddaoudi, M.; Kim, J.; Rosi, N.; Vodak, D.; Wachter, J.; O'Keeffe, M.; Yaghi, O. M. Systematic Design of Pore Size and Functionality in Isoreticular MOFs and Their Application in Methane Storage. *Science* **2002**, *295*, 469-472.
- (36) Loera-Serna, S.; Ortiz, E.; Beltran, H. I. First Trial and Physicochemical Studies on the Loading of Basic Fuchsin, Crystal Violet and Black Eriochrome T on HKUST-1. *New J. Chem.* **2017**, *41*, 3097-3105.
- (37) Abbasi, A. R.; Karimi, M.; Daasbjerg, K. Efficient Removal of Crystal Violet and Methylene Blue from Wastewater by Ultrasound Nanoparticles Cu-MOF in Comparison with Mechanochemical Method. *Ultrason. Sonochem.* **2017**, *37*, 182-191.

- (38) Yang, B. C.; Jiang, Y. D.; Qin, X. J.; Chen, Z. L.; Ren, F. Loaded and *in vitro* Drug Release of Anticancer Drugs in Porous Metal-Organic Frameworks. *Chem. J. Chinese U.* **2012**, *33*, 26-31.
- (39) Gonzalez, J.; Devi, R. N.; Tunstall, D. P.; Cox, P. A.; Wright, P. A. Deuterium NMR Studies of Framework and Guest Mobility in the Metal-Organic Framework Compound MOF-5, $Zn_4O(O_2CC_6H_4CO_2)_3$. *Microporous Mesoporous Mater.* **2005**, *84*, 97-104.
- (40) Hirscher, M.; Panella, B.; Schmitz, B. Metal-Organic Frameworks for Hydrogen Storage. *Microporous Mesoporous Mater.* **2010**, *129*, 335-339.
- (41) Burrows, A. D.; Cassar, K.; Friend, R. M. W.; Mahon, M. F.; Rigby, S. P.; Warren, J. E. Solvent Hydrolysis and Templating Effects in the Synthesis of Metal-Organic Frameworks. *Crystengcomm* **2005**, *7*, 548-550.